



저작자표시-비영리-변경금지 2.0 대한민국

이용자는 아래의 조건을 따르는 경우에 한하여 자유롭게

- 이 저작물을 복제, 배포, 전송, 전시, 공연 및 방송할 수 있습니다.

다음과 같은 조건을 따라야 합니다:



저작자표시. 귀하는 원저작자를 표시하여야 합니다.



비영리. 귀하는 이 저작물을 영리 목적으로 이용할 수 없습니다.



변경금지. 귀하는 이 저작물을 개작, 변형 또는 가공할 수 없습니다.

- 귀하는, 이 저작물의 재이용이나 배포의 경우, 이 저작물에 적용된 이용허락조건을 명확하게 나타내어야 합니다.
- 저작권자로부터 별도의 허가를 받으면 이러한 조건들은 적용되지 않습니다.

저작권법에 따른 이용자의 권리는 위의 내용에 의하여 영향을 받지 않습니다.

이것은 [이용허락규약\(Legal Code\)](#)을 이해하기 쉽게 요약한 것입니다.

[Disclaimer](#)

약학박사 학위논문

**Preparation and characterization of self-assembled nanoparticles
based on low-molecular-weight heparin and stearylamine
conjugates for controlled delivery of docetaxel**

도세탁셀의 약물전달을 위한 저분자량 헤파린과 스테아릴아
민 중합체를 이용한 자가조립나노입자의 제조 및 평가

2015년 2월

서울대학교 대학원

약학과 약제과학 전공

김동환

**Preparation and characterization of self-assembled nanoparticles
based on low-molecular-weight heparin and stearylamine conjugates
for controlled delivery of docetaxel**

**도세탁셀의 약물전달을 위한 저분자량 헤파린과 스테아릴아민
중합체를 이용한 자가조립나노입자의 제조 및 평가**

지도 교수 김 대 덕

이 논문을 약학박사 학위논문으로 제출함

2014 년 11 월

서울대학교 대학원

약학과 약제과학 전공

김 동 환

김동환의 약학박사 학위논문을 인준함

2014년 12월

위원장 정 석 재 (인)

부위원장 최 한 곤 (인)

위원 김 대 덕 (인)

위원 이 우 인 (인)

위원 조 현 종 (인)

Abstract

Preparation and characterization of self-assembled nanoparticles based on low-molecular-weight heparin and stearylamine conjugates for controlled delivery of docetaxel

Dong-Hwan Kim

Department of Pharmaceutical Science

College of Pharmacy

The Graduate School

Seoul National University

Part I. Synthesis and characterization of amphiphilic polymer consisted of low-molecular-weight heparin and stearylamine for the preparation of self-assembled nanoparticles

Low-molecular-weight heparin (LMWH) is a hydrophilic polysaccharide with anticancer activity and reduces anticoagulant activity than unfractionated heparin. Stearylamine (SA) was conjugated to LMWH to prepare amphiphilic polymeric drug carrier that forms self-assembled nanoparticles in aqueous environment. LMWH-SA (LHSA) conjugates were synthesized with various molar ratios (LMWH:SA = 1:1, 1:3 and 1:5) using EDC and NHS as coupling agents. The structures of LHSA conjugates were characterized by $^1\text{H-NMR}$. Physicochemical properties of LHSA-based self-assembled nanoparticles were then characterized in terms of particle size, zeta potential and morphology. Among the conjugates synthesized, stable nanoparticles with the mean diameter of 178 nm was formed in the molar

ratio of 1:5 (LHSA5). The critical micelle concentration (CMC) of LHSA5 conjugate under aqueous condition was 0.044 mg/ml. The anti-coagulant activity of LHSA5 nanoparticles was 31.92% of free LMWH. These results suggest that LHSA5 conjugate could be a potential biomaterial for the preparation of self-assembled nano-sized drug delivery systems which has biological activity of LMWH and can encapsulate poorly water-soluble anticancer drugs for tumor-targeted delivery.

Keywords: Low-molecular-weight heparin, Stearylamine, Amphiphilic polymer, Self-assembled nanoparticle, Drug delivery

Part II. Characterization and evaluation of self-assembled nanoparticles based on low-molecular-weight heparin and stearylamine conjugates for controlled delivery of docetaxel

Low-molecular-weight heparin (LMWH)–stearylamine (SA) conjugates (LHSA)-based self-assembled nanoparticles were prepared for intravenous delivery of docetaxel (DCT). 1-Ethyl-3-(3-dimethylaminopropyl) carbodiimide and N-hydroxysuccinimide were used as coupling agents for synthesis of LHSA conjugates. The physicochemical properties, *in vitro* antitumor efficacy, *in vitro* cellular uptake efficiency, *in vivo* antitumor efficacy, and *in vivo* pharmacokinetics of LHSA nanoparticles were investigated. The LHSA nanoparticles exhibited a spherical shape with a mean diameter of 140–180 nm and a negative surface charge. According to *in vitro* release and *in vivo* pharmacokinetic test results, the DCT-loaded LHSA5 (LMWH:SA = 1:5) nanoparticles exhibited sustained drug release profiles. The blank LHSA nanoparticles demonstrated only an insignificant cytotoxicity in MCF-7 and MDAMB

231 human breast cancer cells; additionally, higher cellular uptake of coumarin 6 (C6) in MCF-7 and MDAMB 231 cells was observed in the LHS A5 nanoparticles group than that in the C6 solution group. The *in vivo* tumor growth inhibition efficacy of DCT-loaded LHS A5 nanoparticles was also significantly higher than the Taxotere-treated group in the MDAMB 231 tumor xenografted mouse model. These results indicated that the LHS A5-based nanoparticles could be a promising anticancer drug delivery system.

Keywords: Amphiphilic polymer, Docetaxel, Drug delivery, Low-molecular-weight heparin, Self-assembled nanoparticle

Student Number: 2011-30499

Contents

Abstract.....	I
List of Tables.....	IV
List of Figures.....	IV

Part I. Synthesis and characterization of amphiphilic polymer consisted of low-molecular-weight heparin and stearylamine for the preparation of self-assembled nanoparticles

1. Introduction.....	2
2. Materials and methods.....	3
2.1. Materials.....	3
2.2. Synthesis of LHSa conjugates.....	4
2.3. Characterization of LHSa conjugates.....	5
2.4. Preparation and characterization of LHSa-based nanoparticles.....	5
3. Results.....	6
3.1. Synthesis and characterization of LHSa conjugates.....	6
3.2. Quantitative analysis of LMWH in LHSa conjugate and its anticoagulant activity.....	7
3.3. CMC determination of blank LHSa nanoparticles.....	7
3.4. Preparation and characterization of LHSa-based self-assembled nanoparticles.....	7
4. Discussion.....	8
5. Conclusion.....	10

6. References.....	11
---------------------------	-----------

Part II. Characterization and evaluation of self-assembled nanoparticles based on low-molecular-weight heparin and stearylamine conjugates for controlled delivery of docetaxel

1. Introduction.....	26
2. Materials and methods.....	28
2.1. Materials.....	28
2.2. Synthesis and characterization of LHSA conjugates.....	29
2.3. Preparation and characterization of LHSA-based nanoparticles.....	29
2.4. In vitro docetaxel release studies.....	30
2.5. In vitro cytotoxicity of conjugate.....	31
2.6. In vitro antitumor efficacy studies.....	31
2.7. Cellular uptake studies.....	32
2.8. In vivo antitumor efficacy.....	33
2.9. In vivo pharmacokinetic study in rats.....	33
2.10. Statistical analysis.....	35
3. Results.....	35
3.1. Synthesis and characterization of LHSA conjugates.....	35
3.2. Preparation and characterization of LHSA-based self-assembled nanoparticles.....	36
3.3. In vitro docetaxel release.....	37
3.4. In vitro cytotoxicity of conjugate.....	37
3.5. In vitro antitumor effect.....	37

3.6. In vitro cellular uptake study.....	38
3.7. In vivo antitumor efficacy.....	39
3.8. In vivo pharmacokinetic study.....	39
4. Discussion.....	40
5. Conclusion.....	43
6. References.....	45
국문초록.....	63
Appendix	65

List of Tables

Part I. Synthesis and characterization of amphiphilic polymer consisted of low-molecular-weight heparin and stearylamine for the preparation of self-assembled nanoparticles

Table 1 Characterization of LHSA conjugates..... 17

Table 2 Characterization of LHSA nanoparticles..... 18

Part II. Characterization and evaluation of self-assembled nanoparticles based on low-molecular-weight heparin and stearylamine conjugates for controlled delivery of docetaxel

Table 1 Characterization of LHSA5 nanoparticles..... 52

Table 2 Pharmacokinetic parameters of Taxotere and DCT-loaded LHSA5 nanoparticles after a single intravenous injection (8mg/kg) in rats (n=4)..... 53

List of Figures

Part I. Synthesis and characterization of amphiphilic polymer consisted of low-molecular-weight heparin and stearylamine for the preparation of self-assembled nanoparticles

Figure 1 Synthetic scheme for LHSA conjugates. 19

Figure 2 ^1H NMR spectra of (a) LMWH and (b) LHSA1 and (c) LHSA3 (d) LHSA5 and (e) SA, respectively. Samples were dissolved in D_2O for ^1H NMR analysis [$\text{R} = -\text{SO}_3^-$ (predominant) or $-\text{COCH}_3$ (peak #13); $\text{R}' = \text{SA}$]. 20

Figure 3 Standard absorbance curve for quantitative analysis of LMWH. 21

Figure 4 Relationship between the ratio of integration area (2.80/1.95 ppm) and molar ratio of SA/LMWH based on their physical mixture. 22

Figure 5 CMC determination of LHSA5 nanoparticles. Fluorescence intensity ratio (I1/I3) according to LHSA5 concentration as plotted and CMC was estimated from the threshold concentration of self-assembled nanoparticles. 23

Figure 6 Size distribution and TEM images of LHSA nanoparticles. 24

Part II. Characterization and evaluation of self-assembled nanoparticles based on low-molecular-weight heparin and stearylamine conjugates for controlled delivery of docetaxel

Figure 1 Schematic illustration of LHSA-based nanoparticles. 54

Figure 2 Size distribution and TEM images of DCT-loaded LHSA5 nanoparticles. The length of the scale bar in TEM images is 500 nm (× 200,000). **55**

Figure 3 *In vitro* release profile of DCT from LHSA5-based nanoparticles. Each point represents as mean ± S.D. (n=3). **56**

Figure 4 *In vitro* cytotoxicity of LHSA5 in (a) MCF-7 and (b) MDAMB 231 cells. Cell viability was measured by MTS-based assay after incubating LMWH or LHSA5 at various polymer concentrations for 24 h. Data represent as mean ± S.D. (n=5). **57**

Figure 5 *In vitro* antitumor efficacy of Taxotere and DCT-loaded LHSA5 nanoparticles in (a) MCF-7 and (b) MDAMB 231 cells. **58**

Figure 6 *In vitro* cellular uptake study of coumarin 6 was observed by CLSM in MCF-7 and MDAMB 231 cells after incubating for 2 h. Merged images composed of coumarin 6 (green color) and DAPI (blue color) were shown. Groups were as follows; control, blank LHSA5 nanoparticles, coumarin 6 solution, coumarin 6-loaded LHSA5 nanoparticles. **59**

Figure 7 *In vitro* cellular uptake study of coumarin 6 was observed by FACS in (a) MCF-7 and (b) MDAMB 231 cells after incubating for 2 h. Groups were as follows; control, blank LHSA5 nanoparticles, coumarin 6 solution, coumarin 6-loaded LHSA5 nanoparticles. Data represent as mean ± S.D. (n=4). **60**

Figure 8 *In vivo* antitumor efficacy in the MDAMB 231 tumor-bearing mouse model. (a) Tumor volume (mm³) profiles according to time (day) are shown. All samples were injected on day 0, 7, and 14. Points indicate the means ± SD (n=5). (b) Body weight (g) was also measured with tumor size measurement for 18 days. Points indicate the means ± SD (n=5). * p < 0.05 compared with the control group; # p < 0.05 compared with the LHSA5 group; + p < 0.05 compared with the Taxotere group. **61**

Figure 9 *In vivo* pharmacokinetic profile after intravenous injection of Taxotere and DCT-loaded LHSAs nanoparticles formulation in rats at a dose of 8 mg/kg as DCT. Points represent the mean \pm SD (n=4). **62**

Part I. Synthesis and characterization of amphiphilic polymer consisted of low-molecular-weight heparin and stearylamine for the preparation of self-assembled nanoparticles

1. Introduction

In the past decades, polymeric nanoparticulate systems have been widely studied for drug delivery [1-3]. Their advantages include the penetration enhancement through capillary vessels to target organs (*i.e.*, passive targeting), prolonged systemic circulation by avoiding phagocytosis, improved efficacy, and reduced toxicity [4, 5]. Numerous biocompatible and biodegradable materials such as poly(lactic acid) [6, 7], poly(glycolic acid) [8], polycaprolactone [9, 10], polysaccharides [11], proteins [12] and polypeptides [13] have been employed for the preparation of polymeric nanoparticles. Among them, polysaccharides have been extensively used to prepare nanoparticles for drug delivery [4]. Polysaccharides are natural biomaterials, and they thus are generally safe, non-toxic, biocompatible and biodegradable. They have various derivable groups which can be readily modified with other chemicals. For instance, several polysaccharide derivatives including chitosan [14, 15] and hyaluronic acid derivatives [16, 17] have been synthesized and evaluated.

Heparin is a biocompatible, biodegradable, and water-soluble natural polysaccharide, which is reported to have diverse biological activities including anti-coagulation, anti-inflammation, and anti-angiogenesis [18]. In addition to its well-known anticoagulant activity, heparin has been studied for anticancer activity [19, 20]. However, unfractionated heparin (UFH) may cause several adverse effects including bleeding, which is the major drawback restricting its clinical applications. On the other hand, low-molecular-weight heparin (LMWH) exerts a reduced anticoagulant activity, but improved anticancer activity than UFH [21]. Thus, LMWH is preferable to UFH for the initial treatment of venous thromboembolism prevalent in cancer patients [22]. LMWH exerts its anticancer activity by affecting the proliferation, adhesion, angiogenesis, migration, and invasion of cancer cells. Although the exact

mechanism of LMWH interference with cancer biology still remains unclear, it may involve the inhibition of both coagulation and non-coagulation-dependent pathways of tumor progression [23]. In addition, heparin has affinity to laminin $\alpha 1$ chain, a major component of the basement membrane matrix in several cells, that can directly promote the cell adhesion and spreading of B16F10, M2, HT1080, and PC12 cells [24]. Thus, researchers have studied heparin derivatives to apply LMWH as anticancer drug carriers, as well as targeting to cancer cells [25, 26]. These idiosyncratic properties make heparin an attractive biomaterial for anticancer drug delivery system [27, 28].

It is also well known that amphiphilic polymers can be synthesized by grafting hydrophobic residues to the hydrophilic polymer, such as heparin. They can form self-assembled nanoparticles composed of a hydrophilic shell and a hydrophobic core in the aqueous environment. Heparin-drug conjugates have been evaluated for their feasibility as anticancer agents in the form of macromolecular prodrugs [29, 30]. However, poorly water-soluble drugs can also be encapsulated in the internal hydrophobic core, and drug solubility can be increased [31, 32]. Thus, the objective was to design novel amphiphilic LMWH-stearylamine (LHSA) conjugates, which form self-assembled nanoparticles for targeted anticancer drug delivery. Stearylamine (SA), an aminated fatty acid, was conjugated to LMWH by EDC/NHS-coupled reaction to produce amphiphilic LMWH derivatives. LHSA-based self-assembled nanoparticles were then prepared and characterized in terms of their particle size, zeta potential, morphology, CMC, and composition.

2. Materials and methods

2.1. Materials

Low-molecular-weight heparin (LMWH, 101 IU/mg, average molecular weight : 4,500 Da) was purchased from Nanjing King-Friend Biochemical Pharmaceutical Co. Ltd. 1-Ethyl-3-(3-dimethylaminopropyl) carbodiimide (EDC), N-hydroxysuccinimide (NHS), toluidine blue and stearylamine (SA) were obtained from Sigma-Aldrich Co. (St. Louis, MO, USA). Docetaxel was purchased from Taihua Co. (Xi'an, China). Formamide (FA), tetrahydrofuran (THF), acetonitrile (HPLC grade) were supplied by Fisher Scientific Korea Ltd. Coatest Factor Xa assay kits were purchased from Chromogenix (Milano, Italy). Water was purified by distillation, deionization, and reverse osmosis (Milli-Q plus). All other reagents were of analytical grade and obtained from commercial sources.

2.2. Synthesis of LHSA conjugates

Amphiphilic LHSA conjugates were synthesized from LMWH and SA. Briefly, LMWH (1g) was dissolved in formamide (200 mL) by gentle heating. To synthesize the LHSA conjugates, different amounts of EDC and NHS (3 mol/mol, SA) were mixed with LMWH solutions at room temperature, followed by the addition of different amounts of SA (1, 3, and 5 mol/mol, LMWH) dissolved in THF (132 mL). This solution was stirred at room temperature for 24 h. The mixtures were precipitated in excess cold acetone (5 times the volume of mixture) under vigorous agitation, filtered by glass filter (G4), and stirred for 30 min. The residues on the glass filter were carefully washed three times with cold acetone to remove excess EDC, NHS, and SA, followed by filtering with 50 mL of DDW. The filtrate was dialyzed with dialysis membrane (molecular weight cut-off = 1 kDa; Spectrum Laboratories, Laguna Hills, CA, USA) against distilled deionized water (DDW) for 48 h and lyophilized.

2.3. Characterization of LHSA conjugates

The $^1\text{H-NMR}$ spectra were obtained using a Varian FT 500-MHz NMR spectrometer (Varian Inc., Palo Alto, CA, USA). Samples (10 mg/mL) were dissolved in D_2O . Additionally, The values of the proton peaks from the $^1\text{H-NMR}$ spectra were integrated to determine the molar substitution of LHSA. Linear regression was prepared from the physical mixture of LMWH and SA at various molar ratios (LMWH:SA =0.5:1, 1:1, 1:2, and 1:4) dissolved in the mixture of $\text{D}_2\text{O/THF-d}_8$ (1:1). The ratio of the integration area (2.80/1.95 ppm) of each physical mixture was calculated. The content of the conjugated LMWH was analyzed by the colorimetric method using toluidine blue [33]. Briefly, 0.1 mL aliquot of toluidine blue solution (0.05 g of toluidine blue dissolved in 1 L of 0.01 N HCl containing 0.2 % NaCl) was transferred into the test tubes. LMWH standard solution (0.1 mL) with various concentrations (0.1~2.0 $\mu\text{g/mL}$ in 0.2 % NaCl) was added to the toluidine blue solution. After adding hexane (1.0 mL), the solution was vortexed for 30s, after which was allowed for a phase separation. The absorbance of the aqueous layers was determined at 631 nm on a UV spectrophotometer. The anticoagulant activities of LMWH and LHSA conjugates were determined by Coatest anti-FXa chromogenic assay (Chromogenix, Milano, Italy). Critical micelle concentration (CMC) of LHSA was investigated by using pyrene as a fluorescence probe, as described previously [34]. Pyrene solution in THF (2×10^{-6} M) was prepared, and the THF was evaporated under a gentle nitrogen (N_2) gas stream for 1 h at 60°C . LHSA solution in DDW (1 mL), in the concentration range of 10^{-5} to 1 mg/mL, was added to each tube to achieve a final pyrene concentration of 6×10^{-7} M. Intensity ratio (I_1/I_3) in the excitation spectra was calculated and plotted. The excitation wavelength was fixed at 334 nm after scanning from 350 nm to 550 nm, and the slit openings for excitation and emission were

set at 10 and 3 nm, respectively. Fluorescence measurements were performed using a fluorescent spectrometer FP-6500 (JASCO CO., Tokyo, Japan).

2.4. Preparation and characterization of LHSA-based nanoparticles

Mean diameter, poly-dispersity index and zeta potential of the nanoparticles were determined using a light scattering spectrophotometer ELS-Z (Otsuka Electronics, Japan). LHSA conjugates (10 mg) were resuspended in DDW (1 mL) by vortexing for 30 s, and filtered through a 0.22- μ m pore size syringe filter (Minisart RC 15, Sartorius Stedium Biotech GmbH, Goettingen, Germany). The morphology of LHSA-based nanoparticles was assessed by transmission electron microscopy (TEM, JEM 1010, JEOL, Japan). The nanoparticle suspensions were stained with 2 % (w/v) phosphotungstic acid (PTA), placed on a copper grid coated with carbon film, air-dried for 10 min, and photographed.

3. Results

3.1. Synthesis and characterization of LHSA conjugates

Heparin and its derivatives have been widely used as drug delivery systems [26, 35, 36]. In this study, SA, an aminated fatty acid, was conjugated to LMWH to produce an amphiphilic polymer. The amine group of SA was covalently coupled to carboxylic group of LMWH in the presence of EDC and NHS, thus producing amphiphilic LHSA conjugates (Figure 1). In this coupling reaction, several LHSA conjugates were synthesized by adjusting the feed ratio of SA to LMWH (LHSA1- LMWH:SA = 1:1, LHSA3- LMWH:SA = 1:3, LHSA5- LMWH:SA = 1:5, respectively). The synthesized LHSA conjugates were confirmed by $^1\text{H-NMR}$ analysis (Figure 2). The $^1\text{H-NMR}$ spectra of LHSA conjugate exhibited proton

signals for both LMWH and SA. Although the existence of broad proton peaks of the LMWH, the presence of SA in LHSA conjugate was confirmed by its chemical shifts at 0.8- 1.2 ppm. The results indicated that the degree of substitution of LHSA increased with the increase in the feed ratio of SA.

3.2. Quantitative analysis of LMWH in LHSA conjugate and its anticoagulant activity

For quantitative determination of LMWH in LHSA conjugate, the toluidine blue-based colorimetric method was utilized. The standard curve of LMWH (0.2–2.0 $\mu\text{g/mL}$ concentration) shows linearity in the range (Figure 3). The physical mixtures of LMWH and SA with various molar ratios, prepared for calculation of the molar substitution ratio of LHSA, were analyzed by $^1\text{H-NMR}$. The linear regression line was plotted by the ratio of the integration area between the SA peak (2.80 ppm) and the LMWH peak (1.95 ppm). The degree of substitution of LHSA5 was calculated to be 34.0%, which indicates that approximately 1.7 of SA is conjugated to each LMWH (Figure 4). The amount of LMWH associated with LHSA conjugate was determined (Table 1). The anticoagulant activity of the LHSA1, LHSA3 and LHSA5 was calculated to be 60.41, 32.09 and 31.92 % as compared to free LMWH (Table 1). The anticoagulant activity of LHSA conjugate decreased as its LMWH content decreased, which is consistent with previously reported heparin derivatives [37, 38].

3.3. CMC determination of blank LHSA nanoparticles

CMC of LHSA nanoparticles was determined by fluorescence intensity measurements in the presence of pyrene as a probe. The fluorescence intensity ratio (I_1/I_3) was measured at a various concentration of LHSA conjugate and the CMC was estimated from the threshold

concentration of self-assembled nanoparticles (Figure 5). The CMC value of LHSA5 was 0.044 mg/ml but those of LHSA1 and LHSA3 could not be determined (Table1). This result suggests that LHSA5 conjugate can form more stable nanoparticulate structures in aqueous environment rather than LHSA1 or LHSA3.

3.4. Preparation and characterization of LHSA-based self-assembled nanoparticles

The mean diameter and zeta potential values are shown in Table 2. Mean diameter of self-assembled nanoparticles based on LHSA was ranged in 140-180 nm. LHSA5 nanoparticle has a narrow size distribution (< 0.2 of polydispersity index), compared to LHSA1 and LHSA3 nanoparticles (> 0.2 of polydispersity index). This result indicates the higher substitution ratio of SA to LMWH can make more compact and stable LHSA nanoparticle. The zeta potential values of the nanoparticles were negatively charged due to the LMWH located on the surface of the shell. It implies LHSA nanoparticles may also exert the biological activity of heparin. The shape of the LHSA nanoparticles was observed by TEM (Figure 6). LHSA5 nanoparticles exhibited spherical shape, on the other hand, LHSA1 and LHSA3 nanoparticles rendered broken or slightly aggregated morphology.

4. Discussion

Novel amphiphilic LHSA conjugates with different LMWH to SA mole ratio were synthesized and the feasibility of forming stable self-assembled nanoparticles was studied. From ¹H NMR analysis of LHSA conjugates, the proton peak of SA (chemical shifts at 0.8-1.2 ppm) in LHSA1 and LHSA3 was lower than LHSA5 (Figure 2). Accurate substitution ratio (SA to LMWH) can be determined from ¹H NMR spectrum of LHSA. In previously

study [39], the correlation of molar ratio of arachidic acid (AA) to chitosan oligosaccharide (CSO) was evaluated using ^1H NMR from physical mixture of AA and CSO in DMSO-d_6 . In this study, however, LMWH has a strong hydrophilic property, while SA has a strong hydrophobic property. Therefore, none of NMR solvent could simultaneously dissolve physical mixture of SA and LMWH. Because of this limitation, the content of LMWH in LHSA was indirectly analyzed by the toluidine blue colorimetric method [33]. It is assumed that established assay (Figure 3) could help identify the synthesis of LHSA and calculate the weight ratio of heparin and SA. These results are in consistent with those of the anticoagulant activity of LHSA conjugates calculated by anti-FXa chromogenic assay (Table 1). The anticoagulant activity of LHSA conjugates decreased as the amount of chemically coupled SA increased (Table 1)

All LHSA1, LHSA3 and LHSA5 conjugates prepared in this study could form self-assembled nanoparticles with the particle size of 140–180 nm. It is well known that nanoparticles with a mean diameter < 200 nm can effectively accumulate in the tumor *via* the enhanced permeation and retention (EPR) effect and exhibit reduced uptake by reticuloendothelial system (RES) [40, 41]. Among them, LHSA5 nanoparticles showed more narrow size distribution and stable spherical morphology than LHSA1 and LHSA3 nanoparticles (Figure 6). However, LHSA1 and LHSA3 conjugates did not possess the hydrophobicity necessary for the formation of stable nanoparticle due to low substitution ratio of SA. Additionally, CMC value of LHSA5 conjugate was significantly lower (44 $\mu\text{g/ml}$) than those of other low-molecular-weight surfactants or amphiphilic polymers [42, 43], indicating that it can form stable nanoparticle structure even in the lower polymer concentration after dilution with body fluids.

SA of LHSA could constitute an internal hydrophobic core, while LMWH of LHSA

could constitute a hydrophilic outer shell of the nanoparticles in aqueous environment. SA located in the core could provide the area that can encapsulate insoluble drugs [44]. It was interesting to note that the zeta potential values of LHSA nanoparticles were negatively charged, indicating that LMWH located on the surface of the shell. Therefore, even the anticoagulant activity of LHSA seems to be lower than unmodified LMWH, LHSA still can possess the activity of heparin after forming nanoparticles. Since LMWH is effective in reducing the risk of embolic event in patients with malignancy and acute venous thromboembolism [45], use of LMWH in cancer patients is recommended in numerous guidelines and is now regarded as a standard of care [46]. Thus, the self-assembled LHSA5 nanoparticle could be attractive as an anticancer drug carrier, which has a synergic effect with poorly water-soluble anticancer drug encapsulated in the core. Further studies are underway in this laboratory to evaluate the feasibility of LMWH nanoparticles as a novel anticancer drug carrier for tumor-targeted delivery.

5. Conclusion

LHSA conjugates were successfully synthesized and self-assembled nanoparticles based on LHSA were prepared. The LHSA-based nanoparticle has LMWH moiety on the outer shell resulting in negative surface charge. Among synthesized conjugates, LHSA5 could form stable self-assembled nanoparticles in the aqueous environment with a narrow size distribution. Since LHSA5 nanoparticle showed 30% anticoagulant activity compared to free LMWH, it is also expected to maintain the other heparin activities. These results suggested that LHSA5-based nanoparticles could be an attractive tumor-targeted delivery system for anticancer drugs.

6. References

- [1] T. Jung, W. Kamm, A. Breitenbach, E. Kaiserling, J. Xiao, T. Kissel, Biodegradable nanoparticles for oral delivery of peptides: is there a role for polymers to affect mucosal uptake?, *European Journal of Pharmaceutics and Biopharmaceutics*, 50 (2000) 147-160.
- [2] C. Pinto Reis, R.J. Neufeld, A.J. Ribeiro, F. Veiga, Nanoencapsulation I. Methods for preparation of drug-loaded polymeric nanoparticles, *Nanomedicine: Nanotechnology, Biology and Medicine*, 2 (2006) 8-21.
- [3] J. Kreuter, Nanoparticles and microparticles for drug and vaccine delivery, *Journal of Anatomy*, 189 (1996) 503-505.
- [4] Z. Liu, Y. Jiao, Y. Wang, C. Zhou, Z. Zhang, Polysaccharides-based nanoparticles as drug delivery systems, *Advanced Drug Delivery Reviews*, 60 (2008) 1650-1662.
- [5] A. Bhardwaj, V. Balakrishnan, P. Srivastava, H. Sehgal, Self assembled nanoparticle $Pb_{1-x}Fe_xSe$ /single crystal Si heterojunctions, *Current Applied Physics*, 10 (2010) 203-207.
- [6] T. Verrecchia, G. Spenlehauer, D. Bazile, A. Murry-Brelier, Y. Archimbaud, M. Veillard, Non-stealth (poly (lactic acid/albumin)) and stealth (poly (lactic acid-polyethylene glycol)) nanoparticles as injectable drug carriers, *Journal of Controlled Release*, 36 (1995) 49-61.
- [7] X. Shao, Q. Liu, C. Zhang, X. Zheng, J. Chen, Y. Zha, Y. Qian, X. Zhang, Q. Zhang, X. Jiang, Concanavalin A-conjugated poly (ethylene glycol)-poly (lactic acid) nanoparticles for intranasal drug delivery to the cervical lymph nodes, *Journal of Microencapsulation*, (2013) 1-7.
- [8] V. Labhasetwar, C. Song, W. Humphrey, R. Shebuski, R.J. Levy, Arterial uptake of biodegradable nanoparticles: effect of surface modifications, *Journal of Pharmaceutical Sciences*, 87 (1998) 1229-1234.

- [9] J. Molpeceres, M. Guzman, M.R. Aberturas, M. Chacon, L. Berges, Application of central composite designs to the preparation of polycaprolactone nanoparticles by solvent displacement, *Journal of Pharmaceutical Sciences*, 85 (1996) 206-213.
- [10] S. Aishwarya, S. Mahalakshmi, P.K. Sehgal, Collagen-coated polycaprolactone microparticles as a controlled drug delivery system, *Journal of Microencapsulation*, 25 (2008) 298-306.
- [11] S. Sharma, H.A. Benson, T.K. Mukkur, P. Rigby, Y. Chen, Preliminary studies on the development of IgA-loaded chitosan-dextran sulphate nanoparticles as a potential nasal delivery system for protein antigens, *Journal of Microencapsulation*, 30 (2013) 283-294.
- [12] M. Jahanshahi, Z. Babaei, Protein nanoparticle: A unique system as drug delivery vehicles, *African Journal of Biotechnology*, 7 (2008) 4926-4934.
- [13] Y. Wu, J.A. MacKay, J. R. McDaniel, A. Chilkoti, R.L. Clark, Fabrication of elastin-like polypeptide nanoparticles for drug delivery by electrospraying, *Biomacromolecules*, 10 (2008) 19-24.
- [14] G.-B. Jiang, D. Quan, K. Liao, H. Wang, Novel polymer micelles prepared from chitosan grafted hydrophobic palmitoyl groups for drug delivery, *Molecular Pharmaceutics*, 3 (2006) 152-160.
- [15] X.-G. Chen, C.M. Lee, H.-J. Park, O/W emulsification for the self-aggregation and nanoparticle formation of linoleic acid modified chitosan in the aqueous system, *Journal of Agricultural and Food Chemistry*, 51 (2003) 3135-3139.
- [16] K.Y. Choi, H. Chung, K.H. Min, H.Y. Yoon, K. Kim, J.H. Park, I.C. Kwon, S.Y. Jeong, Self-assembled hyaluronic acid nanoparticles for active tumor targeting, *Biomaterials*, 31 (2010) 106-114.
- [17] H.-Y. Lee, Y.-I. Jeong, D.-H. Kim, K.-C. Choi, Permanent hair dye-incorporated

hyaluronic acid nanoparticles, *Journal of Microencapsulation*, 30 (2013) 189-197.

[18] A.J. Wood, J.I. Weitz, Low-molecular-weight heparins, *New England Journal of Medicine*, 337 (1997) 688-699.

[19] T.M.H. Niers, C.P.W. Klerk, M. DiNisio, C.J.F. Van Noorden, H.R. Büller, P.H. Reitsma, D.J. Richel, Mechanisms of heparin induced anti-cancer activity in experimental cancer models, *Critical Reviews in Oncology/Hematology*, 61 (2007) 195-207.

[20] R. Castelli, F. Porro, P. Tarsia, The heparins and cancer: review of clinical trials and biological properties, *Vascular Medicine*, 9 (2004) 205-213.

[21] S.M. Smorenburg, C.J. Van Noorden, The complex effects of heparins on cancer progression and metastasis in experimental studies, *Pharmacological Reviews*, 53 (2001) 93-106.

[22] D. Farge, P. Debourdeau, M. Beckers, C. Baglin, R.M. Bauersachs, B. Brenner, D. Brillhante, A. Falanga, G.T. Gerotzafias, N. Haim, A.K. Kakkar, A.A. Khorana, R. Lecumberri, M. Mandala, M. Marty, M. Monreal, S.A. Mousa, S. Noble, I. Pabinger, P. Prandoni, M.H. Prins, M.H. Qari, M.B. Streiff, K. Syrigos, H. Bounameaux, H.R. Bü Ller, International clinical practice guidelines for the treatment and prophylaxis of venous thromboembolism in patients with cancer, *Journal of Thrombosis and Haemostasis*, 11 (2013) 56-70.

[23] M. Marchetti, A. Vignoli, L. Russo, D. Balducci, M. Pagnoncelli, T. Barbui, A. Falanga, Endothelial capillary tube formation and cell proliferation induced by tumor cells are affected by low molecular weight heparins and unfractionated heparin, *Thrombosis Research*, 121 (2008) 637-645.

[24] I. Yoshida, K.I. Tashiro, A. Monji, I. Nagata, Y. Hayashi, Y. Mitsuyama, N. Tashiro, Identification of a heparin binding site and the biological activities of the laminin α 1 chain carboxy-terminal globular domain, *Journal of Cellular Physiology*, 179 (1999) 18-28.

- [25] L. Hou, J. Yao, J. Zhou, Q. Zhang, Pharmacokinetics of a paclitaxel-loaded low molecular weight heparin-all-*trans*-retinoid acid conjugate ternary nanoparticulate drug delivery system, *Biomaterials*, 33 (2012) 5431-5440.
- [26] K. Park, G.Y. Lee, R.-W. Park, I.-S. Kim, S.Y. Kim, Y. Byun, Combination therapy of heparin–deoxycholic acid conjugate and doxorubicin against squamous cell carcinoma and B16F10 melanoma, *Pharmaceutical Research*, 25 (2008) 268-276.
- [27] K.H. Bae, H. Mok, T.G. Park, Synthesis, characterization, and intracellular delivery of reducible heparin nanogels for apoptotic cell death, *Biomaterials*, 29 (2008) 3376-3383.
- [28] B. Casu, M. Guerrini, S. Guglieri, A. Naggi, M. Perez, G. Torri, G. Cassinelli, D. Ribatti, P. Carminati, G. Giannini, Undersulfated and glycol-split heparins endowed with antiangiogenic activity, *Journal of Medicinal Chemistry*, 47 (2004) 838-848.
- [29] Y. Wang, D. Xin, K. Liu, M. Zhu, J. Xiang, Heparin– Paclitaxel conjugates as drug delivery system: synthesis, self-assembly property, drug release, and antitumor activity, *Bioconjugate Chemistry*, 20 (2009) 2214-2221.
- [30] I.-K. Park, Y.J. Kim, T.H. Tran, K.M. Huh, Y.-K. Lee, Water-soluble heparin–PTX conjugates for cancer targeting, *Polymer*, 51 (2010) 3387-3393.
- [31] S. Kaida, H. Cabral, M. Kumagai, A. Kishimura, Y. Terada, M. Sekino, I. Aoki, N. Nishiyama, T. Tani, K. Kataoka, Visible drug delivery by supramolecular nanocarriers directing to single-platformed diagnosis and therapy of pancreatic tumor model, *Cancer Research*, 70 (2010) 7031-7041.
- [32] K. Kolishetti, S. Dhar, P.M. Valencia, L.Q. Lin, R. Karnik, S.J. Lippard, R. Langer, O.C. Farokhzad, Engineering of self-assembled nanoparticle platform for precisely controlled combination drug therapy, *PNAS*, 107 (2010) 17939-17944.
- [33] K.S. Jee, H.D. Park, K.D. Park, Y.H. Kim, J.-W. Shin, Heparin conjugated polylactide as

a blood compatible material, *Biomacromolecules*, 5 (2004) 1877-1881.

[34] H.-J. Cho, H.Y. Yoon, H. Koo, S.-H. Ko, J.-S. Shim, J.-H. Lee, K. Kim, I. Chan Kwon, D.-D. Kim, Self-assembled nanoparticles based on hyaluronic acid-ceramide (HA-CE) and Pluronic® for tumor-targeted delivery of docetaxel, *Biomaterials*, 32 (2011) 7181-7190.

[35] K. Park, G.Y. Lee, Y.-S. Kim, M. Yu, R.-W. Park, I.-S. Kim, S.Y. Kim, Y. Byun, Heparin–deoxycholic acid chemical conjugate as an anticancer drug carrier and its antitumor activity, *Journal of Controlled Release*, 114 (2006) 300-306.

[36] J.S. Lee, D.H. Go, J.W. Bae, I.K. Jung, J.W. Lee, K.D. Park, Synthesis and characterization of heparin conjugated Tetronic® –PCL copolymer for protein drug delivery, *Current Applied Physics*, 7 (2007) e49-e52.

[37] K. Park, K. Kim, I.C. Kwon, S.K. Kim, S. Lee, D.Y. Lee, Y. Byun, Preparation and characterization of self-assembled nanoparticles of heparin-deoxycholic acid conjugates, *Langmuir*, 20 (2004) 11726-11731.

[38] R.D. Rosenberg, Heparin, antithrombin, and abnormal clotting, *Annual Review of Medicine*, 29 (1978) 367-378.

[39] U. Termsarasab, H.-J. Cho, D.H. Kim, S. Chong, S.-J. Chung, C.-K. Shim, H.T. Moon, D.-D. Kim, Chitosan oligosaccharide–arachidic acid-based nanoparticles for anti-cancer drug delivery, *International Journal of Pharmaceutics*, 441 (2013) 373-380.

[40] G. Gaucher, M.-H. Dufresne, V.P. Sant, N. Kang, D. Maysinger, J.-C. Leroux, Block copolymer micelles: preparation, characterization and application in drug delivery, *Journal of Controlled Release*, 109 (2005) 169-188.

[41] H. Maeda, J. Wu, T. Sawa, Y. Matsumura, K. Hori, Tumor vascular permeability and the EPR effect in macromolecular therapeutics: a review, *Journal of Controlled Release*, 65 (2000) 271-284.

- [42] J.S. Lee, D.H. Go, J.W. Bae, S.J. Lee, K.D. Park, Heparin conjugated polymeric micelle for long-term delivery of basic fibroblast growth factor, *Journal of Controlled Release*, 117 (2007) 204-209.
- [43] J.P. Kratochvil, W.P. Hsu, D.I. Kwok, How large are the micelles of di- α -hydroxy bile salts at the critical micellization concentrations in aqueous electrolyte solutions? Results for sodium taurodeoxycholate and sodium deoxycholate, *Langmuir*, 2 (1986) 256-258.
- [44] N. Rizkalla, C. Range, F.-X. Lacasse, P. Hildgen, Effect of various formulation parameters on the properties of polymeric nanoparticles prepared by multiple emulsion method, *Journal of Microencapsulation*, 23 (2006) 39-57.
- [45] A.Y. Lee, M.N. Levine, R.I. Baker, C. Bowden, A.K. Kakkar, M. Prins, F.R. Rickles, J.A. Julian, S. Haley, M.J. Kovacs, Low-molecular-weight heparin versus a coumarin for the prevention of recurrent venous thromboembolism in patients with cancer, *New England Journal of Medicine*, 349 (2003) 146-153.
- [46] J. Nishioka, S. Goodin, Low-molecular-weight heparin in cancer-associated thrombosis: treatment, secondary prevention, and survival, *Journal of Oncology Pharmacy Practice*, 13 (2007) 85-97.

Table 1 Characterization of LHSA conjugates

Sample	FXa (%)	CMC (mg/ml)	LMWH content ($\mu\text{g}/\mu\text{g}$)
LHSA1	60.41	N.D	0.96
LHSA3	32.09	N.D	0.91
LHSA5	31.92	0.044	0.85

Abbreviations: FXa, Factor Xa; CMC, Critical micelle concentration; LMWH, low-molecular-weight heparin; N.D, not determined.

Table 2 Characterization of LHSA-based nanoparticles.

Sample	Particle size (nm)	Polydispersity index	Zeta potential (mV)
LHSA1 nanoparticles	146.1 ± 8.92	0.251 ± 0.07	-15.39 ± 8.44
LHSA3 nanoparticles	175.6 ± 6.54	0.225 ± 0.08	-33.92 ± 1.34
LHSA5 nanoparticles	177.9 ± 7.22	0.169 ± 0.04	-33.13 ± 0.72

Note: Data presented as mean ± SD (n=4).

Abbreviations: LHSA, LMWH-SA; SD, standard deviation.

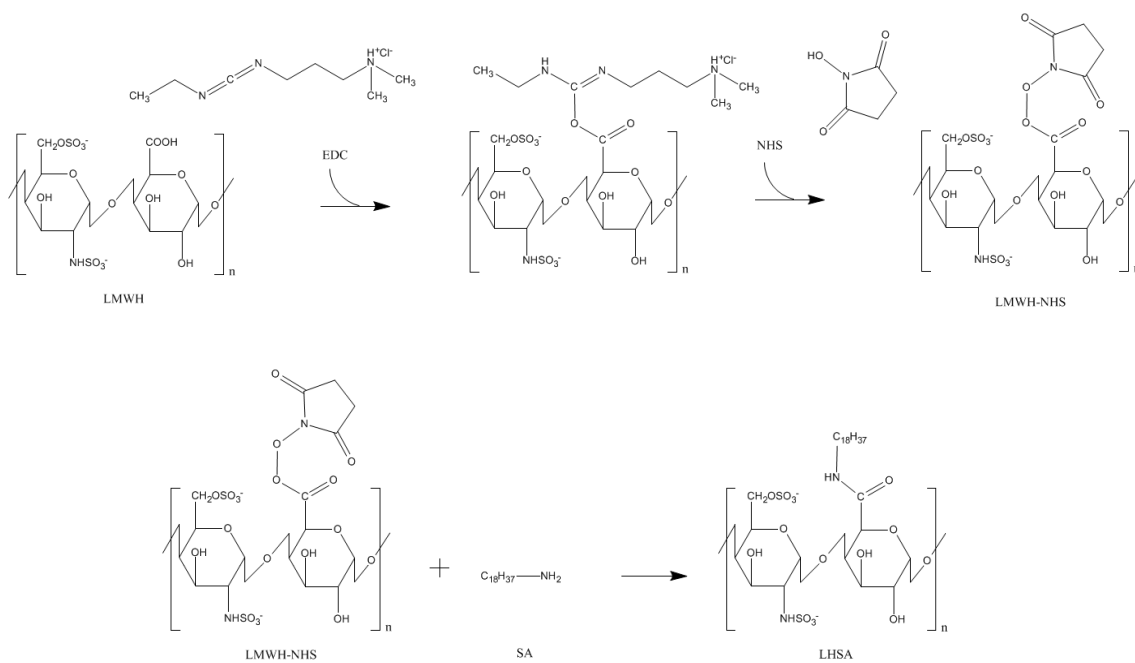


Figure 1 Synthetic scheme for LHSa conjugates.

Abbreviations: LMWH, low-molecular-weight heparin; SA, stearylamine; EDC, 1-ethyl-3-(3-dimethylaminopropyl) carbodiimide; NHS, N-hydroxysuccinimide.

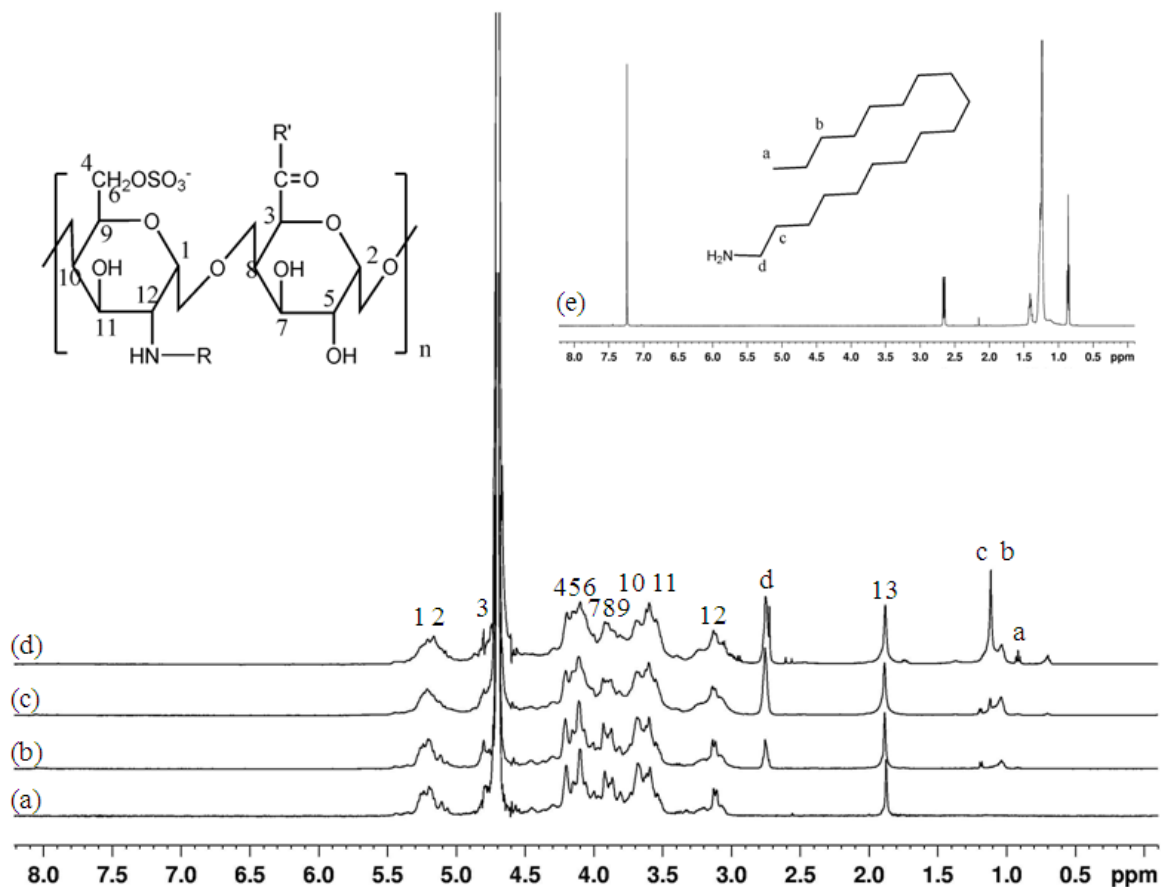


Figure 2 ^1H NMR spectra of (a) LMWH and (b) LHAS1 and (c) LHAS3 (d) LHAS5 and (e) SA, respectively. Samples were dissolved in D_2O for ^1H NMR analysis [$\text{R} = -\text{SO}_3^-$ (predominant) or $-\text{COCH}_3$ (peak #13); $\text{R}' = \text{SA}$].

Abbreviations: ^1H -NMR, proton nuclear magnetic resonance; LMWH, low-molecular-weight heparin; SA, stearylamine.

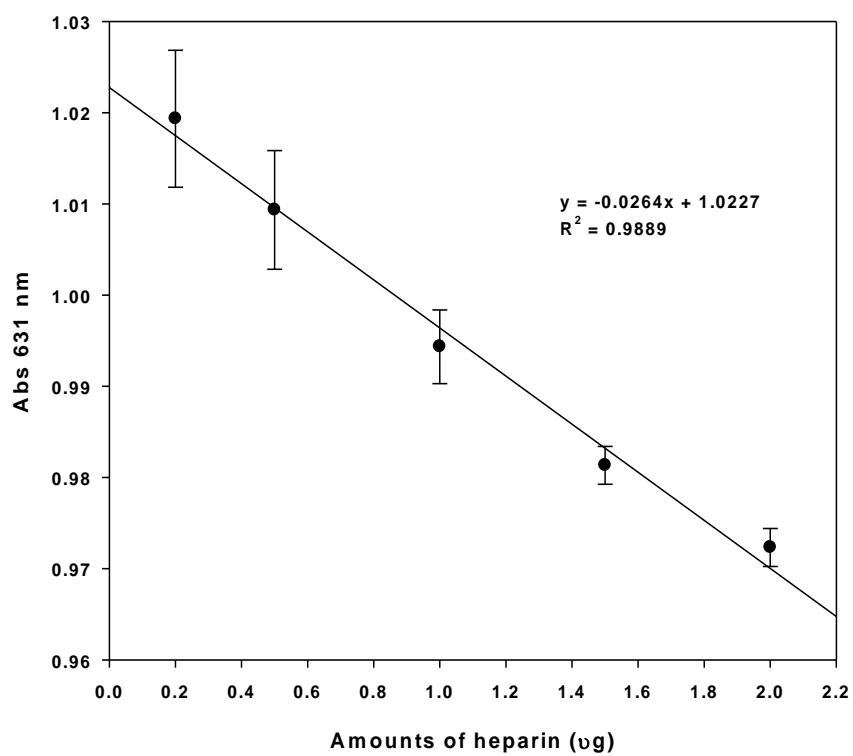


Figure 3 Relationship between the amounts of heparin and those determined UV absorbance at 631 nm.

Abbreviations: UV, ultra violet; Abs, absorbance.

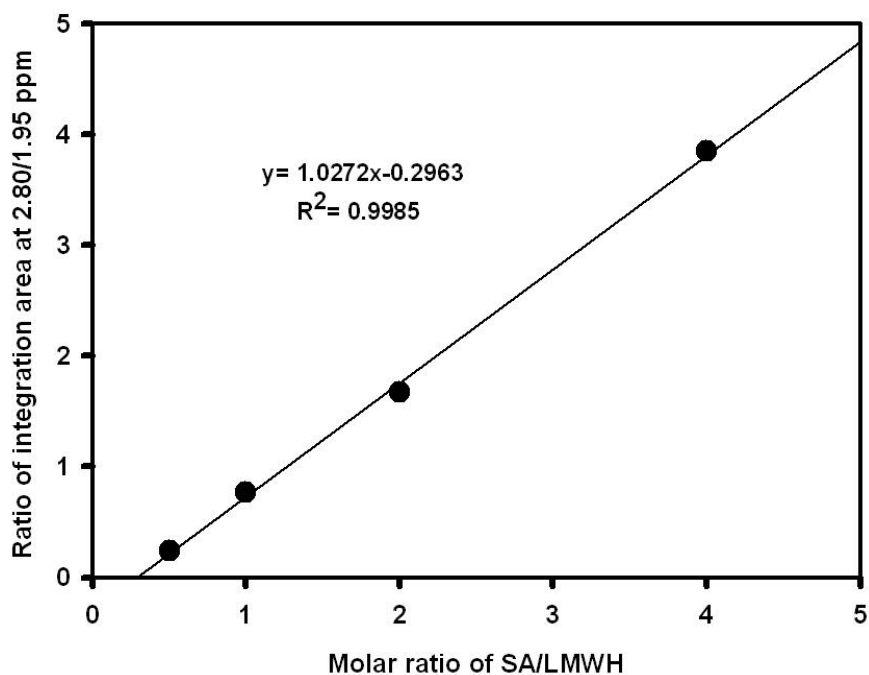


Figure 4 Relationship between the ratio of integration area (2.80/1.95 ppm) and molar ratio of SA/LMWH based on their physical mixture.

Note: Samples were dissolved in $D_2O/THF-d_8$ mixture (1:1) for 1H NMR analysis. Each point represents the mean \pm SD (n=3).

Abbreviation: SA, stearylamine; LMWH, low-molecular-weight heparin.

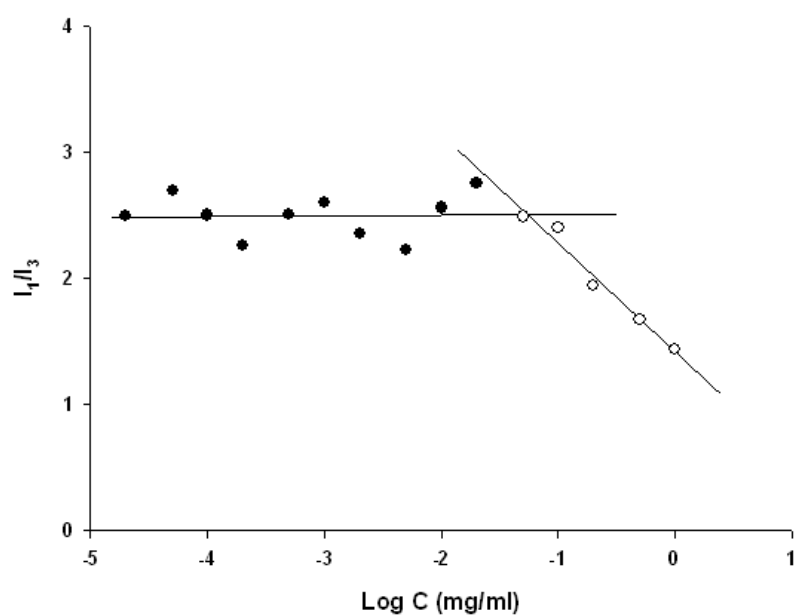
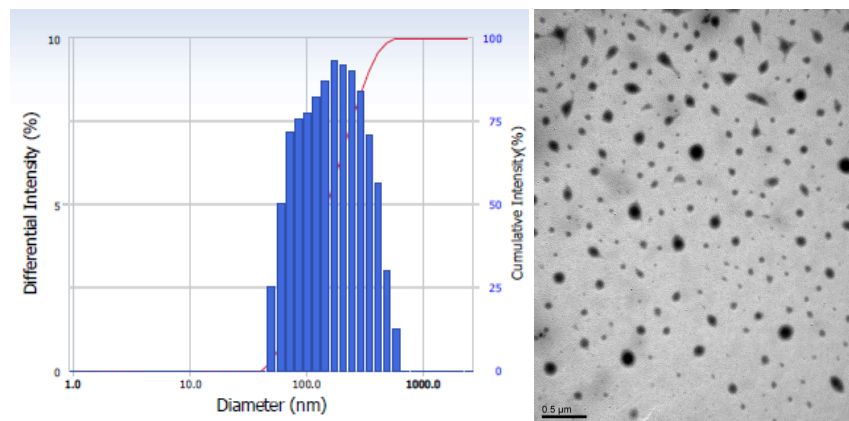


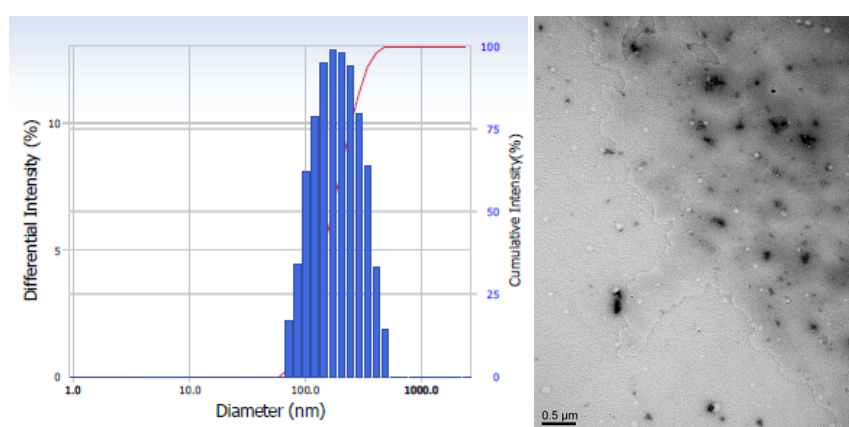
Figure 5 CMC determination of LHS A5 nanoparticles. Fluorescence intensity ratio (I₁/I₃) according to LHS A5 concentration as plotted and CMC was estimated from the threshold concentration of self-assembled nanoparticles.

Notes: Pyrene is used as fluorescence probe. Ratio of intensities of the first and third vibronic peak (I₁/I₃) is considered to estimate the CMC of LHS A5.

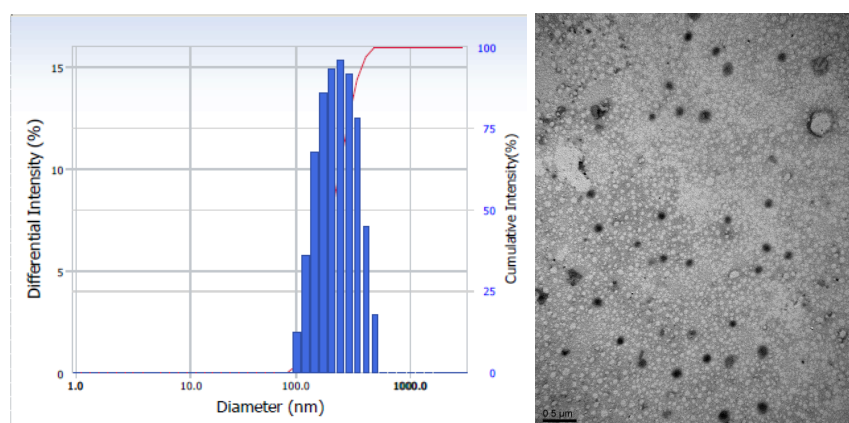
Abbreviations: CMC, critical micelle concentration; LHS A, LMWH-SA.



(a) LHS A1 nanoparticles



(b) LHS A3 nanoparticles



(c) LHS A5 nanoparticles

Figure 6 Size distribution and TEM images of LHS A nanoparticles. The length of the scale bar in the TEM image is 500 nm (x200,000).

Abbreviations: TEM, transmission electron microscopy; LHS A, LMWH-SA.

Part II. Characterization and evaluation of self-assembled nanoparticles based on low-molecular-weight heparin and stearylamine conjugates for controlled delivery of docetaxel

1. Introduction

Over the past decade, nanoparticulate drug delivery systems containing anti-cancer agents have been investigated extensively due to their specific accumulation behavior at the tumor site [1, 2]. Nanoparticulate drugs can be distributed to tumor vasculatures by the enhanced permeability and retention (EPR) effect, taking advantage of the leaky vascular nature of tumor tissues that provides for passive tumor targeting [3, 4]. Additionally, these nanoparticulate drugs offer the advantages of prolonged systemic circulation by avoiding phagocytosis, improved efficacy, and reduced toxicity. Numerous biocompatible and biodegradable materials, such as poly(lactic acid) [5, 6], poly(glycolic acid) [7], polycaprolactone [8, 9], polysaccharides [10], proteins [11], and polypeptides [12], have been used for the preparation of polymeric nanoparticles. Among them, polysaccharides have been used extensively to prepare nanoparticles for drug delivery [2]. Polysaccharides are natural biomaterials; thus, they are generally safe, non-toxic, biocompatible, and biodegradable. They have various derivable groups that can be modified with other chemicals. Among the drug delivery systems, self-assembled nanoparticles have been studied for the encapsulation and sustained release of poorly soluble drugs [13-15]. The use of amphiphilic polymers can be used to form nanoparticles with a hydrophobic core and a hydrophilic shell. This structure enables the encapsulation and deliver of poorly soluble drugs, extending the circulation time of nanoparticles in the bloodstream.

Docetaxel (DCT), an antimetabolic chemotherapy medication and a semi-synthetic analogue of paclitaxel, is a particularly important anticancer agent that has been used for the treatment of many cancers, exhibiting cytotoxic activity in breast, ovarian, prostate, and non-small cell lung cancer cells [16-18]. As with all chemotherapies, however, adverse effects are

common; side effects, such as neutropenia, peripheral neuropathy, musculoskeletal toxicity, and hypersensitivity reactions, have been verified. In its commercial formulation (Taxotere®), non-ionic surfactant Tween 80 (polysorbate 80) and 13% ethanol in saline have been used to dissolve DCT, due to its poor solubility in water [19]; however, this formulation is associated with unpredictable hypersensitivity reactions and other side-effects [20]. Thus, many new systems—including micelles, emulsions, and conjugates with other polymers—have been developed to deliver DCT to tumor sites with minimal adverse reactions [21-23].

Heparin is a biocompatible, biodegradable, water-soluble natural polysaccharide coupled with various biological activity, including anti-coagulation, anti-inflammatory, and anti-angiogenesis effects [24, 25]. In addition to its well-known anticoagulant activity, the anticancer activity of heparin has been evaluated [26, 27]. Low-molecular-weight heparin (LMWH) exerts its anticancer activity by affecting the proliferation, adhesion, angiogenesis, migration, and invasion of cancer cells. Although the exact mechanism of LMWH interference with cancer biology still remains unclear, it may involve the inhibition of both coagulation and non-coagulation-dependent pathways of tumor progression [28]. Furthermore, in a study of venous thromboembolism (VTR) therapy, a significant reduction in the mortality rate was noted in the LMWH treatment group among the cancer patients [26]. Thus, these idiosyncratic properties facilitate the development of heparin-based delivery systems [29, 30]. However, unfractionated heparin (UFH) causes adverse effects, such as bleeding, which have limited its application. LMWH has a reduced anticoagulant activity and, thus far, appears to have a greater anticancer effect than UFH [31]; thus, LMWH is preferable to UFH for the initial treatment of VTR prevalent in cancer patients [32].

In this study, the objective was to synthesize an amphiphilic polymer comprised of LMWH and stearylamine (octadecylamine, SA) for the preparation of self-assembled

nanoparticles for anticancer drug delivery. This negatively charged nanoparticle was prepared using LMWH-SA (LHSA) conjugates, with LMWH as the hydrophilic segment and SA as its hydrophobic counterpart. SA (18-carbon saturated fatty amine) is used for the synthesis of uniform nanoparticles [33]. The physicochemical properties of LHSA-based nanoparticles containing DCT were characterized by determining size, zeta potential, and DCT-loading efficacy. DCT release from nanoparticles and the cytotoxicity of blank nanoparticles were also investigated. Moreover, the optimized formulation was evaluated via *in vitro* cellular uptake study using confocal laser scanning microscopy (CLSM) and fluorescence-activated cell sorter (FACS) measurements, and *in vivo* antitumor efficacy and pharmacokinetic studies.

2. Materials and methods

2.1. Materials

LMWH (101 IU mg⁻¹), with an average molecular weight of ~4500 Da, was purchased from Nanjing King-Friend Biochemical Pharmaceutical Co. Ltd. 1-Ethyl-3-(3-dimethylaminopropyl) carbodiimide (EDC), N-hydroxysuccinimide (NHS), SA, coumarin 6 (C6), and pyrene were obtained from Sigma-Aldrich Co. (St. Louis, MO, USA). DCT was purchased from Taihua Co. (Xi'an, China). Formamide (FA), tetrahydrofuran (THF), and acetonitrile (HPLC grade) were supplied by Fisher Scientific Korea Ltd. Dulbecco's modified Eagle's medium (DMEM), RPMI 1640 (developed by Roswell Park Memorial Institute), heat-inactivated fetal bovine serum (FBS), streptomycin, and penicillin were obtained from Gibco Life Technologies (Karlsruhe, Germany). Water was purified by distillation, deionization, and reverse osmosis (Milli-Q Plus). All other chemicals were of analytical grade which were purchased from commercial sources.

2.2. Synthesis and characterization of LHSA conjugates

Amphiphilic LHSA conjugates were synthesized from LMWH and SA as described in previous report. In brief, LMWH (1g) was dissolved in formamide (200mL) by gentle heating. To synthesize the LHSA conjugates, EDC (636 mg) and NHS (384 mg) were mixed with LMWH solutions at room temperature, followed by the addition of SA (300 mg) dissolved in THF (132mL). This solution was stirred at room temperature for 24h. The mixture was precipitated in excess cold acetone under vigorous agitation. This mixture was filtered by glass filter (G4) and stirred for 30 min. The residues on the glass filter were carefully washed three times with cold acetone to remove excess EDC, NHS and SA, followed by filtering with 50ml of DDW. The filtrate was dialyzed with dialysis membrane (molecular weight cut-off= 1 kDa; Spectrum Laboratories, Laguna Hills, CA, USA) against DDW for 48 h. The dialyzed products were lyophilized. LHSA conjugate was dissolved in D₂O and analyzed by ¹H NMR (500 MHz)

Aliquot of conjugates were dissolved in D₂O (10 mg mL⁻¹), and ¹H-NMR spectra were obtained by using a Varian FT 500-MHz NMR spectrometer (Varian Inc., Palo Alto, CA, USA). The values of the proton peaks from the ¹H-NMR spectra were integrated to determine the molar substitution of LHSA. Linear regression was prepared from the physical mixture of LMWH and SA at various molar ratio (LMWH:SA =0.5:1, 1:1, 1:2, and 1:4) dissolved in the mixture of D₂O/THF-d₈ (1:1). The ratio of the integration area (2.80/1.95 ppm) of each physical mixture was calculated.

2.3. Preparation and characterization of LHSA-based nanoparticles

A simple modification of our previous methods was used for the self-assembly of LHSA

and drug encapsulation [34]. LHSA (5 mg) and 1 mg of DCT were completely solubilized in 1 mL of FA; the solvent was evaporated under gentle nitrogen (N₂) flow for 5 h at 80°C. LHSA and DCT-coated tubes were resuspended with 1 mL of DDW by vortexing for 3 min, followed by filtering through a 0.22- μ m pore-size syringe filter (Minisart RC 15, Sartorius Stedium Biotech GmbH, Goettingen, Germany).

The mean diameter, polydispersity, and zeta potential of the nanoparticles were determined using a light scattering spectrophotometer (ELS-Z, Otsuka Electronics, Japan) at a polymer concentration of 5 mg mL⁻¹. The morphology of the LHSA nanoparticles was assessed by transmission electron microscopy (TEM) (JEM 1010, JEOL, Japan). The nanoparticle suspensions were stained with 2% (w/v) phosphotungstic acid (PTA), placed on a copper grid coated with carbon film, air-dried for 10 min, and photographed.

The nanoparticle suspensions were distilled with FA to disrupt the self-assembled structure. The drug encapsulation efficiency of drug-loaded nanoparticles was measured using high-performance liquid chromatography (HPLC).³⁴ The HPLC instrument consisted of a dual pump (Waters 515), an auto-sampler (Waters 717 plus), an ultraviolet detector (Waters 2487) and a reverse-phase C-18 column (250 \times 4.4 mm, 5 μ m, Shiseido, Japan). The mobile phase was a mixture of acetonitrile and DDW (55:45, v/v). The eluent was monitored at 230 nm and a flow rate of 1.0 mL min⁻¹. The DCT concentrations were determined using 20 μ L of injection volume at room temperature. The lower limit of quantitation (LLOQ) was 500 ng mL⁻¹.

2.4. In vitro docetaxel release studies

The LHSA5 nanoparticles (the volume equivalent of 100 μ g of DCT) were loaded in semi-permeable Mini-Gebaflex-tubes with a molecular weight cut-off of 6–7 kDa (Gene Bio-

Application Ltd., Israel), and were immersed in the medium (10 mL). The dissolution medium was phosphate-buffered saline (PBS, pH: 7.4) containing 0.5% (w/v) Tween 80 at 37°C, and was rotated at 50 rpm. Aliquot (0.2 mL) of medium was collected at predetermined times (1, 2, 3, 4, 6, 9, 12, 24, 48, 72, 96, and 144 h), and fresh media (37°C) of equal volume of was added to maintain sink condition. The amounts of DCT released into the medium were analyzed by HPLC.

2.5. In vitro cytotoxicity of conjugate

MCF-7 and MDAMB 231 cells were purchased from the Korean cell line bank (Seoul, Korea), and were cultured in RPMI-1640 medium with 1% (v/v) penicillin (100 U mL⁻¹), streptomycin (0.1 mg mL⁻¹) and 10% (v/v) FBS. They were incubated in a humidified 5% CO₂ atmosphere at 37°C.

The cytotoxicity of LHSA5 conjugate polymer was evaluated in MCF-7 and MDAMB 231 cells by using MTS-based assay. MCF-7 and MDAMB 231 cells (1.0×10^4 cells) were seeded in 96-well plates. Various concentrations of LHSA5 polymer in the culture medium were incubated for 24 h at 37°C, after which the cells were treated with an MTS-based CellTiter 96 AQ_{ueous} One Solution Cell Proliferation Assay reagent (Promega Corp., WI, USA) for 4 h at 37°C by the manufacturer's protocol. The absorbance of the medium was read at 490 nm using the Emax Precision Microplate Reader (Molecular Devices, CA, USA)

2.6. In vitro antitumor efficacy studies

In vitro antitumor efficacy was evaluated using MTS-based assays. MCF-7 and MDAMB 231 cells (1.0×10^4 cells) were seeded in 96-well plates for 24 h. After washing cells twice with PBS, they were incubated with various concentrations (0.1, 1.0 and 5.0 μM) of DCT

solution (Taxotere) or DCT-loaded LHSA5 nanoparticles for 24 h at 37°C. Then, the cells were treated with an MTS-based CellTiter 96 AQueous One Solution Cell Proliferation Assay reagent for 4 h at 37°C by the manufacturer's instructions. The absorbance at 490 nm was read using an Emax Precision Microplate Reader, and are expressed as percentage of viable cells compared with the control group (*i.e.*, without DCT).

2.7. Cellular uptake studies

The cellular uptake efficiency of the LHSA5 nanoparticles was investigated by CLSM with C6-loaded nanoparticles [34]. C6 was also loaded in nanoparticles using a similar DCT loading method. Either MCF-7 or MDAMB 231 cells were seeded on culture plates (BD Falcon, Bedford, MA, USA) at a density of 1.0×10^5 per well (1.7-cm² surface area), and incubated for 24 h at 37°C. C6 (2 µg) was added alone or entrapped in the LHSA5 nanoparticles, after which was incubated for 2 h at 37°C. Then, the cells were washed with PBS (pH: 7.4), and were fixed with formaldehyde solution (4%, v/v) for 10 min. After completely drying the liquid content, A VECTASHIELD mounting medium with 4', 6-diamidino-2-phenylindone (DAPI; H-1200 Vector Laboratories, Inc., CA, USA) was added to prevent fading. Finally, the cells on the slides were observed by using CLSM (LSM 510, Carl-Zeiss, Thornwood, NY, USA).

The cellular uptake efficiency the LHSA5 nanoparticles was also determined by flow cytometry. MCF-7 and MDAMB 231 cells were seeded on 24-well plates at a density of 5×10^5 per well and incubated overnight at 37°C. After removing the culture medium, the cells were incubated with free C6 or C6-loaded LHSA5 nanoparticles for 2 h. The cells were then completely washed with PBS (pH: 7.4). After they were detached and centrifuged, the supernatant was then removed. The cell pellets were suspended again with PBS containing 2%

(v/v) FBS. The uptake efficiency was analyzed by a BD FACSCalibur flow cytometry system equipped with the Cell Quest Pro software (Becton Dickinson Bioscience, San Jose, CA, USA).

2.8. *In vivo antitumor efficacy*

Tumor-xenografted mouse model was prepared by using female BALB/c nude mice (5 weeks old; Charles River, Washington, MA) for *in vivo* anticancer efficacy evaluation. They were kept in a light-controlled room at $22 \pm 2^\circ\text{C}$ temperature and $55 \pm 5\%$ relative humidity (Animal Center for Pharmaceutical Research, College of Pharmacy, Seoul National University, Seoul, Korea). The experimental protocols were approved by the Animal Care and Use Committee of the College of Pharmacy, Seoul National University. Tumor-xenografted mouse were prepared by subcutaneous injection of MDAMB 231 cells (3×10^6 cells per mouse) in the right lateral flank. After measuring the tumor size with Vernier calipers, the tumor volume (mm^3) was calculated by the following formula: volume = $0.5 \times$ longest diameter \times shortest diameter². After 14 days, when the MDAMB 231 tumor became palpable, tumor volume and body weight measurements commenced. The mice were randomly divided into four groups: the control (no treatment), blank LHSA5 nanoparticles, DCT solution (Taxotere), and DCT-loaded LHSA5 nanoparticles groups. DCT solution or DCT-loaded LHSA5 nanoparticles were intravenously injected at a dose of 30 mg kg^{-1} as DOC on days 0, 7, and 14. Tumor volume and body weight were measured for 18 days.

2.9. *In vivo pharmacokinetic study in rats*

Male Sprague-Dawley rats (280-300 g body weight) were used for pharmacokinetic studies. Under light anesthesia (30 mg kg^{-1} Zoletil[®], intramuscular injection), femoral artery

and vein of each rat were cannulated with a polyethylene tube (PE-50; Clay Adams, Parsippany, NJ). DCT solution (Taxotere) or DCT-loaded LHSA5 nanoparticles (8 mg kg⁻¹ as DCT) were administered to rats *via* the femoral vein within 1 min. Blood samples (approximately 300 μL) were collected *via* the femoral artery at 0 (control), 1, 5, 15, 30, 60, 120, 180, 240, 360, and 720 min after intravenous administration of Taxotere and DCT-loaded LHSA5 nanoparticles. After the blood samples underwent centrifugation, aliquots of plasma (100 μL) were stored at -70°C (Model DF8517; Ilshin Laboratory Company, Seoul, Korea) until liquid chromatography–mass spectrometry/mass spectrometry (LC-MS/MS) analysis of DCT. Immediately after each blood sampling, equal volume of 0.9% sodium chloride-injectable solution containing 20 U mL⁻¹ of heparin was injected.

The concentration of DCT in the plasma samples was determined by LC-MS/MS. The LC-MS/MS system consisted of an Agilent 1260 series HPLC system (equipped with a G 1312B binary pump, a G 1367E high-performance auto sampler, a G1322A vacuum degasser, a G1330B FC/ALS thermostat, and a G1316C TCC), an Agilent 6430 triple quadrupole mass spectrometer, and the MassHunter Workstation software (version B.03.01).

Plasma samples (100-μL) were deproteinized with acetonitrile (300 μL) and methanol (100 μL) containing 1 μL mL⁻¹ paclitaxel (as an internal standard). They were vortexed and centrifugated at 16,000 g for 10 min. The supernatant (400 μL) were transferred to a clean tube and completely evaporated under a gentle stream of N₂ gas at room temperature. Then, the residue was reconstituted with 60 μL of the mobile phase. After vortexing and centrifugation again, a 10 μL aliquot of supernatant was injected into a poroshell 120 EC-C16 column (2.7 μm, 4.6 × 50 mm, Agilent Technologies Inc., USA) under isocratic elution of the mobile phase consisting of ammonium formate and acetonitrile (30:70, v/v) at a flow rate of 0.2 mL min⁻¹. The column temperature was maintained at 30°C. Data were acquired with

electrospray ionization in the positive mode. Reaction monitoring was used to monitor the transitions from molecular ion to dominant product ion at m/z 808-527 for DCT and m/z 876-591 for paclitaxel, respectively. The LLOQ value of DCT in rat plasma was 10 ng mL^{-1} .

The following pharmacokinetic parameters were calculated using WinNonlin[®] (Pharsight, Mountain View, CA): total area under the plasma concentration–time curve from time zero to the end time point (AUC), terminal half-life ($t_{1/2}$), time-averaged total body clearance (CL), the apparent volume of the distribution under steady-state conditions (V_{ss}), and the mean residence time (MRT).

2.10. Statistical analysis

Statistical analyses were performed using analysis of variance. P values < 0.05 indicated statistical significance. All experiments were performed at least three times and the data were presented as the mean \pm standard deviation (SD).

3. Results

3.1. Synthesis and characterization of LHSA conjugates

Heparin and its derivatives have been widely used as drug delivery systems [35-37]. In this study, SA (an aminated fatty acid) was conjugated to LMWH to produce an amphiphilic polymer, which is to form the self-assembled nanoparticles in aqueous environment (Figure 1). The amine group of SA was covalently coupled to the carboxylic group of LMWH in the presence of EDC and NHS, thus producing amphiphilic LHSA conjugates. The synthesized LHSA conjugates were confirmed by ¹H-NMR analysis. The ¹H-NMR spectra of the LHSA conjugate exhibited proton signals for both LMWH and SA; a broad proton peak was

observed for LMWH and the presence of SA in the LHSA conjugate was confirmed by its chemical shift at 0.8–1.2 ppm. An alkyl chain (-CH₂-) and a terminal methyl group (-CH₃) of SA corresponded to the proton peaks at 1.10 and 0.90 ppm, respectively. The physical mixtures of LMWH and SA with various molar ratios, prepared for calculation of the molar substitution ratio of LHSA, were analyzed by ¹H-NMR. The linear regression line was plotted by the ratio of the integration area between the SA peak (2.80 ppm) and LMWH peak (1.95 ppm). The degree of substitution (DS) of LHSA5 was calculated to be 34.0%, which indicates that approximately 1.7 of SA is conjugated to each LMWH.

3.2. Preparation and characterization of LHSA-based self-assembled nanoparticles

A solvent evaporation method was used to load DCT into the LHSA-based nanoparticles. Blank self-assembled LHSA nanoparticles were prepared without DCT loading by dissolving LHSA conjugate in an aqueous solution. The mean diameter, zeta potential, and drug loading values are shown in Table 1. All samples successfully formed nanoparticles with a mean diameter of 140 to 180 nm, which were confirmed by the size distribution and TEM of LHSA nanoparticles. It is interesting to note that the incorporation of DCT in the LHSA5 nanoparticles leads to a decrease of the particle size from 177.9 nm to 155.20 nm (Table 1). The loading of hydrophobic drugs in the inner-core can enhance the stability of self-assembled nanoparticles by inducing morphology transition in order to decrease the total free energy, thereby resulting in the reduction of particle size [38, 39]. The nanoparticles showed the negative zeta potential values due to the LMWH located in the shell.

The encapsulation efficiency and the drug loading content in the LHSA5 nanoparticles was 59.82% and 10.68%, respectively (Table 1). TEM images showed that the DCT-loaded LHSA5-based nanoparticles were also spherical in shape with narrow size distribution

(Figure 2).

3.3. In vitro docetaxel release

Figure 3 shows the *in vitro* DCT release profile. DCT was incorporated in the LHSA5 nanoparticles and the sink condition was adequately maintained in the release test. The *in vitro* release of DCT from LHSA5 nanoparticles was investigated for 6 days. After initial release for 24 h, the release rate of DCT slightly decreased with incubation time, and showed a sustained DCT release pattern. The release level of DCT within 24 h was 48.24%; additional release continued up to 96 h. A sustained DCT release pattern can lead to reduction in *in vivo* drug clearance, which results in maintenance of adequate drug concentrations for tumor growth inhibition.

3.4. In vitro cytotoxicity of LHSA conjugate

The cytotoxicity of blank LHSA5 conjugate was investigated in MCF-7 (Figure 4a) and MDAMB 231 (Figure 4b) breast cancer cell lines. Cell viability was measured after treating with various concentrations of LMWH and blank LHSA5 conjugate for 24 h. At all blank LHSA5 conjugate polymer concentrations (0–200 $\mu\text{g mL}^{-1}$), no significant viability differences between the LMWH and blank LHSA5 conjugate groups were observed, indicating that the blank LHSA5 conjugate polymer exerted no severe cytotoxicity on MCF-6 and MDAMB 231 cells.

3.5. In vitro antitumor effect

In vitro antitumor effects were evaluated using MCF-7 (Figure 5a) and MDAMB 231 (Figure 5b) cells. Free DCT (Taxotere) and DCT-loaded LHSA5 nanoparticles have antitumor

efficacy against MCF-7 and MDAMB 231 cells. The DCT-loaded LHSA5 nanoparticle exhibited a similar or slightly lower efficacy than free DCT, possibly due to sustained release of free DCT from LHSA5 nanoparticles.

3.6. In vitro cellular uptake study

MCF-7 and MDAMB 231 are human breast cancer cell lines, and were selected since DCT is mainly used for the treatment of breast cancer [40]. To investigate the cellular uptake efficiency of LHSA5 nanoparticles, LHSA5 nanoparticles loaded with C6 were observed using CLSM, with 4',6-diamidino-2-phenylindole (DAPI) staining of nuclei in MCF-7 and MDAMB 231 cells. C6 is a fluorescence probe that has been widely used in cellular uptake studies of nanoparticles [34, 41]. In Figure 6, the stronger green fluorescent signals indicate higher intracellular accumulation of C6 from LHSA5 nanoparticles compared to that from the C6 solution.

Cellular uptake efficiency was also quantitatively determined in MCF-7 (Figure 7a) and MDAMB 231 (Figure 7b) cells by a flow cytometry. The fluorescence intensity was assumed to be proportional to the amount of C6 in the cells; however, fluorescence was barely detected in the control (no treatment) and blank nanoparticle groups. Figure 7 shows that significantly higher amounts of C6 from LHSA5-based nanoparticles were taken up by the cells, compared with the C6 solution, which is consistent with the results of the CLSM study (Figure 6). This result can be explained by the endocytosis of the nanoparticles [42, 43]. A previous study showed that fatty acid-modified polysaccharide-based nanoparticles form self-assembled nanoparticles with a multi-hydrophobic core [44]. A hydrophobic minor core could facilitate the internalization of nanoparticles into cells via interaction with the plasma membrane. Although LHSA5-based nanoparticles are negatively charged due to their many

sulfate and carboxyl groups, the nanoparticle was taken up in higher amounts, compared with the C6 solution.

3.7. *In vivo antitumor efficacy*

In vivo antitumor efficacy of the DCT-loaded LHSA5 nanoparticle formulation was evaluated in the MDAMB 231 tumor-bearing mouse model. Blank LHSA5 nanoparticles, DCT solution (Taxotere), and DCT-loaded LHSA5 nanoparticles were injected intravenously on days 0, 7, and 14. Then, tumor volume (mm³) and body weight (g) were monitored for 18 days.

The tumor volumes of the blank LHSA5 nanoparticle, DCT solution (Taxotere), and DCT-loaded LHSA5 nanoparticle-treated groups on day 18 were 94.6, 63.2, and 47.1% that of the control group, respectively (Figure 8a). The most effective inhibition of tumor growth was observed in DCT-loaded LHSA5 nanoparticles, while the blank LHSA5 nanoparticle treatment group had little effect on tumor growth inhibition. Moreover, the tumor growth inhibition effect of the DCT-loaded LHSA5 nanoparticles group was significantly greater than that of the Taxotere group ($p < 0.05$).

The safety of DCT-loaded LHSA nanoparticles was evaluated by measuring changes in body weight. For most groups, there was no significant difference in body weight (Figure 8b). However, the body weight of the Taxotere-treated group was significantly lower than that of the control group. The DCT-loaded LHSA5 nanoparticle-treated group showed no significant difference compared with the control group, suggesting that the DCT-loaded LHSA nanoparticle treatment was less toxic than Taxotere group.

3.8. *In vivo pharmacokinetic study*

Figure 9 shows the plasma concentration–time profiles of DCT solution (Taxotere) and DCT-loaded LHSA5 nanoparticles, at a dose of 8 mg kg⁻¹ to Sprague-Dawley rats; relevant pharmacokinetic parameters are listed in Table 2. The results showed that DCT was rapidly eliminated from the bloodstream in both the Taxotere and LHSA5 nanoparticle groups over the first 30 min after dosing. However, after dose normalization, the DCT in LHSA5 nanoparticles yielded a higher plasma concentration than Taxotere. Non-compartmental analysis of the plasma concentrations showed a significant change in the pharmacokinetic parameters of DCT in LHSA5 nanoparticles. Compared with Taxotere, the LHSA5 nanoparticles provided a significantly higher AUC (2.48-fold), terminal t_{1/2} (3.02-fold), and MRT (3.64-fold). The LHSA5 nanoparticles also significantly decreased the clearance (CL, 2.54-fold) of DCT. These *in vivo* pharmacokinetic properties were thought to be related to its *in vitro* sustained release pattern. This result indicates that the LHSA5 nanoparticles prolonged the circulation of DCT in the bloodstream, thereby improving its therapeutic efficacy (Figure 8a).

4. Discussion

An accurate substitution ratio (SA to LMWH) can be determined from the ¹H-NMR spectrum of the physical mixtures of LMWH and SA. In our previous study [45], the correlation of the molar ratio of arachidic acid (AA) to chitosan oligosaccharide (CSO) was evaluated using ¹H-NMR from a physical mixture of AA and CSO in DMSO-d₆. However, LMWH has a strong hydrophilic property, while SA has a strong hydrophobic property; thus, an NMR cosolvent consisting of D₂O and THF-d₈ was used to dissolve

It is known that nanoparticles with a mean diameter <200 nm accumulate in tumors *via*

the EPR effect and exhibit reduced uptake by the reticuloendothelial system (RES) [3, 46]. The LMWH of LHSA creates a hydrophilic outer shell of the nanoparticles in an aqueous environment. The SA of LHSA provides an internal hydrophobic core that can be used to encapsulate insoluble drugs [47]. It was interesting to note that the zeta potential values of LHSA nanoparticles were negative, indicating that the LMWH was located on the surface of the shell. Therefore, LHSA could possess heparin activity after nanoparticle formation, yet the anticoagulant activity of LHSA was lower than that of the unmodified LMWH. Because LMWH reduces the risk of embolic events in patients with malignancy and acute VTR [48], its use in cancer patients is recommended by numerous guidelines and is now regarded as a standard of care [49]. Thus, the self-assembled LHSA5 nanoparticle could be attractive as an anticancer drug carrier, which has a synergic effect with poorly water-soluble anticancer drugs encapsulated in the core.

After characterization of the blank LHSA-based nanoparticles, we evaluated DCT-loaded LHSA nanoparticles was evaluated using the LHSA5 conjugate, due to its more stable nanoparticle configuration compared with the other structures. The encapsulation efficacy of the DCT-loaded LHSA5 nanoparticle was 59.82%, with TEM images revealing a spherical shape. The *in vitro* release of DCT from the LHSA5 nanoparticle continued for ~96 h, as shown in Figure 3. From these results, a reduction in the *in vivo* drug clearance was expected, allowing a drug concentration adequate for tumor growth inhibition to be sustained. When intravenously administered in Sprague-Dawley rats, the concentration profile of DCT in plasma was sustained for 6 h, as compared with 2 h for Taxotere administration, as shown in Figure 9.

The effects of the DCT-loaded LHSA5 nanoparticles on *in vitro* cytotoxicity and antitumor efficacy in MCF-7 and MDAMB 231 cells were investigated, as shown in Figures

4 and 5. The LMWH and blank LHSA5 nanoparticles exhibited no severe *in vitro* cytotoxicity. Free DCT and DCT-loaded LHSA5 nanoparticles were cytotoxic to MCF-7 and MDAMB 231 cells. DCT-loaded LHSA5 nanoparticles had a similar or slightly lower efficacy than free DCT, thus contributing to the sustained release of free DCT from LHSA5 nanoparticles. As shown in Figure 3, only 40% of the free DCT was released from LHSA5 nanoparticles in 24 h in the *in vitro* release study.

C6 has been widely used in cellular uptake studies [34, 41], and was used in this study as a fluorescence probe to investigate the cellular uptake efficiency of the LHSA nanoparticles. LHSA5 nanoparticles loaded with C6 in MCF-7 and MDAMB 231 cells were visualized by CLSM in Figure 6. Significant difference was observed in the fluorescence intensities of the C6 solution and the C6-loaded LHSA nanoparticles. In addition, a significantly higher amount of C6 from the LHSA5 nanoparticles was taken up by the cells compared to from the C6 solution, as shown in Figure 7. This result could be attributable to endocytosis of the nanoparticles [42, 43]. Moreover, the fatty acid-modified polysaccharide-based nanoparticles are capable of forming self-assembled nanoparticles with a multi-hydrophobic core [44]. The hydrophobic part of the nanoparticles could facilitate drug internalization into the cells *via* interactions with the cell membrane. Although the LHSA5-based nanoparticles was negatively charged due to its sulfate and carboxyl groups, the nanoparticles was taken up in significantly higher amounts compared with the C6 solution. In addition to drug uptake by nanoparticles, long-term cellular drug retention can play key roles in drug efficacy in microtubule-targeted anticancer drugs [50]. Thus, LHSA5 nanoparticles could induce synergy effect by enhancing drug uptake and retention time, which are shown in *in vivo* antitumor efficacy study (Figure 8).

The DCT-loaded LHSA5 nanoparticles exhibited significant inhibitory effects on

MDAMB 231 tumor growth, compared with the other groups (Figure 8a). This can be explained in terms of the physicochemical properties of the drug-loaded nanoparticles that induce sustained drug release (as shown in Figure 9) and passive targeting to tumor tissue *via* an EPR effect. Although the blank LHSA5 nanoparticles showed insignificant *in vivo* inhibition of MDAMB 231 tumor growth in this study, others have reported the antitumor effects of several heparin derivatives in tumor-bearing mice [36, 51, 52]. This discrepancy can be attributed to the differences in tumor type, heparin injection frequency and capacity, administration route, and heparin-modifying molecules.

The concentration profile of DCT in plasma was sustained up to 6 h (Figure 9). This result indicates that LHSA5 nanoparticles contributed to prolonged circulation of DCT in the bloodstream and is consistent with the improved its therapeutic efficacy (Figure 8a). Compared with the DCT solution, the DCT-loaded LHSA5 nanoparticles provided a significantly higher AUC, $t_{1/2}$, and MRT and a lower CL, as shown in Table 2. These *in vivo* pharmacokinetic parameters were related to its *in vitro* sustained DCT release pattern. Moreover, the increased retention time and decreased clearance of the DCT plasma may contribute to enhanced *in vivo* antitumor efficacy in the tumor xenograft model, as shown in Figure 8a.

5. Conclusion

LHSA conjugates were successfully synthesized and self-assembled nanoparticles based on LHSA were prepared. The LHSA-based nanoparticles have an LMWH moiety on the outer shell resulting in a negative surface charge. Among the synthesized conjugates, LHSA5 formed stable self-assembled nanoparticles in an aqueous environment, with a narrow size

distribution. Because the LHSA5 nanoparticles showed 30% of the anticoagulant activity exhibited by free LMWH, it likely also maintains the other heparin activities. The DCT-loaded LHSA5 nanoparticles showed sustained drug-release profiles, *in vitro* and *in vivo*, compared with Taxotere. The nanoparticulate structure influenced cellular uptake; consequently, the DCT-loaded LHSA5 nanoparticles formulation improved the half-life of DCT and significantly inhibited MDAMB 231 tumor growth in xenograft mice. Thus, LHSA5-based self-assembled nanoparticles may be useful as an anticancer drug delivery system.

6. References

- [1] G.S. Kwon and T. Okano, Polymeric micelles as new drug carriers, *Adv. Drug Deliv. Rev.* 21 (1996) 107-116.
- [2] Z. Liu, Y. Jiao, Y. Wang, C. Zhou. and Z. Zhang, Polysaccharides-based nanoparticles as drug delivery systems, *Adv. Drug Deliv. Rev.* 60 (2008) 1650-1662.
- [3] H. Maeda, J. Wu, T. Sawa, Y. Matsumura. and K. Hori, Tumor vascular permeability and the EPR effect in macromolecular therapeutics: a review, *J. Control. Release.* 65 (2000) 271-284.
- [4] H. Maeda, Tumor-selective delivery of macromolecular drugs via the EPR effect: background and future prospects, *Bioconjugate Chem.* 21 (2010) 797-802.
- [5] T. Verrecchia, G. Spenlehauer, D. Bazile, A. Murry-Brelier, Y. Archimbaud. and M. Veillard, Non-stealth (poly (lactic acid/albumin)) and stealth (poly (lactic acid-polyethylene glycol)) nanoparticles as injectable drug carriers, *J. Control. Release.* 36 (1995) 49-61.
- [6] X. Shao, Q. Liu, C. Zhang, X. Zheng, J. Chen, Y. Zha, Y. Qian, X. Zhang, Q. Zhang. and X. Jiang, Concanavalin A-conjugated poly (ethylene glycol)-poly (lactic acid) nanoparticles for intranasal drug delivery to the cervical lymph nodes, *J. Microencapsul.* (2013) 1-7.
- [7] V. Labhasetwar, C. Song, W. Humphrey, R. Shebuski. and R.J. Levy, Arterial uptake of biodegradable nanoparticles: effect of surface modifications, *J. Pharm. Sci.* 87 (1998) 1229-1234.
- [8] J. Molpeceres, M. Guzman, M.R. Aberturas, M. Chacon. and L. Berges, Application of central composite designs to the preparation of polycaprolactone nanoparticles by solvent displacement, *J. Pharm. Sci.* 85 (1996) 206-213.
- [9] S. Aishwarya, S. Mahalakshmi. and P.K. Sehgal, Collagen-coated polycaprolactone

- microparticles as a controlled drug delivery system, *J. Microencapsul.* 25 (2008) 298-306.
- [10] S. Sharma, H.A. Benson, T.K. Mukkur, P. Rigby. and Y. Chen, Preliminary studies on the development of IgA-loaded chitosan-dextran sulphate nanoparticles as a potential nasal delivery system for protein antigens, *J. Microencapsul.* 30 (2013) 283-294.
- [11] M. Jahanshahi and Z. Babaei, Protein nanoparticle: A unique system as drug delivery vehicles, *Afr. J. Biotechnol.* 7 (2008) 4926-4934.
- [12] Y. Wu, J.A. MacKay, J. R. McDaniel, A. Chilkoti. and R.L. Clark, Fabrication of elastin-like polypeptide nanoparticles for drug delivery by electrospraying, *Biomacromolecules.* 10 (2008) 19-24.
- [13] G.S. Kwon and T. Okano, Soluble self-assembled block copolymers for drug delivery, *Pharm. Res.* 16 (1999) 597-600.
- [14] G. Saravanakumar, K.H. Min, D.S. Min, A.Y. Kim, C.-M. Lee, Y.W. Cho, S.C. Lee, K. Kim, S.Y. Jeong. and K. Park, Hydrotropic oligomer-conjugated glycol chitosan as a carrier of paclitaxel: Synthesis, characterization, and *in vivo* biodistribution, *J. Control. Release.* 140 (2009) 210-217.
- [15] P. Sun, Y. Zhang, L. Shi. and Z. Gan, Thermosensitive Nanoparticles Self-Assembled from PCL-b-PEO-b-PNIPAAm Triblock Copolymers and their Potential for Controlled Drug Release, *Macromolecular bioscience.* 10 (2010) 621-631.
- [16] K.A. Lyseng-Williamson and C. Fenton, Docetaxel, *Drugs.* 65 (2005) 2513-2531.
- [17] S.D. Baker, A. Sparreboom. and J. Verweij, Clinical pharmacokinetics of docetaxel, *Clinical pharmacokinetics.* 45 (2006) 235-252.
- [18] A. Michael, K. Syrigos. and H. Pandha, Prostate cancer chemotherapy in the era of targeted therapy, *Prostate cancer and prostatic diseases.* 12 (2008) 13-16.
- [19] E. Persohn, A. Canta, S. Schoepfer, M. Traebert, L. Mueller, A. Gilardini, S. Galbiati, G.

Nicolini, A. Scuteri. and F. Lanzani, Morphological and morphometric analysis of paclitaxel and docetaxel-induced peripheral neuropathy in rats, *European journal of cancer*. 41 (2005) 1460-1466.

[20] F.K. Engels, R.A. Mathot. and J. Verweij, Alternative drug formulations of docetaxel: a review, *Anti-cancer drugs*. 18 (2007) 95-103.

[21] M.L. Immordino, P. Brusa, S. Arpicco, B. Stella, F. Dosio. and L. Cattel, Preparation, characterization, cytotoxicity and pharmacokinetics of liposomes containing docetaxel, *J. Control. Release*. 91 (2003) 417-429.

[22] Y.-M. Yin, F.-D. Cui, C.-F. Mu, M.-K. Choi, J.S. Kim, S.-J. Chung, C.-K. Shim. and D.-D. Kim, Docetaxel microemulsion for enhanced oral bioavailability: Preparation and *in vitro* and *in vivo* evaluation, *J. Control. Release*. 140 (2009) 86-94.

[23] F. Esmaeili, R. Dinarvand, M.H. Ghahremani, M. Amini, H. Rouhani, N. Sepehri, S.N. Ostad. and F. Atyabi, Docetaxel–albumin conjugates: preparation, *in vitro* evaluation and biodistribution studies, *J. Pharm. Sci*. 98 (2009) 2718-2730.

[24] H. Buller, M. Gent, A. Gallus, J. Ginsberg, M. Prins, R. Baildon. and J. ten Cate, Low-molecular weight heparin in the treatment of patients with venous thromboembolism: the Columbus Investigators, *The New England Journal of Medicine*. 337 (1997) 657-662.

[25] E. Young, The anti-inflammatory effects of heparin and related compounds, *Thromb. Res*. 122 (2008) 743-752.

[26] T.M.H. Niers, C.P.W. Klerk, M. DiNisio, C.J.F. Van Noorden, H.R. Büller, P.H. Reitsma. and D.J. Richel, Mechanisms of heparin induced anti-cancer activity in experimental cancer models, *Crit. Rev. Oncol./Hematol*. 61 (2007) 195-207.

[27] R. Castelli, F. Porro. and P. Tarsia, The heparins and cancer: review of clinical trials and biological properties, *Vascular Medicine*. 9 (2004) 205-213.

- [28] M. Marchetti, A. Vignoli, L. Russo, D. Balducci, M. Pagnoncelli, T. Barbui. and A. Falanga, Endothelial capillary tube formation and cell proliferation induced by tumor cells are affected by low molecular weight heparins and unfractionated heparin, *Thromb. Res.* 121 (2008) 637-645.
- [29] K.H. Bae, H. Mok. and T.G. Park, Synthesis, characterization, and intracellular delivery of reducible heparin nanogels for apoptotic cell death, *Biomaterials.* 29 (2008) 3376-3383.
- [30] B. Casu, M. Guerrini, S. Guglieri, A. Naggi, M. Perez, G. Torri, G. Cassinelli, D. Ribatti, P. Carminati. and G. Giannini, Undersulfated and glycol-split heparins endowed with antiangiogenic activity, *J. Med. Chem.* 47 (2004) 838-848.
- [31] S.M. Smorenburg and C.J. Van Noorden, The complex effects of heparins on cancer progression and metastasis in experimental studies, *Pharmacol. Rev.* 53 (2001) 93-106.
- [32] D. Farge, P. Debourdeau, M. Beckers, C. Baglin, R.M. Bauersachs, B. Brenner, D. Brillhante, A. Falanga, G.T. Gerotzafias, N. Haim, A.K. Kakkar, A.A. Khorana, R. Lecumberri, M. Mandala, M. Marty, M. Monreal, S.A. Mousa, S. Noble, I. Pabinger, P. Prandoni, M.H. Prins, M.H. Qari, M.B. Streiff, K. Syrigos, H. Bounameaux. and H.R. Bü Ller, International clinical practice guidelines for the treatment and prophylaxis of venous thromboembolism in patients with cancer, *J. Thromb. Haemost.* 11 (2013) 56-70.
- [33] Y. Min, M. Akbulut, K. Kristiansen, Y. Golan. and J. Israelachvili, The role of interparticle and external forces in nanoparticle assembly, *Nature Materials.* 7 (2008) 527-538.
- [34] H.-J. Cho, H.Y. Yoon, H. Koo, S.-H. Ko, J.-S. Shim, J.-H. Lee, K. Kim, I. Chan Kwon. and D.-D. Kim, Self-assembled nanoparticles based on hyaluronic acid-ceramide (HA-CE) and Pluronic® for tumor-targeted delivery of docetaxel, *Biomaterials.* 32 (2011) 7181-7190.
- [35] K. Park, G.Y. Lee, R.-W. Park, I.-S. Kim, S.Y. Kim. and Y. Byun, Combination Therapy of Heparin–Deoxycholic Acid Conjugate and Doxorubicin against Squamous Cell Carcinoma

and B16F10 Melanoma, *Pharm. Res.* 25 (2008) 268-276.

[36] K. Park, G.Y. Lee, Y.-S. Kim, M. Yu, R.-W. Park, I.-S. Kim, S.Y. Kim. and Y. Byun, Heparin–deoxycholic acid chemical conjugate as an anticancer drug carrier and its antitumor activity, *J. Control. Release.* 114 (2006) 300-306.

[37] J.S. Lee, D.H. Go, J.W. Bae, I.K. Jung, J.W. Lee. and K.D. Park, Synthesis and characterization of heparin conjugated Tetronic® –PCL copolymer for protein drug delivery, *Curr. Appl. Phys.* 7 (2007) e49-e52.

[38] S. Li, B. Byrne, J. Welsh. and A.F. Palmer, Self-Assembled Poly (butadiene)-b-poly (ethylene oxide) Polymersomes as Paclitaxel Carriers, *Biotechnology progress.* 23 (2007) 278-285.

[39] P. Lim Soo and A. Eisenberg, Preparation of block copolymer vesicles in solution, *Journal of Polymer Science Part B: Polymer Physics.* 42 (2004) 923-938.

[40] S.J. Clarke and L.P. Rivory, Clinical pharmacokinetics of docetaxel, *Clinical pharmacokinetics.* 36 (1999) 99-114.

[41] C.F. Mu, P. Balakrishnan, F.D. Cui, Y.M. Yin, Y.B. Lee, H.G. Choi, C.S. Yong, S.J. Chung, C.K. Shim. and D.D. Kim, The effects of mixed MPEG-PLA/Pluronic® copolymer micelles on the bioavailability and multidrug resistance of docetaxel, *Biomaterials.* 31 (2010) 2371-2379.

[42] C. He, Y. Hu, L. Yin, C. Tang. and C. Yin, Effects of particle size and surface charge on cellular uptake and biodistribution of polymeric nanoparticles, *Biomaterials.* 31 (2010) 3657-3666.

[43] S.D. Conner and S.L. Schmid, Regulated portals of entry into the cell, *Nature.* 422 (2003) 37-44.

[44] J. You, F.-Q. Hu, Y.-Z. Du, H. Yuan. and B.-F. Ye, High cytotoxicity and resistant-cell

reversal of novel paclitaxel loaded micelles by enhancing the molecular-target delivery of the drug, *Nanotechnology*. 18 (2007) 495101-495107.

[45] U. Termsarasab, H.-J. Cho, D.H. Kim, S. Chong, S.-J. Chung, C.-K. Shim, H.T. Moon. and D.-D. Kim, Chitosan oligosaccharide–arachidic acid-based nanoparticles for anti-cancer drug delivery, *Int. J. Pharm.* 441 (2013) 373-380.

[46] G. Gaucher, M.-H. Dufresne, V.P. Sant, N. Kang, D. Maysinger. and J.-C. Leroux, Block copolymer micelles: preparation, characterization and application in drug delivery, *J. Control. Release*. 109 (2005) 169-188.

[47] N. Rizkalla, C. Range, F.-X. Lacasse. and P. Hildgen, Effect of various formulation parameters on the properties of polymeric nanoparticles prepared by multiple emulsion method, *J. Microencapsul.* 23 (2006) 39-57.

[48] A.Y. Lee, M.N. Levine, R.I. Baker, C. Bowden, A.K. Kakkar, M. Prins, F.R. Rickles, J.A. Julian, S. Haley. and M.J. Kovacs, Low-molecular-weight heparin versus a coumarin for the prevention of recurrent venous thromboembolism in patients with cancer, *N. Engl. J. Med.* 349 (2003) 146-153.

[49] J. Nishioka and S. Goodin, Low-molecular-weight heparin in cancer-associated thrombosis: treatment, secondary prevention, and survival, *J. Oncology Pharm. Practice*. 13 (2007) 85-97.

[50] M.A. Jordan and K. Kamath, How do microtubule-targeted drugs work? An overview, *Current Cancer Drug Targets*. 7 (2007) 730-742.

[51] P.E. Thorpe, E.J. Derbyshire, S.P. Andrade, N. Press, P.P. Knowles, S. King, G.J. Watson, Y.-C. Yang. and M. Rao-Betté, Heparin-steroid conjugates: new angiogenesis inhibitors with antitumor activity in mice, *Cancer Res.* 53 (1993) 3000-3007.

[52] F. Lapierre, K. Holme, L. Lam, R.J. Tressler, N. Storm, J. Wee, R.J. Stack, J. Castellot.

and D.J. Tyrrell, Chemical modifications of heparin that diminish its anticoagulant but preserve its heparanase-inhibitory, angiostatic, anti-tumor and anti-metastatic properties, *Glycobiology*. 6 (1996) 355-366.

Table 1 Characterization of LHSA5 and DCT-loaded LHSA5 nanoparticles

Formulation	Particle size (nm)	Polydispersity index	Zeta potential (mV)	Encapsulation efficiency (%)	Drug loading content (%)
LHSA5	177.9 ± 7.2	0.17 ± 0.04	-33.1 ± 0.7	-	-
LHSA5/DCT (5:1,w/w)	155.2 ± 3.5	0.16 ± 0.04	-35.3 ± 0.3	59.8 ± 3.9	10.7 ± 0.6

Notes: Data present as mean ± SD (n=4)

Encapsulation efficiency (%) = $\frac{\text{actual amount of docetaxel in formulation}}{\text{input amount of docetaxel in formulation}} \times 100$.

Drug loading content (%) = $\frac{\text{amount of docetaxel in formulation (mg)}}{\text{amount of formulation (mg)}} \times 100$.

Abbreviations: LHSA, LMWH-SA; DCT, docetaxel; SD, standard deviation.

Table 2 Pharmacokinetic parameters of Taxotere and DCT-loaded LHSA5 nanoparticles after a single intravenous injection (8mg/kg) in rats (n=4)

Parameter	Taxotere	LHSA5/DCT
AUC ($\mu\text{g min/mL}$)	75.1 \pm 10.2	186.8 \pm 24.6*
Terminal $t_{1/2}$ (min)	38.0 \pm 6.3	121.8 \pm 11.8*
CL (mL/min/kg)	100.4 \pm 15.6	39.4 \pm 5.0*
V_{ss} (mL/kg)	5401.3 \pm 131.5	6910.5 \pm 979.3
MRT (min)	23.5 \pm 2.2	85.4 \pm 4.0*

Notes: Data present as mean \pm SD (n=4)

* A *p*-value of less than 0.05 was considered to be statistically significant using a t-test between Taxotere and LHSA5/DCT groups.

Abbreviations: DCT, docetaxel; LHSA, LMWH-SA; AUC, total area under the plasma concentration-time curve from time zero to the end point; CL, time-averaged total body clearance; V_{ss}, the apparent volume of distribution under steady-state conditions; MRT, the mean residence time; SD, standard deviation.

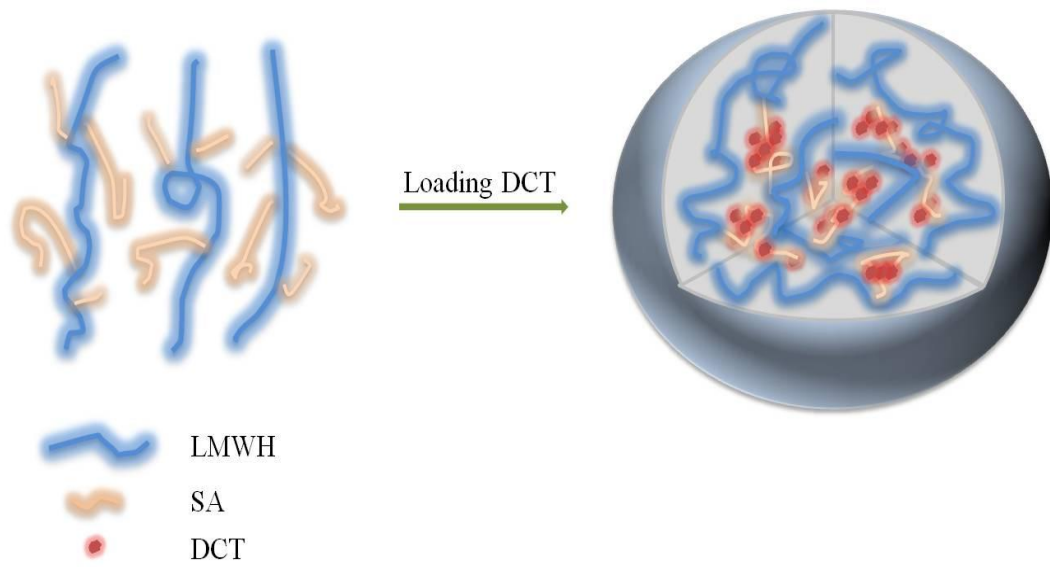


Figure 1 Schematic illustration of LHSa-based nanoparticles.

Abbreviations: LMWH, low-molecular-weight heparin; SA, stearylamine; DCT, docetaxel; LHSa, LMWH-SA.

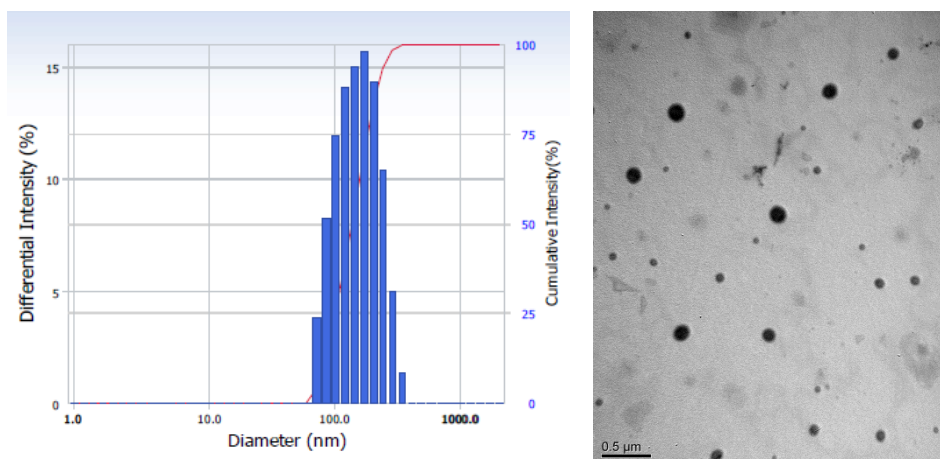


Figure 2 Size distribution and TEM images of DCT-loaded LHSA5 nanoparticles. The length of the scale bar in TEM images is 500 nm ($\times 200,000$).

Abbreviations: TEM, transmission electron microscopy; DCT, docetaxel; LHSA, LMWH-SA.

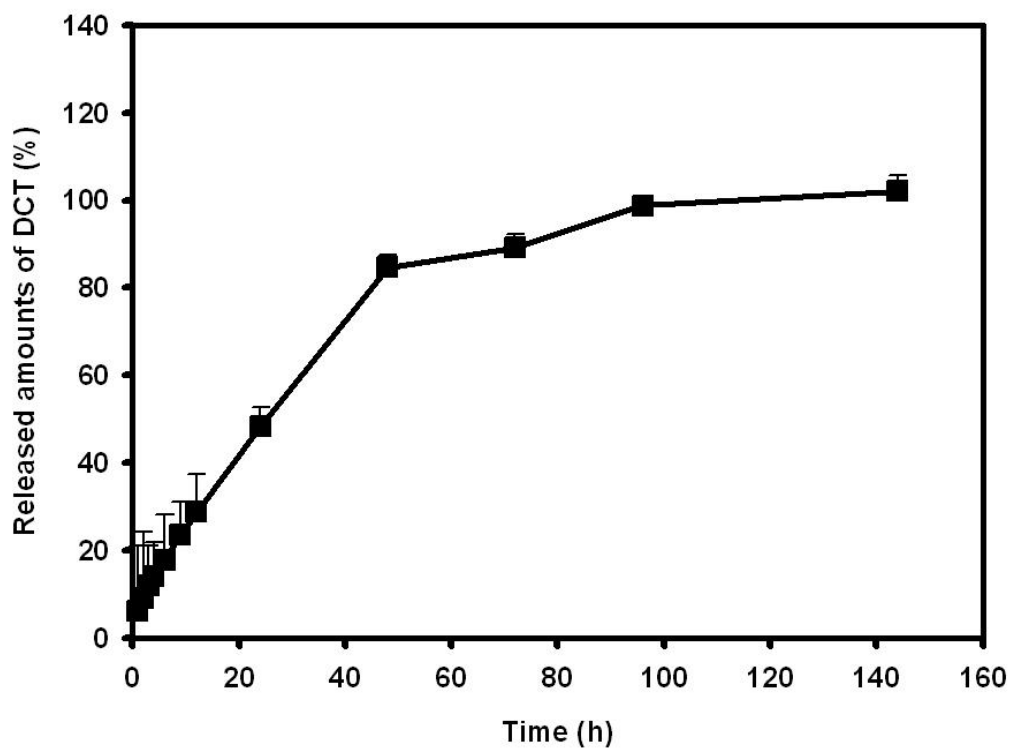
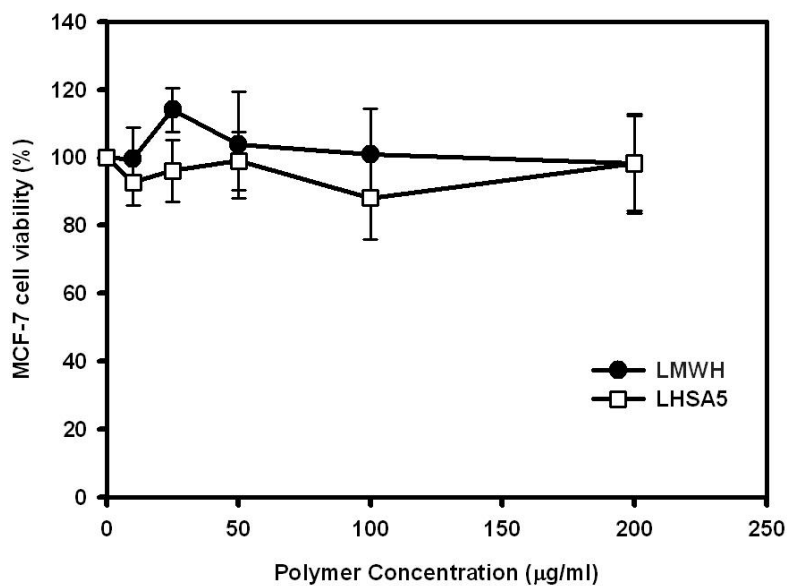


Figure 3 *In vitro* release profile of DCT from LHS A5-based nanoparticles. Each point represents as mean \pm S.D. (n=3).

Abbreviations: DCT, docetaxel; LHS A, LMWH-SA; S.D, standard deviation.

(a)



(b)

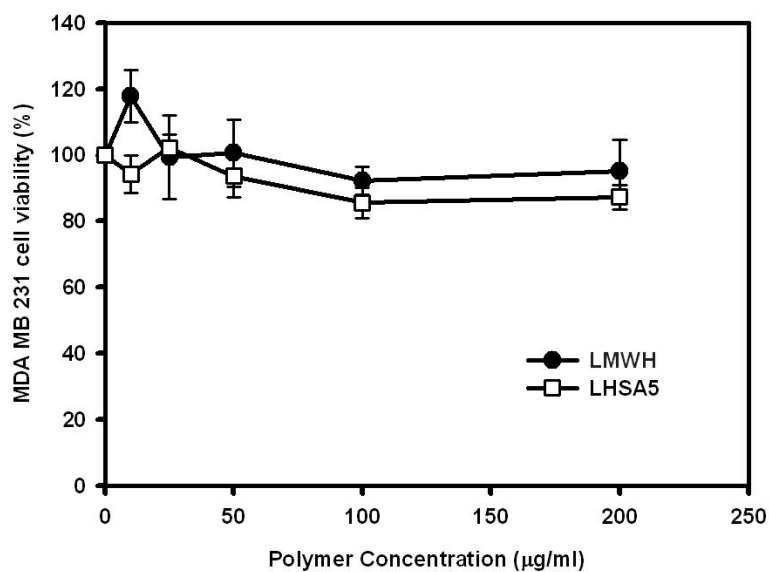
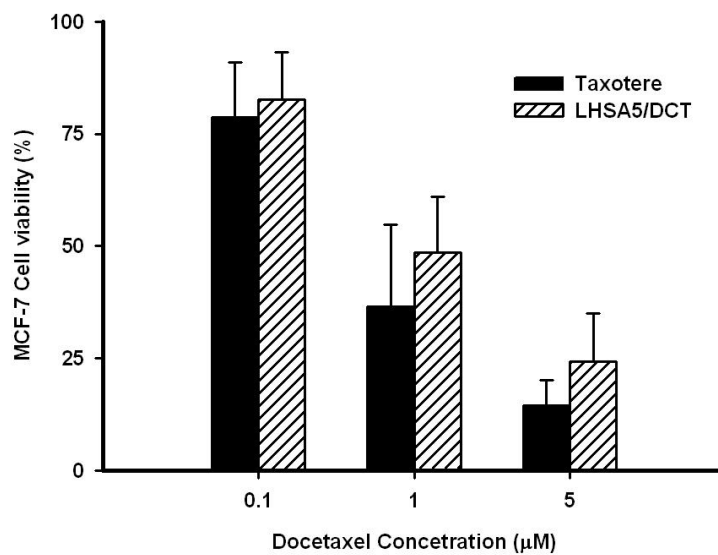


Figure 4 *In vitro* cytotoxicity of LHS A5 in (a) MCF-7 and (b) MDAMB 231 cells. Cell viability was measured by MTS-based assay after incubating LMWH or LHS A5 at various polymer concentrations for 24 h. Data represent as mean \pm S.D. (n=5).

Abbreviations: LHS A, LMWH-SA; S.D, standard deviation.

(a)



(b)

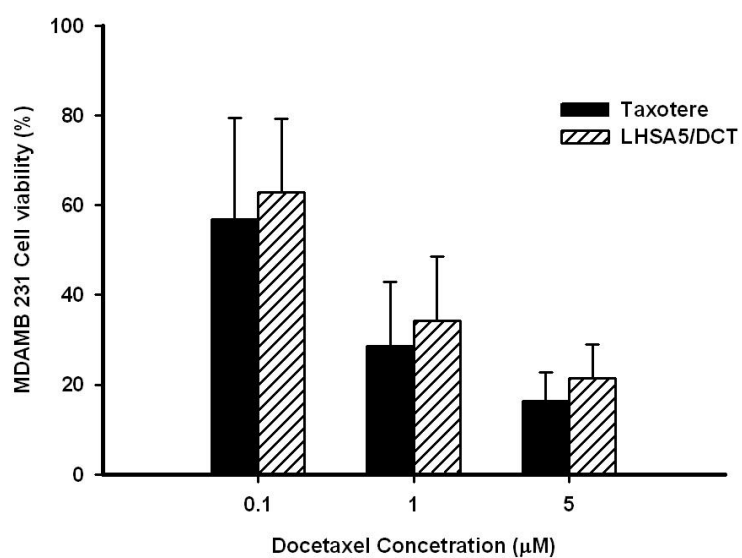


Figure 5 *In vitro* antitumor efficacy of Taxotere and DCT-loaded LHS A5 nanoparticles in (a) MCF-7 and (b) MDAMB 231 cells.

Abbreviations: DCT, docetaxel; LHS A, LMWH-SA.

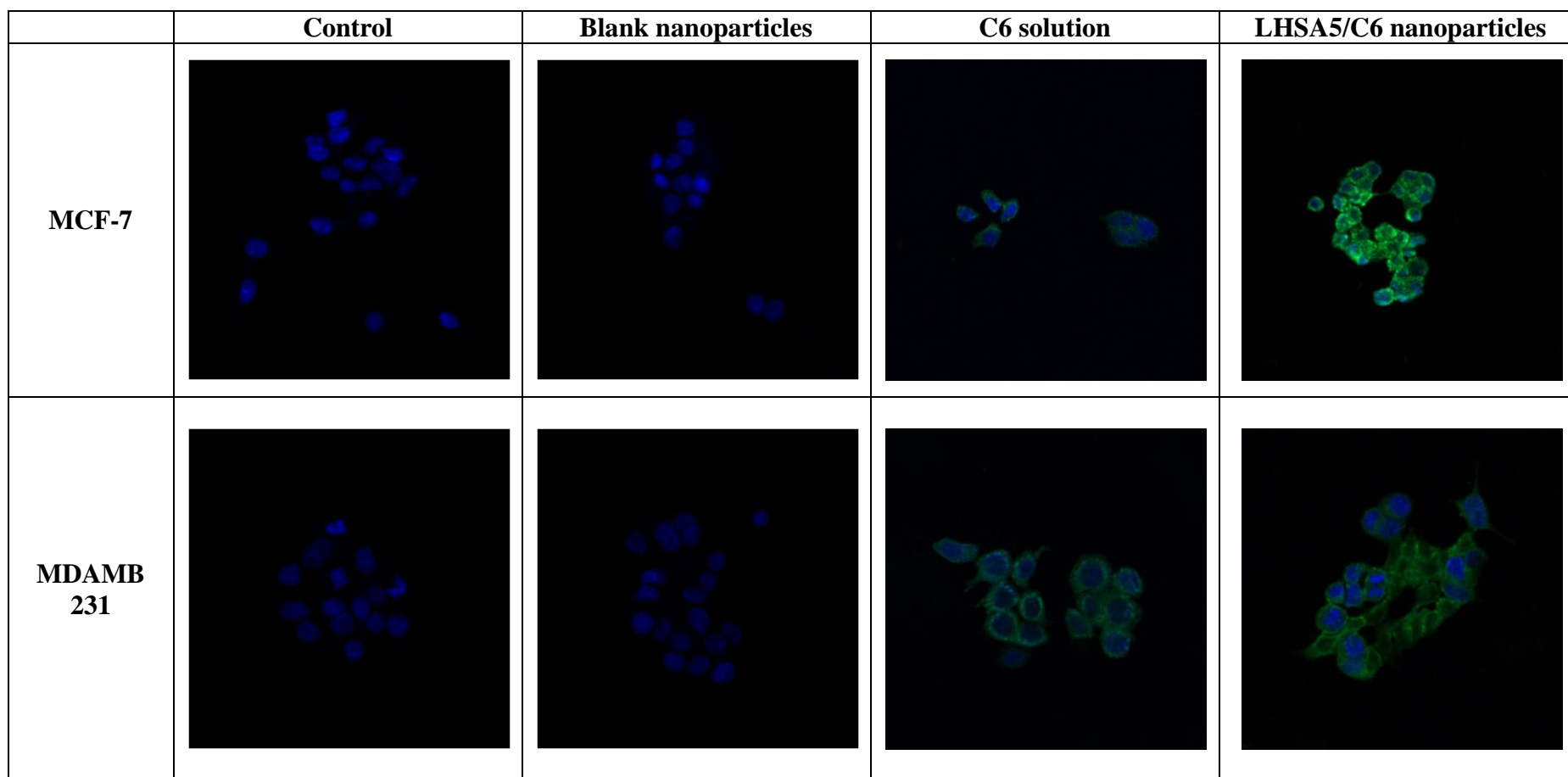
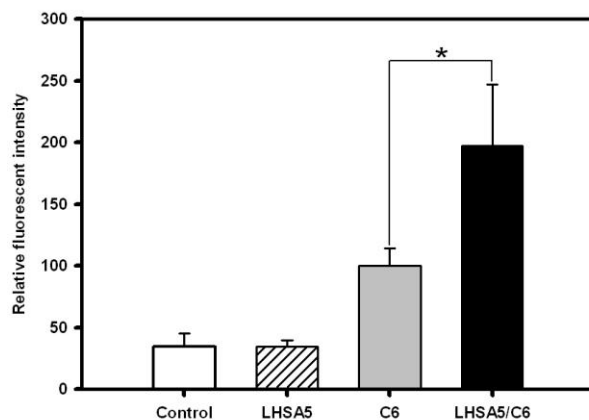


Figure 6 *In vitro* cellular uptake study of coumarin 6 was observed by CLSM in MCF-7 and MDAMB 231 cells after incubating for 2 h. Merged images composed of coumarin 6 (green color) and DAPI (blue color) were shown. Groups were as follows; control, blank LHSA5 nanoparticles, coumarin 6 solution, coumarin 6-loaded LHSA5 nanoparticles.

Abbreviations: CLSM, confocal laser scanning microscope; C6, coumarin 6; LHSA, LMWH-SA.

(a) MCF-7 cell



(b) MDAMB 231 cell

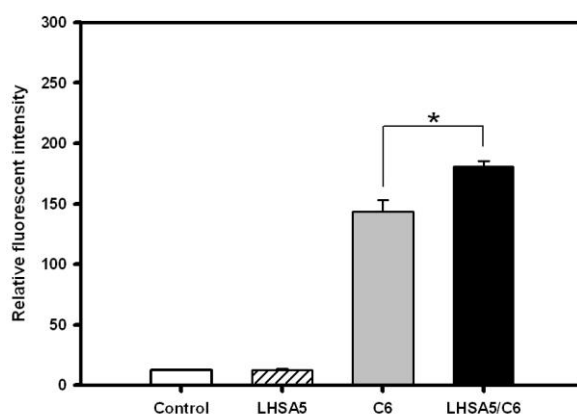


Figure 7 *In vitro* cellular uptake study of coumarin 6 was observed by FACS in (a) MCF-7 and (b) MDAMB 231 cells after incubating for 2 h. Groups were as follows; control, blank LHSA5 nanoparticles, coumarin 6 solution, coumarin 6-loaded LHSA5 nanoparticles. Data represent as mean \pm S.D. (n=4).

Notes: * A *p*-value of less than 0.05 was considered to be statistically significant using a t-test between C6 and LHSA5/C6 groups.

Abbreviations: FACS, fluorescence-activated cell sorter; C6, coumarin 6; LHSA, LMWH-SA.

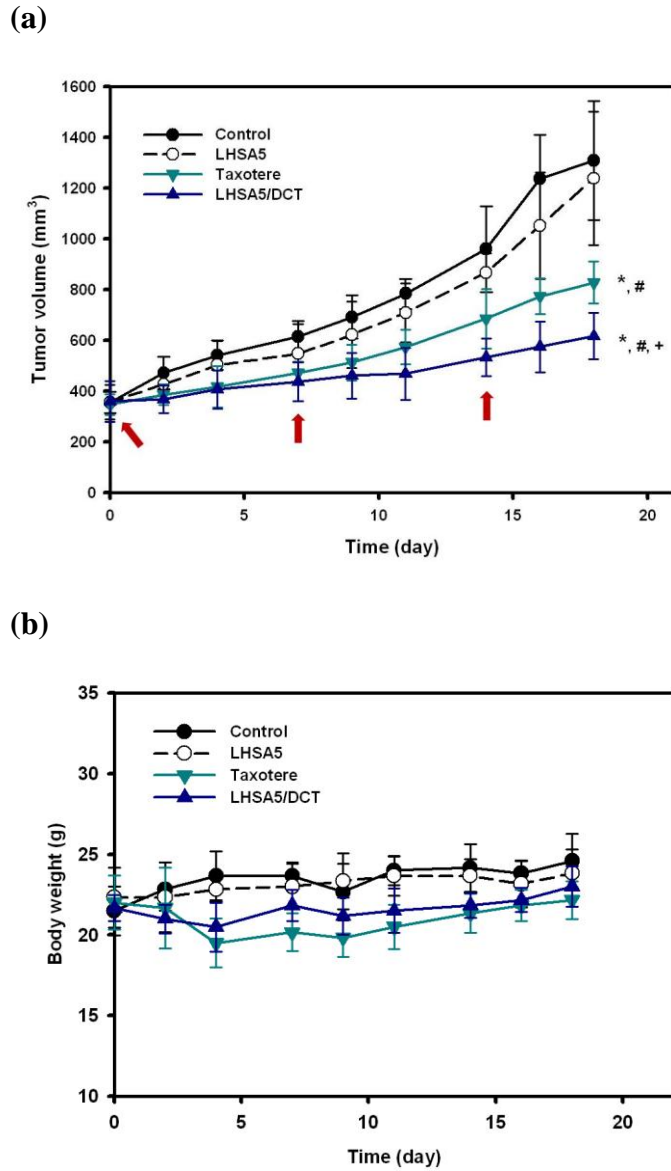


Figure 8 *In vivo* antitumor efficacy in the MDAMB 231 tumor-bearing mouse model. (a) Tumor volume (mm³) profiles according to time (day) are shown. All samples were injected on day 0, 7, and 14 (red arrows). Points indicate the means \pm SD (n=5). (b) Body weight (g) was also measured with tumor size measurement for 18 days.

Notes: Points indicate the means \pm SD (n=5). The data were analyzed with two-way ANOVA. * p < 0.05 compared with the control group; # p < 0.05 compared with the LHSA5 group; + p < 0.05 compared with the Taxotere group.

Abbreviations: LHSA, LMWH-SA; DCT, docetaxel; SD, standard deviation.

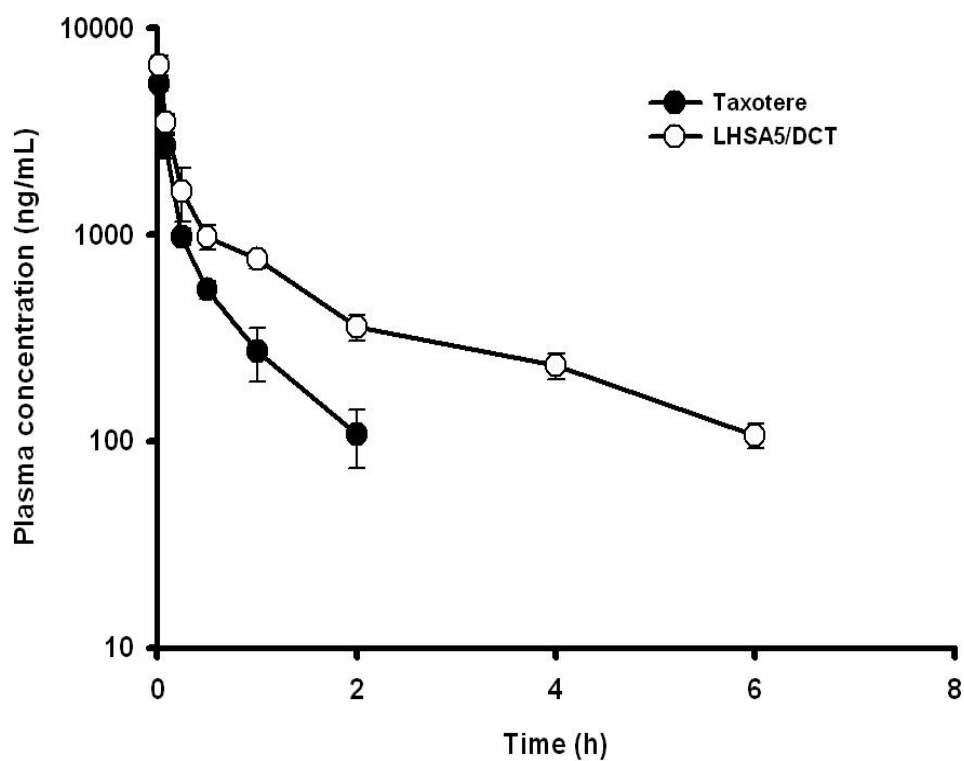


Figure 9 *In vivo* pharmacokinetic profile after intravenous injection of Taxotere and DCT-loaded LHS5 nanoparticles formulation in rats at a dose of 8 mg/kg DCT. Points represent the mean \pm SD (n=4).

Abbreviations: DCT, docetaxel; LHS5, LMWH-SA; SD, standard deviation.

국문초록

Preparation and characterization of self-assembled nanoparticles based on low-molecular-weight heparin and stearylamine conjugates for controlled delivery of docetaxel

Part I. Synthesis and characterization of amphiphilic polymer consisted of low-molecular-weight heparin and stearylamine for the preparation of self-assembled nanoparticle

본 연구의 목적은 자가조립나노입자 제조를 위한 저분자량 헤파린과 스테아릴아민을 이용한 양친매성 고분자를 합성 및 평가하는 것이다. 저분자량 헤파린은 친수성 다당류로 항응고 작용 및 항암작용이 있다. 여기에 소수성 지방산유도체인 스테아릴아민을 저분자량헤파린에 결합시켜 양친매성 고분자를 합성하였다. EDC, NHS를 촉매로 하여 분자량헤파린 1몰 당 스테아릴아민을 각각 1, 3, 5 배의 몰비율을 합성하였다. 저분자량 헤파린과 스테아릴아민 결합체(LHSA)의 합성은 $^1\text{H-NMR}$ 을 이용하여 확인하였다. LHSA들을 이용한 자가조립나노입자를 제조하여 입자크기, 제타전위, 입자모양 등을 평가하였다. 합성된 LHSA들 중 저분자량헤파린과 스테아릴아민 1:5의 비율로 합성한 LHSA5 결합체가 178 nm의 크기를 가지는 가장 안정한 자가조립나노입자를 형성하였다. LHSA5의 임계미셀농도는 0.044 mg/ml 이하로 측정되었고, LHSA5의 항응고활성은 저분자량헤파린의 31.92%로 측정되었다. 이런 결과들을 통해 LHSA5 결합체는 소수성 항암제 약물전달을 위한 효과적인 나노입자전달체로 활용가능하다는 것을 시사하였다.

Part II. Characterization and evaluation of self-assembled nanoparticles based on low-molecular-weight heparin and stearylamine conjugates for controlled delivery of docetaxel

본 연구의 목적은 LHSA 기반의 자가조립나노입자를 이용하여 도세탁셀 항암제의 정맥주사 제제의 제조 및 평가이다. 도세탁셀 항암제를 봉입한 자가조립나노입자를 제조하여 *in vitro* 항암효과, *in vitro* 세포 내 흡수, *in vivo* 항종양효과 및 *in vivo* 약물동태 등을 평가하였다. 도세탁셀을 봉입한 자가조립나노입자는 155 nm 크기를 가지는 표면에 음전하를 띤 구형의 형태를 나타내었다. *In vitro*, *in vivo* 에서 도세탁셀 약물의 방출 패턴을 확인한 결과 자가조립나노입자에서 도세탁셀의 서방형 방출패턴을 확인하였다. 쿠마린6을 봉입한 자가조립나노입자를 이용하여 MCF-7과 MDAMB-231 세포에서의 흡수를 평가해 본 결과 자가조립나노입자 제제에서 쿠마린6 용액에 비해 높은 흡수율을 나타내었다. 최종적으로 MDAMB-231 종양을 이식한 마우스모델에서의 항종양효과 평가에서 도세탁셀을 봉입한 나노입자 제제가 기존의 도세탁셀 제형보다 유의성 있게 높은 항종양효과를 나타내는 것을 확인하였다. 이러한 실험 결과는 LHSA 기반의 자가조립나노입자 제제가 항암제의 약물전달시스템으로서 효과적인 방법이라는 것을 시사하였다.

주요어: Low-molecular-weight heparin, Anticancer drug delivery, Docetaxel, Self-assembled nanoparticle, Amphiphilic polymer

학번: 2011-30499

Appendix

Preparation and characterization of self-assembled nanoparticles based on low-molecular-weight heparin and stearylamine conjugates for controlled delivery of docetaxel

Dong-Hwan Kim¹
Ubonvan Termsarasab¹
Hyun-Jong Cho²
In-Soo Yoon³
Jae-Young Lee¹
Hyun Tae Moon¹
Dae-Duk Kim¹

¹College of Pharmacy and Research Institute of Pharmaceutical Sciences, Seoul National University, Seoul, Republic of Korea; ²College of Pharmacy, Kangwon National University, Chuncheon, Republic of Korea; ³College of Pharmacy and Natural Medicine Research Institute, Mokpo National University, Jeonnam, Republic of Korea

Abstract: Low-molecular-weight heparin (LMWH)–stearylamine (SA) conjugates (LHSA)-based self-assembled nanoparticles were prepared for intravenous delivery of docetaxel (DCT). 1-Ethyl-3-(3-dimethylaminopropyl) carbodiimide and *N*-hydroxysuccinimide were used as coupling agents for synthesis of LHSA conjugates. The physicochemical properties, in vitro antitumor efficacy, in vitro cellular uptake efficiency, in vivo antitumor efficacy, and in vivo pharmacokinetics of LHSA nanoparticles were investigated. The LHSA nanoparticles exhibited a spherical shape with a mean diameter of 140–180 nm and a negative surface charge. According to in vitro release and in vivo pharmacokinetic test results, the docetaxel-loaded LHSA5 (LMWH:SA =1:5) nanoparticles exhibited sustained drug release profiles. The blank LHSA nanoparticles demonstrated only an insignificant cytotoxicity in MCF-7 and MDAMB 231 human breast cancer cells; additionally, higher cellular uptake of coumarin 6 (C6) in MCF-7 and MDAMB 231 cells was observed in the LHSA5 nanoparticles group than that in the C6 solution group. The in vivo tumor growth inhibition efficacy of docetaxel-loaded LHSA5 nanoparticles was also significantly higher than the Taxotere[®]-treated group in the MDAMB 231 tumor-xenografted mouse model. These results indicated that the LHSA5-based nanoparticles could be a promising anticancer drug delivery system.

Keywords: amphiphilic polymer, docetaxel, drug delivery, low-molecular-weight heparin, self-assembled nanoparticle

Introduction

Over the past decade, nanoparticulate drug delivery systems containing anticancer agents have been investigated extensively due to their specific accumulation behavior at the tumor site.^{1,2} Nanoparticulate drugs can be distributed to tumor vasculatures by the enhanced permeability and retention (EPR) effect, taking advantage of the leaky vascular nature of tumor tissues that provides for passive tumor targeting.^{3,4} Additionally, these nanoparticulate drugs offer the advantages of prolonged systemic circulation by avoiding phagocytosis, improved efficacy, and reduced toxicity. Numerous biocompatible and biodegradable materials, such as poly(lactic acid),^{5,6} poly(glycolic acid),⁷ polycaprolactone,^{8,9} polysaccharides,¹⁰ proteins,¹¹ and polypeptides,¹² have been used for the preparation of polymeric nanoparticles. Among them, polysaccharides have been used extensively to prepare nanoparticles for drug delivery.² Polysaccharides are natural biomaterials; thus, they are generally safe, nontoxic, biocompatible, and biodegradable. They have various derivable groups that can be modified with other

Correspondence: Dae-Duk Kim
College of Pharmacy and Research
Institute of Pharmaceutical Sciences,
Seoul National University, Seoul 151-742,
Republic of Korea
Tel +82 2 8807 870
Fax +82 2 8739 177
Email ddkim@snu.ac.kr



chemicals. Among the drug delivery systems, self-assembled nanoparticles have been studied for the encapsulation and sustained release of poorly soluble drugs.^{13–15} Amphiphilic polymers can be used to form nanoparticles with a hydrophobic core and a hydrophilic shell. This structure enables the encapsulation and delivery of poorly soluble drugs, extending the circulation time of nanoparticles in the bloodstream.

Docetaxel (DCT), an antimitotic chemotherapy medication and a semisynthetic analog of paclitaxel, is a particularly important anticancer agent that has been used for the treatment of many cancers, exhibiting cytotoxic activity in breast, ovarian, prostate, and non-small-cell lung cancer cells.^{16–18} As with all chemotherapies, however, adverse effects are common; side effects such as neutropenia, peripheral neuropathy, musculoskeletal toxicity, and hypersensitivity reactions have been verified. In its commercial formulation (Taxotere[®], Sanofi-Aventis, Bridgewater, NJ, USA), non-ionic surfactant Tween 80 (polysorbate 80) and 13% ethanol in saline have been used to dissolve DCT, due to its poor solubility in water;¹⁹ however, this formulation is associated with unpredictable hypersensitivity reactions and other side effects.²⁰ Thus, many new systems – including micelles, emulsions, and conjugates with other polymers – have been developed to deliver DCT to tumor sites with minimal adverse reactions.^{21–23}

Heparin is a biocompatible, biodegradable, water-soluble natural polysaccharide coupled with various biological activities, including anticoagulation, anti-inflammatory, and antiangiogenesis effects.^{24,25} In addition to its well-known anticoagulant activity, the anticancer activity of heparin has been evaluated.^{26,27} Low-molecular-weight heparin (LMWH) exerts its anticancer activity by affecting the proliferation, adhesion, angiogenesis, migration, and invasion of cancer cells. Although the exact mechanism of LMWH interference with cancer biology still remains unclear, it may involve the inhibition of both coagulation and noncoagulation-dependent pathways of tumor progression.²⁸ Furthermore, in a study of venous thromboembolism therapy, a significant reduction in the mortality rate was noted in the LMWH treatment group among cancer patients.²⁶ Thus, these idiosyncratic properties facilitate the development of heparin-based delivery systems.^{29,30} However, unfractionated heparin (UFH) causes adverse effects, such as bleeding, which have limited its application. LMWH has a reduced anticoagulant activity and, thus far, appears to have a greater anticancer effect than UFH;³¹ thus, LMWH is preferable to UFH for the initial treatment of venous thromboembolism prevalent in cancer patients.³²

In this study, we synthesized an amphiphilic polymer composed of LMWH and stearylamine (octadecylamine, SA) for the preparation of self-assembled nanoparticles for anti-cancer drug delivery. This negatively charged nanoparticle was prepared using LMWH-SA (LHSA) conjugates, with LMWH as the hydrophilic segment and SA as its hydrophobic counterpart. SA (18-carbon saturated fatty amine) is used for the synthesis of uniform nanoparticles.³³ The physicochemical properties of LHSA-based nanoparticles containing DCT were characterized by determining size, zeta potential, and DCT-loading efficacy. DCT release from nanoparticles and the cytotoxicity of blank nanoparticles were also investigated. Moreover, the optimized formulation was evaluated via in vitro cellular uptake study using confocal laser scanning microscopy (CLSM) and fluorescence-activated cell sorter (FACS) measurements, and in vivo antitumor efficacy and pharmacokinetic studies.

Materials and methods

Materials

LMWH (101 IU mg⁻¹), with an average molecular weight of ~4,500 Da, was purchased from Nanjing King-Friend Biochemical Pharmaceutical Co. Ltd (Nanjing, People's Republic of China). 1-Ethyl-3-(3-dimethylaminopropyl) carbodiimide (EDC), *N*-hydroxysuccinimide (NHS), SA, coumarin 6 (C6), and pyrene were obtained from Sigma-Aldrich Co. (St Louis, MO, USA). DCT was purchased from Taihua Co. (Xi'an, People's Republic of China). Formamide (FA), tetrahydrofuran (THF), and acetonitrile (HPLC [high-performance liquid chromatography] grade) were supplied by Fisher Scientific Korea Ltd. (Seoul, Republic of Korea). Dulbecco's Modified Eagle's Medium (DMEM), RPMI 1640 (developed by Roswell Park Memorial Institute), heat-inactivated fetal bovine serum, streptomycin, and penicillin were obtained from Gibco Life Technologies (Karlsruhe, Germany). Water was purified by distillation, deionization, and reverse osmosis (Milli-Q Plus). All other chemicals were of analytical grade, which were purchased from commercial sources.

Synthesis and characterization of LHSA conjugates

Amphiphilic LHSA conjugates were synthesized from LMWH and SA. LMWH (1 g) was dissolved in FA (200 mL) by gentle heating. To synthesize the LHSA conjugates, LMWH solutions were mixed with different amounts of EDC and NHS (3 mol/mol of SA, each) at room temperature. The solutions were then added with different amounts of SA

(1, 3, and 5 mol/mol of LMWH) dissolved in THF (132 mL), followed by stirring at room temperature for 24 hours. The mixtures were then precipitated in excess cold acetone (at 5× the mixture volume) under vigorous agitation, filtered by a glass filter (G4), and stirred for 30 minutes. To remove excess EDC, NHS, and SA, the residues on the glass filter were carefully washed three times with cold acetone, followed by filtering with 50 mL of distilled deionized water (DDW). The filtrate was dialyzed against DDW for 48 hours using a dialysis membrane with molecular weight cutoff of 1 kDa (Spectrum Laboratories, Laguna Hills, CA, USA) and lyophilized. The LHSA conjugate was dissolved in D₂O and analyzed by proton nuclear magnetic resonance (¹H-NMR) spectroscopy (500 MHz).

Aliquots of conjugates were dissolved in D₂O (10 mg mL⁻¹), and ¹H-NMR spectra were obtained by using a Varian FT 500-MHz NMR spectrometer (Varian Inc., Palo Alto, CA, USA). The values of the proton peaks from the ¹H-NMR spectra were integrated to determine the molar substitution of LHSA. Linear regression was prepared from the physical mixture of LMWH and SA at various molar ratios (LMWH:SA = 0.5:1, 1:1, 1:2, and 1:4) dissolved in the mixture of D₂O/THF-d₈ (1:1). The ratio of the integration area (2.80/1.95 ppm) of each physical mixture was calculated.

The anticoagulant activity of LMWH and the LHSA conjugates was determined using the Coatest anti-FXa chromogenic assay (Chromogenix, Milan, Italy). The critical micellar concentration (CMC) of LHSA was investigated using pyrene as a fluorescence probe, as described previously.³⁴ A pyrene solution in THF (2×10⁻⁶ M) was prepared, and the THF was evaporated under gentle nitrogen gas (N₂) flow for 1 hour at 60°C. An LHSA solution in DDW (1 mL), in the concentration range of 10⁻⁵ to 1 mg mL⁻¹, was added to each tube to achieve a final pyrene concentration of 6×10⁻⁷ M. The intensity ratio (I₁/I₃) in the excitation spectra was calculated and plotted. The excitation wavelength was fixed at 334 nm after scanning from 350 to 550 nm, and the slit openings for excitation and emission were set at 10 and 3 nm, respectively. Fluorescence measurements were performed using a fluorescent spectrometer FP-6500 (JASCO Co., Tokyo, Japan).

Preparation and characterization of LHSA-based nanoparticles

A simple modification of our previous methods was used for the self-assembly of LHSA and drug encapsulation.³⁴ LHSA (5 mg) and 1 mg of DCT were completely solubilized in 1 mL of FA; the solvent was evaporated under gentle N₂

flow for 5 hours at 80°C. LHSA and DCT-coated tubes were resuspended with 1 mL of DDW by vortexing for 3 minutes, followed by filtering through a 0.22 μm pore-size syringe filter (Minisart RC 15, Sartorius Stedium Biotech GmbH, Goettingen, Germany).

The mean diameter, polydispersity, and zeta potential of the nanoparticles were determined using a light scattering spectrophotometer (ELS-Z, Otsuka Electronics, Osaka, Japan) at a polymer concentration of 5 mg mL⁻¹. The morphology of the LHSA nanoparticles was assessed by transmission electron microscopy (TEM) (JEM 1010, JEOL, Tokyo, Japan). The nanoparticle suspensions were stained with 2% (w/v) phosphotungstic acid, placed on a copper grid coated with carbon film, air-dried for 10 minutes, and photographed.

The nanoparticle suspensions were distilled with FA to disrupt the self-assembled structure. The drug encapsulation efficiency of drug-loaded nanoparticles was measured using HPLC.³⁴ The HPLC instrument consisted of a dual pump (Waters 515, Waters Corporation, Milford, MA, USA), an autosampler (Waters 717 plus, Waters Corporation), an ultraviolet detector (Waters 2487, Waters Corporation), and a reverse-phase C-18 column (250×4.4 mm², 5 μm, Shiseido, Japan). The mobile phase was a mixture of acetonitrile and DDW (55:45, v/v). The eluent was monitored at 230 nm and a flow rate of 1.0 mL min⁻¹. The DCT concentrations were determined using 20 μL of injection volume at room temperature. The lower limit of quantitation was 500 ng mL⁻¹.

In vitro DCT release studies

The LHSA5 nanoparticles (the volume equivalent of 100 μg of DCT) were loaded in semipermeable Mini-Gebaflex-tubes with a molecular weight cutoff of 6–7 kDa (Gene Bio-Application Ltd., Kfar Hanagid, Israel) and were immersed in the medium (10 mL). The dissolution medium was phosphate-buffered saline (PBS, pH: 7.4) containing 0.5% (w/v) Tween 80 at 37°C, and was rotated at 50 rpm. Aliquots (0.2 mL) of medium were collected at predetermined times (1, 2, 3, 4, 6, 9, 12, 24, 48, 72, 96, and 144 hours), and fresh media (37°C) of equal volume was added to maintain sink condition. The amounts of DCT released into the medium were analyzed by HPLC.

In vitro cytotoxicity of conjugate

MCF-7 and MDAMB 231 cells were purchased from the Korean cell line bank (Seoul, Republic of Korea) and were cultured in RPMI-1640 medium with 1% (v/v) penicillin (100 U mL⁻¹), streptomycin (0.1 mg mL⁻¹), and 10% (v/v)

fetal bovine serum. They were incubated in a humidified 5% CO₂ atmosphere at 37°C.

The cytotoxicity of LHSA5 conjugate polymer was evaluated in MCF-7 and MDAMB 231 cells by using MTS-based assays. MCF-7 and MDAMB 231 cells (1×10⁴ cells) were seeded in 96-well plates. Various concentrations of LHSA5 polymer in the culture medium were incubated for 24 hours at 37°C, after which the cells were treated with an MTS-based CellTiter 96 AQ_{ueous} One Solution Cell Proliferation Assay reagent (Promega Corp., Fitchburg, WI, USA) for 4 hours at 37°C following the manufacturer's protocol. The absorbance of the medium was read at 490 nm using the Emax Precision Microplate Reader (Molecular Devices LLC, Sunnyvale, CA, USA).

In vitro antitumor efficacy studies

In vitro antitumor efficacy was evaluated using MTS-based assays. MCF-7 and MDAMB 231 cells (1×10⁴ cells) were seeded in 96-well plates for 24 hours. After washing the cells twice with PBS, they were incubated with various concentrations (0.1, 1.0, and 5.0 μM) of DCT solution (Taxotere, Sanofi-Aventis) or DCT-loaded LHSA5 nanoparticles for 24 hours at 37°C. Then, the cells were treated with an MTS-based CellTiter 96 AQ_{ueous} One Solution Cell Proliferation Assay reagent (Promega) for 4 hours at 37°C following the manufacturer's instructions. The absorbance at 490 nm was read using an Emax Precision Microplate Reader (Molecular Devices LLC), and is expressed as percentage of viable cells compared with the control group (ie, without DCT).

Cellular uptake studies

The cellular uptake efficiency of the LHSA5 nanoparticles was investigated by CLSM with C6-loaded nanoparticles.³⁴ C6 was also loaded in nanoparticles using a similar DCT loading method. Either MCF-7 or MDAMB 231 cells were seeded on culture plates (BD Falcon, Bedford, MA, USA) at a density of 1×10⁵ per well (1.7 cm² surface area) and incubated for 24 hours at 37°C. C6 (2 μg) was added alone or entrapped in the LHSA5 nanoparticles and incubated for 2 hours at 37°C. Then, the cells were washed with PBS (pH: 7.4) and were fixed with formaldehyde solution (4%, v/v) for 10 minutes. After completely drying the liquid content, a VECTASHIELD mounting medium with 4',6-diamidino-2-phenylindole (H-1200 Vector Laboratories, Inc., Burlingame, CA, USA) was added to prevent fading. Finally, the cells on the slides were observed using CLSM (LSM 510, Carl-Zeiss, Thornwood, NY, USA).

The cellular uptake efficiency of the LHSA5 nanoparticles was also determined by flow cytometry. MCF-7 and MDAMB 231 cells were seeded on 24-well plates at a density of 5×10⁵ per well and incubated overnight at 37°C. After removing the culture medium, the cells were incubated with free C6 or C6-loaded LHSA5 nanoparticles for 2 hours. The cells were then completely washed with PBS (pH: 7.4). After they were detached and centrifuged, the supernatant was removed. The cell pellets were suspended again with PBS containing 2% (v/v) fetal bovine serum. The uptake efficiency was analyzed by a BD FACSCalibur flow cytometry system equipped with the Cell Quest Pro software (Becton Dickinson Bioscience, San Jose, CA, USA).

In vivo antitumor efficacy

Tumor-xenografted mouse model was prepared using female BALB/c nude mice (5 weeks old; Charles River, Washington, MA) for in vivo anticancer efficacy evaluation. The mice were kept in a light-controlled room at 22°C±2°C temperature and 55%±5% relative humidity (Animal Center for Pharmaceutical Research, College of Pharmacy, Seoul National University, Seoul, Republic of Korea). The experimental protocols were approved by the Animal Care and Use Committee of the College of Pharmacy, Seoul National University. Tumor-xenografted mice were prepared by subcutaneous injection of MDAMB 231 cells (3×10⁶ cells per mouse) in the right lateral flank. After measuring the tumor size with Vernier calipers, the tumor volume (mm³) was calculated by the following formula: volume = 0.5× longest diameter × shortest diameter². After 14 days, when the MDAMB 231 tumor became palpable, tumor volume and body weight measurements were commenced. The mice were randomly divided into four groups: the control (no treatment), blank LHSA5 nanoparticles, DCT solution (Taxotere), and DCT-loaded LHSA5 nanoparticles groups. DCT solution or DCT-loaded LHSA5 nanoparticles were intravenously injected at a dose of 30 mg kg⁻¹ as DOC on days 0, 7, and 14. Tumor volume and body weight were measured for 18 days.

In vivo pharmacokinetic study in rats

Male Sprague Dawley rats (280–300 g body weight) were used for pharmacokinetic studies. Under light anesthesia (30 mg kg⁻¹ Zoletil®, intramuscular injection, Virbac Korea Co. Ltd, Seoul, Republic of Korea), the femoral artery and vein of each rat were cannulated with a polyethylene tube (PE-50; Clay Adams, Parsippany, NJ, USA). DCT solution (Taxotere) or DCT-loaded LHSA5 nanoparticles (8 mg kg⁻¹

as DCT) were administered to rats via the femoral vein within 1 minute. Blood samples (~300 μL) were collected via the femoral artery at 0 (control), 1, 5, 15, 30, 60, 120, 180, 240, 360, and 720 minutes after intravenous administration of Taxotere and DCT-loaded LHSA5 nanoparticles. After centrifugation of the blood samples, aliquots of plasma (100 μL) were stored at -70°C (Model DF8517; Ilshin Laboratory Co., Seoul, Republic of Korea) until liquid chromatography–mass spectrometry/mass spectrometry (LC–MS/MS) analysis of DCT. Immediately after each blood sampling, equal volume of 0.9% sodium chloride injectable solution containing 20 U mL^{-1} of heparin was injected.

The concentration of DCT in the plasma samples was determined by LC-MS/MS. The LC-MS/MS system consisted of an Agilent 1260 series HPLC system (equipped with a G1312B binary pump, a G1367E high-performance autosampler, a G1322A vacuum degasser, a G1330B FC/ALS thermostat, and a G1316C TCC, Agilent Technologies, Santa Clara, CA, USA), an Agilent 6430 triple quadrupole mass spectrometer (Agilent Technologies), and the MassHunter Workstation software (version B.03.01, Agilent Technologies).

Plasma samples (100 μL) were deproteinized with acetonitrile (300 μL) and methanol (100 μL) containing 1 μL mL^{-1} paclitaxel (as an internal standard). They were vortexed and centrifuged at 16,000 \times g for 10 minutes. The supernatant (400 μL) was transferred to a clean tube and completely evaporated under a gentle stream of N_2 gas at room temperature. Then, the residue was reconstituted with 60 μL of the mobile phase. After vortexing and centrifugation again, a 10 μL aliquot of supernatant was injected into a poroshell 120 EC-C16 column (2.7 μm , 4.6 \times 50 mm, Agilent Technologies) under isocratic elution of the mobile phase consisting of ammonium formate and acetonitrile (30:70, v/v) at a flow rate of 0.2 mL min^{-1} . The column temperature was maintained at 30 $^\circ\text{C}$. Data were acquired with electrospray ionization in the positive mode. Reaction monitoring was used to monitor the transitions from molecular ion to dominant product ion at charge-to-mass ratio of (m/z) 808 to 527 for DCT and m/z 876 to 591 for paclitaxel, respectively. The lower limit of quantitation value of DCT in rat plasma was 10 ng mL^{-1} .

The following pharmacokinetic parameters were calculated using WinNonlin[®] (Pharsight, Mountain View, CA, USA): total area under the plasma concentration–time curve from time zero to the end time point (AUC), terminal half-life ($t_{1/2}$), time-averaged total body clearance (CL), the apparent volume of the distribution under steady-state conditions (V_{ss}), and the mean residence time.

Statistical analysis

Statistical analyses were performed using analysis of variance. P -values <0.05 indicated statistical significance. All experiments were performed at least three times, and the data were presented as the mean \pm standard deviation.

Results

Synthesis and characterization of LHSA conjugates

Heparin and its derivatives have been widely used as drug delivery systems.^{35–37} In this study, SA (an aminated fatty acid) was conjugated to LMWH to produce an amphiphilic polymer, which is to form the self-assembled nanoparticles in aqueous environment (Figure 1A). As shown in Figure 1B, the amine group of SA was covalently coupled to the carboxylic group of LMWH in the presence of EDC and NHS, thus producing amphiphilic LHSA conjugates. In this coupling reaction, several LHSA conjugates were synthesized by adjusting the feed ratio of SA (mol) to LMWH (g) (LHSA1–LMWH:SA =1:1, LHSA3–LMWH:SA =1:3, and LHSA5–LMWH:SA =1:5). The synthesized LHSA conjugates were confirmed by $^1\text{H-NMR}$ analysis, as shown in Figure 2 (Figure 2A, LMWH; Figure 2B, LHSA1; Figure 2C, LHSA3; Figure 2D, LHSA5; Figure 2E, SA). The $^1\text{H-NMR}$ spectra of the LHSA conjugate exhibited proton signals for both LMWH and SA; a broad proton peak was observed for LMWH, and the presence of SA in the LHSA conjugate was confirmed by its chemical shift at 0.8–1.2 ppm. An alkyl chain ($-\text{CH}_2-$) and a terminal methyl group ($-\text{CH}_3$) of SA corresponded to the proton peaks at 1.10 and 0.90 ppm, respectively. These results indicated that the degree of substitution of LHSA increased with an increase in the feed ratio of SA. The physical mixtures of LMWH and SA with various molar ratios, prepared for calculation of the molar substitution ratio of LHSA, were analyzed by $^1\text{H-NMR}$. The linear regression line was plotted by the ratio of the integration area between the SA peak (2.80 ppm) and the LMWH peak (1.95 ppm). The degree of substitution of LHSA5 was calculated to be 34.0%, which indicates that approximately 1.7 of SA is conjugated to each LMWH (Figure S1).

The anticoagulant activities of LHSA1, LHSA3, and LHSA5 were 60.41%, 32.09%, and 31.92%, respectively, compared with that of free LMWH (Table 1). It is notable that the anticoagulant activity of LHSA5 did not significantly change with the encapsulation of DCT at 5:1 (LHSA5/DCT, w/w).

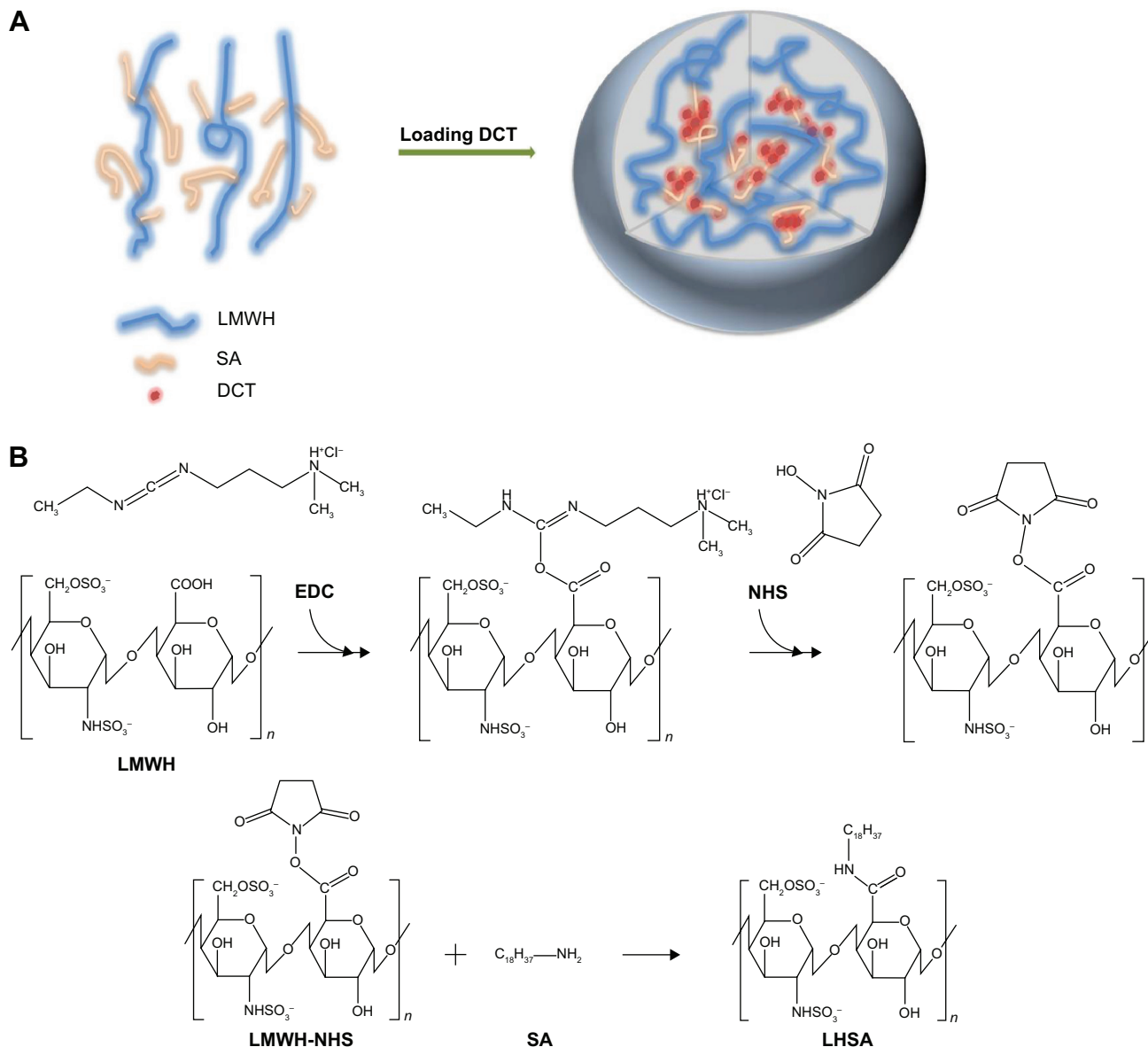


Figure 1 (A) Schematic illustration of LHSAs-based nanoparticles and (B) synthetic scheme for LHSAs conjugates.

Abbreviations: LMWH, low-molecular-weight heparin; SA, stearylamine; DCT, docetaxel; LHSA, LMWH-SA; NHS, N-hydroxysuccinimide; EDC, 1-ethyl-3-(3-dimethylaminopropyl) carbodiimide.

Preparation and characterization of LHSAs-based self-assembled nanoparticles

A solvent evaporation method was used to load DCT into the LHSAs-based nanoparticles. Blank self-assembled LHSAs nanoparticles were prepared without DCT loading by dissolving the LHSAs conjugate in an aqueous solution. The mean diameter, zeta potential, and drug loading values are shown in Table 1. All samples successfully formed nanoparticles with a mean diameter of 140–180 nm, which was confirmed by the size distribution and TEM of LHSAs nanoparticles (Figure 3A, LHSAs1; Figure 3B, LHSAs3; Figure 3C, LHSAs5). The polydispersity index of blank and DCT-loaded nanoparticles were 0.171 ± 0.04 and 0.161 ± 0.04 , respectively, indicating a

narrow size distribution of the nanoparticles (Figure 3). It is interesting to note that the incorporation of DCT in the LHSAs5 nanoparticles leads to a decrease of the particle size from 177.9 to 155.20 nm (Table 1). The loading of hydrophobic drugs in the inner core can enhance the stability of self-assembled nanoparticles by inducing morphology transition in order to decrease the total free energy, thereby resulting in the reduction of particle size.^{38,39} The nanoparticles showed negative zeta potential values due to the LMWH located in the shell. The CMC of LHSAs nanoparticles was determined by measuring the fluorescence intensity in the presence of pyrene as a probe. After measuring the fluorescence intensity ratio (I_1/I_3) at various concentrations of the LHSAs conjugate,

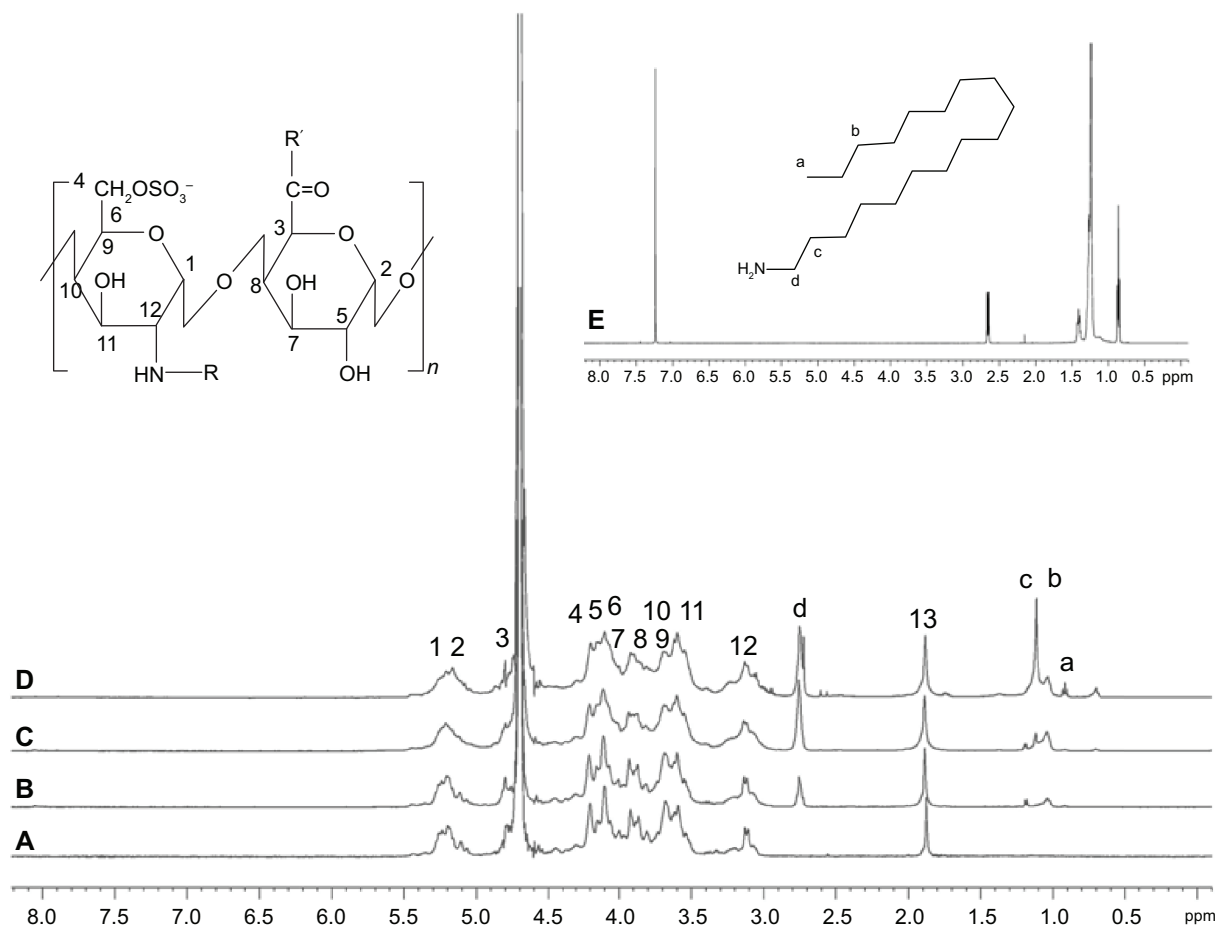


Figure 2 ^1H NMR spectra of (A) LMWH, (B) LHAS1, (C) LHAS3, (D) LHAS5, and (E) SA.

Notes: Samples were dissolved in D_2O for ^1H NMR analysis ($\text{R} = -\text{SO}_3^-$ [predominant] or $-\text{COCH}_3$ [peak 13]; $\text{R}' = \text{SA}$).

Abbreviations: ^1H -NMR, proton nuclear magnetic resonance; LMWH, low-molecular-weight heparin; LHAS, LMWH-SA; SA, stearylamine.

the CMC was determined from the threshold concentration of self-assembled nanoparticles (Figure 4A). The CMC value of LHAS5 was 0.044 mg mL^{-1} ; however, the CMC values for LHAS1 and LHAS3 could not be determined (Table 1). This result suggests that the LHAS5 conjugate can form more

stable nanoparticulate structures in an aqueous environment, compared with LHAS1 or LHAS3.

The encapsulation efficiency and the drug loading content in the LHAS5/DCT nanoparticles was 59.82% and 10.68%, respectively (Table 1). TEM images showed that the

Table 1 Characterization of LHAS-based nanoparticles

Formulation	Particle size (nm)	Polydispersity index	Zeta potential (mV)	Encapsulation efficiency (%)	Drug loading content (%)	CMC (mg/mL)	Factor Xa (%)
LHAS1	146.10 ± 8.92	0.25 ± 0.07	-15.39 ± 8.44	–	–	ND	60.41
LHAS3	175.60 ± 6.54	0.23 ± 0.08	-33.92 ± 1.34	–	–	ND	32.09
LHAS5	177.90 ± 7.22	0.17 ± 0.04	-33.13 ± 0.72	–	–	0.044	31.92
LHAS5/DCT (5:1, w/w)	155.20 ± 3.46	0.16 ± 0.04	-35.34 ± 0.26	59.82 ± 3.86	10.68 ± 0.61	–	33.48

Notes:

Encapsulation efficiency (%) = $\frac{\text{Actual amount of docetaxel in formulation}}{\text{Input amount of docetaxel in formulation}} \times 100$.

Drug loading content (%) = $\frac{\text{Amount of docetaxel in formulation (mg)}}{\text{Amount of formulation (mg)}} \times 100$.

Abbreviations: CMC, critical micelle concentration; ND, not determined.

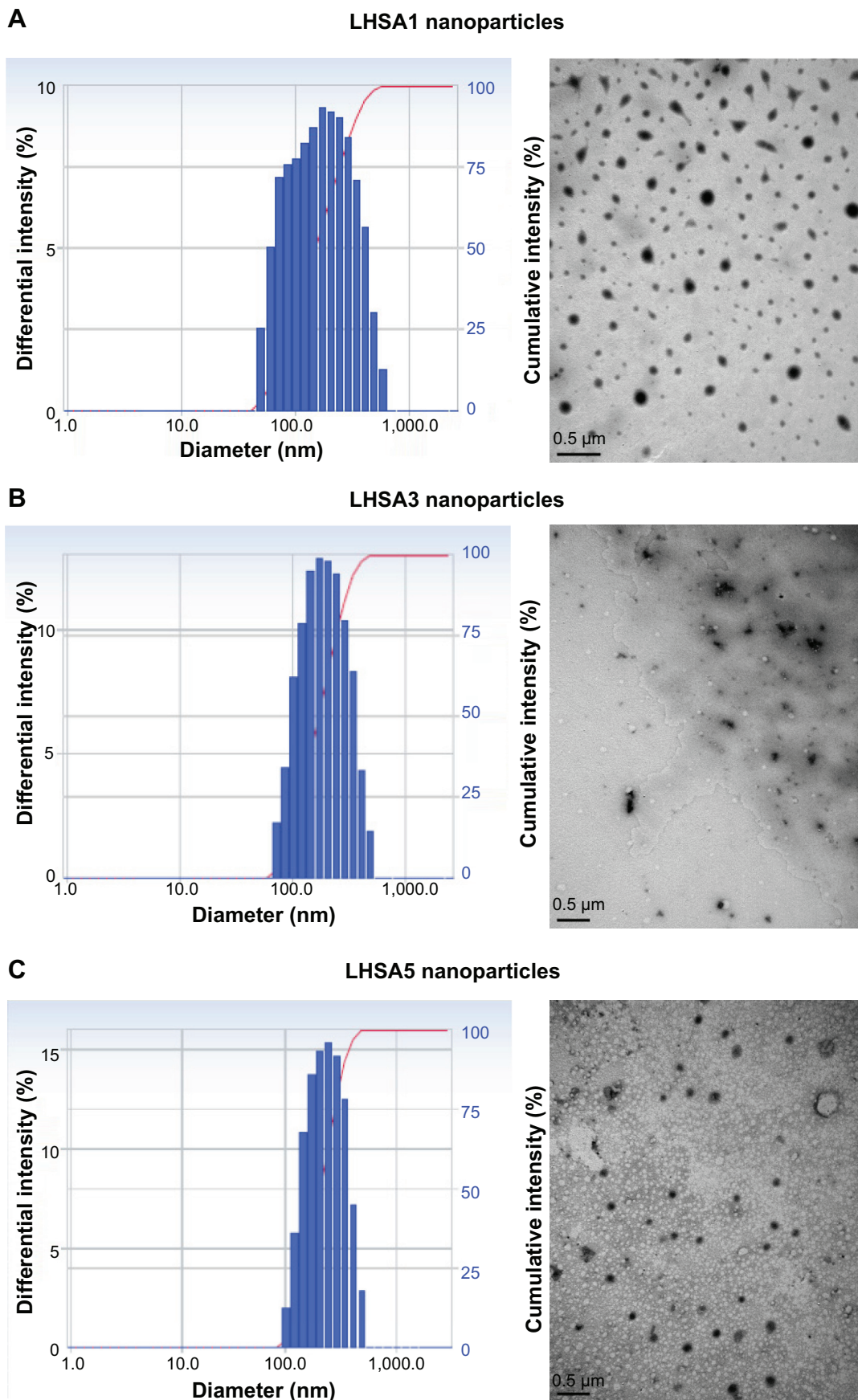


Figure 3 Size distribution and TEM images of LHSA nanoparticles.

Note: (A) LHSA1 nanoparticles, (B) LHSA3 nanoparticles, (C) LHSA5 nanoparticles. The length of the scale bar in the TEM images is 500 nm ($\times 200,000$).

Abbreviations: TEM, transmission electron microscopy; LHSA, LMWH-SA; LMWH, low-molecular-weight heparin; SA, stearylamine.

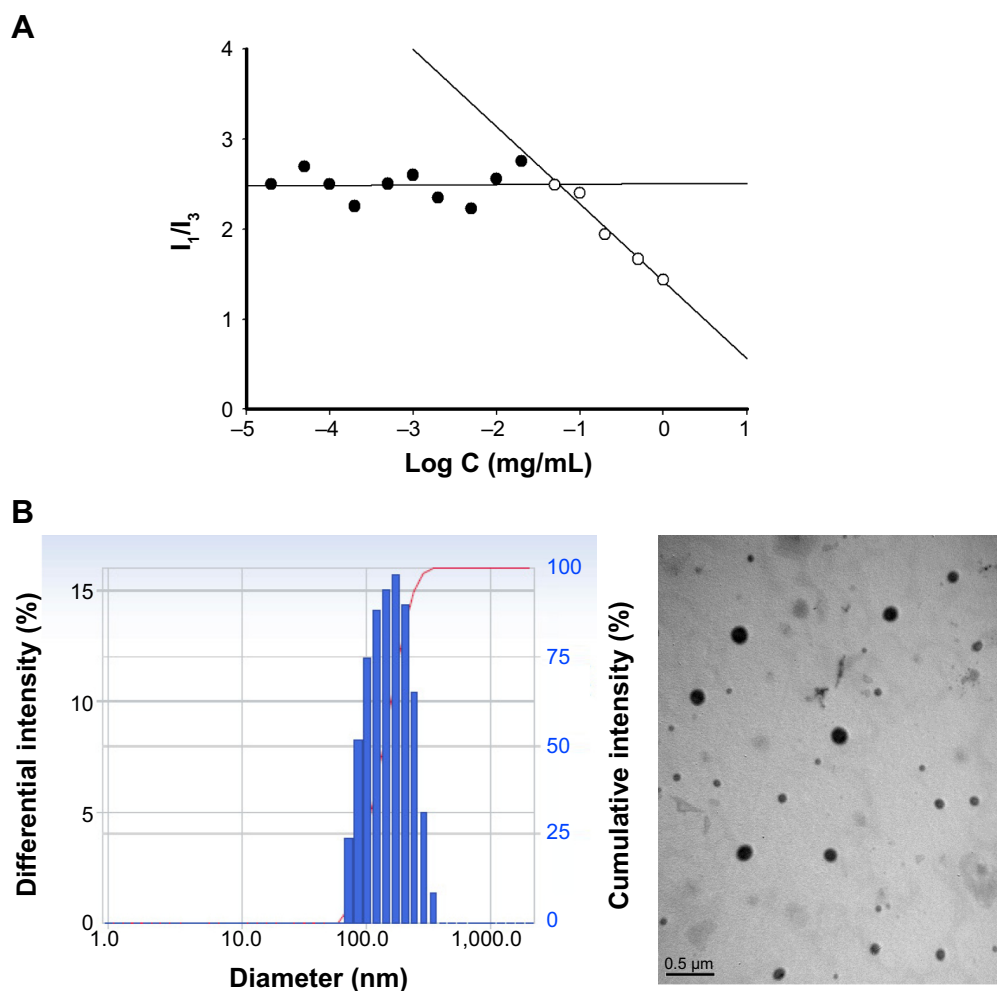


Figure 4 Characterization of DCT-loaded LHSAs nanoparticles. **(A)** CMC determination of LHSAs nanoparticles. **(B)** Size distribution and TEM image of DCT-loaded LHSAs nanoparticles.

Note: The length of the scale bar in the TEM image is 500 nm ($\times 200,000$).

Abbreviations: DCT, docetaxel; LHSAs, LMWH-SA; LMWH, low-molecular-weight heparin; SA, stearylamine; CMC, critical micelle concentration; TEM, transmission electron microscopy.

DCT-loaded LHSAs-based nanoparticles were also spherical in shape with narrow size distribution (Figure 4B).

In vitro DCT release

Figure 5 shows the in vitro DCT release profile. DCT was incorporated in the LHSAs nanoparticles and the sink condition was adequately maintained in the release test. The in vitro release of DCT from LHSAs nanoparticles was investigated for 6 days. After the initial release for 24 hours, the release rate of DCT slightly decreased with incubation time, and showed a sustained DCT release pattern. The release level of DCT within 24 hours was 48.24%; additional release continued up to 96 hours. A sustained DCT release pattern can lead to reduction in in vivo drug clearance, which results in maintenance of adequate drug concentrations for tumor growth inhibition.

In vitro cytotoxicity of LHSAs conjugate

The cytotoxicity of blank LHSAs conjugate was investigated in MCF-7 (Figure 6A) and MDAMB 231 (Figure 6B) breast cancer cell lines. Cell viability was measured after treating with various concentrations of LMWH and blank LHSAs conjugate for 24 hours. At all blank LHSAs conjugate polymer concentrations ($0\text{--}200\ \mu\text{g mL}^{-1}$), no significant viability differences between the LMWH and blank LHSAs conjugate groups were observed, indicating that the blank LHSAs conjugate polymer exerted no severe cytotoxicity on MCF-6 and MDAMB 231 cells.

In vitro antitumor effect

In vitro antitumor effects were evaluated using MCF-7 (Figure 7A) and MDAMB 231 (Figure 7B) cells. Free DCT (Taxotere) and DCT-loaded LHSAs nanoparticles

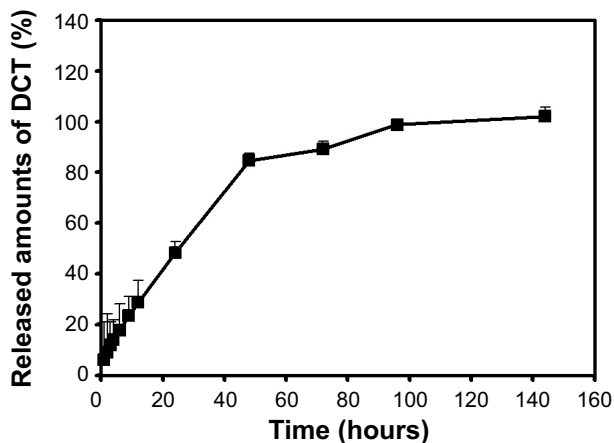


Figure 5 In vitro release profile of DCT from LHSAs5-based nanoparticles.

Note: Each point represents mean \pm SD (n=3).

Abbreviations: DCT, docetaxel; LHSAs, LMWH-SA; LMWH, low-molecular-weight heparin; SA, stearylamine; SD, standard deviation.

have antitumor efficacy against MCF-7 and MDAMB 231 cells. The DCT-loaded LHSAs5 nanoparticle exhibited a similar or slightly lower efficacy than free DCT, possibly due to sustained release of free DCT from LHSAs5 nanoparticles.

In vitro cellular uptake study

MCF-7 and MDAMB 231 cells are human breast cancer cell lines, and were selected since DCT is mainly used for the treatment of breast cancer.⁴⁰ To investigate the cellular uptake efficiency of LHSAs5 nanoparticles, LHSAs5 nanoparticles loaded with C6 were observed using CLSM, with 4',6-diamidino-2-phenylindole staining of nuclei in MCF-7 and MDAMB 231 cells. C6 is a fluorescence probe that has been widely used in cellular uptake studies of nanoparticles.^{34,41} In Figure 8A, the stronger green fluorescent signals indicate

higher intracellular accumulation of C6 from LHSAs5 nanoparticles compared to that from the C6 solution.

Cellular uptake efficiency was also quantitatively determined in MCF-7 (Figure S2A) and MDAMB 231 cells (Figure S2B) by a flow cytometry. The fluorescence intensity was assumed to be proportional to the amount of C6 in the cells; however, fluorescence was barely detected in the control (no treatment) and blank nanoparticle groups. Figure 8B shows that significantly higher amounts of C6 from LHSAs5-based nanoparticles were taken up by the cells, compared with the C6 solution, which is consistent with the results of the CLSM study (Figure 8A). This result can be explained by the endocytosis of the nanoparticles.^{42,43} A previous study showed that fatty acid-modified polysaccharide-based nanoparticles form self-assembled nanoparticles with a multihydrophobic core.⁴⁴ A hydrophobic minor core could facilitate the internalization of nanoparticles into cells via interaction with the plasma membrane. Although LHSAs5-based nanoparticles are negatively charged due to their many sulfate and carboxyl groups, the nanoparticle was taken up in higher amounts, compared with the C6 solution.

In vivo antitumor efficacy

In vivo antitumor efficacy of the DCT-loaded LHSAs5 nanoparticle formulation was evaluated in the MDAMB 231 tumor-bearing mouse model. Blank LHSAs5 nanoparticles, DCT solution (Taxotere), and DCT-loaded LHSAs5 nanoparticles were injected intravenously on days 0, 7, and 14. Then, tumor volume (mm³) and body weight (g) were monitored for 18 days.

The tumor volumes of the blank LHSAs5 nanoparticle-treated, DCT solution (Taxotere)-treated, and DCT-loaded

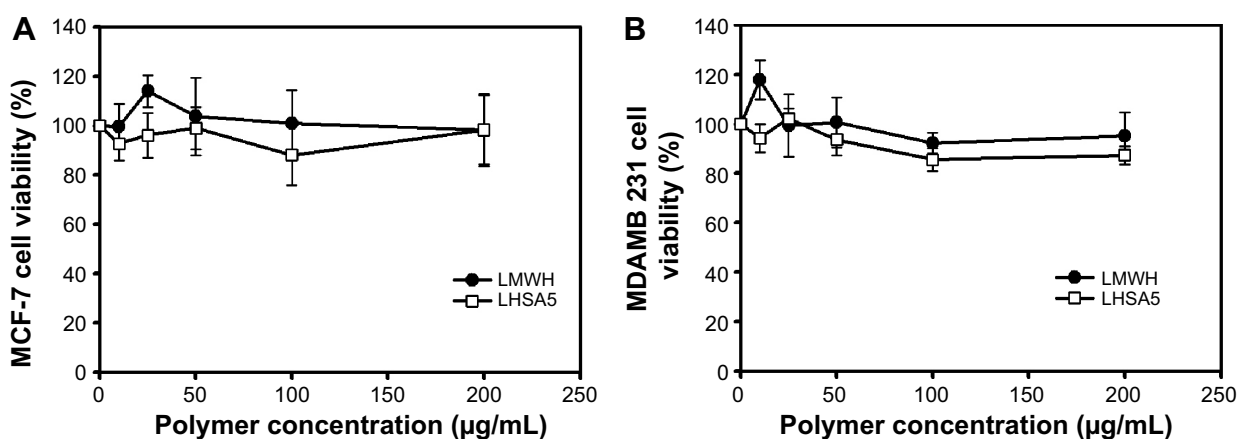


Figure 6 In vitro cytotoxicity of LHSAs5 in (A) MCF-7 and (B) MDAMB 231 cells.

Notes: Cell viability was measured by MTS-based assay after incubating LMWH or LHSAs5 at various polymer concentrations for 24 hours. Data are presented as mean \pm SD (n=5).

Abbreviations: LMWH, low-molecular-weight heparin; LHSAs, LMWH-SA; LMWH, low-molecular-weight heparin; SA, stearylamine; SD, standard deviation.

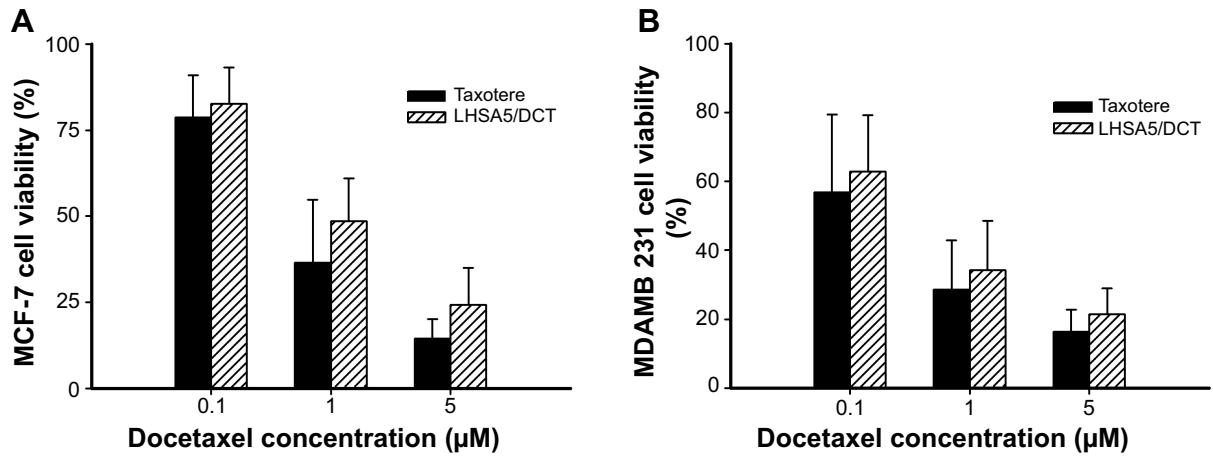


Figure 7 In vitro antitumor efficacy of Taxotere and DCT-loaded LHSAs in (A) MCF-7 and (B) MDAMB 231 cells. **Abbreviations:** LHSA, LMWH-SA; LMWH, low-molecular-weight heparin; SA, stearylamine; DCT, docetaxel.

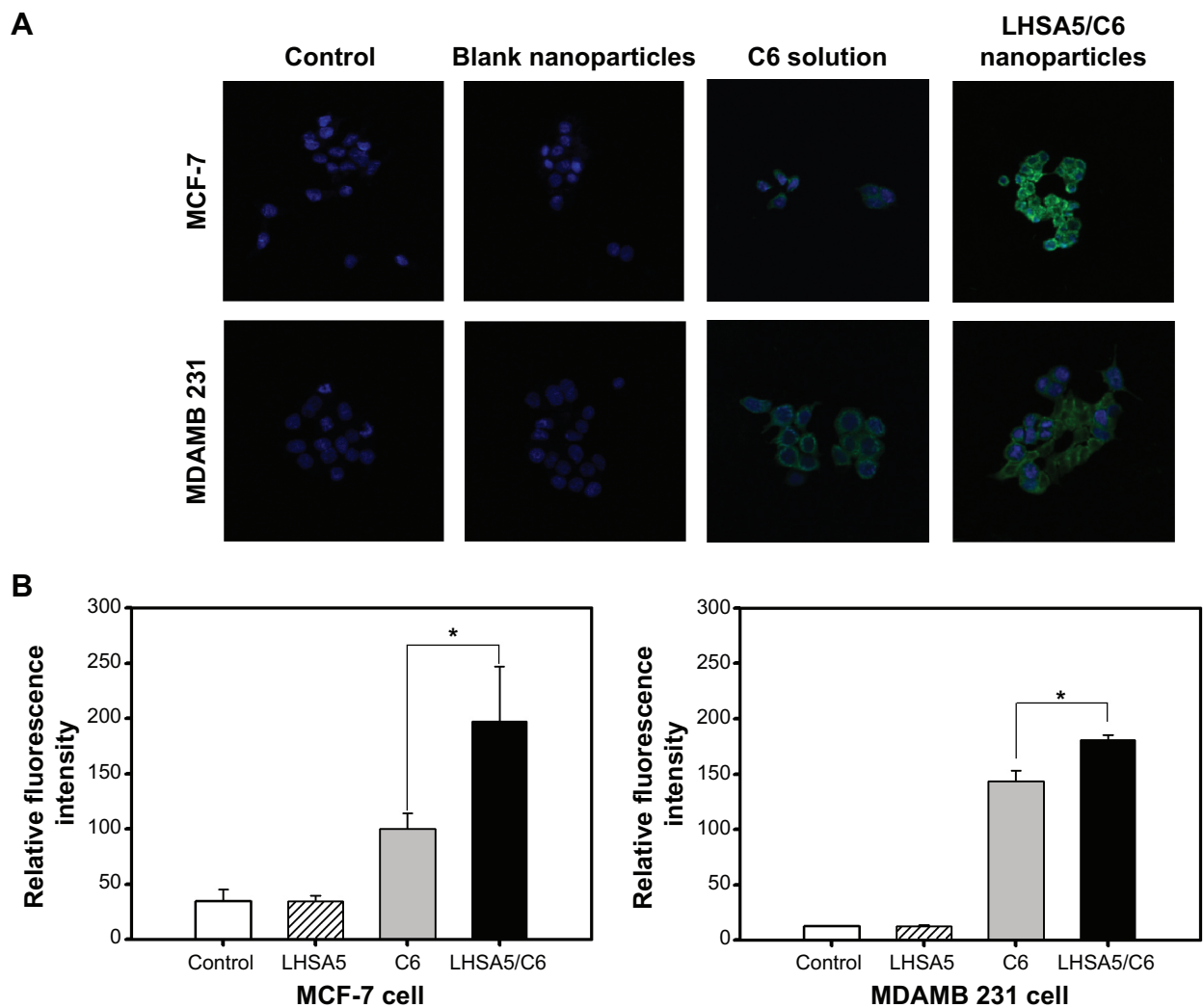


Figure 8 In vitro cellular uptake of coumarin 6. **Notes:** The cellular uptake was observed by (A) CLSM and (B) FACS in MCF-7 and MDAMB 231 cells after incubating for 2 hours. Merged images composed of coumarin 6 (green color) and DAPI (blue color) are shown. Groups were as follows: control, blank LHSA5 nanoparticles, coumarin 6 solution, coumarin 6-loaded LHSA5 nanoparticles. * $P < 0.05$, between two groups. **Abbreviations:** FACS, fluorescence-activated cell sorter; CLSM, confocal laser scanning microscope; LHSA, LMWH-SA; LMWH, low-molecular-weight heparin; SA, stearylamine.

International Journal of Nanomedicine downloaded from <http://www.dovepress.com/> by 147.47.36.90 on 09-Dec-2014 For personal use only.

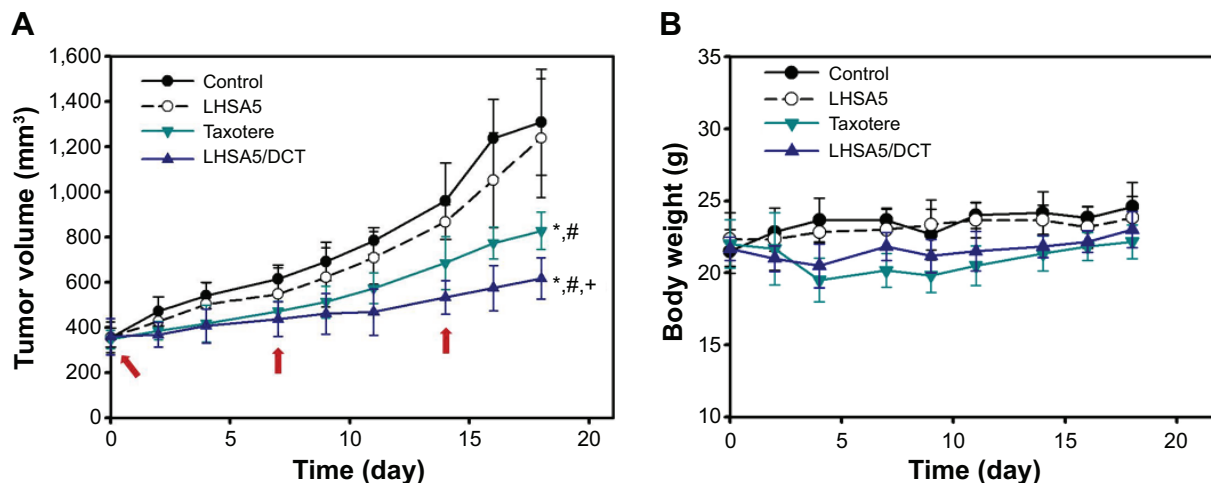


Figure 9 In vivo antitumor efficacy in the MDAMB 231 tumor-bearing mouse model.

Notes: (A) Tumor volume (mm³) profiles according to time (day) are shown. All samples were injected on day 0, 7, and 14 (red arrows). Points indicate the means \pm SD (n=5). (B) Body weight (g) was also measured with tumor size measurement for 18 days. Points indicate the means \pm SD (n=5). *P<0.05 compared with the control group; #P<0.05 compared with the LHSA5 group; +P<0.05 compared with the Taxotere group.

Abbreviations: LHSA, LMWH-SA; LMWH, low-molecular-weight heparin; SA, stearylamine; DCT, docetaxel; SD, standard deviation.

LHSA5 nanoparticle-treated groups on day 18 were 94.6%, 63.2%, and 47.1% that of the control group, respectively (Figure 9A). The most effective inhibition of tumor growth was observed in the group treated with DCT-loaded LHSA5 nanoparticles, while the blank LHSA5 nanoparticle treatment had little effect on tumor growth inhibition. Moreover, the tumor growth inhibition effect of the DCT-loaded LHSA5 nanoparticles was significantly greater than that of Taxotere ($P<0.05$).

The safety of DCT-loaded LHSA nanoparticles was evaluated by measuring changes in body weight. For most groups, there was no significant difference in body weight (Figure 9B). However, the body weight of the Taxotere-treated group was significantly lower than that of the control group. The DCT-loaded LHSA5 nanoparticle-treated group showed no significant difference compared with the control group, suggesting that the DCT-loaded LHSA nanoparticle treatment was less toxic than Taxotere.

In vivo pharmacokinetic study

Figure 10 shows the plasma concentration–time profiles of DCT solution (Taxotere) and DCT-loaded LHSA5 nanoparticles, at a dose of 8 mg kg⁻¹, in Sprague Dawley rats; relevant pharmacokinetic parameters are listed in Table 2. Our results showed that DCT was rapidly eliminated from the bloodstream in both the Taxotere and LHSA5 nanoparticle groups over the first 30 minutes after dosing. However, after dose normalization, the DCT in LHSA5 nanoparticles yielded a higher plasma concentration than did Taxotere. Noncompartmental analysis of the plasma concentrations showed

a significant change in the pharmacokinetic parameters of DCT in LHSA5 nanoparticles. Compared with Taxotere, the LHSA5 nanoparticles provided a significantly higher AUC (2.48-fold), terminal $t_{1/2}$ (3.02-fold), and mean residence time (3.64-fold). The LHSA5 nanoparticles also significantly decreased the clearance (CL, 2.54-fold) of DCT. These in vivo pharmacokinetic properties were thought to be related to its in vitro sustained release pattern. This result indicates that the LHSA5 nanoparticles prolonged the circulation of DCT in the bloodstream, thereby improving its therapeutic efficacy (Figure 9A).

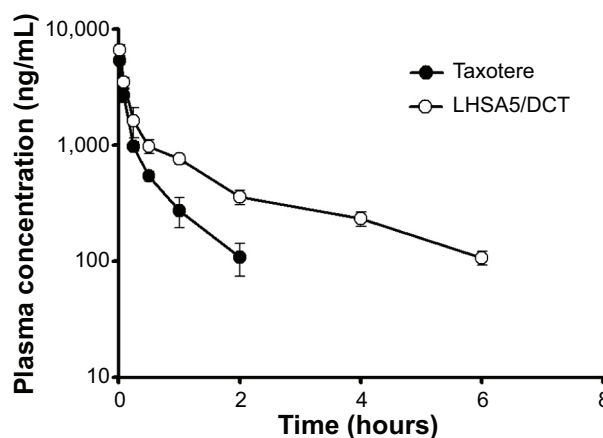


Figure 10 In vivo pharmacokinetic profile.

Notes: The pharmacokinetic profile was studied after intravenous injection of Taxotere and DCT-loaded LHSA5 nanoparticle formulation in rats at a dose of 8 mg/kg DCT. Points represent the mean \pm SD (n=4).

Abbreviations: DCT, docetaxel; LHSA, LMWH-SA; LMWH, low-molecular-weight heparin; SA, stearylamine; SD, standard deviation.

Table 2 Pharmacokinetic parameters of Taxotere and DCT-loaded LHSA5 nanoparticles after a single intravenous injection (8 mg/kg) in rats (n=4)

Parameter	Taxotere	LHSA5/DCT
AUC ($\mu\text{g min/mL}$)	75.075 \pm 10.191	186.767 \pm 24.621*
Terminal $t_{1/2}$ (min)	38.024 \pm 6.265	121.789 \pm 11.805*
CL (mL/min/kg)	100.374 \pm 15.558	39.441 \pm 4.999*
V_{ss} (mL/kg)	5,401.316 \pm 131.480	6,910.463 \pm 979.348
MRT (min)	23.466 \pm 2.227	85.432 \pm 4.043*

Notes: Data presented as mean \pm SD (n=4). * $P < 0.05$ compared with Taxotere group.

Abbreviations: DCT, docetaxel; LHSA, LMWH-SA; LMWH, low-molecular-weight heparin; SA, stearylamine; AUC, total area under the plasma concentration-time curve from time zero to the end time point; CL, time-averaged total body clearance; V_{ss} , the apparent volume of the distribution under steady-state conditions; MRT, the mean residence time; SD, standard deviation.

Discussion

The synthetic scheme for the amphiphilic LHSA conjugate is shown in Figure 1. Amphiphilic LHSA conjugates with various LMWH to SA molar ratios were synthesized to investigate the feasibility of forming stable self-assembled nanoparticles. From $^1\text{H-NMR}$ analysis of LHSA conjugates, the proton peak of SA (chemical shifts at 0.8–1.2 ppm) in LHSA1 and LHSA3 was lower than that for LHSA5 (Figure 2). An accurate substitution ratio (SA to LMWH) can be determined from the $^1\text{H-NMR}$ spectrum of the physical mixtures of LMWH and SA. In our previous study,⁴⁵ the correlation of the molar ratio of arachidic acid to chitosan oligosaccharide (CSO) was evaluated using $^1\text{H-NMR}$ from a physical mixture of arachidic acid and CSO in DMSO-d_6 . However, LMWH has a strong hydrophilic property, while SA has a strong hydrophobic property; thus, an NMR cosolvent consisting of D_2O and THF-d_8 was used to dissolve LMWH and SA. The molar substitution ratios increased with increasing feed SA molar ratio. Note that these results are contrary to those of the anticoagulant activity of LHSA conjugates calculated using an anti-FXa chromogenic assay (Table 1); the anticoagulant activity of LHSA conjugates decreased as the amount of chemically coupled SA increased (Table 1), which is consistent with previously reported heparin derivative studies.^{46,47}

All LHSA1, LHSA3, and LHSA5 conjugates prepared in this study formed self-assembled nanoparticles that were 140–180 nm in size. It is known that nanoparticles with a mean diameter < 200 nm accumulate in tumors via the enhanced permeability and retention effect and exhibit reduced uptake by the reticuloendothelial system.^{3,48} Among them, the LHSA5 nanoparticles showed a narrower size distribution and a more stable spherical morphology than the LHSA1 and LHSA3 nanoparticles, as shown in Figure 3. However, the LHSA1 and LHSA3 conjugates did not

possess the hydrophobicity necessary for the formation of stable nanoparticles due to the low substitution ratio of SA. Additionally, the CMC value of the LHSA5 conjugate was significantly lower ($44 \mu\text{g mL}^{-1}$) than those of other low-molecular-weight surfactants or amphiphilic polymers,^{49,50} indicating that it can form stable nanoparticle structures, even in the presence of the reduced polymer concentrations after dilution with body fluids.

The LMWH of LHSA creates a hydrophilic outer shell of the nanoparticles in an aqueous environment. The SA of LHSA provides an internal hydrophobic core that can be used to encapsulate insoluble drugs.⁵¹ It was interesting to note that the zeta potential values of LHSA nanoparticles were negative, indicating that the LMWH was located on the surface of the shell. Therefore, LHSA could possess heparin activity after nanoparticle formation, yet the anticoagulant activity of LHSA was lower than that of the unmodified LMWH. Because LMWH reduces the risk of embolic events in patients with malignancy and acute venous thromboembolism,⁵² its use in cancer patients is recommended by numerous guidelines and is now regarded as a standard of care.⁵³ Thus, the self-assembled LHSA5 nanoparticle could be attractive as an anticancer drug carrier, which has a synergic effect with poorly water-soluble anticancer drugs encapsulated in the core.

After characterization of the blank LHSA-based nanoparticles, we evaluated the DCT-loaded LHSA nanoparticles using the LHSA5 conjugate, due to its more stable nanoparticle configuration compared with the other structures. The encapsulation efficacy of the DCT-loaded LHSA5 nanoparticle was 59.82%, with TEM images revealing a spherical shape. The in vitro release of DCT from the LHSA5 nanoparticle continued for ~96 hours, as shown in Figure 5. From these results, we expected a reduction in the in vivo drug clearance, allowing a drug concentration adequate for tumor growth inhibition to be sustained. When intravenously administered in Sprague Dawley rats, the concentration profile of DCT in plasma was sustained for 6 hours, as compared with 2 hours for Taxotere administration (Figure 10).

The effects of the DCT-loaded LHSA5 nanoparticles on in vitro cytotoxicity and antitumor efficacy in MCF-7 and MDAMB 231 cells were investigated, as shown in Figures 6 and 7. The LMWH and blank LHSA5 nanoparticles exhibited no severe in vitro cytotoxicity. Free DCT and DCT-loaded LHSA5 nanoparticles were cytotoxic to MCF-7 and MDAMB 231 cells. DCT-loaded LHSA5 nanoparticles had a similar or slightly lower efficacy than free DCT, thus contributing to the sustained release of free DCT from LHSA5

nanoparticles. As shown in Figure 5, only 40% of the free DCT was released from LHSA5 nanoparticles in 24 hours in the in vitro release study.

C6 has been widely used in cellular uptake studies,^{34,41} and was used in this study as a fluorescence probe to investigate the cellular uptake efficiency of the LHSA nanoparticle. LHSA5 nanoparticles loaded with C6 in MCF-7 and MDAMB 231 cells were visualized by CLSM (Figure 8A). A significant difference was observed in the fluorescence intensities of the C6 solution and the C6-loaded LHSA nanoparticles. In addition, a significantly higher amount of C6 from the LHSA5 nanoparticle was taken up by the cells compared to that from the C6 solution, as shown in Figure 8B. This result could be attributable to endocytosis of the nanoparticles.^{42,43} Moreover, the fatty acid-modified polysaccharide-based nanoparticles are capable of forming self-assembled nanoparticles with a multihydrophobic core.⁴⁴ The hydrophobic part of the nanoparticles could facilitate drug internalization into the cells via interactions with the cell membrane. Although the LHSA5-based nanoparticles were negatively charged due to their sulfate and carboxyl groups, the nanoparticles were taken up in significantly higher amounts compared with the C6 solution. In addition to drug uptake by nanoparticles, long-term cellular drug retention can play key roles in drug efficacy in microtubule-targeted anticancer drugs.⁵⁴ Thus, LHSA5 nanoparticles could induce a synergy effect by enhancing drug uptake and retention time, which are shown in in vivo antitumor efficacy study (Figure 9).

The DCT-loaded LHSA5 nanoparticles exhibited significant inhibitory effects on MDAMB 231 tumor growth, compared with the other groups (Figure 9A). This can be explained in terms of the physicochemical properties of the drug-loaded nanoparticles that induce sustained drug release (Figure 10) and passive targeting to tumor tissue via an enhanced permeability and retention effect. Although the blank LHSA5 nanoparticles showed insignificant in vivo inhibition of MDAMB 231 tumor growth in this study, others have reported the antitumor effects of several heparin derivatives in tumor-bearing mice.^{36,55,56} This discrepancy can be attributed to the differences in tumor type, heparin injection frequency and capacity, administration route, and heparin-modifying molecules.

The concentration profile of DCT in plasma was sustained up to 6 hours (Figure 10). This result indicates that LHSA5 nanoparticles contributed to prolonged circulation of DCT in the bloodstream and is consistent with the improved

therapeutic efficacy (Figure 9A). Compared with the DCT solution, the DCT-loaded LHSA5 nanoparticles provided a significantly higher AUC, $t_{1/2}$, and mean residence time and a lower time-averaged total body clearance, as shown in Table 2. These in vivo pharmacokinetic parameters were related to its in vitro sustained DCT release pattern. Moreover, the increased retention time and decreased clearance of the DCT from plasma may contribute to enhanced in vivo antitumor efficacy in the tumor xenograft model, as shown in Figure 9A.

Conclusion

LHSA conjugates were successfully synthesized, and self-assembled nanoparticles based on LHSA were prepared. The LHSA-based nanoparticles have an LMWH moiety on the outer shell resulting in a negative surface charge. Among the synthesized conjugates, LHSA5 formed stable self-assembled nanoparticles in an aqueous environment, with a narrow size distribution. Because the LHSA5 nanoparticles showed 30% of the anticoagulant activity exhibited by free LMWH, it likely also maintains the other heparin activities. The DCT-loaded LHSA5 nanoparticle showed sustained drug-release profiles, in vitro and in vivo, compared with Taxotere. The nanoparticulate structure influenced cellular uptake; consequently, the DCT-loaded LHSA5 nanoparticle formulation improved the half-life of DCT and significantly inhibited MDAMB 231 tumor growth in xenograft mice. Thus, LHSA5-based self-assembled nanoparticles may be useful as an anticancer drug delivery system.

Acknowledgments

This work was supported by the National Research Foundation of Korea (NRF) grant funded by the Korean government (MSIP) (Number 2009-0083533) and the MarineBio Research Program (NRF-C1ABA001-2011-0018561).

Disclosure

The authors report no conflicts of interest in this work.

References

1. Kwon GS, Okano T. Polymeric micelles as new drug carriers. *Adv Drug Deliv Rev.* 1996;21(2):107–116.
2. Liu Z, Jiao Y, Wang Y, et al. Polysaccharides-based nanoparticles as drug delivery systems. *Adv Drug Deliv Rev.* 2008;60(15):1650–1662.
3. Maeda H, Wu J, Sawa T, et al. Tumor vascular permeability and the EPR effect in macromolecular therapeutics: a review. *J Control Release.* 2000; 65(1):271–284.

4. Maeda H. Tumor-selective delivery of macromolecular drugs via the EPR effect: background and future prospects. *Bioconjugate Chem.* 2010; 21(5):797–802.
5. Verrecchia T, Spenlehauer G, Bazile D, et al. Non-stealth (poly(lactic acid/albumin)) and stealth (poly(lactic acid-polyethylene glycol)) nanoparticles as injectable drug carriers. *J Control Release.* 1995;36(1):49–61.
6. Shao X, Liu Q, Zhang C, et al. Concanavalin A-conjugated poly(ethylene glycol)-poly(lactic acid) nanoparticles for intranasal drug delivery to the cervical lymph nodes. *J Microencapsul.* 2013;30(8):780–786.
7. Labhasetwar V, Song C, Humphrey W, et al. Arterial uptake of biodegradable nanoparticles: effect of surface modifications. *J Pharm Sci.* 1998; 87(10):1229–1234.
8. Molpeceres J, Guzman M, Aberturas MR, et al. Application of central composite designs to the preparation of polycaprolactone nanoparticles by solvent displacement. *J Pharm Sci.* 1996;85(2):206–213.
9. Aishwarya S, Mahalakshmi S, Sehgal PK. Collagen-coated polycaprolactone microparticles as a controlled drug delivery system. *J Microencapsul.* 2008;25(5):298–306.
10. Sharma S, Benson HA, Mukkur TK, et al. Preliminary studies on the development of IgA-loaded chitosan-dextran sulphate nanoparticles as a potential nasal delivery system for protein antigens. *J Microencapsul.* 2013;30(3):283–294.
11. Jahanshahi M, Babaei Z. Protein nanoparticle: a unique system as drug delivery vehicles. *Afr J Biotechnol.* 2008;7(25):4926–4934.
12. Wu Y, MacKay JA, McDaniel JR, et al. Fabrication of elastin-like polypeptide nanoparticles for drug delivery by electrospraying. *Biomacromolecules.* 2008;10(1):19–24.
13. Kwon GS, Okano T. Soluble self-assembled block copolymers for drug delivery. *Pharm Res.* 1999;16(5):597–600.
14. Saravanakumar G, Min KH, Min DS, et al. Hydrotropic oligomer-conjugated glycol chitosan as a carrier of paclitaxel: synthesis, characterization, and *in vivo* biodistribution. *J Control Release.* 2009;140(3): 210–217.
15. Sun P, Zhang Y, Shi L, et al. Thermosensitive nanoparticles self-assembled from PCL-b-PEO-b-PNIPAAm triblock copolymers and their potential for controlled drug release. *Macromol Biosci.* 2010;10(6): 621–631.
16. Lyseng-Williamson KA, Fenton C. Docetaxel. *Drugs.* 2005;65(17): 2513–2531.
17. Baker SD, Sparreboom A, Verweij J. Clinical pharmacokinetics of docetaxel. *Clin Pharmacokinet.* 2006;45(3):235–252.
18. Michael A, Syrigos K, Pandha H. Prostate cancer chemotherapy in the era of targeted therapy. *Prostate Cancer Prostatic Dis.* 2008;12(1): 13–16.
19. Persohn E, Canta A, Schoepfer S, et al. Morphological and morphometric analysis of paclitaxel and docetaxel-induced peripheral neuropathy in rats. *Eur J Cancer.* 2005;41(10):1460–1466.
20. Engels FK, Mathot RA, Verweij J. Alternative drug formulations of docetaxel: a review. *Anticancer Drugs.* 2007;18(2):95–103.
21. Immordino ML, Brusa P, Arpicco S, et al. Preparation, characterization, cytotoxicity and pharmacokinetics of liposomes containing docetaxel. *J Control Release.* 2003;91(3):417–429.
22. Yin Y-M, Cui F-D, Mu C-F, et al. Docetaxel microemulsion for enhanced oral bioavailability: preparation and *in vitro* and *in vivo* evaluation. *J Control Release.* 2009;140(2):86–94.
23. Esmaeili F, Dinarvand R, Ghahremani MH, et al. Docetaxel–albumin conjugates: preparation, *in vitro* evaluation and biodistribution studies. *J Pharm Sci.* 2009;98(8):2718–2730.
24. Buller H, Gent M, Gallus A, et al. Low-molecular weight heparin in the treatment of patients with venous thromboembolism: the Columbus Investigators. *N Engl J Med.* 1997;337:657–662.
25. Young E. The anti-inflammatory effects of heparin and related compounds. *Thromb Res.* 2008;122(6):743–752.
26. Niers TMH, Klerk CPW, DiNisio M, et al. Mechanisms of heparin induced anti-cancer activity in experimental cancer models. *Crit Rev Oncol Hematol.* 2007;61(3):195–207.
27. Castelli R, Porro F, Tarsia P. The heparins and cancer: review of clinical trials and biological properties. *Vasc Med.* 2004;9(3):205–213.
28. Marchetti M, Vignoli A, Russo L, et al. Endothelial capillary tube formation and cell proliferation induced by tumor cells are affected by low molecular weight heparins and unfractionated heparin. *Thromb Res.* 2008;121(5):637–645.
29. Bae KH, Mok H, Park TG. Synthesis, characterization, and intracellular delivery of reducible heparin nanogels for apoptotic cell death. *Biomaterials.* 2008;29(23):3376–3383.
30. Casu B, Guerrini M, Guglieri S, et al. Undersulfated and glycol-split heparins endowed with antiangiogenic activity. *J Med Chem.* 2004; 47(4):838–848.
31. Smorenburg SM, Van Noorden CJ. The complex effects of heparins on cancer progression and metastasis in experimental studies. *Pharmacol Rev.* 2001;53(1):93–106.
32. Farge D, Debourdeau P, Beckers M, et al. International clinical practice guidelines for the treatment and prophylaxis of venous thromboembolism in patients with cancer. *J Thromb Haemost.* 2013;11(1):56–70.
33. Min Y, Akbulut M, Kristiansen K, et al. The role of interparticle and external forces in nanoparticle assembly. *Nat Mater.* 2008;7(7): 527–538.
34. Cho H-J, Yoon HY, Koo H, et al. Self-assembled nanoparticles based on hyaluronic acid-ceramide (HA-CE) and Pluronic® for tumor-targeted delivery of docetaxel. *Biomaterials.* 2011;32(29):7181–7190.
35. Park K, Lee GY, Park R-W, et al. Combination therapy of heparin–deoxycholic acid conjugate and doxorubicin against squamous cell carcinoma and B16F10 melanoma. *Pharm Res.* 2008;25(2): 268–276.
36. Park K, Lee GY, Kim Y-S, et al. Heparin–deoxycholic acid chemical conjugate as an anticancer drug carrier and its antitumor activity. *J Control Release.* 2006;114(3):300–306.
37. Lee JS, Go DH, Bae JW, et al. Synthesis and characterization of heparin conjugated Tetronic®–PCL copolymer for protein drug delivery. *Curr Appl Phys.* 2007;7:e49–e52.
38. Li S, Byrne B, Welsh J, et al. Self-assembled poly(butadiene)-b-poly(ethylene oxide) polymersomes as paclitaxel carriers. *Biotechnol Prog.* 2007;23(1):278–285.
39. Lim Soo P, Eisenberg A. Preparation of block copolymer vesicles in solution. *J Polym Sci B Polym Phys.* 2004;42(6):923–938.
40. Clarke SJ, Rivory LP. Clinical pharmacokinetics of docetaxel. *Clin Pharmacokinet.* 1999;36(2):99–114.
41. Mu CF, Balakrishnan P, Cui FD, et al. The effects of mixed MPEG-PLA/Pluronic copolymer micelles on the bioavailability and multidrug resistance of docetaxel. *Biomaterials.* 2010;31(8):2371–2379.
42. He C, Hu Y, Yin L, et al. Effects of particle size and surface charge on cellular uptake and biodistribution of polymeric nanoparticles. *Biomaterials.* 2010;31(13):3657–3666.
43. Conner SD, Schmid SL. Regulated portals of entry into the cell. *Nature.* 2003;422(6927):37–44.
44. You J, Hu F-Q, Du Y-Z, et al. High cytotoxicity and resistant-cell reversal of novel paclitaxel loaded micelles by enhancing the molecular-target delivery of the drug. *Nanotechnology.* 2007;18(49):495101.
45. Termsarasab U, Cho H-J, Kim DH, et al. Chitosan oligosaccharide–arachidic acid-based nanoparticles for anti-cancer drug delivery. *Int J Pharm.* 2013;441(1–2):373–380.
46. Park K, Kim K, Kwon IC, et al. Preparation and characterization of self-assembled nanoparticles of heparin–deoxycholic acid conjugates. *Langmuir.* 2004;20(26):11726–11731.
47. Rosenberg RD. Heparin, antithrombin, and abnormal clotting. *Annu Rev Med.* 1978;29(1):367–378.
48. Gaucher G, Dufresne M-H, Sant VP, et al. Block copolymer micelles: preparation, characterization and application in drug delivery. *J Control Release.* 2005;109(1):169–188.
49. Lee JS, Go DH, Bae JW, et al. Heparin conjugated polymeric micelle for long-term delivery of basic fibroblast growth factor. *J Control Release.* 2007;117(2):204–209.

50. Kratochvil JP, Hsu WP, Kwok DI. How large are the micelles of di- α -hydroxy bile salts at the critical micellization concentrations in aqueous electrolyte solutions? Results for sodium taurodeoxycholate and sodium deoxycholate. *Langmuir*. 1986;2(2):256–258.
51. Rizkalla N, Range C, Lacasse F-X, et al. Effect of various formulation parameters on the properties of polymeric nanoparticles prepared by multiple emulsion method. *J Microencapsul*. 2006;23(1):39–57.
52. Lee AY, Levine MN, Baker RI, et al. Low-molecular-weight heparin versus a coumarin for the prevention of recurrent venous thromboembolism in patients with cancer. *N Engl J Med*. 2003;349(2):146–153.
53. Nishioka J, Goodin S. Low-molecular-weight heparin in cancer-associated thrombosis: treatment, secondary prevention, and survival. *J Oncol Pharm Pract*. 2007;13(2):85–97.
54. Jordan MA, Kamath K. How do microtubule-targeted drugs work? An overview. *Curr Cancer Drug Targets*. 2007;7(8):730–742.
55. Thorpe PE, Derbyshire EJ, Andrade SP, et al. Heparin-steroid conjugates: new angiogenesis inhibitors with antitumor activity in mice. *Cancer Res*. 1993;53(13):3000–3007.
56. Lapierre F, Holme K, Lam L, et al. Chemical modifications of heparin that diminish its anticoagulant but preserve its heparanase-inhibitory, angiostatic, anti-tumor and anti-metastatic properties. *Glycobiology*. 1996;6(3):355–366.

Supplementary materials

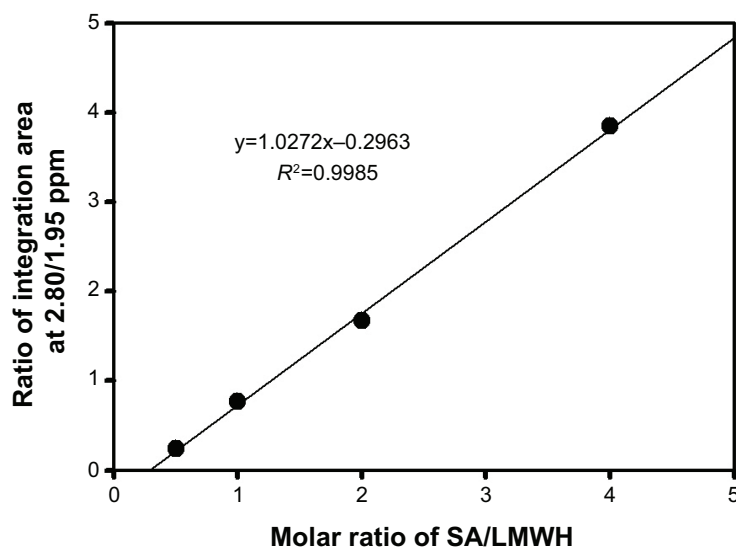


Figure S1 Relationship between the ratio of integration area (2.80/1.95 ppm) and molar ratio of SA/LMWH based on their physical mixture.

Notes: Samples were dissolved in D₂O/THF-d₈ mixture (1:1) for ¹H NMR analysis. Each point represents the mean ± SD (n=3).

Abbreviations: SA, stearylamine; LMWH, low-molecular-weight heparin.

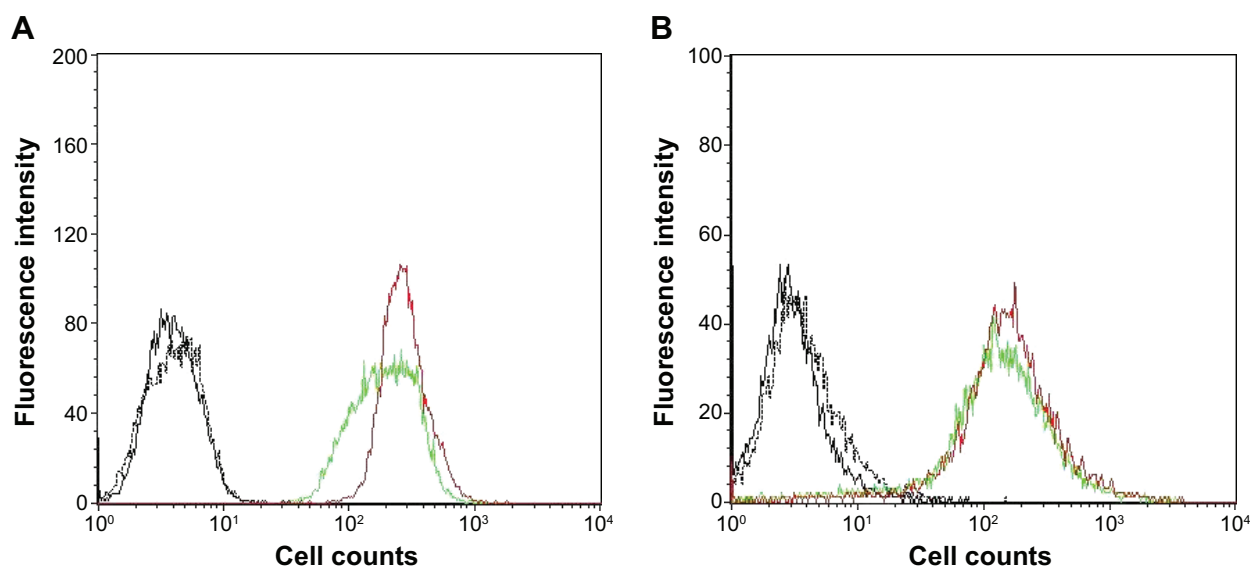


Figure S2 In vitro cellular uptake of coumarin 6 was observed by flow cytometry in (A) MCF-7 and (B) MDAMB 231 cells after incubating for 2 hours.

Note: Groups were as follows: control (black, solid), blank LHSAs nanoparticles (black, dotted), coumarin 6 solution (green, solid), coumarin 6-loaded LHSAs nanoparticles (red, solid).

International Journal of Nanomedicine

Publish your work in this journal

The International Journal of Nanomedicine is an international, peer-reviewed journal focusing on the application of nanotechnology in diagnostics, therapeutics, and drug delivery systems throughout the biomedical field. This journal is indexed on PubMed Central, MedLine, CAS, SciSearch®, Current Contents®/Clinical Medicine,

Submit your manuscript here: <http://www.dovepress.com/international-journal-of-nanomedicine-journal>

Dovepress

Journal Citation Reports/Science Edition, EMBase, Scopus and the Elsevier Bibliographic databases. The manuscript management system is completely online and includes a very quick and fair peer-review system, which is all easy to use. Visit <http://www.dovepress.com/testimonials.php> to read real quotes from published authors.

A microemulsion-based hydrogel formulation containing voriconazole for topical skin delivery

Yo-Han Kim · Chung Kil Song · Eunjae Jung ·
Dong-Hwan Kim · Dae-Duk Kim

Received: 5 August 2014 / Accepted: 17 October 2014 / Published online: 16 November 2014
© The Korean Society of Pharmaceutical Sciences and Technology 2014

Abstract Microemulsion-based hydrogels (MBHs) containing voriconazole were prepared as a possible topical delivery system for enhancing drug absorption at the site of action, as well as reducing the frequency of systemic side effects. Microemulsions were prepared with *N*-methyl-2-pyrrolidone as a surfactant, benzyl alcohol as an oil, and an ethanol/phosphatidylcholine mixture (3:2, w/w) as a cosurfactant. MBHs were prepared by adding carbopol 940 or xanthan gum as a gelling agent. In vitro skin permeation and deposition studies were performed using static vertical diffusion Franz cells and hairless mouse skin. The in vitro permeation data showed that the optimized microemulsion formulations consisting of voriconazole (1 %, w/w) and benzyl alcohol (10 %, w/w) showed significantly higher drug permeation rates and skin deposition compared to propylene glycol (control). However, the addition of a gelling agent did not significantly change the permeation profiles compared to the microemulsions. In vivo skin deposition studies conducted on hairless mice with MBHs also confirmed the superiority of MBHs compared to the control. These results suggested the MBH system to be a promising vehicle for topical delivery of voriconazole.

Keywords Microemulsion · Hydrogel · Skin · Voriconazole · Topical delivery

Introduction

Voriconazole, a new broad-spectrum triazole antifungal agent, was approved by the US Food and Drug Administration in May 2002. It is structurally derived from fluconazole (Jeu et al. 2003) and is indicated for the treatment of invasive aspergillosis and serious fungal infections caused by *Scedosporium apiospermum* and *Fusarium* species in patients who are unable to tolerate, or are refractory to, other therapy. The chemical structure of voriconazole is (2*R*,3*S*)-2-(2,4-difluorophenyl)-3-(5-fluoro-4-pyrimidinyl)-1-(1*H*-1,2,4-triazol-1-yl)-2-butanol, with a molecular formula of C₁₆H₁₄F₃N₅O and a molecular weight of 349.3 g/mol. Voriconazole, like other antifungal azole compounds, has low water solubility, which in most cases translates into low bioavailability. As a means to address the poor water solubility and bioavailability of voriconazole, complexes of voriconazole and sulfobutyl- β -cyclodextrin have been developed (Harding 2003), which are now available for clinical use (Vfend[®] Pfizer Pharmaceutical Company) as oral and intravenous solutions. Though it has been reported that the estimated oral bioavailability of voriconazole is 96 % (Leveque et al. 2006), it is likely that most physicians will not opt for oral therapy when initiating voriconazole due to the side effects, such as visual disturbances, skin rashes, drug interactions, elevated hepatic enzyme levels, abdominal pain, and nausea and vomiting (Johnson and Kauffman 2003). Moreover, β -cyclodextrin derivatives containing an intravenous injection limit the application of the drug due to its nephrotoxicity and hemolysis. Thus, development of a topical delivery system of voriconazole is of great interest for the treatment of skin fungal infection.

Microemulsion-based hydrogel (MBH) formulations have generated considerable interest recently as potential topical delivery systems (Lawrence and Rees 2000; Chen

Y.-H. Kim · C. K. Song · E. Jung · D.-H. Kim · D.-D. Kim (✉)
College of Pharmacy and Research Institute of Pharmaceutical
Sciences, Seoul National University, Seoul 151-742, South
Korea
e-mail: ddkim@snu.ac.kr

et al. 2006; Santos et al. 2008). The existence of microdomains of different polarity within the same single-phase solution enables both hydrophilic and lipophilic materials to be solubilized. Advantages associated with microemulsions include their thermodynamic stability, optical clarity, ease of preparation, and high diffusion and absorption rates compared to solvents without a surfactant system (Lawrence and Rees 2000; Jadhav et al. 2006). Moreover, it has been reported that the ingredients of a microemulsion may reduce the diffusion barrier of stratum corneum (SC) and enhance the permeation of drugs (Peltola et al. 2003). Hence, it is promising for both transdermal and dermal delivery of drugs. However, the low viscosity of a microemulsion limits its application in the pharmaceutical industry (Santos et al. 2008). As for many other dispersion systems, the usual method of solving this problem seems to be adding a suitable polymer that imparts the desired rheological properties without significantly modifying the other properties of the microemulsion (i.e., stability, high oil/water interface area, Lapasin et al. 2001). The polymer system generally displays weak gel properties and can be profitably used to confer a marked elasticity as well as pronounced shear-thinning properties on the dispersion, with sufficiently high fluidity at a high shear rate. Polymers such as carbopol 940, xanthan gum and carrageenan have been used recently to increase the viscosity of microemulsions for topical delivery, which makes them more suitable skin delivery systems (Gulsen and Chauhan 2005; Chen et al. 2006; Zhu et al. 2009).

It has been reported that phospholipid-based formulations have a high probability of 'recognizing' and adhering to membranes, thereby improving the permeation of the active molecules (Spermath et al. 2007). Therefore, voriconazole-loaded microemulsions containing phosphatidylcholine (PC) were prepared and characterized in terms of phase diagrams and particle size, and by transmission electron microscopy (TEM). MBH formulations were prepared using carbopol and xanthan gum as gelling agents, and their physicochemical properties were characterized in terms of solubility and viscosity. The *in vitro* drug permeation through excised hairless mouse skin and *in vivo* drug deposition in the SC and dermis were also evaluated.

Materials and methods

Materials

Voriconazole was purchased from HuaFeng United Technology Co. Ltd. (Beijing, China). Benzyl alcohol and *N*-methyl-2-pyrrolidone (NMP) were obtained from Junsei Chemical Co. Ltd. (Tokyo, Japan). Cotton oil, tetraglycol,

soybean oil, propylene glycol (PG) and Transcutol (diethylene glycol monoethyl ether) were purchased from Sigma-Aldrich (MO, USA). Tween 20, Tween 80, and Span 80 were purchased from Tokyo Chemical Industry Co. Ltd. (Tokyo, Japan). Soybean PC was provided by Lipoid Company (Ludwigshafen, Germany) at no charge. Carbopol 940 was purchased from Noveon, Inc. (Cleveland, USA). Xanthan gum was purchased from Arthur Branwell Co. Ltd. (Wicklow, Ireland). All other chemicals were of reagent grade and used without further purification.

Determination of solubility

Solubility studies were conducted by placing an excess amount of voriconazole (~500 mg) in a 2-ml microtube containing 1 ml of each vehicle (Table 1). The mixture was then vortexed and kept for 3 days at 37 °C in a sonicating water bath to facilitate solubilization (Lee et al. 2010). The samples were centrifuged at 10,000 rpm for 10 min to remove undissolved voriconazole. The supernatant was taken and diluted with methanol for quantification of voriconazole by high-performance liquid chromatography (HPLC). The HPLC system was equipped with a Waters 515 pump, Waters 2487 UV detector and Waters 717 autosampler. The Capcell pak C₁₈ column (4.6 × 250 mm, Shiseido) was used at room temperature. The mobile phase was a mixture of acetonitrile, methanol and water (30:30:40 v/v/v), filtered through a 0.45-μm membrane filter and eluted at a flow rate of 1.0 ml/min. Effluents were monitored at 256 nm.

Construction of pseudo-ternary phase diagrams

Based on the solubility study (Table 1), benzyl alcohol was selected as an oil phase, and NMP was as a surfactant. The mixture of ethanol and PC was used as a cosurfactant at a 3:2 weight ratio. Then, the pseudo-ternary phase diagrams were constructed by instillation of homogenous liquid mixtures of oil, surfactant, and cosurfactant, with water at ambient temperature (Yin et al. 2009). The surfactant and cosurfactant mixture (S_{mix}) was first prepared with a 1:2 or 1:3 weight ratio. Aliquots of each S_{mix} were then mixed with oil at room temperature to vary the ratio from 0.5:9.5 to 9.5:0.5. Finally, these oil and S_{mix} mixtures at various weight ratios were gradually diluted with water under gentle stirring. After equilibration, the compositions of the microemulsion at which phase separation of the homogeneous microemulsion to heterogeneous phase occurred were recorded.

Selection of microemulsions and MBH formulations

From the phase diagrams, the optimized microemulsion formulations were selected based on the following

Table 1 Solubility of voriconazole in various pharmaceutical vehicles at 25 °C

Vehicles	Components	Solubility (mg/ml)
Oil	Benzyl alcohol	397.35 ± 24.33
Oil	Tetraglycol	76.96 ± 7.73
Oil	Cotton oil	1.70 ± 0.28
Oil	Soybean oil	1.95 ± 0.11
Oil	Ethyl oleate	9.42 ± 0.55
Surfactant	NMP	418.79 ± 13.16
Surfactant	Transcutol	161.54 ± 4.74
Surfactant	Tween 20	34.11 ± 1.68
Surfactant	Tween 80	23.55 ± 1.72
Surfactant	Span 80	14.86 ± 2.98
Cosurfactant	Ethanol	81.10 ± 2.48

All data are expressed as the mean ± standard deviation ($n = 3$)

considerations: (1) 10 % (w/w) benzyl alcohol (oil) was selected to minimize skin irritation (Bagley et al. 1996), (2) 49–50 % (w/w) water was selected because it was reported that specific hydration of the SC affected the skin permeability (Changez et al. 2006), and (3) 39–40 % (w/w) S_{mix} was selected to facilitate formation of stable microemulsions. Formulations with the surfactant/cosurfactant mixture (S_{mix}) at 1:2 and 1:3 weight ratios were designated F1 and F2, respectively. Loaded microemulsions were prepared by dissolving voriconazole in oil and S_{mix} together, followed by dropwise addition of water to the oily phase under magnetic stirring at ambient temperature.

Carbopol 940 and xanthan gum were selected as gelling agents for the MBH formulations. MBHs were prepared by adding carbopol 940 or xanthan gum into microemulsions containing 1 % (w/w) voriconazole under stirring (Lee et al. 2010). Triethanolamine (TEA) was used as a neutralizer of carbopol 940 (Schwarz et al. 1995). The compositions of voriconazole-loaded microemulsions and MBHs are shown in Table 2.

Characterization of microemulsions and MBH

Solubility of voriconazole in microemulsions

The solubility of voriconazole in the F1 and F2 formulations was determined by adding an excess amount of voriconazole and vortex mixing. The samples were then sonicated in a water bath at 37 °C for 72 h to promote solubilization. The samples were centrifuged at 10,000 rpm for 10 min and the supernatant was subjected to HPLC after filtration through a membrane filter.

Morphology of microemulsions

The morphology of the microemulsions was examined using an energy-filtering transmission electron microscope (TEM; Libra 120, Carl Zeiss, Germany) with 80-kV accelerating voltage. The microemulsions were negatively stained using uranyl acetate and placed on carbon-coated 400 mesh copper grids, followed by drying at room temperature before measurements.

Droplet size analysis

The droplet size of the voriconazole-loaded microemulsions was measured using an electrophoretic light-scattering spectrophotometer (ELS-8000, Otsuka Electronics Co. Ltd., Japan). The microemulsions were transferred to a standard quartz cuvette, and the droplet size was determined via dynamic He–Ne laser (10 mW) light-scattering at an angle of 90° at 25 °C. Data analysis was conducted using the ELS-8000 software provided by the manufacturer.

Viscosity of MBHs

The viscosity of MBHs was determined using a viscometer (Brookfield, USA) at 50 rpm with spindle # LV4 at room temperature.

Table 2 Composition of microemulsions and microemulsion-based hydrogels (MBHs) containing 1 % (w/w) of voriconazole

Components	F1	F1-1	F1-2	F2	F2-1	F2-2
Voriconazole	1	1	1	1	1	1
Benzyl alcohol	10	10	10	10	10	10
NMP	13	13	13	10	10	10
Ethanol:PC (3:2)	26	26	26	30	30	30
Triethanolamine		0.2			0.2	
Carbopol 940		0.8			0.8	
Xanthan gum			1			1
Water	50	49	49	49	48	48

In vitro skin permeation and skin deposition

Male hairless mice (4 weeks old) were purchased from Orient Bio, Inc. (Sungnam, Korea) and reared in a light-controlled room maintained at 22 ± 2 °C with 55 ± 5 % relative humidity (Animal Center for Pharmaceutical Research, College of Pharmacy, Seoul National University, Seoul, Korea). The experimental protocols were approved by the Animal Care and Use Committee of the College of Pharmacy, Seoul National University.

Franz diffusion cells with an effective diffusion area of 2.0 cm^2 at 37 °C were used to perform the in vitro skin permeation and deposition studies. Mice were sacrificed by cervical dislocation, and the excised skin of dorsal side were clamped between the donor and receptor chambers of Franz diffusion cells, with the SC facing the donor chamber. Then, 1 g of microemulsions, MBH or the control (i.e., PG) containing 1 % (w/w) of voriconazole was applied to the donor compartment. The receptor chamber was filled with 12 ml of phosphate-buffered saline. The receptor medium was maintained at 37 ± 0.5 °C and stirred at 600 rpm throughout the experiment. For each experiment, 0.4 ml of receptor medium was sampled at predetermined time intervals; an identical volume of pure medium was immediately added to the receptor chamber. All samples were filtered through a $0.45\text{-}\mu\text{m}$ pore size cellulose membrane filter and analyzed by HPLC.

After 12 h, the surface of the skin specimens was washed with methanol to remove skin-bound formulations. The effective surface area of the skin (2.0 cm^2) was separated and the SC layer was removed by stripping 20 times using cellophane adhesive tape (CuDerm Corporation, Dallas, USA). After SC removal, the skin was weighed and minced using a surgical sterile scalpel. It was then homogenized in a vial filled with methanol (1 ml/cm^2) using an ultra Turrax homogenizer at 23,000 rpm for 5 min (T25 Basic, Germany) on an ice bath (4 °C). The tissue suspension was centrifuged for 5 min at $3,000\times g$, and the supernatants were filtered and assayed in terms of their voriconazole content by HPLC.

In vivo skin deposition study

Male hairless mice (4 weeks old, 18–20 g) were anaesthetized with ether and fixed on the abdominals. MBH formulations (0.3 g of F1-1 or F1-2) containing 1 % (w/w) voriconazole were applied to the dorsal surface (3 cm^2). At 1, 4, and 8 h after dorsal application, the mice were euthanized by cervical dislocation. The skin was subsequently stripped and thoroughly washed using methanol, after which the skin surface was dried with a cotton swab and the drug content in the SC layer and dermis determined as described in “[In vivo skin deposition study](#)” section.

Data analysis

All experiments were performed in at least triplicate and the data expressed as mean \pm standard deviation. The statistical analysis was performed using a two-tailed Student's *t* test. A value of $p < 0.05$ was considered to indicate statistical significance.

Results and discussion

Solubility of voriconazole

The solubility of voriconazole in various pharmaceutically acceptable vehicles was determined to identify the optimum oil and surfactants for use in microemulsion formulations (Table 1). Among the vehicles evaluated, benzyl alcohol and NMP were selected as the oil and surfactant phases, respectively, due to their exhibiting the highest drug solubility.

Phase studies

Pseudo-ternary phase diagrams were constructed to determine the existence range of microemulsions. The pseudo-ternary phase diagrams with 1:2 and 1:3 weight ratios of surfactant (i.e., NMP) to cosurfactant (i.e., 3:2 mixture of ethanol and PC) are shown in Fig. 1A, B, respectively, in which the transparent microemulsion region is presented. The remainder of the phase diagram represents turbid or conventional emulsions based on visual observation. Phase behavior investigations of this system enabled determination of the water phase, oil phase, surfactant, and cosurfactant concentrations that resulted in formation of the transparent one-phase microemulsion system (Ghosh et al. 2006).

Preparation and characterization of microemulsions and MBHs

Two microemulsion formulations (F1 and F2) were selected from the phase diagram in Fig. 1A, B, respectively. The oil, surfactant, cosurfactant, and aqueous phase contents are described in Table 2. For topical delivery of antifungal agents, formulations with higher solubilization of voriconazole are preferred, to enhance skin absorption. The solubility of voriconazole in F1 and F2 was 35.43 ± 0.17 and 30.5 ± 0.82 mg/ml (Table 3), respectively, being 35- and 30-fold higher than its aqueous solubility (0.97 mg/ml). The particle sizes of the microemulsions F1 and F2 are presented in Table 3, and were consistent with the TEM results (Fig. 2). The MBHs were prepared by adding carbopol 940 or xanthan gum (Table 2), since the viscosity of

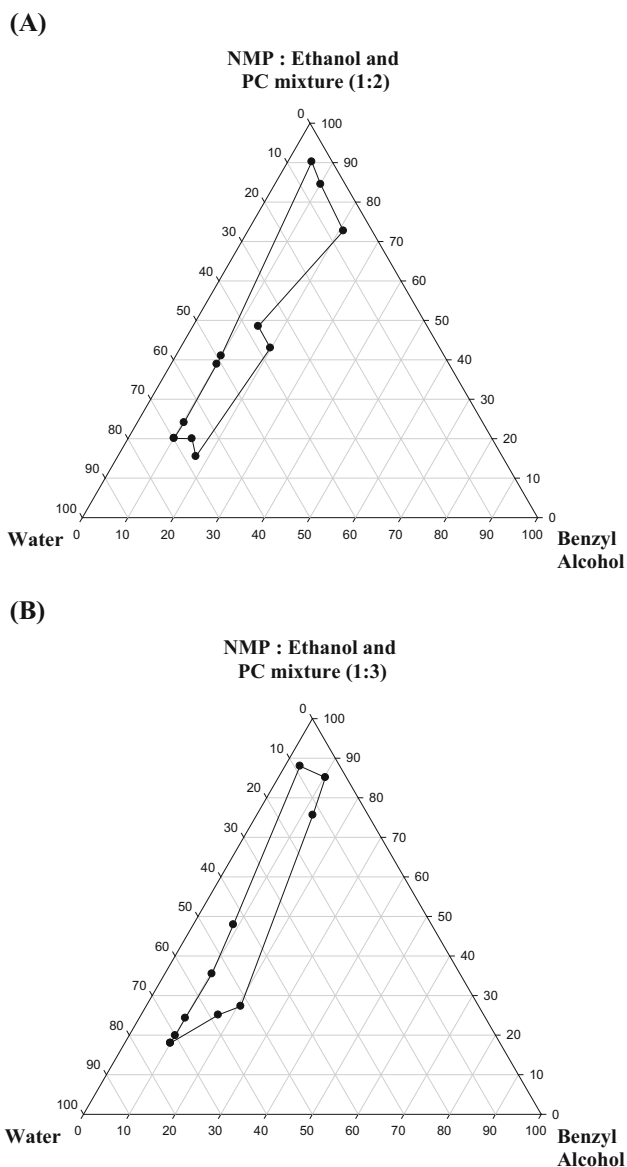


Fig. 1 The pseudo-ternary phase diagrams of the oil–surfactant–water system at (A) NMP:Cosurfactant = 1:2 and (B) 1:3 weigh ratio of NMP–cosurfactant mixture (ethanol:PC at 3:2 ratio) at 25 °C

the optimized microemulsions (F1 and F2) was not suitable for topical delivery (less than 10 cp). The viscosity of MBHs was significantly higher by 380–1,090 cp compared to the microemulsion following the addition of 0.8 % carbopol 940 and 0.2 % TEA, or 1 % xanthan gum (Table 3), which made the preparation more suitable for topical administration (Lapasin et al. 2001; Špiclin et al. 2003). Among the MBHs, the MBHs prepared with carbopol 940 showed higher viscosity than those prepared with xanthan gum. This may be due to the weak gelation of xanthan gum at 1 % (w/w) (Špiclin et al. 2003; Chen et al. 2006).

The gel-like property of the MBHs might be due to the fact that carbopol 940, as an aqueous gel matrix in a continuous phase, displayed non-covalent intermolecular associations (Chen et al. 2006, 2007). These physical interactions could lead to the formation of a three-dimensional gel network, within which the dispersed oil droplets were contained. In the case of MBHs based on xanthan gum, it has been reported that the system is transformed from a polymeric solution at 0.25 % xanthan gum in the dispersion (with no significant interaction between xanthan molecules) into a structured system at 0.5–0.75 %, and to a system with weak-gel behavior at 1.0 % (which is attributed to physical entanglement of polymer chains; Špiclin et al. 2003).

In vitro skin permeation studies

MBHs are composed of nonionic surfactants and gelling polymers, which are biocompatible and relatively nontoxic. Moreover, they serve as excellent penetration enhancers (Schwarz et al. 1995; Chen et al. 2006; Zhu et al. 2009). In this study, to assess the influence of the drug carriers on drug accumulation and diffusion, in vitro permeation studies using hairless mouse skin and static vertical Franz diffusion cells were carried out under non-occlusive conditions.

The permeation profiles of voriconazole in various formulations through hairless mouse skin are shown in Fig. 3. The permeation parameters of the test and the control formulations are presented in Table 4. PG was selected as the control vehicle to maintain high drug concentration in the donor side for poorly water-soluble voriconazole (Jung et al. 2013). The microemulsions (F1 and F2) showed significantly higher drug permeation rates than PG (control). Such enhanced voriconazole solubility in microemulsions could enhance the permeation rate of the drug. Several mechanisms for the enhanced skin permeation from microemulsions have been proposed (Kreilgaard 2002), including (1) the high drug loading capacity of microemulsions, (2) the possibility of direct drug transfer from the microemulsion droplet to the SC (Peltola et al. 2003), and (3) the penetration-enhancing effect of the microemulsion components (Lee et al. 2003). NMP was used as the surfactant, and its skin penetration-enhancing effect has been reported (Sasaki et al. 1990). Ethanol, used as a cosurfactant, also exerts a penetration-enhancing effect by altering the skin texture (Williams and Barry 2004). PC is one of the main components of biological membranes, and is also reported to have a permeation-enhancing effect (Kim et al. 2002). These mechanisms could explain the superiority of the microemulsion formulations compared to the control (PG).

Table 3 Physicochemical properties of microemulsions and MBHs

Formulation	Solubility of voriconazole (mg/ml)	Particle size (nm)	Viscosity (cp)
F1	35.43 ± 0.17	30.31 ± 8.49	<10
F1-1 (carbopol 940)	–	–	1,090 ± 112
F1-2 (xanthan gum)	–	–	380 ± 23
F2	30.50 ± 0.82	32.78 ± 6.49	<10
F2-1 (carbopol 940)	–	–	1,150 ± 98
F2-2 (xanthan gum)	–	–	411 ± 31

All data are expressed as the mean ± standard deviation (*n* = 3)

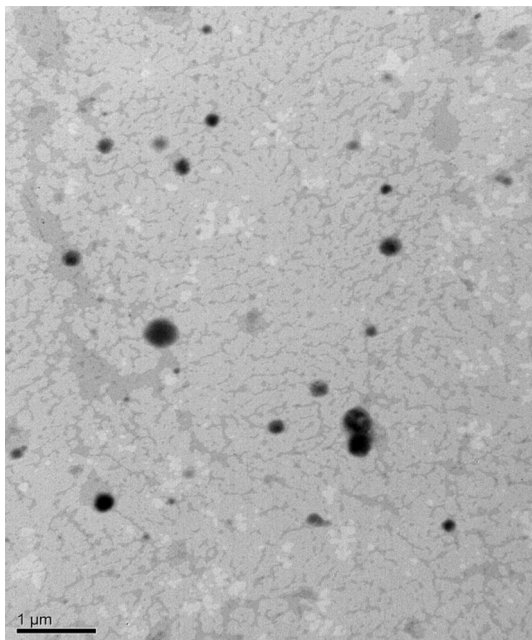


Fig. 2 Morphology of voriconazole microemulsion (F1) observed by TEM

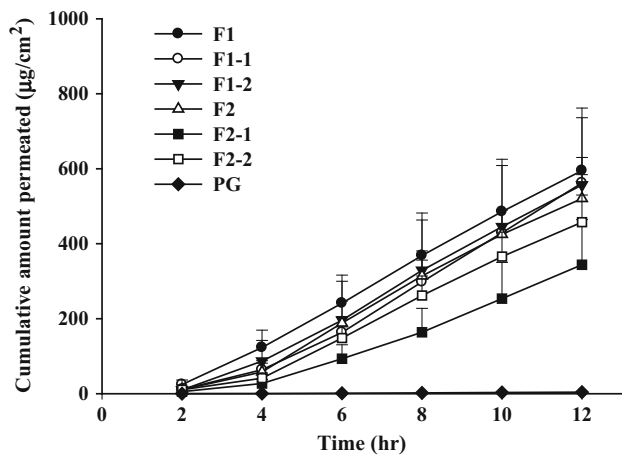


Fig. 3 In vitro permeation profiles of voriconazole across hairless mouse skin from various formulations (*n* = 3)

It is interesting to note that the presence of the gelling agent did not result in significant differences in permeation profiles compared to F1 and F2, and the MBH formulations

Table 4 In vitro permeation parameters of voriconazole from various formulations through hairless mouse skin

Formulation	Permeation rate (μg/cm ² /h)	Lag time (h)
F1	58.89 ± 15.68	1.8 ± 0.6
F1-1 (carbopol 940)	66.36 ± 5.54	3.5 ± 0.6
F1-2 (xanthan gum)	59.91 ± 16.94	2.7 ± 1.6
F2	55.37 ± 5.82	2.4 ± 1.3
F2-1 (carbopol 940)	42.05 ± 14.34	4.0 ± 0.4
F2-2 (xanthan gum)	53.99 ± 6.98	3.0 ± 0.2
PG (control)	0.53 ± 0.18	4.2 ± 1.1

All data are expressed as the mean ± standard deviation (*n* = 3). Each formulation contains 1 % (w/w) of voriconazole

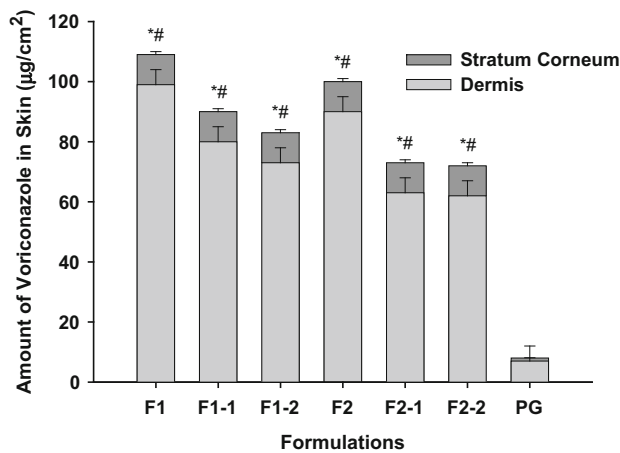


Fig. 4 Amount of voriconazole retained in the skin at the end of 12 h of in vitro permeation studies using various formulations (*n* = 6). **p* < 0.05, compared to PG in stratum corneum; #*p* < 0.05, compared to PG in dermis

significantly increased the voriconazole permeation and content of the skin compared to PG (Fig. 4). The high viscosity of gelling agents may not retard the diffusion of the drug. One possible mechanism of the ability of MBHs to modulate drug transfer across the skin is the tight contact between the drug preparation with the skin due to the presence of carbopol 940 and xanthan gum (Chen et al. 2006; Zhu et al. 2009). Moreover, gel viscosity did not cause significant unfavorable effects on the drug permeation and deposition properties of microemulsions. The

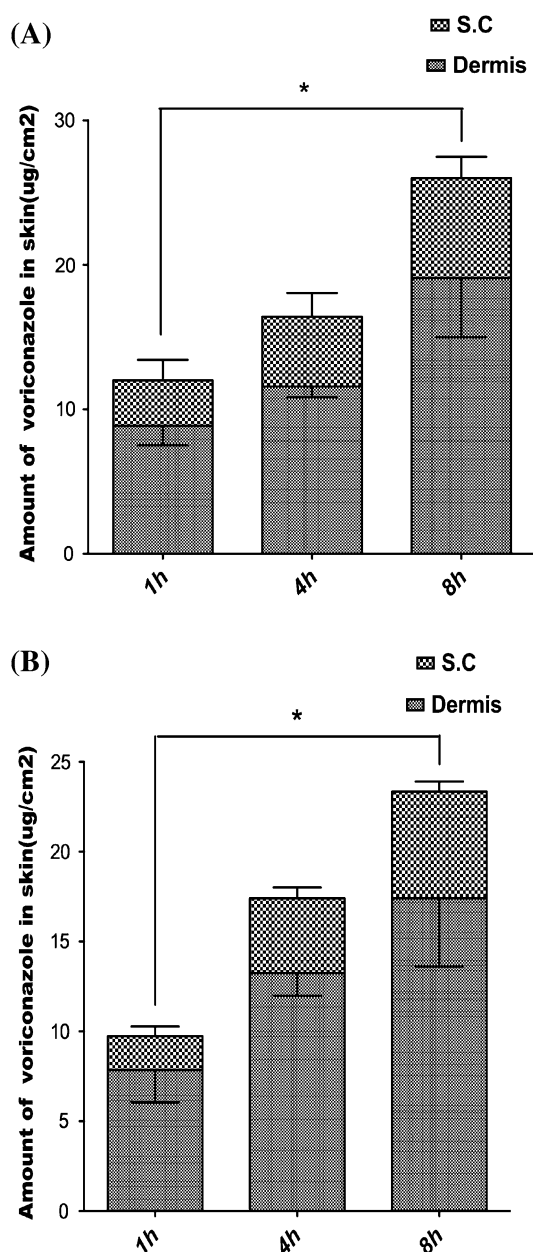


Fig. 5 Amount of voriconazole retained in the skin during the in vivo skin deposition studies using (A) F1-1 and (B) F1-2. * $p < 0.05$

skin permeation and deposition results suggest MBHs to be a potential topical delivery system for voriconazole.

In vivo skin deposition studies

As MBHs with carbopol 940 (F1-1) and xanthan gum (F1-2) showed higher skin permeation rates and skin deposition than F2-1 and F2-2, with sufficient viscosity for topical application, they were selected for further in vivo studies. The amounts of voriconazole deposited in the SC and dermis layers are shown in Fig. 5. The MBHs (F1-1 and

F1-2) showed no significant difference in skin drug content profile at each time point. However, the skin drug content increased with increasing application time, which indicates that the skin deposition has not reached the steady-state for 8 h. The plasma drug concentrations following topical application on normal skin were below the detection limit for both formulations (data not shown). Our results suggested that the prepared MBHs have potential for the topical delivery of voriconazole.

Conclusion

In summary, this investigation showed the potential of MBHs in terms of enhancing the bioavailability of voriconazole in hairless mouse skin compared to the control. In vitro permeation experiments showed that both microemulsions and MBHs significantly increased voriconazole skin permeation and deposition, compared to the control PG solution. This was confirmed by an in vivo study. Thus, our data suggest that these MBHs have potential as a carrier for the topical delivery of voriconazole.

Acknowledgments All authors (Y.-H. Kim, C. K. Song, E. Jung, D.-H. Kim, D.-D. Kim) declare that they have no conflict of interest. This work was supported by the National Research Foundation of Korea (NRF) Grant funded by the Korean government (MSIP, No. 2009-0083533) and the MarineBio Research Program (NRF-C1ABA001-2011-0018561).

References

- Bagley DM, Gardner JR, Holland G, Lewis RW, Regnier JF, Stringer DA, Walker AP (1996) Skin irritation: reference chemicals data bank. *Toxicol In Vitro* 10:1–6
- Changez M, Varshney M, Chander J, Dinda AK (2006) Effect of the composition of lecithin/*n*-propanol/isopropyl myristate/water microemulsions on barrier properties of mice skin for transdermal permeation of tetracaine hydrochloride: in vitro. *Colloid Surf B* 50:18–25
- Chen H, Chang X, Du D, Li J, Xu H, Yang X (2006) Microemulsion-based hydrogel formulation of ibuprofen for topical delivery. *Int J Pharm* 315:52–58
- Chen H, Mou D, Du D, Chang X, Zhu D, Liu J, Xu H, Yang X (2007) Hydrogel-thickened microemulsion for topical administration of drug molecule at an extremely low concentration. *Int J Pharm* 341:78–84
- Ghosh PK, Majithiya RJ, Umrethia ML, Murthy RSR (2006) Design and development of microemulsion drug delivery system of acyclovir for improvement of oral bioavailability. *AAPS PharmSciTech* 7(3):77
- Gulsen D, Chauhan A (2005) Dispersion of microemulsion drops in HEMA hydrogel: a potential ophthalmic drug delivery vehicle. *Int J Pharm* 292:95–117
- Harding DH (2003) Pharmaceutical formulations containing voriconazole. United States Patent 6,632,803, B1
- Jadhav KR, Shaikh IM, Ambade KW, Kadam VJ (2006) Applications of microemulsion based drug delivery system. *Curr Drug Deliv* 3:267–273

- Jeu L, Piacenti FJ, Lyakhovetskiy AG, Fung HB (2003) Voriconazole. *Clin Ther* 25:1321–1381
- Johnson LB, Kauffman CA (2003) Voriconazole: a new triazole antifungal agent. *Clin Infect Dis* 36:630–637
- Jung E, Kang YP, Yoon IS, Kim JS, Kwon SW, Chung SJ, Shim CK, Kim DD (2013) Effect of permeation enhancers on transdermal delivery of fexofenadine: in vitro and in vivo evaluation. *Int J Pharm* 456:362–369
- Kim C, Shim J, Han S, Chang I (2002) The skin-permeation-enhancing effect of phosphatidylcholine: caffeine as a model active ingredient. *J Cosmet Sci* 53:363–374
- Kreilgaard M (2002) Influence of microemulsions on cutaneous drug delivery. *Adv Drug Deliv Rev* 54(Suppl 1):S77–S98
- Lapasin R, Grassi M, Coceani N (2001) Effects of polymer addition on the rheology of o/w microemulsions. *Rheol Acta* 40:185–192
- Lawrence MJ, Rees GD (2000) Microemulsion-based media as novel drug delivery systems. *Adv Drug Deliv Rev* 45:89–121
- Lee PJ, Langer R, Prasad Shastri V (2003) Novel microemulsion enhancer formulation for simultaneous transdermal delivery of hydrophilic and hydrophobic drugs. *Pharm Res* 20:264–269
- Lee EA, Balakrishnan P, Song CK, Cho JH, Noh GY, Park CG, Choi AJ, Chung SJ, Shim CK, Kim DD (2010) Microemulsion-based hydrogel formulation of itraconazole for topical delivery. *J Pharm Investig* 40:305–311
- Leveque D, Nivoix Y, Jehl F, Herbrecht R (2006) Clinical pharmacokinetics of voriconazole. *Int J Antimicrob Agents* 27:274–284
- Peltola S, Saarinen-Savolainen P, Kiesvaara J, Suhonen TM, Urtti A (2003) Microemulsions for topical delivery of estradiol. *Int J Pharm* 254:99–107
- Santos P, Watkinson AC, Hadgraft J, Lane ME (2008) Application of microemulsions in dermal and transdermal drug delivery. *Skin Pharmacol Physiol* 21:246–259
- Sasaki H, Kojima M, Nakamura J, Shibasaki J (1990) Enhancing effect of combining two pyrrolidone vehicles on transdermal drug delivery. *J Pharm Pharmacol* 42:196–199
- Schwarz JS, Weisspapier MR, Friedman DI (1995) Enhanced transdermal delivery of diazepam by submicron emulsion (SME) creams. *Pharm Res* 12:687–692
- Spornath A, Aserin A, Ziserman L, Danino D, Garti N (2007) Phosphatidylcholine embedded microemulsions: physical properties and improved Caco-2 cell permeability. *J Control Release* 119:279–290
- Špiclin P, Homar M, Zupančič-Valant A, Gašperlin M (2003) Sodium ascorbyl phosphate in topical microemulsions. *Int J Pharm* 256:65–73
- Williams AC, Barry BW (2004) Penetration enhancers. *Adv Drug Deliv Rev* 56:693–918
- Yin YM, Cui FD, Mu CF, Choi MK, Kim JS, Chung SJ, Shim CK, Kim DD (2009) Docetaxel microemulsion for enhanced oral bioavailability: preparation and in vitro and in vivo evaluation. *J Control Release* 140:86–94
- Zhu W, Guo C, Yua A, Gao Y, Cao F, Zhai GX (2009) Microemulsion-based hydrogel formulation of penciclovir for topical delivery. *Int J Pharm* 378:152–158



Glycoengineering of Interferon- β 1a Improves Its Biophysical and Pharmacokinetic Properties

Kyoung Song^{1,3}, In-Soo Yoon⁴, Nam Ah Kim⁵, Dong-Hwan Kim¹, Jongmin Lee⁶, Hee Jung Lee³, Saehyung Lee¹, Sunghyun Choi³, Min-Koo Choi⁷, Ha Hyung Kim⁸, Seong Hoon Jeong⁵, Woo Sung Son⁹, Dae-Duk Kim¹, Young Kee Shin^{1,2*}

1 College of Pharmacy and Research Institute of Pharmaceutical Sciences, Seoul National University, Seoul, Republic of Korea, **2** Institutes of Entrepreneurial BioConvergence, Seoul National University, Seoul, Republic of Korea, **3** Research Institute of Reference Biolabs, Inc., Seoul, Republic of Korea, **4** College of Pharmacy and Natural Medicine Research Institute, Mokpo National University, Jeonnam, Republic of Korea, **5** College of Pharmacy, Dongguk University-Seoul, Gyeonggi-do, Republic of Korea, **6** PanGen Biotech Inc., Gyeonggi-do, Republic of Korea, **7** College of Pharmacy, Dankook University, Chungnam, Republic of Korea, **8** Biotherapeutics and Glycomics Laboratory, College of Pharmacy, Chung-Ang University, Seoul, Republic of Korea, **9** College of Pharmacy, CHA University, Gyeonggi-do, Republic of Korea

Abstract

The purpose of this study was to develop a biobetter version of recombinant human interferon- β 1a (rhIFN- β 1a) to improve its biophysical properties, such as aggregation, production and stability, and pharmacokinetic properties without jeopardizing its activity. To achieve this, we introduced additional glycosylation into rhIFN- β 1a via site-directed mutagenesis. Glycoengineering of rhIFN- β 1a resulted in a new molecular entity, termed R27T, which was defined as a rhIFN- β mutein with two N-glycosylation sites at 80th (original site) and at an additional 25th amino acid due to a mutation of Thr for Arg at position 27th of rhIFN- β 1a. Glycoengineering had no effect on rhIFN- β ligand-receptor binding, as no loss of specific activity was observed. R27T showed improved stability and had a reduced propensity for aggregation and an increased half-life. Therefore, hyperglycosylated rhIFN- β could be a biobetter version of rhIFN- β 1a with a potential for use as a drug against multiple sclerosis.

Citation: Song K, Yoon I-S, Kim NA, Kim D-H, Lee J, et al. (2014) Glycoengineering of Interferon- β 1a Improves Its Biophysical and Pharmacokinetic Properties. PLoS ONE 9(5): e96967. doi:10.1371/journal.pone.0096967

Editor: Michael Massiah, George Washington University, United States of America

Received: January 21, 2014; **Accepted:** February 23, 2014; **Published:** May 23, 2014

Copyright: © 2014 Song et al. This is an open-access article distributed under the terms of the Creative Commons Attribution License, which permits unrestricted use, distribution, and reproduction in any medium, provided the original author and source are credited.

Funding: This research was supported by Basic Science Research Program through the National Research Foundation (NRF)(NRF-2012R1A1A1043288, URL https://www.nrf.re.kr/nrf_tot/cms/index.jsp?pmi-ss0-return2=none) and Project through Korea Drug Development Fund (20100030032, URL <http://www.kddf.org/Main/>) of Korea funded by the Ministry of Education, Science and Technology. The funders had no role in study design, data collection and analysis, decision to publish, or preparation of the manuscript.

Competing Interests: Kyoung Song, Dae-Duk Kim, and Young Kee Shin currently hold stock in Reference Biolabs, Inc. This submission is related to Patent 10-0781666, USA 8,101,716 B2, 4637913, ZL 2005 8 0045291.5, 1809661, TU201108302TA, 3075773, PU110085EP and DK/EP1809661 in which inventor included Young Kee Shin, Kyoung Song, Joung Mim Lee. Reference Biolabs, Inc. is currently developing the R27T product. This does not alter the authors' adherence to all the PLOS ONE policies on sharing data and materials.

* E-mail: ykeeshin@snu.ac.kr

Introduction

Multiple sclerosis (MS) is a chronic neurodegenerative disease affecting the brain and spinal cord, leading to symptoms, including blurred vision, muscle weakness, trouble with mobility and balance, cognitive and memory problems, and sensory disturbances [1–3]. It typically occurs between the ages of 20 to 50, is more common in women than in men, and has a variable course [3,4]. As gold standard MS therapeutics, recombinant human interferon- β (rhIFN- β) products are widely used as a first-line treatment and have had a good long-term safety record over the last few decades [5,6]. Although rhIFN- β is currently competitive with newer oral medicines that provide improved compliance and tolerance, it is still uncertain whether injectable treatments can be completely replaced by oral drugs, at least until oral drugs demonstrate good long-term safety records [6,7]. This is particularly important because drug safety is one of the biggest issues in MS therapeutics, as MS is not a life-threatening disease but a life-long disease (since it occurs at an early age) [4,6]. Therefore, the production of biobetter versions of rhIFN- β would fulfill considerable unmet needs in the MS therapy, both with respect to

considerations within the pharmaceutical industry, such as biophysical stability and low production costs, and in medicine, such as fewer side effects, longer dosing intervals and route of administration.

Protein modification with polyethylene glycol (PEG) or oligosaccharide moieties is an approach often used to improve bioactive proteins, especially in regard to physical and thermal stability, increased solubility, protection against enzymatic digestion, increased circulating half-life, and in some cases, decreased immunogenicity [8–10]. Notably, next generation rhIFN- β therapeutics has been created using Fc fusions or PEGylation of rhIFN- β at its N- or C-terminal region, or at cysteine residues. PEGylated-Avonex is currently undergoing phase III clinical trials [11]. However, production problems with rhIFN- β 1a still remain a concern for the development of PEG-rhIFN- β 1a, because of rhIFN- β 1a aggregation, and the increased production cost associated with PEGylation.

Unlike PEGylation, glycoengineering requires no additional manipulation processes after the construction of a relevant cell line because glycosylation is a natural protein modification within mammalian cells. In addition, it is well known that glycosylation is

important for the activity of rhIFN- β [12,13]. There are two types of therapeutic rhIFN- β in clinical use: rhIFN- β 1a (Avonex and Rebif), which is produced in CHO cells and is singly glycosylated, and rhIFN- β 1b (Betaseron), which is produced in *Escherichia coli* and is not glycosylated [14–16]. In many reports, rhIFN- β 1a shows a higher specific activity, lower immunogenicity and decreased propensity for aggregation than rhIFN- β 1b [13,16]. Runkel *et al.* demonstrated that this remarkable difference is due to glycosylation, in which the glycan moiety confers protein stability, solubility and biological activity. Thus, glycoengineering may be a promising approach for improving the biophysical properties of glycoproteins, such as their structural stability and pharmacokinetics [17].

Although rhIFN- β 1a is remarkably more stable and active than rhIFN- β 1b, manufacturing of rhIFN- β 1a still continues to suffer from variable levels of expression and stability in mammalian cell lines, which often results in a low product yield [18,19]. The main challenge for developing rhIFN- β 1a is aggregation and poor stability, which can occur at very different stages in the development processes, and can result in low host viability, low productivity and the development of precipitates in solutions [19,20].

The approach outlined in the present study used site-specific hyperglycosylation via site-directed mutagenesis, which resulted in the development of a new molecular entity, termed R27T. Site-specific hyperglycosylation of R27T was confirmed by western blot analysis, isoelectric focusing, enzyme immunoassay, PNGase treatment and quantification of sialic acid. R27T displayed superior stability, solubility, productivity and pharmacokinetic properties without loss of specific activity or alterations in ligand-receptor binding.

Materials and Methods

Ethics Statement

All experimental procedures and protocols for animal study had been approved by the Institutional Animal Care and Use Committee of the Seoul National University (protocol #SNU-200909-33). All efforts were made to minimize suffering of animals.

Gene Construction, Expression and Purification of rhIFN- β 1a Glycosylation Analogs

Glycosylation analogs were constructed by performing site-direct mutagenesis via PCR on wild-type human IFN- β . The full-length gene was recovered and cloned into the pMSG expression vector (Patent#. US20040038394 A1, PanGen Biotech Inc., Gyeonggi-do, Korea). Stable transfection into CHO cells was performed using a dihydrofolate reductase selection system and selected methotrexate resistance clones were grown in methotrexate selective medium. Purification of rhIFN- β 1a and rhIFN- β mutant proteins, such as D110N, R27T and R27T-(NITV)2 was performed by PanGen Biotech Inc., in the same way. Firstly, for their purification, culture fluid containing proteins was applied to a column of blue Sepharose 6FF (GE Healthcare, Buckinghamshire, UK), which was then eluted with 35% propylene glycol-based phosphate buffer. After elution, the eluate was sequentially loaded onto CM Sepharose FF (GE Healthcare) and to C4 Reverse phase-high performance liquid chromatography (RP-HPLC) (Vydac, CA, USA). Purified proteins were concentrated and diafiltrated using a 10 kDa cut-off membrane in a Millipore Labscale Tangential Flow Filtration System (Millipore, MA, USA). Finally, gel filtration chromatography was performed on a Sephacryl 100HR column at 2.5 mL/min. An additional product,

termed R27T Δ Glyc, during R27T purification was also obtained from the C4 RP-HPLC purification step, which was separated from R27T in this step. R27T Δ Glyc consisted of singly or double glycosylated rhIFN- β mutein at a ratio of approximately 7:3 (data not shown). As control material, Rebif was purchased from Merck KGaA (Hesse, Germany), respectively.

Analysis of Expressed Proteins

Purified rhIFN- β mutant samples were assessed by SDS-PAGE and western blotting using Anti-rhIFN- β antibody (R&D Systems, MN, USA) as a primary antibody. To confirm the presence of glycosylation, 1 mg/mL R27T in 20 mM sodium phosphate monobasic dihydrate, pH 7.5, was treated with PNGase F (Sigma-Aldrich, MO, USA) at 37°C. Samples were taken at different times over a period of 1 hr. Deglycosylation was monitored by SDS-PAGE. Isoelectric focusing was used to determine the isoelectropoint (pI) of the protein and was performed using a pH 3–10 isoelectric focusing (IEF) gel (Invitrogen, CA, USA). R27T in media samples was quantified using a rhIFN- β ELISA kit (IBL, Hamburg, Germany) according to the manufacturer's instructions.

Glycosylation Site Confirmation

LC/ESI MS/MS was used for site-specific glycosylation analysis of R27T. R27T was reduced and then digested with trypsin/Glu-C. Presence of carbohydrate specific fragment ions, such as *m/z* 204 and 366, in the product ion spectra, was analyzed from glycopeptide ions. For identification of the exact site of glycosylation, PNGase F was used to remove N-linked glycans from trypsin/Glu-C glycopeptides, and for conversion of Asn to Asp. Deglycosylated peptides were sequenced using LC/MS/MS.

Monosaccharide and Sialic Acid Composition Analysis

A Dionex HPAEC (ThermoFisher Scientific, MA, USA) was used to analyze monosaccharide and sialic acid composition. AminoTrap Columns (ThermoFisher Scientific) and CarboPac PA10 analytical columns (ThermoFisher Scientific) were used at a flow rate of 1 mL/min at 30°C. Acidic sugars were analyzed by exposing the samples in 100 mM NaOH and 1 M NaOAc. All monosaccharides, including neutral and amino sugars, were analyzed by exposing the samples to 18 mM NaOH for 25 min. The waveform used for pulsed amperometric detection (PAD) was the Dionex default program for carbohydrates.

Dynamic Light Scattering (DLS) and Attenuated Total Reflectance Fourier Transform Infrared (ATR-FTIR)

Spectroscopy

Hydrodynamic size was investigated using a Zetasizer Nano ZS90 (Malvern Instruments, Baden-Württemberg, Germany). The temperature in the Zetasizer chamber was equilibrated to 10°C. Each sample was measured in a disposable sizing cuvette (Sarstedt, Germany). Hydrodynamic size and polydispersity index (PDI) were calculated from the auto-correlation function using Zetasizer software, version 6.32 (Malvern Instruments). ATR-FTIR spectra (4000–600 cm^{-1}) were collected at 4 cm^{-1} resolution using a Nicolet 6700 spectrophotometer (ThermoFisher Scientific) with a golden gate accessory (diamond crystal). The α -helix, β -sheet, β -turn, and random coil contents of the proteins were estimated from the amide I region of ATR-FTIR spectra. Peaks of the amide I region were first treated by Fourier self-deconvolution and then curve-fitted using the Gauss and Lorentz formula with OMNIC Peak Resolve software (ThermoFisher Scientific). The area corresponding to each secondary structure was calculated accordingly and expressed as a percentage of the sum of areas. To

measure kinetic thermostability, rhIFN- β 1a and R27T were incubated over 96 hr at 37°C and decay curves were generated for each protein. Detectable rhIFN- β was quantified by using the cytopathic effect (CPE) assay at each sampling time.

In vitro Antiviral, Anti-proliferative and Immunomodulatory Activity

Antiviral activities were measured to determine the capacity of rhIFN- β to protect A549 cells against the CPE of a lytic virus over a range of rhIFN- β concentrations. World Health Organization natural rhIFN (NIBSC code: 00/572) was utilized as a standard. To measure antiviral activity, A549 cells were seeded in 96-well plates and serial dilutions of the proteins were added. Plates were incubated for 22 hr and encephalomyocarditis virus (EMCV, 1000 TCID₅₀/mL) was added. Following a further 22 hr incubation, cells were dyed with crystal violet, at room temperature for 1 hr, and then the dye was extracted with 2-methoxyethanol. Absorbance at 570 nm was then measured. For measurement of anti-proliferation effects, Daudi cells were seeded and serial dilutions of the proteins were added, followed by incubation for 48 hr. Cell proliferation assays were performed using an EZ-Cytox cell viability assay kit following the manufacturer's protocol. Immunomodulatory effects of drugs were measured by analyzing the

presentation of MHC Class I in A549 cells. A549 cells were seeded in 100 mm dishes and treated with a serial dilution of each protein, followed by incubation for 48 hr. After harvesting cells and adjusting each sample for equal cell density with FACS buffer, FACS was used to measure the expression of MHC class I peptides.

Molecular Modeling of the R27T/IFNAR2 Complex

Molecular models of glycosylated rhIFN- β 1a were built from the crystal structure of wild-type rhIFN- β 1a (PDB ID: 1AU1) [21]. Mutation of arginine to threonine at the 27th residue, and N-linked glycosylation of 1AU1 were performed using UCSF Chimera [22,23] and GLYCAM [24–26]. Due to the high amino acid sequence identity (about 30%) between IFN- β 1a and IFN- α 2a, initial IFN- β 1a/IFNAR2 complex structures were generated using structural alignment with a model of IFN- α 2a/IFNAR2, whose structure was previously determined by NMR based docking methods (PDB ID: 2HYM) [27]. For modeling N-glycosylation, one of the major oligosaccharide structures (FA2G2S2, F: Core fucosylated, A2: biantennary with both GlcNAcs as b1–2 linked, G2: two galactose linked beta 1–4 to antenna, S2: two sialic acids linked to galactose) was chosen using a structure obtained from the hydrophilic interaction liquid chromatography (HILIC) profiles of R27T. The oligosaccharide

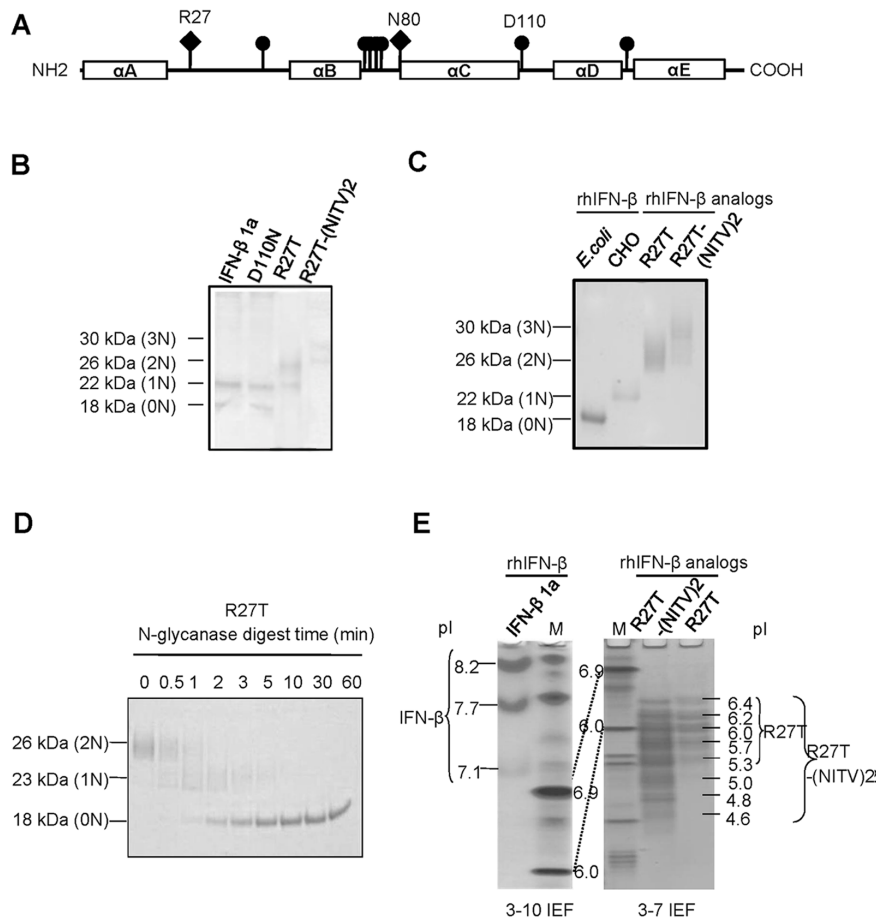


Figure 1. Construction and testing of rhIFN- β glycosylation analogs. (A) A schematic of the rhIFN- β protein. Boxes represented the locations of the five α -helices. Each vertical line represented a position with potential for an additional N-linked glycosylation site, as predicted by NetNGlyc. Introduced N-linked glycosylation consensus sequence sites were showed by diamonds(?). Purified samples were separated by (B) SDS-PAGE and (C) western blot analysis. (D) Analogues were subjected to N-glycanase digestion for the indicated times. (E) IEF analysis was performed over a pH range of 3–10.

doi:10.1371/journal.pone.0096967.g001

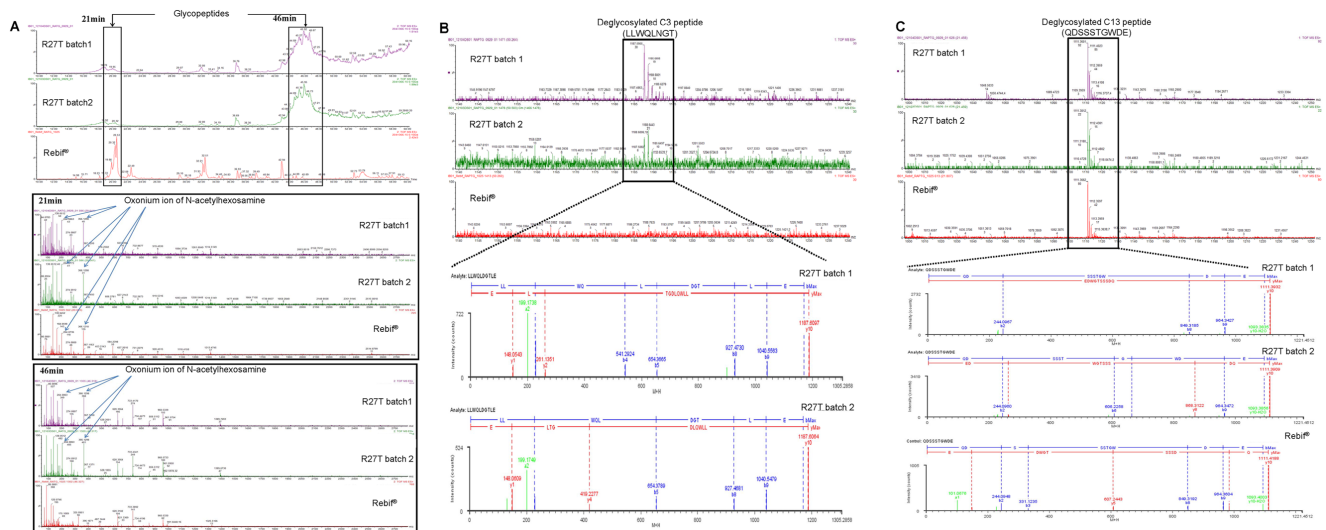


Figure 2. LC/ESI MS/MS of trypsin/Glu-C digests of R27T and Rebif. (A) Extraction ion chromatogram at m/z 204 and 366 for product ion spectra at 21 min and 46 min, respectively. Amino acid sequencing of deglycosylated C3 and C13 peptides by LC/ESI MS/MS. (B) Deglycosylated C3 peptide MS spectrum and fragmentation information for R27T (Lot: 12104DS01 and 12103DS01) and Rebif. (C) MS spectrum of the deglycosylated C13 peptide and fragmentation information for R27T (Lot: 12104DS01 and 12103DS01) and Rebif. doi:10.1371/journal.pone.0096967.g002

was built using Carbohydrate Builder (Woods Group, 2005–2013, GLYCAM Web, Complex Carbohydrate Research Center, University of Georgia, Athens, GA., <http://www.glycam.com>) and was attached to the N-glycosylation site of the wild-type IFN-β 1a/IFNAR2 structure. The final structures were minimized using Amber force field (AMBER99SB) [28]. During minimization, Amber parameters were used for standard residues, and the Antechamber module was used to make parameters for non-standard residues. Steepest minimization was performed (using 100 steps) to relieve unfavorable clashes, followed by 100 steps of conjugate gradient minimization. Steepest descent and conjugate gradient minimization size was 0.02 Å. Molecular visualization was done using UCSF Chimera and PyMOL (The PyMOL Molecular Graphics System, Version 1.2r3pre, Schrödinger, CA, USA).

In vivo Pharmacokinetic Analysis in Rats

Sprague Dawley rats were purchased from Orient Bio, Inc. (Gyeonggi-do, Korea), and maintained on a 12 hr light/dark cycle in a temperature- and humidity-controlled animal research facility. All rats were 8 weeks old, weighing 280–300 g at the beginning of each experiment. Each experiment included 9 groups ($n = 3$ per group). The femoral artery and vein were cannulated with a polyethylene tube (PE-50; Clay Adams, NJ, USA) under anesthesia. rhIFN-β substances (R27T, R27TAGlyc and Rebif) were bolus-injected intravenously (via the femoral vein;

IV), subcutaneously (at the abdomen; SC), or intramuscularly (at the leg; IM) at a dose of 1 MIU/kg to rats (total injection volume of approximately 0.3 mL). Approximately 120 μL of blood was collected via the femoral artery at 0 (to serve as a control), 1, 5, 15, 30, 60, 120, 240, 480, 720, and 1440 min after IV administration and at 0 (to serve as a control), 15, 30, 45, 60, 120, 180, 240, 360, 480, 720, and 1440 min after SC and IM administration. Approximately 0.3 mL of heparinized 0.9% NaCl-injectable solution (20 IU/mL) was used to flush each cannula immediately after blood sampling. Blood samples were centrifuged immediately, and a 50 μL aliquot of each plasma sample was stored in a -80°C freezer. All animals were humanely sacrificed at the end of experiments by euthanasia method: CO₂ inhalation in a non-precharged 4L chamber of a moderate fill rate. Standard non-compartmental analysis methods were used to calculate pharmacokinetic parameters (WinNonlin; standard version 3.1; Pharsight, CA, USA) [29,30].

Statistical Analysis

A p -value less than 0.05 was considered to be statistically significant. Statistical analysis was performed using Statistical Package for the Social Sciences (SPSS, IBM Corporation, NY, USA). Statistical significance was determined by analysis of variance (ANOVA) with Duncan's multiple range test posteriori. All results were expressed as mean \pm standard deviation, except

Table 1. Sugar composition analysis of R27T and Rebif (mol/mol protein).

	Fucose ^a	N-acetyl-glucosamine ^b	N-acetyl-galactosamine ^b	Galactose ^a	Mannose ^a	Sialic acid ^c
R27T	2.4	12.3	N.D.	7.7	7.1	3.2
Rebif	1.1	4.7	N.D.	3.0	3.5	1.2

^a2 M TFA for neutral sugars at 100°C at 4 hr.

^b6 N HCl for amino sugars at 100°C at 4 hr.

^c0.1 N HCl for sialic acids(NANA+NGNA) at 80°C at 1 hr.

doi:10.1371/journal.pone.0096967.t001

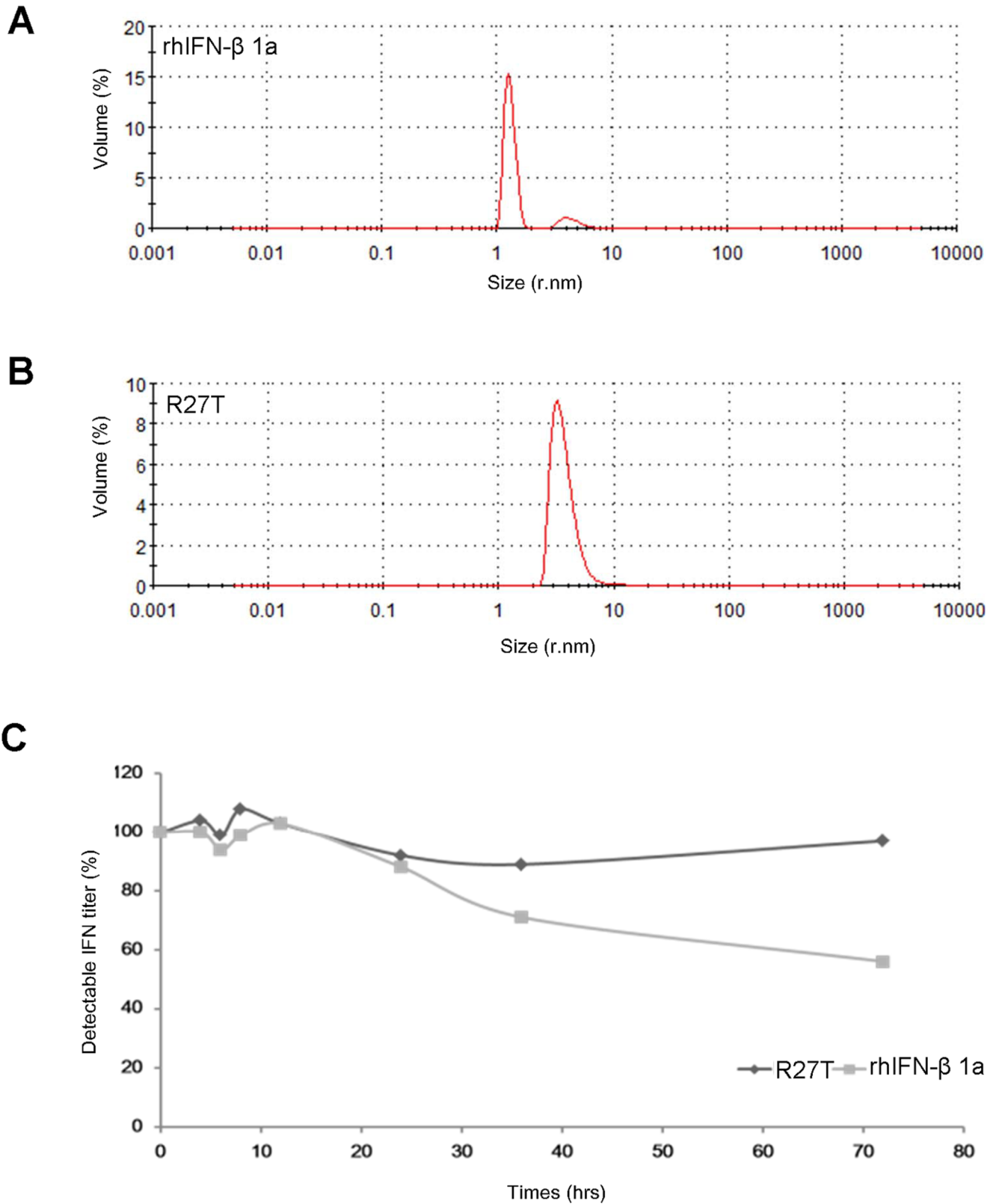


Figure 3. Size distribution of rhIFN- β 1a and R27T. The analysis of (A) rhIFN- β 1a and (B) R27T was performed at a scattering angle of 90° and distributed sizes, PDI, and Zeta averages were shown. (r.nm: radius in nanometers). (C) rhIFN- β s were quantified by CPE at each time up to 72 hr. doi:10.1371/journal.pone.0096967.g003

Table 2. Secondary structure ratios derived from the ATR-FTIR spectra of rhIFN- β 1a and R27T in solution.

Samples	Amide I region in ATR FTIR spectra			
	α -helix (%)	β -sheet (%)	β -Turn (%)	Random Coil (%)
rhIFN- β 1a	17.3	37.0	24.5	21.2
R27T	29.8	31.3	25.6	13.3

doi:10.1371/journal.pone.0096967.t002

for time to reach a C_{\max} (T_{\max}), which was expressed as the median (ranges).

Results

Construction of the rhIFN- β Glycosylation Analogs, R27T

To best maintain the structural and functional properties of the protein, additional N-glycosylation sites were not created in the five helical regions, consisting of amino acid residues A(2–22), B(51–71), C(80–107), D(112–136) and E(139–162). A number of sites including Arg27, Asp39, Gln72, Asp73, Ser74, Ser75, Asp110 and Glu137 were then screened for the additional introduction of a consensus N-glycosylation sequence (Asn-X-Ser/Thr, where X is any amino acid except Pro). Each site was analyzed using NetNGlyc software on the Center for Biological Sequence Analysis website (Technical University of Denmark) (Table S1). Based on our analysis, we selected the most flexible overhand AB loop and the highest mobility CD loop to minimize the structural modification, remaining at Arg27, Asp39 and Asp110 (Figure 1A). A substitution at Arg27 of rhIFN- β 1a was chosen as the most promising site, as it had the highest substitution potential score in NetNGlyc, whereas Asp110 was chosen as a negative control. The substitutions made were Arg27 and Asp110 with Thr and Asn, respectively. In addition, a hyper-glycosylated rhIFN- β model was created by extension of the sequence “ANITVNITV, termed (NITV)₂” into the C-terminus. Both R27T and R27T-(NITV)₂ showed a clear increase in molecular weight (by 26 and 30 kDa, respectively) in western blots (Figure 1B). No change in molecular weight was observed for the D110N analog, compared with native rhIFN- β , at 22 kDa. This was confirmed by SDS-PAGE of rhIFN- β after purification (Figure 1C). Treatment with PNGase, which catalyzes the release of N-linked oligosaccharides, resulted in the appearance of three bands of 26, 22 and 18 kDa in the R27T sample (Figure 1D). The upper and middle bands were doubly or singly glycosylated respectively, whereas the lower band contained only the peptide. Thus the molecular weight increment was attributed to additional glycosylation. Negative charge was increased in R27T and R27T-(NITV)₂, which had pI values of 5.3–6.4 and 4.6–6.4 respectively, compared to native rhIFN- β , with a pI of 7–8 (Figure 1E). Notably, R27T, which had one additional glycan at the 25th amino acid, was selected as the lead protein because the amino acid change for the additional glycosylation site was minimal. This could be advantageous, as it could result in lower immunogenicity than that for R27T-(NITV)₂.

Glycosylation Site Confirmation of R27T Analogs with Additional Glycosylation

Specific glycosylation sites were conclusively confirmed by determination of the carbohydrate attachment site on the polypeptide backbone of the protein. Glycopeptides were identified by performing quadrupole-time of flight (Q-TOF) MS on trypsin/Glu-C digests of R27T and the control Rebif, in which the

C3 and C13 peptide fragment had potential glycosylation sites at Asn25 and Asn80 in R27T, and Asn80 in Rebif (Figure S1A and S1B). Glycopeptide ions were extracted and confirmed by examining for the presence of oxonium ions, such as m/z 204 (HexNAc) and 366 (HexHexNAc), with retention times of 21 min and 46 min, respectively, on the extracted ion chromatogram (Figure 2A). The presence of oxonium ions was again determined in the product ion spectrum at 21 min and 46 min (Figure 2A). The identification of N-glycosylation sites by MS depends on the specific deamidation of asparagines to aspartic acid within the consensus sequence NX(S/T) upon cleavage of the glycan moiety by PNGase F. The deglycosylated peptide was sequenced by LC/MS/MS (Figure 2B and 2C). Glycosylation sites of R27T were identified at Asn25 and Asn80 in R27T.

Monosaccharide and Sialic Acid Composition Analysis

We performed glycosylation analysis to compare the relative proportion of monosaccharide content, mono-, di-, tri- and tetra-antennary structures with those of the reference, Rebif. Individual sugar residues were identified and quantitated as moles of monosaccharide per moles of protein. The monosaccharide contents in 1 mol of R27T and Rebif were shown in Table 1. The contents of each monosaccharide and sialic acid per moles of protein were increased with additional glycosylation, compared to Rebif. All carbohydrate moieties consisted of fucose, N-acetylglucosamine, galactose, mannose and sialic acid without N-acetylgalactosamine. Therefore, they were N-linked complex-type sugar chains.

Biophysical Analysis of Protein Stability by DSC, DLS and ATR-FTIR

DSC thermograms of rhIFN- β 1a and R27T in 20 mM acetate buffer pH 4.2 were evaluated to obtain thermal unfolding events (Figure S2). Unfolding transition temperature (T_m), calorimetric enthalpy (ΔH) and van't Hoff enthalpy (ΔH_v) of rhIFN- β 1a were 61.90°C, 39.88 kcal/mol and 106.3 kcal/mol, respectively. In addition, T_m , ΔH and ΔH_v of R27T were 59.07°C, 36.87 kcal/mol and 103.6 kcal/mol, respectively. Even though R27T exhibited lower T_m than rhIFN- β 1a while having almost similar ΔH and ΔH_v , it did not exhibit any visible particles after withdrawn from the DSC scan (data not provided). DLS was used to observe hydrodynamic size of rhIFN- β 1a and R27T and existence of aggregates in the aqueous environment as well. DLS measurements of the proteins were provided in Figure 3. rhIFN- β 1a gave two volume distribution peaks at around 2.700 nm and 9.825 nm with 98.9% and 1.3% volume ratio, respectively. However, R27T had only single size distribution peak at around 3.722 nm by volume distribution.

Polydispersity index (PDI) is dimensionless and scaled from 0 to 1 where values less than 0.05 are rarely seen other than with highly monodisperse standards. However, values higher than 0.7 suggest that the sample has a very polydisperse distribution and is not

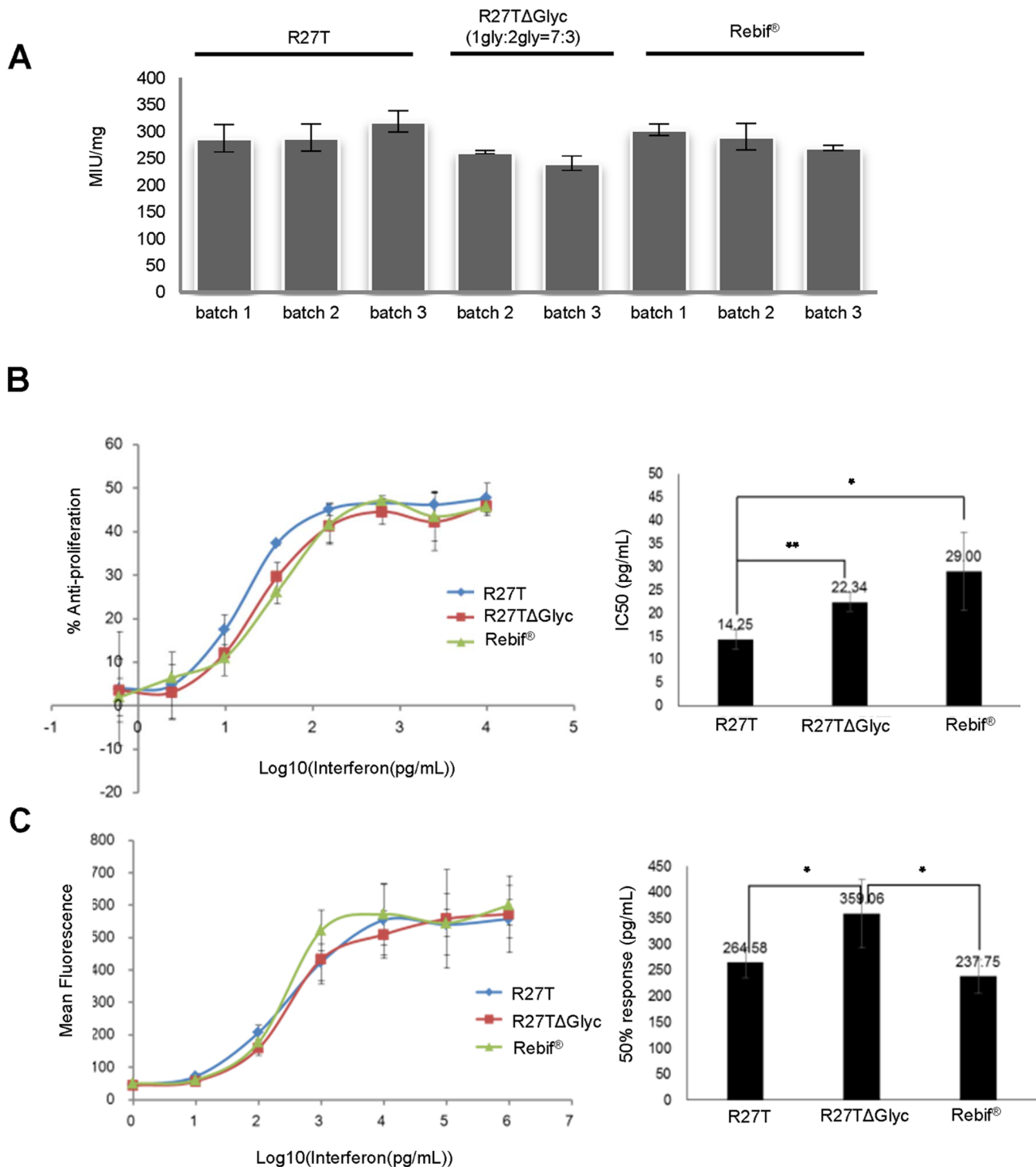


Figure 4. *In vitro* activity. (A) Anti-viral, (B) anti-proliferative and (C) immunomodulatory activities of R27T (?), R27T Δ Glyc (■) and Rebif (▲). doi:10.1371/journal.pone.0096967.g004

suitable for the DLS measurement. PDI values of rhIFN- β 1a and R27T were 0.607 and 0.306, respectively. Since rhIFN- β 1a had higher PDI value than R27T, the protein was more polydispersed and might not be stable in the aqueous environment compared to R27T. Therefore, the result may indicate that rhIFN- β 1a possess instability issue in the aqueous solution compared to R27T. In order to investigate secondary structural stability of the proteins,

ATR FT-IR was selected to analyze the amide group I (1700–1600 cm^{-1}) in proteins. The amide group I region of ATR-FTIR spectra was separated into nine peaks with Fourier self-deconvoluted spectra of rhIFN- β 1a and R27T. Each ratio of composite area represented the corresponding percentage of each structure from peak 1 to 9; peak #1, 2, 6 and 7 (1692 cm^{-1} , 1676 cm^{-1} , 1636 cm^{-1} and 1623 cm^{-1} , respectively; β -sheet),

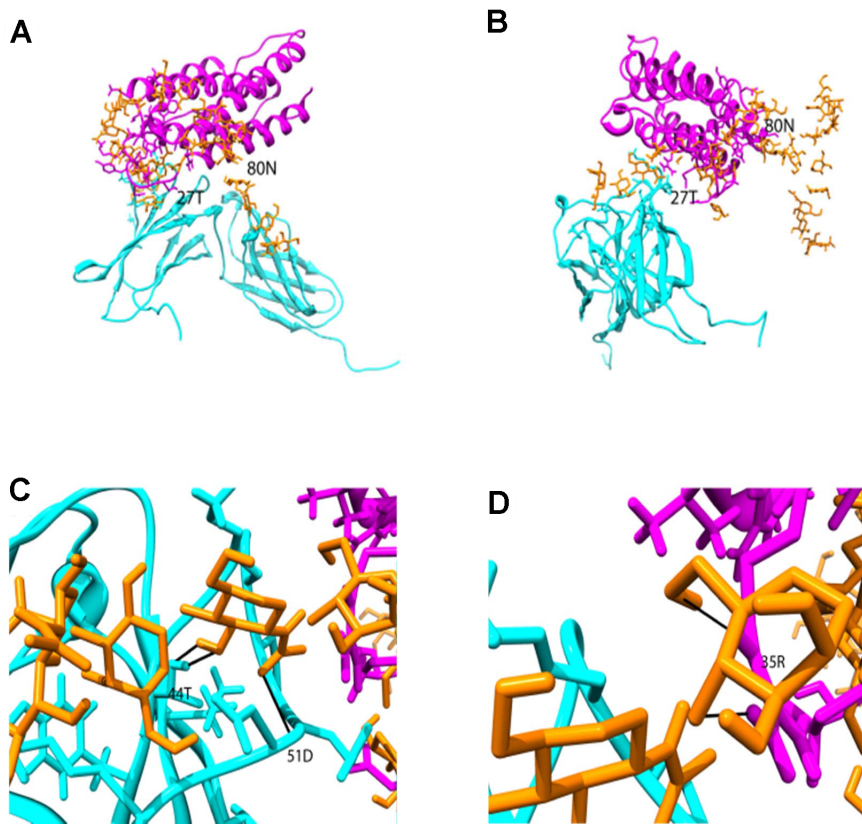


Figure 5. Model of the N-glycosylated R27T/IFNAR2 complex. (A) front view and (B) side view. The complex structure oligosaccharides, R27T, and IFNAR2 were shown as orange, magenta, and cyan color, respectively. New hydrogen bonds between the oligosaccharide and complex were presented as red bold line in C (with IFNAR2) and D (R27T). Also, 27T and 80N in R27T protein were colored by yellow (A,B) and hydrogen-bonded residues in R27T and IFNAR2 were colored by green (C,D). doi:10.1371/journal.pone.0096967.g005

peak #3 (1665 cm^{-1} ; reverse turn), peak #4 (1655 cm^{-1} ; α -helix), peak #5 (1646 cm^{-1} ; random coil), peak #8 (1615 cm^{-1} ; side chain vibration) and peak #9 (1598 cm^{-1} ; β -turn) were resolved accordingly. After resolving the peaks, relative percentage of the contents was calculated. Table 2 showed the relative ratio of α -helix, β -sheet, β -turn and random coil of rhIFN- β 1a and R27T. R27T contained more α -helix and less β -sheet than rhIFN- β 1a. It was already known from the crystal structure of rhIFN- β 1a that there was no β -sheet secondary structure. However, recent spectroscopy studies give that increasing intermolecular β -sheet structure is a common feature of protein aggregation although interferon consists of only α -helix [31–33]. Since β -sheet contents of rhIFN- β 1a were about 5.69% higher than R27T, it might suggest higher potential of protein aggregations [32].

To confirm the actual effect of stability issue, the aggregation kinetics was shown in figure 3C. CPE assay was used to detect bioactivity of R27T and rhIFN- β 1a in accelerated condition 37°C up to for 96 hr. The bioactivity with aggregation of R27T compared with rhIFN- β 1a had a less decrease within the first 96 hr. The calculated half-life for rhIFN- β 1a was 96 hr in contrast to 503 hr for R27T.

Maintenance of *In vitro* Activity

R27T and Rebif was analyzed for *in vitro* anti-viral activity together with an R27T Δ Glyc. Values of 299×10^6 , 252×10^6 and 288×10^6 IU/mg were obtained from the average activity of the three lots of R27T, two lots of R27T Δ Glyc and Rebif, respectively (Figure 4A). No decrease in antiviral activity was observed with

additional glycosylation. We also examined the relative potencies of R27T, R27T Δ Glyc, and Rebif in anti-proliferative and immunomodulation assays. Similar activities were observed in these assays. In the antiproliferative assay, IC₅₀s of 14, 22 and 29 pg/mL were obtained for R27T, R27T Δ Glyc and Rebif respectively (Figure 4B). In a FACS assay, which measured IFN-inducible expression of MHC class I on the surface of A549 cells, 50% responses were observed at approximately 265, 359 and 238 pg/mL, respectively (Figure 4C).

Molecular Modeling of the R27T/IFNAR2 Complex

An R27T structure was generated *in silico*, based on the crystal structure of human IFN- β 1a. The R27T/IFNAR2 docking structure was shown in Figure 5A and 5B. N-glycosylation was predicted to readily occur at the 80th amino acid, regardless of oligosaccharide structure or the distance (solvent accessible surface area 76.7 \AA by Naccess V2.1.1.1) at which glycosylation could have no effect on the R27T/IFNAR2 complex due to far distance between oligosaccharide and receptor [34]. By contrast, glycosylation at the 25th amino acid was more difficult to model *in silico* than at the 80th residue, as the 25th amino acid side chain was oriented towards the inside of the protein. However, “wet” experiments, including SDS-PAGE, confirmed that it was possible to glycosylate the 25th amino acid, in a similar manner to that of the 80th amino acid (Figure 1B and 1C). A structure for R27T with the 25th residue glycosylated was obtained from the *in silico* data. This showed that glycosylation of R27T at the 25th amino acid could stabilize the interaction between R27T and IFNAR2. In

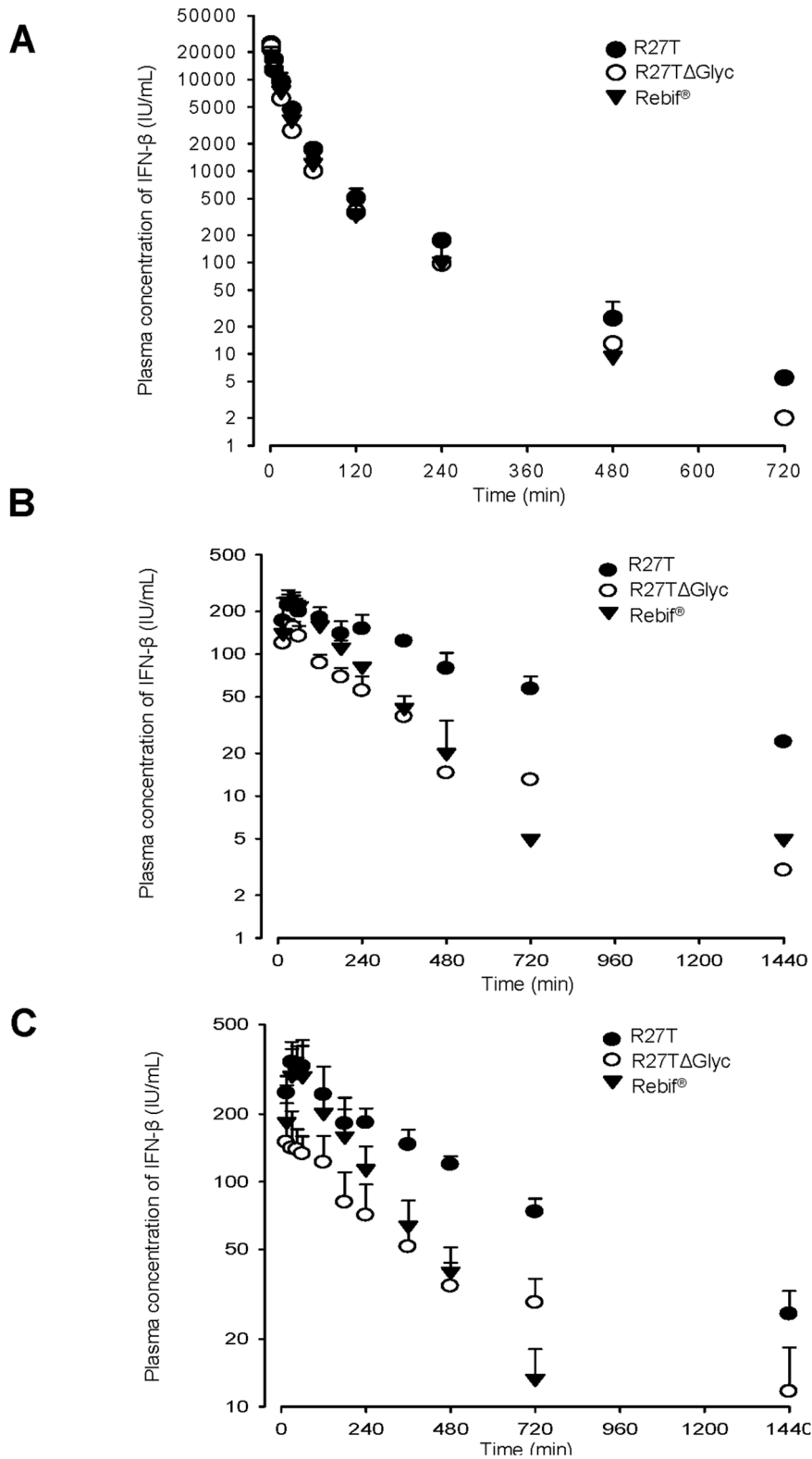


Figure 6. Mean arterial plasma concentration-time profiles for rhIFN- β s. (A) IV, (B) SC and (C) IM administration of R27T, R27T Δ Glyc and Rebif at a dose of 1 MIU/kg in rats. Vertical bars indicated standard deviations. doi:10.1371/journal.pone.0096967.g006

particular, new hydrogen bonds were formed between Thr44 and Asp51 of IFNAR2 and the oligosaccharide moiety of R27T, thereby increasing R27T/IFNAR2 complex stability (Figure 5C).

Similarly, hydrogen bonding between Arg35 of R27T and the oligosaccharide moiety contributed towards the overall stability of the helical conformations within R27T (Figure 5D).

Table 3. Pharmacokinetic parameters for IFN-β after IV, SC, and IM administration of R27T, R27TΔGlyc, and Rebif at a dose of 1 MIU/kg to rats (n = 3).

Parameters	R27T	R27TΔGlyc	Rebif
IV			
AUC ($\times 10^4$ IU·min/mL)	54.8 \pm 7.4*	37.2 \pm 2.1	40.3 \pm 2.4
$t_{1/2}$ (min)	88.0 \pm 4.4	63.3 \pm 11.5	61.3 \pm 21.6
CL (mL/min/kg)	1.9 \pm 0.2*	2.7 \pm 0.1	2.5 \pm 0.2
V_{ss} (mL/kg)	90.1 \pm 8.7	110 \pm 17.1	107 \pm 36.2
SC			
AUC ($\times 10^4$ IU·min/mL)	12.2 \pm 1.5*	4.1 \pm 1.3	5.2 \pm 0.5
$t_{1/2}$ (min)	423 \pm 154	247 \pm 121	180 \pm 69.3
C_{max} (IU/mL)	235 \pm 54.0	161 \pm 14.9	246 \pm 42.0
T_{max} (min)	30 (15–45)	30 (30)	45 (30–45)
F (%)	22.3	11.1	13.0
IM			
AUC ($\times 10^4$ IU·min/mL)	16.3 \pm 2.0*	6.9 \pm 1.3	7.3 \pm 2.1
$t_{1/2}$ (min)	426 \pm 44.7	534 \pm 211	150 \pm 11.8*
C_{max} (IU/mL)	374 \pm 59.7	172 \pm 35.1*	314 \pm 98.4
T_{max} (min)	45 (30–60)	15 (15–120)	45 (30–60)
F (%)	29.7	18.8	18.0

*Significantly different to the other groups ($p < 0.05$).

doi:10.1371/journal.pone.0096967.t003

In vivo Pharmacokinetic Studies in Rats

Plasma concentration-time profiles for the rhIFN-β variants were obtained in rats after IV, SC and IM administration of R27T, R27TΔGlyc and Rebif at a dose of 1 MIU/kg (Figure 6). Relevant pharmacokinetic parameters were listed in Table 3. After IV administration of the three rhIFN-β formulations, bi-exponential declines in plasma IFN concentration were observed. The area under curve (AUC) values for R27T were significantly higher than those of R27TΔGlyc and Rebif by 1.47 and 1.36 fold, respectively. Thus, the total body clearance (CL) values were significantly lower in R27T than in the other rhIFN-β formulations. Moreover, the terminal half-life ($t_{1/2}$) values of R27T tended to be higher than those of the other rhIFN-β formulations by 1.39 and 1.44 fold, respectively. The apparent volume of distribution at steady state (V_{ss}) values were comparable among the three rhIFN-β formulations. After SC administration, the AUC and extent of absolute bioavailability (F) values of R27T were significantly higher than those of R27TΔGlyc by 2.95 and 2.01 fold, respectively, and those of Rebif by 2.33 and 1.72 fold, respectively. Moreover, the $t_{1/2}$ values of R27T tended to be higher than those of R27TΔGlyc and Rebif by 1.71 and 2.35 fold, respectively. The peak plasma concentration (C_{max}) and T_{max} values were comparable among the three rhIFN-β formulations. After IM administration, the AUC and F values of R27T were significantly higher than those of R27TΔGlyc by 2.36 and 1.58 fold, respectively, and those of Rebif by 2.24 and 1.65 fold, respectively. The $t_{1/2}$ values of R27T and R27TΔGlyc were significantly higher than those of Rebif by 2.84 and 3.56 fold, respectively. The C_{max} values of R27TΔGlyc were significantly lower than those of R27T and Rebif, and the T_{max} values were comparable among the three rhIFN-β formulations. The $t_{1/2}$ values after SC and IM administration were much higher than those after IV administration, indicating that each substance is subject to flip-flop kinetics.

Discussion

We have constructed a biobetter version of rhIFN-β 1a, termed R27T, as evidenced the results of structure-function studies of rhIFN-β 1a and the type I IFN-β receptor. R27T contained a substitution of Thr for Arg at position 27th of rhIFN-β 1a, which resulted in additional glycosylation at the 25th position. Glycoengineering was successfully performed, as demonstrated by the bioassay, MS spectrometry and *in vitro* data. Notably, the *in vitro* assays, including measures of antiviral, anti-proliferation and immunomodulation, showed that additional glycosylation at the 25th amino acid (as a result of the R27T mutation) had no effect on ligand-receptor binding. However, these results were different to the results of Runkel et al [35,36]. Using alanine-scanning mutagenesis, they showed that the 27th amino acid, arginine, was a solvent exposed residue important for antiviral and reporter gene activity. Although alanine-scanning mutagenesis is a widely used technique to determine the functional role of each amino acid, mutagenesis of the Arg27, which has a polar residue group, to alanine, which has nonpolar, aliphatic residue group, could cause different effects than mutation into threonine, which has a polar residue group. In addition, glycosylation at the 25th amino acid could cause conformational changes without influencing receptor binding.

Glycosylation could also affect molecular stability. Stability issues, such as aggregation, have been one of the biggest challenges for the production of therapeutic proteins. Moreover, these issues occur at very different stages in the development processes, including drug production, purification, storage and delivery. To address these issues, the behavior of rhIFN-β 1a and R27T in solution was investigated using biophysical methods. Conformational stability (T_m value) of R27T by glycoengineering compared to rhIFN-β 1a was observed by DSC. T_m of R27T was less than that of rhIFN-β 1a. Although glycosylation generally enhance the conformational stability, the position of glycosylation on protein is

Table 4. Comparative rhIFN- β 1a productivity in CHO cells; rhIFN- β productivity in CHO cells was compared.

Culture condition	Temperature (°C)	Additives	Culture period (day)	Max cell density (cells/mL)	Specific Productivity Qp (β-IFN units/cell/day)	Total volumetric production (×10 ⁶ units/ml)	End culture viability (%)	Reference
						(×10 ⁶ units/mL, Non-denatured)	(×10 ⁶ units/mL, denatured)	
Batch (Spinner Flask)	34		6	2.00E+06		10		
Batch (Bioreactor 7.5 L)	34		6	4.00E+06		16		In our study
Batch (Bioreactor 30 L)	34		6	4.00E+06		9		
Batch (Spinner Flask)	37		7	3.00E+06		1	3.7	
Batch, Microcarrier (Cytopore 1 1 mg/ml)	37		7	1.50E+06		5	14	
Batch, Microcarrier (Cytopore 2 1 mg/ml)	37		7	1.50E+06		5	8	Maureen Spearman et al, Biotech. Prog. 2005, 21,31–39
Batch (Bioreactor 2 L)	37		7	3.80E+06		1.5	7.5	
Batch, Microcarrier (Cytopore 1 1 mg/ml)	37		7	3.00E+06		5.8	10	
Batch (Bioreactor 2 L)	37		7	4.20E+06*	0.95	1.3	14	
Batch (Bioreactor 2 L)	37	2% Glycerol	7	3.20E+06*	0.85	6.7	9.6	
Batch (Bioreactor 2 L)	37	1% DMSO	7	2.00E+06*	2	2.5	12.8	J. Rodriguez et al, Biotechnol. Prog. 2005,21,22–30
Batch (Bioreactor 2 L)	37	1 mM NaBu	5	1.30E+06*	3.5	1.5	8.9	
Batch (Spinner Flask)	37		8	3.50E+06		0.5	1.5	
Batch (Spinner Flask)	30		14	7.50E+05		3.3	3.6	>90%
Batch (Spinner Flask)	37 → 30 shift		12	1.80E+06		4.2	9	
Batch (Bioreactor 2 L)	37		7	3.20E+06		0.4	3	Maureen Spearman et al, Cell Technology for Cell Products,2007, 71~85
Batch (Bioreactor 2 L)	37	1 mM NaBu	5	1.50E+06		2	7.5	
Batch (Bioreactor 2 L)	37	40 mM NaCl	7	2.30E+06		2.1	5.5	
Batch, Microcarrier (Cytopore 1 1 mg/mL)	37		7	2.50E+06		2.2	4	
Batch (Spinner Flask)	37		6	3.45E+06		0.96	1.7	
Batch (Spinner Flask)	37 → 30 shift		6	1.80E+06		4.4	5.6	>90%
Batch (Spinner Flask)	30		10	6.90E+05		1.5	2.35	
Batch (Spinner Flask)	37	2% Glycerol	6	2.05E+06		1.7	4.5	

Table 4. Cont.

Culture condition	Temperature (°C)	Additives	Culture period (day)	Max cell density (cells/mL)	Specific Productivity Qp (β-IFN units/cell/day)	Total volumetric production (×10 ⁶ units/ml)	End culture viability (%)	Reference
						(×10 ⁶ units/mL, Non-denatured)	(×10 ⁶ units/mL, denatured)	
Batch (Spinner Flask)**	32		10	1.6E+05		2.2	93%	
Batch (Spinner Flask)**	37 → 32 shift		10	6.9E+05		2.4	98%	
Batch (Spinner Flask)**	37		6	4.1E+06	0.341	4.24		
Batch, Microcarrier (Cytopore 2 1 mg/ml)**	37		6	2.5E+06	0.954	5.19		
Batch (Spinner Flask)**	32		12	1.7E+05	0.784	1.32		Kelvin Sunley et al., Biotechnol. Prog. 2008, 24,898–906
Batch, Microcarrier (Cytopore 2 1 mg/ml)**	32		12	8.2E+05	0.847	3.27		
Batch (Spinner Flask)**	37		10	1.1E+06		5.7	93%	
Batch (Spinner Flask)**	37 → 32 shift		10	2.5E+06		7.1	88%	
Batch (Spinner Flask)**	32		12	2.5E+05	0.233	0.73		
Batch, Microcarrier (Cytopore 2 1 mg/ml)**	32		12	5.0E+06	0.92	10.1		
Batch (Bioreactor 2 L)	37		0–3	1.39E+06	0.75	0.9	1.5	
Batch (Bioreactor 2 L)	32		3–8	2.55E+06	1.2	12.4	17.4	J. Rodriguez et al, Journal of Biotechnology 2010,150,120
Perfusion (Bioreactor 2L)	32		8–16	3.70E+06	2.6	9.3	9.9	>95%

The cultures of R27T were established in a shake flask and 7.5 L (working volume: 5 L), or 30 L (working volume: 20 L) bioreactors. For ELISA, R27T was obtained from bioreactors on day 7, or from shake flasks on day 6 of culture.

Atmosphere: 10% CO₂.

*Final Cell Yield(cells/mL).

**Low Temperature Non-adopted.

***Low Temperature adopted.

doi:10.1371/journal.pone.0096967.t004

known to be a key factor to modulate the stability [37]. Thus, additional glycosylation at Asn25 on R27T seemed to have less effect on conformational stability. However, DLS and ATR-FTIR data suggested that rhIFN- β 1a was more susceptible to biophysical stability, such as aggregation, than R27T. In particular, ATR-FTIR indicated that a significant amount of α -helical structure had been retained, whereas intermolecular β -sheet content (which reflects aggregation) was decreased by the additional glycosylation (at the 25th amino acid). These results were consistent with the DLS data since rhIFN- β 1a was more polydispersed than R27T. Furthermore, these results were also confirmed by the aggregation kinetic profiles, which demonstrated the beneficial effect of additional glycosylation on stability during accelerated storage conditions. This effect could be caused by enhanced biophysical stability of R27T by glycoengineering. In addition, R27T productivity was approximately 3–6 times higher than that of rhIFN- β 1a under low temperature conditions of 30°C–34°C for 6–14 days without additional manipulations like low temperature adapted cells, using cytopore, intermediate temperature shift and perfusion for production (Table 4). It was likely that this was a consequence of the lower aggregation resulting from the additional glycosylation, since it was well known that the low productivity of rhIFN- β 1a was caused by molecular aggregation.

To investigate the effect of glycosylation at the 25th amino acid on stability, a computational simulation of R27T/IFNAR2 docking was performed. Intrinsic stability was improved by glycosylation at the 25th amino acid, which enabled hydrogen bonding between residue 35R on R27T and the oligosaccharide. Structural simulations of R27T/IFNAR2 suggested that the oligosaccharide could also interact with IFNAR2, resulting in the stabilization of ligand-receptor binding interactions. These results imply that glycosylation may be important for fine-tuning glycoprotein bioactivity although X-ray crystallography experiments may be required to obtain a more detailed structure [38].

Glycans play a very prominent role in determining therapeutic efficacy, including the *in vivo* half-life. We therefore compared the pharmacokinetic properties of R27T, R27T Δ Glyc and Rebif. After IV administration, the pharmacokinetic parameters (CL, V_{ss} , and $t_{1/2}$) of Rebif (1 MIU/kg) were consistent with those obtained in a previous study on the pharmacokinetics of native rhIFN- β , administered at a dose of 21 MIU/kg [39]. The AUC and CL values of R27T were significantly higher and lower, respectively, than those of Rebif and R27T Δ Glyc. Although little information on the elimination route of rhIFN- β 1a is currently available, the reduced CL is likely due to the fact that R27T is a hyperglycosylated form of rhIFN- β . The reduced CL may be attributed

to the increased molecular weight and/or sialylation status. It has also been reported that the CL of hyper-glycosylated erythropoietin is significantly lower than that of native erythropoietin [40,41]. In this regard, sialylation status could be a critical pharmacokinetic parameter [42,43]. In fact, the terminal monosaccharide of the N-linked complex glycan of R27T was occupied by a sialic acid moiety, which could affect absorption, serum half-life and clearance as well as various other physicochemical properties. Moreover, after SC and IM administration, the AUC and F values of R27T were significantly higher than those of Rebif and R27T Δ Glyc. This result could be attributed to the lower CL and/or higher stability of R27T compared to that of Rebif. However, the exact reasons for the increased SC and IM absorption, and reduced elimination of R27T were unclear; thus, further investigation is required. Taken together, after IV, SC, and IM dosing in rats, R27T achieved a higher and more prolonged systemic rhIFN- β 1a exposure than Rebif or R27T Δ Glyc. This demonstrates the potential of R27T as a long-acting IFN analog.

Supporting Information

Figure S1 Amino acid sequence of Rebif and R27T.

Shadow on amino acid showed predicted glycopeptides and circles showed potential glycosylation sites of (A) Rebif and (B) R27T. (TIF)

Figure S2 DSC thermograms of rhIFN- β 1a and R27T.

Measured T_m values of (A) rhIFN- β 1a and (B) R27T was displayed above the peaks. Graphs also showed curve fitting of the DSC thermograms for rhIFN- β 1a and R27T, which was performed using a non-two-state model. (TIF)

Table S1 Glycosylation site prediction.

(DOCX)

Materials & Methods S1

(DOCX)

Acknowledgments

We wish to thank Dr. Young Deug Kim at Reference Biolabs Inc. for his excellent technical comment.

Author Contributions

Conceived and designed the experiments: YKS KS. Performed the experiments: KS NAK DHK JL HJL SL SC. Analyzed the data: KS SHJ WSS DDK ISY HHK MKC. Wrote the paper: KS.

References

- Noseworthy JH, Lucchinetti C, Rodriguez M, Weinshenker BG (2000) Multiple sclerosis. *N Engl J Med* 343: 938–952.
- Fitzner D, Simons M (2010) Chronic progressive multiple sclerosis - pathogenesis of neurodegeneration and therapeutic strategies. *Curr Neuropharmacol* 8: 305–315.
- Amedi A, Prisco D, D'Elios MM (2012) Multiple sclerosis: the role of cytokines in pathogenesis and in therapies. *Int J Mol Sci* 13: 13438–13460.
- de Seze J, Borgel F, Brudon F (2012) Patient perceptions of multiple sclerosis and its treatment. *Patient Prefer Adherence* 6: 263–273.
- Castro-Borrero W, Graves D, Frohman TC, Flores AB, Hardeman P, et al. (2012) Current and emerging therapies in multiple sclerosis: a systematic review. *Ther Adv Neurol Disord* 5: 205–220.
- Gasparini C, Ruggieri S (2011) Emerging oral drugs for relapsing-remitting multiple sclerosis. *Expert Opin Emerg Drugs* 16: 697–712.
- Nicholas R, Giannetti P, Alsanousi A, Friede T, Muraro PA (2011) Development of oral immunomodulatory agents in the management of multiple sclerosis. *Drug Des Devel Ther* 5: 255–274.
- Harris JM, Martin NE, Modi M (2001) Pegylation: a novel process for modifying pharmacokinetics. *Clin Pharmacokinet* 40: 539–551.
- Watt GM, Lund J, Levens M, Kolli VS, Jefferis R, et al. (2003) Site-specific glycosylation of an aglycosylated human IgG1-Fc antibody protein generates neoglycoproteins with enhanced function. *Chem Biol* 10: 807–814.
- Katre NV (1993) The Conjugation of Proteins with Polyethylene-Glycol and Other Polymers - Altering Properties of Proteins to Enhance Their Therapeutic Potential. *Advanced Drug Delivery Reviews* 10: 91–114.
- Kieser BC, Calabresi PA (2012) PEGylation of interferon-beta-1a: a promising strategy in multiple sclerosis. *CNS Drugs* 26: 205–214.
- Karpusas M, Whitty A, Runkel L, Hochman P (1998) The structure of human interferon-beta: implications for activity. *Cell Mol Life Sci* 54: 1203–1216.
- Runkel L, Meier W, Pepinsky RB, Karpusas M, Whitty A, et al. (1998) Structural and functional differences between glycosylated and non-glycosylated forms of human interferon-beta (IFN-beta). *Pharm Res* 15: 641–649.
- Derynck R, Remaut E, Saman E, Stanssens P, De Clercq E, et al. (1980) Expression of human fibroblast interferon gene in *Escherichia coli*. *Nature* 287: 193–197.
- Mark DF, Lu SD, Creasey AA, Yamamoto R, Lin LS (1984) Site-specific mutagenesis of the human fibroblast interferon gene. *Proc Natl Acad Sci U S A* 81: 5662–5666.

16. Kagawa Y, Takasaki S, Utsumi J, Hosoi K, Shimizu H, et al. (1988) Comparative study of the asparagine-linked sugar chains of natural human interferon-beta 1 and recombinant human interferon-beta 1 produced by three different mammalian cells. *J Biol Chem* 263: 17508–17515.
17. Sola RJ, Griebenow K (2009) Effects of glycosylation on the stability of protein pharmaceuticals. *J Pharm Sci* 98: 1223–1245.
18. Wang W (2005) Protein aggregation and its inhibition in biopharmaceuticals. *Int J Pharm* 289: 1–30.
19. Rodriguez J, Spearman M, Tharmalingam T, Sunley K, Lodewyck C, et al. (2010) High productivity of human recombinant beta-interferon from a low-temperature perfusion culture. *J Biotechnol* 150: 509–518.
20. Rodriguez J, Spearman M, Huzel N, Butler M (2005) Enhanced production of monomeric interferon-beta by CHO cells through the control of culture conditions. *Biotechnol Prog* 21: 22–30.
21. Karpusas M, Nolte M, Benton CB, Meier W, Lipscomb WN, et al. (1997) The crystal structure of human interferon beta at 2.2-Å resolution. *Proc Natl Acad Sci U S A* 94: 11813–11818.
22. Pettersen EF, Goddard TD, Huang CC, Couch GS, Greenblatt DM, et al. (2004) UCSF Chimera—a visualization system for exploratory research and analysis. *J Comput Chem* 25: 1605–1612.
23. Sanner MF, Olson AJ, Spehner JC (1996) Reduced surface: an efficient way to compute molecular surfaces. *Biopolymers* 38: 305–320.
24. Kirschner KN, Woods RJ (2001) Quantum mechanical study of the nonbonded forces in water-methanol complexes. *J Phys Chem A* 105: 4150–4155.
25. Basma M, Sundara S, Calgan D, Vernali T, Woods RJ (2001) Solvated ensemble averaging in the calculation of partial atomic charges. *J Comput Chem* 22: 1125–1137.
26. Kirschner KN, Woods RJ (2001) Solvent interactions determine carbohydrate conformation. *Proc Natl Acad Sci U S A* 98: 10541–10545.
27. Quadt-Akabayov SR, Chill JH, Levy R, Kessler N, Anglister J (2006) Determination of the human type I interferon receptor binding site on human interferon-alpha2 by cross saturation and an NMR-based model of the complex. *Protein Sci* 15: 2656–2668.
28. Hornak V, Abel R, Okur A, Strockbine B, Roitberg A, et al. (2006) Comparison of multiple Amber force fields and development of improved protein backbone parameters. *Proteins* 65: 712–725.
29. Yoon I, Han S, Choi YH, Kang HE, Cho HJ, et al. (2012) Saturable sinusoidal uptake is rate-determining process in hepatic elimination of docetaxel in rats. *Xenobiotica* 42: 1110–1119.
30. Kim JE, Cho HJ, Kim JS, Shim CK, Chung SJ, et al. (2013) The limited intestinal absorption via paracellular pathway is responsible for the low oral bioavailability of doxorubicin. *Xenobiotica* 43: 579–591.
31. Yang CH, Wu PC, Huang YB, Tsai YH (2004) A new approach for determining the stability of recombinant human epidermal growth factor by thermal Fourier transform infrared (FTIR) microspectroscopy. *J Biomol Struct Dyn* 22: 101–110.
32. Dong A, Prestrelski SJ, Allison SD, Carpenter JF (1995) Infrared spectroscopic studies of lyophilization- and temperature-induced protein aggregation. *J Pharm Sci* 84: 415–424.
33. Fan H, Ralston J, Dibiase M, Faulkner E, Middaugh CR (2005) Solution behavior of IFN-beta-1a: an empirical phase diagram based approach. *J Pharm Sci* 94: 1893–1911.
34. Hubbard SJT (1993) NACCESS. Computer Program, Department of Biochemistry and Molecular Biology, University College London.
35. Runkel L, Pfeiffer L, Lewerenz M, Monneron D, Yang CH, et al. (1998) Differences in activity between alpha and beta type I interferons explored by mutational analysis. *J Biol Chem* 273: 8003–8008.
36. Runkel L, deDios C, Karpusas M, Betzenhauser M, Muldowney C, et al. (2000) Systematic mutational mapping of sites on human interferon-beta-1a that are important for receptor binding and functional activity. *Biochemistry* 39: 2538–2551.
37. Shental-Bechor D, Levy Y (2008) Effect of glycosylation on protein folding: a close look at thermodynamic stabilization. *Proc Natl Acad Sci U S A* 105: 8256–8261.
38. Knight P (1989) *The Carbohydrate Frontier. Bio-Technology* 7: 35–&.
39. Pepinsky RB, LePage DJ, Gill A, Chakraborty A, Vaidyanathan S, et al. (2001) Improved pharmacokinetic properties of a polyethylene glycol-modified form of interferon-beta-1a with preserved in vitro bioactivity. *J Pharmacol Exp Ther* 297: 1059–1066.
40. Wanic-Kossowska M, Tykarski A, Kobelski M, Czekalski S (2006) [Effectiveness of darbepoietin alfa in anemic patients with chronic kidney disease (CKD) in predialysis period]. *Pol Arch Med Wewn* 116: 663–670.
41. Fang YW, Chang CH (2009) Subcutaneous administration of darbepoietin alfa effectively maintains hemoglobin concentrations at extended dose intervals in peritoneal dialysis patients. *Perit Dial Int* 29: 199–203.
42. Walsh G, Jeffers R (2006) Post-translational modifications in the context of therapeutic proteins. *Nat Biotechnol* 24: 1241–1252.
43. Delorme E, Lorenzini T, Giffin J, Martin F, Jacobsen F, et al. (1992) Role of glycosylation on the secretion and biological activity of erythropoietin. *Biochemistry* 31: 9871–9876.



Pharmaceutical Nanotechnology

Emulsion-based colloidal nanosystems for oral delivery of doxorubicin: Improved intestinal paracellular absorption and alleviated cardiotoxicity



Ji-Eon Kim^{a,1}, In-Soo Yoon^{b,1}, Hyun-Jong Cho^c, Dong-Hwan Kim^a,
Young-Hee Choi^d, Dae-Duk Kim^{a,*}

^a College of Pharmacy and Research Institute of Pharmaceutical Sciences, Seoul National University, Seoul 151-742, Republic of Korea

^b College of Pharmacy and Natural Medicine Research Institute, Mokpo National University, Jeonnam 534-729, Republic of Korea

^c College of Pharmacy, Kangwon National University, Chuncheon 200-701, Republic of Korea

^d College of Pharmacy, Dongguk University-Seoul, Gyeonggi 410-820, Republic of Korea

ARTICLE INFO

Article history:

Received 21 October 2013

Received in revised form 4 January 2014

Accepted 12 January 2014

Available online 21 January 2014

Keywords:

Colloidal nanosystem

Medium chain glyceride

Doxorubicin

Intestinal paracellular absorption

Cardiotoxicity

Oral delivery

ABSTRACT

We have previously reported that the limited intestinal absorption *via* the paracellular pathway may be the primary cause of the low oral bioavailability of doxorubicin (DOX). In this study, we have formulated medium chain glycerides-based colloidal nanosystems to enhance the intestinal paracellular absorption of DOX and reduce its cardiotoxicity. The DOX formulations prepared by the construction of pseudo-ternary phase diagram were characterized in terms of their droplet size distribution, viscosity, drug loading, and drug release. Further evaluation was conducted by an *in vitro* Caco-2 transport study as well as *in situ/in vivo* intestinal absorption, bioavailability and toxicity studies. Compared with DOX solution, these formulations enhanced the absorptive transport of DOX across Caco-2 cell monolayers at least partly due to the paracellular-enhancing effects of their lipidic components. Moreover, the *in situ* intestinal absorption and *in vivo* oral bioavailability of DOX in rats were markedly enhanced. In addition, no discernible damage was observed in the rat jejunum after oral administration of these DOX formulations while the cardiac toxicity was significantly reduced when compared with intravenous DOX solution. Taken together, the medium chain glycerides-based colloidal nanosystems prepared in this study represent a potentially effective oral delivery system for DOX.

© 2014 Elsevier B.V. All rights reserved.

1. Introduction

Doxorubicin (DOX) is an anthracycline glycoside antibiotic with a mechanism of impairing DNA synthesis during tumor cell division (Schwarzbach et al., 2002). It is one of the most widely used anticancer drugs for the treatment of lymphoma, osteosarcoma and other sarcomas, carcinomas, and melanoma (Choi et al., 2011). The most common dosing mode of DOX is a single intravenous injection but this may lead to an undesired systemic exposure profile with an excessively high (toxic) level in the initial and subsequent fast decay below the minimum therapeutic level (Bromberg and Alakhov, 2003). It has been generally believed that

long-term exposure to drug at modest concentrations would be more beneficial than a pulsed supply of drug at higher concentrations (Kalaria et al., 2009). Thus, much effort has been devoted for achieving prolonged systemic exposure to DOX, and the most successful case has been DOXIL[®], a pegylated liposomal DOX.

However, oral chemotherapy would be more advantageous over the current regimens *via* the intravenous route (DeMario and Ratain, 1998; Le Lay et al., 2007). Oral delivery could provide a relatively prolonged systemic exposure profile with less fluctuation leading to lower toxicity and improved efficacy (Zhang and Feng, 2006). Moreover, the oral mode of cancer treatment is non-invasive, cost (time and labor)-saving, and available for outpatient, resulting in a better patient compliance and improved quality of life, particularly for the elderly and for patients with advanced or relapsed cancer (Bromberg, 2008; Dong and Feng, 2005). Thus, oral chemotherapy may be a potential alternative to the current DOX regimen.

Despite many recent studies on the oral delivery of DOX (Benival and Devarajan, 2012; Choi et al., 2011; Jain et al., 2012; Kalaria et al., 2009; Ke et al., 2008), its development still remains challenging due

Abbreviations: DOX, doxorubicin; AUC, total area under the plasma concentration–time curve from time zero to time infinity; C_{max} , peak plasma concentration; T_{max} , time to reach a C_{max} ; F_{rel} , extent of relative oral bioavailability.

* Corresponding author. Tel.: +82 2 880 7870; fax: +82 2 873 9177.

E-mail address: ddkim@snu.ac.kr (D.-D. Kim).

¹ These authors have equally contributed to this work.

to the limited intestinal absorption and low oral bioavailability. In these previous studies, it has been often assumed that the P-gp-mediated efflux and cytochrome P450 (CYP) 3A-mediated first-pass metabolism in the intestine and liver are the main barriers to the oral absorption of DOX. However, our recent work has revealed that the limited and paracellular intestinal absorption of DOX (corresponding to BCS class III) probably due to its physicochemical properties (aqueous solubility = 50 mM; $\log P = -0.5$; apparent Caco-2 permeability = 0.102×10^{-6} cm/s) may be the major factor that is responsible for the low oral bioavailability in contrary to what had been earlier reported (Kim et al., 2013). Therefore, this necessitates a new formulation strategy for developing an effective oral delivery system of DOX, *i.e.*, enhancing the intestinal absorption of paracellularly transported BCS class III drugs.

Over the past decades, lipid-based colloidal systems including microemulsion have been used mainly for the oral delivery of poorly water-soluble drugs (BCS classes II and IV) (Kawakami et al., 2002a,b; Yin et al., 2009). However, recent studies tend to focus on microemulsion as a drug delivery system for enhancing the oral absorption of BCS class III drugs which include fexofenadine, famotidine, calcein, hydroxysafflor yellow A, and earthworm fibrinolytic enzyme (Cheng et al., 2008; Gundogdu et al., 2011; Jha et al., 2011; Koga et al., 2010; Qi et al., 2011). Microemulsions may enhance the oral absorption of paracellularly transported BCS class III drugs because they contain oils and surfactants, some of which have been well recognized as paracellular permeation enhancers. Microemulsion could thus be applied in developing oral delivery systems for DOX.

Herein, we report on medium chain glycerides-based colloidal nanosystem, based on water-in-oil (W/O) microemulsion, for the oral delivery of DOX, with the expectation to enhance the intestinal permeation of DOX *via* the paracellular pathway. To date, very few attempts have been made to develop an emulsion-based colloidal nanosystem for the oral delivery of paracellularly transported BCS class III drugs including DOX. Therefore, this study could provide new findings regarding the application of microemulsion in these oral drug delivery systems.

2. Materials and methods

2.1. Materials

A human colonic epithelial cell line, Caco-2 cells, was obtained from the American Type Culture Collection (Rockville, MD). DOX (hydrochloride salt) was purchased from Boryung Pharmaceutical Co. (Gunpo, South Korea). [14 C] Mannitol (51 mCi/mmol) was purchased from Amersham Pharmacia Biotech (Buckinghamshire, UK). Dulbecco's modified Eagle's medium (DMEM), fetal bovine serum, penicillin-streptomycin, and trypsin-EDTA were purchased from Gibco Laboratories (Grand Island, NY, USA). Captex and Capmul MCM were kindly donated by Abitec Co. (Columbus, OH, USA). PEG-8 caprylic/capric glycerides (labrasol) were kindly donated by Gattefossé Co. (Saint Priest, Cedex, France). Propranolol hydrochloride (an internal standard for the high-performance liquid chromatographic (HPLC) analysis of DOX), non-essential amino acid solution, Hank's balanced salt solution (HBSS), N-2-hydroxyethylpiperazine-N'-2-ethanesulfonic acid (HEPES), D-glucose, and DMSO were purchased from Sigma-Aldrich Co. (St. Louis, MO). Other chemicals were of reagent grade or HPLC grade.

2.2. Construction of pseudo-ternary phase diagrams

The pseudo-ternary phase diagram was constructed to determine the components and contents for the formation of W/O

microemulsions (Constantinides et al., 1996). The surfactant mixtures (S_{mix}) were prepared by blending Span 80 and Tween 80 (F1) or Capmul MCM and labrasol (F2) in a fixed weight ratio of 2:1. Then, the oil phase (Captex 355) and S_{mix} were mixed, where the ratios of oil to S_{mix} were varied from 9:1 to 1:9 (w/w). Each clear mixture was titrated with distilled water (DW), while stirring the mixture at room temperature to allow equilibrium. Following the addition of aliquot of water phase, the mixture was visually examined for transparency. The points from clear to turbid and turbid to clear were designated as emulsion and microemulsion, respectively. Based on the results of the pseudo ternary phase diagrams, two microemulsion formulations (F1 and F2) were selected for further experiments: 50% Captex 355, 40% Span 80/Tween 80 mixture, and 10% aqueous phase for F1; 55% Captex 355, 35% Capmul MCM/labrasol mixture, and 10% aqueous phase for F2.

2.3. Determination of maximum loading content and preparation of DOX formulations

In order to determine the maximum loading content of DOX in microemulsion formulations, excess amount of DOX was first dissolved into water followed by mixing in a shaking incubator (Jeio-Tech, Seoul, Korea) at 100 rpm for 48 h at 25 °C. Then, excess DOX was removed by centrifugation at $16,000 \times g$ for 5 min at 25 °C. The supernatant (saturated DOX aqueous solution) was taken as an aqueous phase to prepare the microemulsions following the above mentioned compositions. They were further mixed in a shaking incubator at 100 rpm for 48 h at 25 °C. Excess DOX, if any, was removed by centrifugation at $16,000 \times g$ for 5 min at 25 °C. The content of DOX in the formulation was measured by HPLC assay after an appropriate dilution with methanol. Based on these results of the maximum loading content of DOX in microemulsions, 20 mg/mL of DOX aqueous solution was used to prepare F1 and F2 formulations containing 2 mg/mL of DOX for further studies.

2.4. Characterization of DOX formulations

2.4.1. Mean droplet size and distribution

The droplet size and distribution of DOX formulations (F1 and F2) were measured by an electrophoretic light-scattering spectrophotometer (ELS-8000, OTSUKA Electronics Co. Ltd., Japan). The DOX formulations were transferred to a standard quartz cuvette, and their droplet size and polydispersity index were determined *via* dynamic He-Ne laser (10 mW) light-scattering at an angle of 90° at 25 °C. Data analysis was conducted using a software package (ELS-8000 software) supplied by the manufacturer.

2.4.2. Viscosity

The viscosity of F1 and F2 was measured by DV-E Viscometer (BROOKFIELD, USA) using a #16 spindle at a speed of 100 rpm at room temperature.

2.4.3. Transmission electron microscopy

The morphology of F1 and F2 was examined by an energy-filtering transmission electron microscopy (TEM) (LIBRA120, Carl Zeiss, Germany) with a 80 kV accelerating voltage. The DOX formulations were negatively stained by 2% sodium phosphotungstate (pH 7) and placed on carbon-coated 400 mesh copper grids followed by drying at room temperature before measurements.

2.4.4. Changes of DOX formulations after dilution

To evaluate the changes in the droplet size of DOX formulations after dilution, each formulation (F1 and F2) containing 2 mg/mL DOX was 10-fold diluted with normal saline at 37 °C, and then, the droplet size of the diluted formulations was measured as mentioned above. To evaluate the changes in the formulations' colloidal

structure after dilution, the leakage of DOX from each formulation (F1 and F2) after 500-fold dilution with normal saline at 37 °C was measured (Cheng et al., 2008; Koga et al., 2010). After centrifugation at 16,000 × g for 10 min at 25 °C, aliquots from the upper coarse emulsion and lower aqueous phase were collected. The content of DOX in the samples was measured by HPLC assay after an appropriate dilution with methanol.

2.5. *In vitro* drug release study

An aliquot of each DOX solution in DW, F1 and F2 (200 µL) was placed in the mini dialysis kits (MWCO 6–8 kDa) (Kfar-Hanagid, Israel), and was immersed in 100 mL of release medium (PBS, pH 7.4) in a shaking incubator at 100 rpm at 37 °C. Then, aliquots of dissolution media (0.5 mL) were withdrawn, and the concentration of DOX was determined by HPLC analysis after an appropriate dilution with methanol. The percent cumulative amount of DOX released from formulations was calculated as a function of time.

2.6. *Caco-2* cell culture

Caco-2 cells were routinely cultured in DMEM containing 10% FBS, 1% non-essential amino acids, 100 U/mL penicillin, and 0.1 mg/mL streptomycin at 37 °C in an atmosphere of 5% CO₂ and 90% relative humidity. For the transport studies, *Caco-2* cells from passage numbers 40 to 55 were seeded on permeable polycarbonate filter inserts (1.12-cm² surface area, 0.4-µm pore size; Corning Costar Corp., Cambridge, MA) in 12-Transwell plates at a density of 1–1.5 × 10⁵ cells/insert and were cultured for 21 days. The integrity of cell monolayers was evaluated prior to the transport studies by measuring transepithelial electrical resistance (TEER) and [¹⁴C] mannitol permeability across the monolayers. Cell monolayers were considered intact and suitable for use in transport studies when TEER values were 300–600 Ω cm² (Saitoh et al., 2004). Mannitol transport in the *Caco-2* cell monolayers was <0.35% of the dose/h.

2.7. *In vitro* cytotoxicity test in *Caco-2* cells

Cytotoxicity of DOX solution, F1 and F2 on *Caco-2* cells were evaluated by MTT (3-(4,5-dimethylthiazole-2-yl)-2,5-diphenyl tetrazolium bromide) assay. *Caco-2* cells were seeded onto 96-well plates at a seeding density of 1 × 10⁴ cells/well and used for cytotoxicity test after 24-h incubation. MTT assay was performed using a commercially available MTT assay kit (TOX-1, Sigma-Aldrich, St. Louis, MO). The culture medium was replaced with 200 µL of DOX solution in PBS (20 µg/mL) and DOX formulations 500-fold diluted with PBS (final concentration: 4 µg/mL). Blank PBS (pH 7.4) was employed as a negative control. After 2-h incubation, 20 µL of MTT assay reagent in PBS was added to each well and the plate was incubated for another 4 h. The absorbance of the mixture in the 96-well plate was then measured with an Emax[®] microplate spectrophotometer at 560 nm (Molecular Devices, Sunnyvale, CA, USA). The percent viability of the cells was determined from the absorbance values considering that of the negative control as 100%.

2.8. *In vitro* transport study in *Caco-2* cell monolayers

The absorptive transport of DOX solution in transport medium (20 µg/mL) and DOX formulations 500-fold diluted with transport medium (final concentration: 4 µg/mL) in *Caco-2* cell monolayer was evaluated. The transport experiments were conducted in Transwell plates that were placed on an orbital shaker; the plates were shaken at 60 rpm during the transport experiments to minimize the influence of the aqueous boundary layer on transport. Prior to transport experiments, cell monolayers were washed three times

with transport medium (pH 7.4, HBSS containing 25 mM HEPES and 25 mM glucose). After each wash, the plates were incubated in the transport medium for 30 min at 37 °C, and then TEER was measured. For the measurement of absorptive (*i.e.*, apical to basolateral) drug transport, 0.5 mL of DOX solution in transport medium (20 µg/mL) or DOX formulations 500-fold diluted with transport medium containing 1% DMSO (final concentration: 4 µg/mL) was added to the apical side of the cell monolayer, and 1.5 mL of transport medium containing 1% DMSO was added to the basolateral side. The inserts were moved to wells containing fresh transport medium containing 1% DMSO (1.5 mL) every 30 min for 2 h. At each time point, a 0.2-mL aliquot of the transport medium was removed from the basolateral side, and the concentrations of DOX in each sample were determined by HPLC assay. TEER values were measured at 0, 1, 2, 4, 6, 8, and 24 h after the start of transport experiments. The apparent permeability coefficient (P_{app} ; cm/s) was calculated by dividing the unidirectional fluxes by the initial drug concentration:

$$P_{app} = \frac{dQ/dt}{A \cdot C_0}$$

where the dQ/dt , A , and C_0 are the rate of appearance of drug in the basolateral side, surface area of cell monolayer (1.12 cm²), and initial drug concentration in the apical side, respectively.

2.9. Animals

Protocols for the animal studies were approved by the Institutional Animal Care and Use Committee of Seoul National University (Seoul, South Korea). Male ICR mice (5–6 weeks old and weighing 20–25 g) and Sprague-Dawley rats (7–9 weeks old and weighing 200–250 g) were purchased from Orient Bio, Inc. (Seongnam, South Korea). They were maintained in a clean-room (Animal Center for Pharmaceutical Research, College of Pharmacy, Seoul National University) at a temperature of 20–23 °C with 12-h light (07:00–19:00) and dark (19:00–07:00) cycles, and a relative humidity of 50 ± 5%. The mice and rats were housed in metabolic cages (Tecniplast, Varese, Italy) under filtered, pathogen-free air, with food (Agribrands Purina Korea, Pyeongtaek, South Korea) and water available *ad libitum*.

2.10. *In situ* closed loop study in rats

The absorption of DOX solution in 0.9% NaCl-injectable solution, F1 and F2 in various rat intestinal segments were evaluated by *in situ* closed loop study (Kim et al., 2013). After minimal abdominal incision under light ether anesthetization and sufficient washing of the contents within the gastrointestinal (GI) tract, a 5-cm long jejunum and colon loops were closed by ligation made at approximately 2-cm distal to both ends of each intestinal section. Special care was exercised to avoid damaging blood vessels and to include as much of a complete mesenteric blood vessel arch as possible for each loop. After injection of 0.5-mL DOX solution, F1 and F2 (2 mg/mL) into each loop by means of an 1-mL syringe with a 31-gauge needle, the whole GI tract was carefully replaced into the abdominal cavity, and the incision was closed using clamps and kept moist by covering with gauze pads presoaked with normal saline. The rat was warmed by a lamp. At 120 min after drug injection, each loop was removed, transferred into a beaker containing 50 mL of methanol, and the gastrointestinal tract was cut into small pieces using scissors to facilitate the extraction of DOX. After manual shaking and stirring with a glass rod for 1 min, a 50-µL aliquot of the supernatant was collected from each beaker and stored in a –80 °C freezer until the HPLC analysis of DOX.

2.11. *In vivo* pharmacokinetic study in rats

The femoral artery was cannulated with a polyethylene tube (PE-50; Clay Adams, Parsippany, NJ, USA) under light ketamine anesthetization (50 mg/kg, intramuscular injection) as reported previously (Yoon et al., 2011, 2012). DOX solution in 0.9% NaCl-injectable solution and DOX formulations (F1 and F2) at a dose of 10 mg/kg was orally administered (dosing volume: 5 mL/kg) to rats using a feeding tube after overnight fasting with free access to water. An approximately 300- μ L aliquot of blood sample was collected via the femoral artery at 0, 15, 30, 45, 60, 75, 90, 120, 180, and 240 min after oral administration of DOX solution and formulations. An approximately 300- μ L aliquot of heparinized 0.9% NaCl-injectable solution (20 U/mL) was used to flush the cannula immediately after each blood sampling to prevent blood clotting. After centrifugation of blood sample, a 150- μ L aliquot of plasma sample was stored in a -80° C freezer (Model DF8517; Ilshin Laboratory Company, Seoul, South Korea) until the HPLC analysis of DOX.

2.12. *In vivo* toxicity test in mice and rats

To evaluate the intestinal toxicity of DOX formulations, the jejunum (approximately 5 cm) was carved out at 24 h after oral administration of DW, F1 or F2 to rats. The segment was then washed with PBS and fixed in 4% paraformaldehyde for 24 h. A vertical section was prepared, stained with hematoxylin–eosin (H&E), and observed under light microscopy ($\times 200$).

To evaluate the cardiac toxicity of DOX formulations, saline and DOX solution in 0.9% NaCl-injectable solution (5 mg/kg) were administered intravenously, and DOX formulations (F1 and F2, 10 mg/kg) were administered orally to mice and rats on day 1 and on day 15. The animals were sacrificed on day 28, and cardiac toxicity was evaluated by the activity of superoxide dismutase (SOD) in rat heart homogenate. SOD activity was determined using assay kits (Sigma–Aldrich Co., St. Louis, MO). The heart of mice was carved out and processed for H&E staining in the same manner as the rat intestinal toxicity study.

2.13. HPLC analysis of DOX

The concentrations of DOX in the samples of the *in vitro*, *in situ* and *in vivo* experiments were determined by a reported HPLC method (Kim et al., 2013). A 150- μ L aliquot of plasma sample (a 100- μ L aliquot of the other samples) was deproteinized with a 300- μ L aliquot of acetonitrile, and a 100- μ L aliquot of methanol that contained 5 μ g/mL of propranolol (an internal standard) was added. After vortex-mixing and centrifugation at $16,000 \times g$ for 10 min, a 400- μ L aliquot of the supernatant was transferred to another clean eppendorf tube, and then evaporated under a gentle stream of nitrogen gas at room temperature. The residue was reconstituted in 60- μ L mobile phase for plasma sample (100- μ L mobile phase for the other samples). After vortex mixing and centrifugation, a 25- μ L aliquot was injected onto a reversed phase (C18) HPLC column. The mobile phases, 10 mM KH_2PO_4 (pH 4.0):acetonitrile:methanol (70:25:5, v/v/v) with 0.1% TEA (v/v) for *in vivo* studies, and 10 mM KH_2PO_4 (pH 4.0):acetonitrile (70:30, v/v) for *in vitro* and *in situ* studies, were run at a flow-rate of 1 mL/min. The column effluent was monitored by a fluorescence detector set at excitation/emission wavelengths of 470 nm/575 nm for DOX and 230 nm/320 nm for propranolol. The retention times of DOX and propranolol were approximately 3.5 and 6 min, respectively. The quantitation limits of DOX in rat plasma, urine and GI sample were 0.01, 0.1, and 0.1 μ g/mL, respectively. The inter- and intra-day coefficients of variation were below 12.1%.

Table 1

Physicochemical properties of DOX formulations ($n = 3$).

Physicochemical property	F1	F2
Droplet size (nm)	164 \pm 30.5	142 \pm 38.5
Polydispersity index	0.184 \pm 0.0340	0.170 \pm 0.0462
Viscosity (cP)	99.3 \pm 12.2	84.3 \pm 8.08
Maximum drug loading (mg/mL)	3.02 \pm 0.129	2.92 \pm 0.378
Leakage after 500-fold dilution (%)	8.63 \pm 1.03	9.21 \pm 1.20

2.14. Pharmacokinetic analysis

The total area under the plasma concentration–time curve from time zero to time infinity (AUC) was calculated using standard software (WinNonlin®; Pharsight Corporation, Mountain View, CA, USA). The peak plasma concentration (C_{max}) and time to reach C_{max} (T_{max}) were directly read from the experimental data. The extent of relative oral bioavailability (F_{rel}) was calculated by dividing the AUC after oral administration of DOX formulations (F1 and F2) by the AUC after oral administration of DOX solution.

2.15. Statistical analysis

A p -value of less than 0.05 was considered to be statistically significant using a t -test between the two means for the unpaired data or a Duncan's multiple range test of Statistical Package for the Social Sciences (SPSS) *posteriori* analysis of variance (ANOVA) among the more than three means for the unpaired data. All data were expressed as mean \pm standard deviation (SD) except median (ranges) for T_{max} .

3. Results

3.1. Preparation of DOX formulations

Fig. 1 shows the pseudo-ternary phase diagrams of systems containing water, Captex 355, and surfactant mixture (S_{mix}). The S_{mix} was the blend of a low HLB (Span 80, Fig. 1a, HLB = 4.3; Capmul MCM, Fig. 1b, HLB = 5) and high HLB (Tween 80, Fig. 1a, HLB = 15; labrasol, Fig. 1b, HLB = 14) non-ionic surfactant at a fixed ratio of 2:1 w/w. A clear and transparent microemulsion existed in the W/O area. Based on the principle of high drug-loading efficiency and low proportion of surfactants, the DOX formulations were selected from this area, and composed of 50% Captex 355, 40% Span 80/Tween 80 mixture, and 10% aqueous phase for F1 and 55% Captex 355, 35% Capmul MCM/labrasol mixture, and 10% aqueous phase for F2.

3.2. Characterization of DOX formulations

Table 1 summarizes the droplet size, polydispersity, viscosity, and maximal drug loading of the DOX formulations (F1 and F2). Both F1 and F2 had droplet sizes of less than 200 nm and viscosities ranging from 75 to 110 cP. The TEM images of DOX formulations are shown in Fig. 2. A number of spherical droplets were observed, and their sizes seemed to be approximately 100–200 nm. The DOX formulations were changed to the coarse (turbid) emulsion with 10-fold and 500-fold dilution with PBS. After a 10-fold dilution, the mean droplet sizes of F1 and F2 increased by 8.96- and 8.66-fold (1470 ± 336 nm for F1 and 1230 ± 251 nm for F2), respectively. After a 500-fold dilution and subsequent centrifugation, only minor portion (less than 10%) of the loaded DOX was detected in the lower aqueous phase (% leakage), and most of the DOX was still detected in the upper coarse emulsion (Table 1). However, as shown in Table 1, no significant differences between F1 and

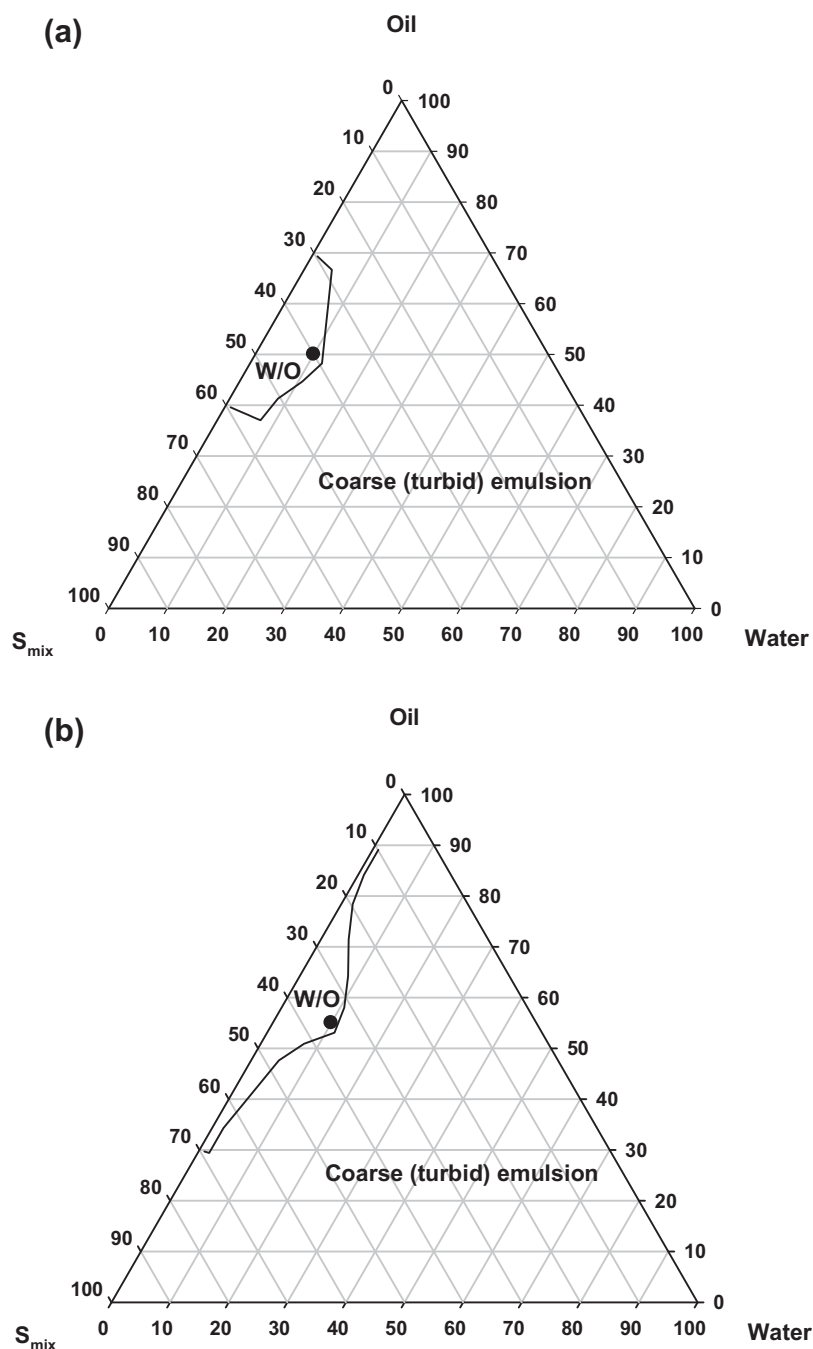


Fig. 1. Pseudo-ternary phase diagrams of systems containing water, Captex 355 (oil), and surfactant mixture (S_{mix}). The S_{mix} was the blend of Span 80 and Tween 80 (a) or Capmul MCM and labrasol (b) at 2:1 w/w. Clear and transparent microemulsions were formed in the W/O area, and other area represents coarse (turbid) emulsion. The closed circles (●) represent the DOX formulations (a, F1 and b, F2).

F2 were observed in terms of the droplet size, polydispersity, viscosity, maximal drug loading, and characteristics after dilution.

3.3. *In vitro* drug release study

The time profiles of *in vitro* release of DOX from solution, F1 and F2 are shown in Fig. 3. The release of DOX from the solution reached the plateau at 4 h, and up to 69.6% cumulative release of DOX was observed within 12 h. However, the cumulative release of DOX from F1 and F2 was significantly lower than that from the DOX solution at all the time points studied. The cumulative release of DOX from F1 was not significantly different from that from F2.

3.4. *In vitro* transport study in Caco-2 cell monolayers

The viability of Caco-2 cells after 2-h exposure to the DOX solution, F1 and F2 is shown in Fig. 4a. The Caco-2 cell viability against DOX solution (20 $\mu\text{g}/\text{mL}$) was not significantly different from that against the control (PBS). Moreover, no significant reduction in cell viability was observed in the presence of F1 and F2. The time profiles of *in vitro* absorptive transport of DOX from the solution, F1 and F2 across Caco-2 cell monolayers are shown in Fig. 4b. The apparent permeability coefficients ($P_{app} \times 10^{-6} \text{ cm/s}$) of DOX from the solution, F1, and F2 were 0.159 ± 0.0229 , 0.968 ± 0.183 , and 1.71 ± 0.443 , respectively. The P_{app} values of DOX from F1 and F2 were significantly higher than those from the solution, and the P_{app}

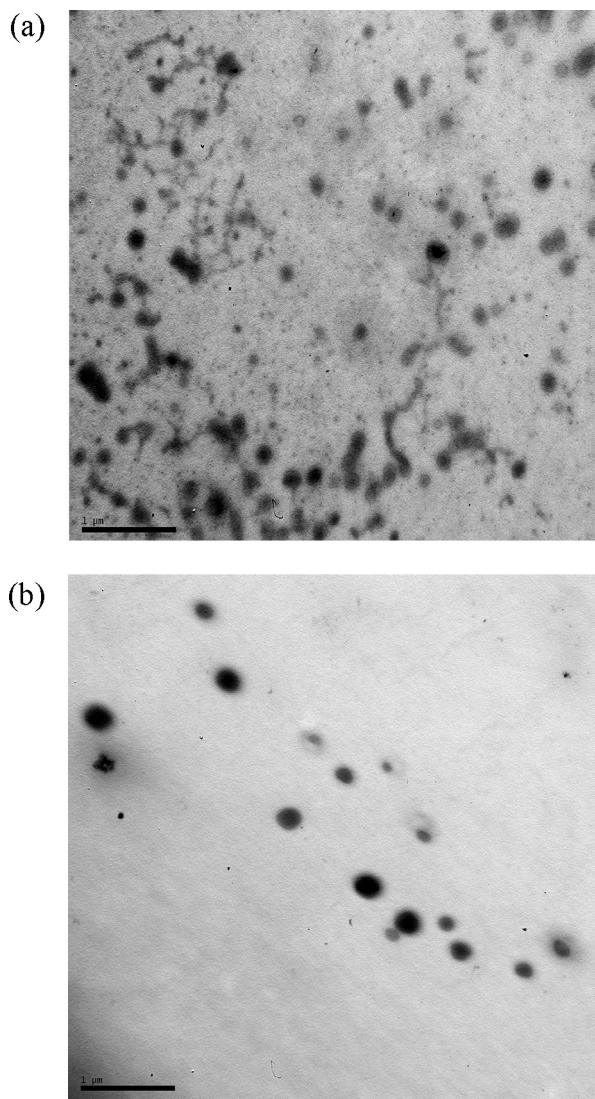


Fig. 2. TEM images of DOX formulations (a, F1 and b, F2). The scale bars represent 1 μm .

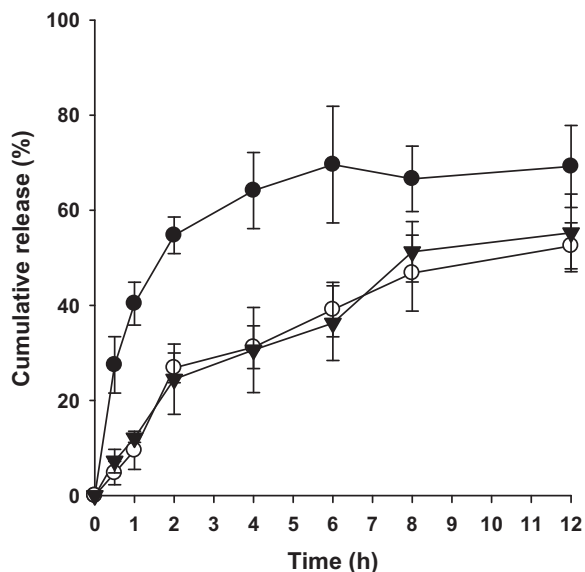


Fig. 3. Time profiles of *in vitro* release of DOX from solution (●), F1 (○), and F2 (▼) at 37 °C in PBS. Vertical bars represent standard deviation ($n=3$).

Table 2

Remaining fractions of DOX at 2 h after injection of the DOX solution, F1 and F2 into the rat jejunum and colon loops ($n=3-4$).

Intestinal segment	DOX remaining (%)		
	Solution	F1	F2
Jejunum	87.6 \pm 19.8 ^a	64.4 \pm 9.52 ^a	40.5 \pm 10.4 ^a
Colon	90.8 \pm 12.8 ^a	57.8 \pm 8.39	46.7 \pm 11.0

^a Significantly different from the other groups ($p < 0.05$).

values of DOX from F2 were significantly higher than those from F1. The time profiles of relative TEER values with respect to the initial TEER value during the 2-h transport study of the DOX solution, F1 and F2 across Caco-2 cell monolayers and subsequent incubation in fresh media up to 24 h are shown in Fig. 4c. There was no significant change in TEER values throughout the transport study of the DOX solution. However, TEER values were reduced to 70.7 and 62.6% of their initial values in the presence of F1 and F2, respectively. After wash-out of the formulations and change to fresh media, the TEER values of Caco-2 cell monolayers increased constantly and reached control level at 24 h.

3.5. *In situ* closed loop study in rats

The remaining fractions of DOX at 2 h after the injection of the DOX solution, F1 and F2 into the rat jejunum and colon loops are listed in Table 2. In both the jejunal and colonic loops, the remaining fractions of DOX after injection of the F1 and F2 were significantly lower than that of the solution, indicating the enhanced intestinal absorption of DOX in F1 and F2 compared with the DOX solution. Moreover, in the jejunal loops, the remaining fractions of DOX after injection of F2 were significantly lower than those of F1, indicating the enhanced intestinal absorption of DOX in F2 compared with F1.

3.6. *In vivo* pharmacokinetic study in rats

Fig. 5 shows the time profiles of arterial plasma concentrations of DOX after oral administration of the DOX solution, F1 and F2 at a dose of 10 mg/kg to rats. Relevant pharmacokinetic parameters of DOX are listed in Table 3. The AUC, C_{max} and F_{rel} values of the DOX solution, F1 and F2 were significantly different from each other, in the following order: F2 > F1 > solution. The T_{max} values were comparable among the DOX solution, F1 and F2, while the detection periods of DOX in rat plasma were 75, 180 and 240 min for the solution, F1 and F2, respectively.

3.7. *In vivo* toxicity study in rats

Fig. 6 shows representative histological sections of jejunal segments at 24 h after oral administration of DW, F1 and F2 to rats. In those three groups of rats, any evidence of damage to the intestinal wall, such as villi fusion, occasional epithelial cell shedding, and congestion of mucosal capillary with blood and focal trauma, was not found in parts of the jejunum. There was no discernible difference among the control (DW), F1 and F2, indicating that oral DOX

Table 3

Pharmacokinetic parameters of DOX after oral administration of the DOX solution, F1 and F2 at a dose of 10 mg/kg to rats ($n=4$).

Parameter	Solution	F1	F2
AUC (ng min/mL)	2740 \pm 1030 ^a	5310 \pm 1310 ^a	9040 \pm 1730 ^a
C_{max} (ng/mL)	17.5 \pm 2.76 ^a	29.4 \pm 6.42 ^a	57.7 \pm 9.28 ^a
T_{max} (min)	45 (30–45)	45 (30–45)	60 (30–60)
F_{rel} (%)	100	214	364

^a Significantly different from the other groups ($p < 0.05$).

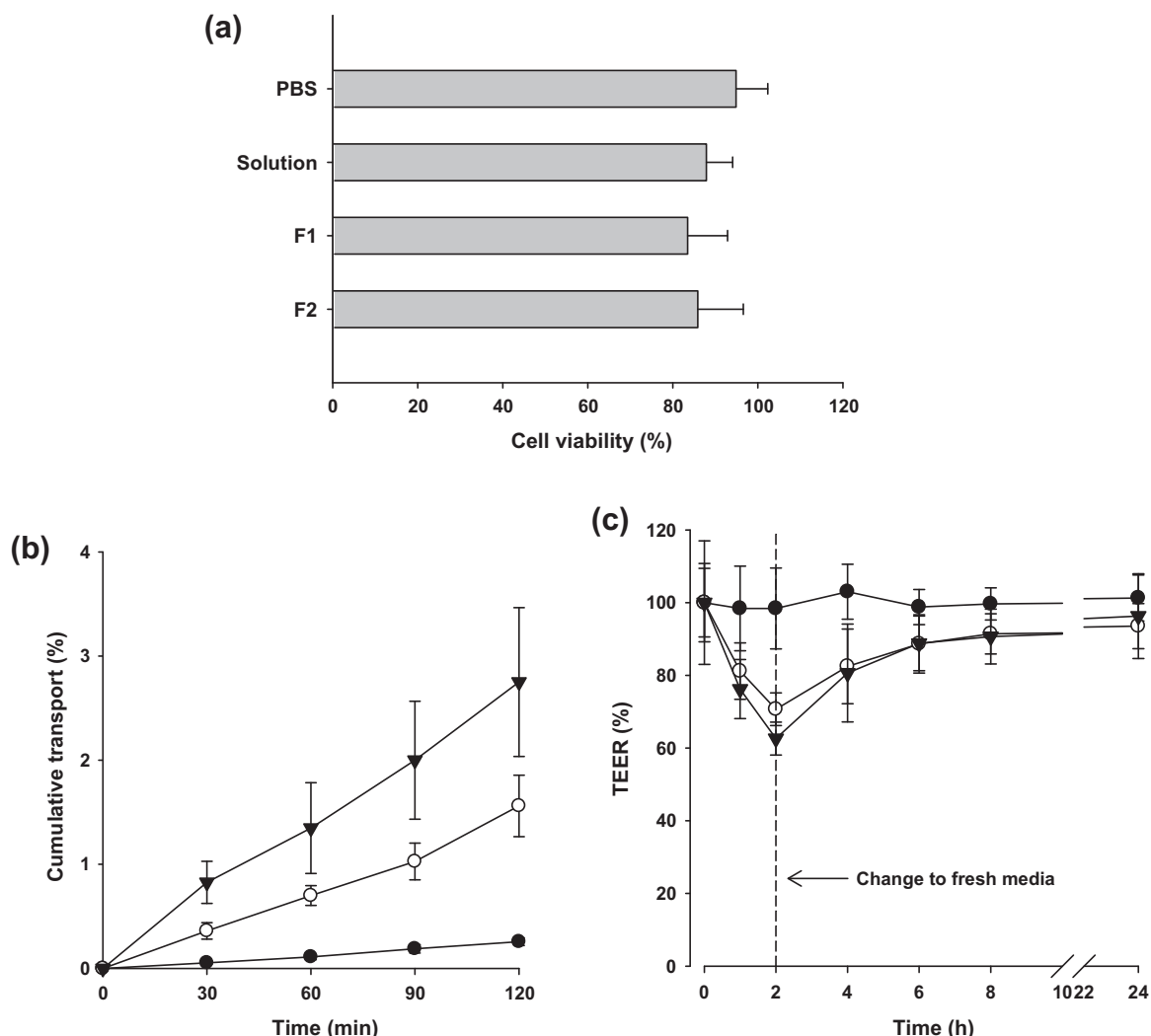


Fig. 4. Viability of Caco-2 cells after 2-h exposure to DOX solution, F1 and F2 ($n=5$; a), time profiles of *in vitro* absorptive transport of DOX from solution (●), F1 (○), and F2 (▼) across Caco-2 cell monolayers at 37°C ($n=4$; b), and time profiles of TEER values during the 2-h transport study of DOX solution (●), F1 (○), and F2 (▼) across Caco-2 cell monolayers and subsequent incubation in fresh media up to 24 h ($n=4$; c). Vertical bars represent standard deviation.

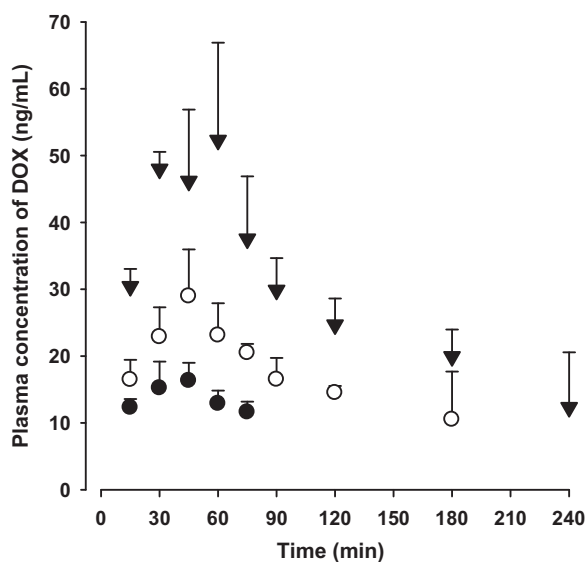


Fig. 5. Time profiles of arterial plasma concentrations of DOX after oral administration of DOX solution (●), F1 (○) and F2 (▼) at a dose of 10 mg/kg to rats ($n=4$). Vertical bars represent standard deviation.

formulations are not toxic to the rat intestinal mucosa (Fig. 6a–c). Fig. 7 shows SOD activity in the heart tissue after intravenous injection of saline and the DOX solution and after oral administration of F1 and F2 to rats. Compared to the control (treated with intravenous saline) group, SOD activities in heart homogenate decreased significantly in rats treated with intravenous DOX solution, indicating the significant cardiac toxicity of intravenous DOX therapy. However, after oral administration of F1 and F2, SOD levels were comparable with the control group, indicating the reduced cardiotoxicity of oral F1 and F2 compared with intravenous DOX solution. Fig. 8 shows representative histological sections of heart segments after intravenous injection of saline and DOX solution and after oral administration of F1 and F2 to mice. As shown in Fig. 8b, a marked disorganization of cardiac muscles and structural changes in heart tissues were observed after intravenous injection of DOX solution to mice. However, no significant difference in the heart histopathology was observed between the control (saline) and the oral DOX formulations (Figs. 8a, c, and d).

4. Discussion

Medium chain glycerides-based colloidal nanosystems, based on W/O microemulsion, containing Captex 355, water and S_{mix}

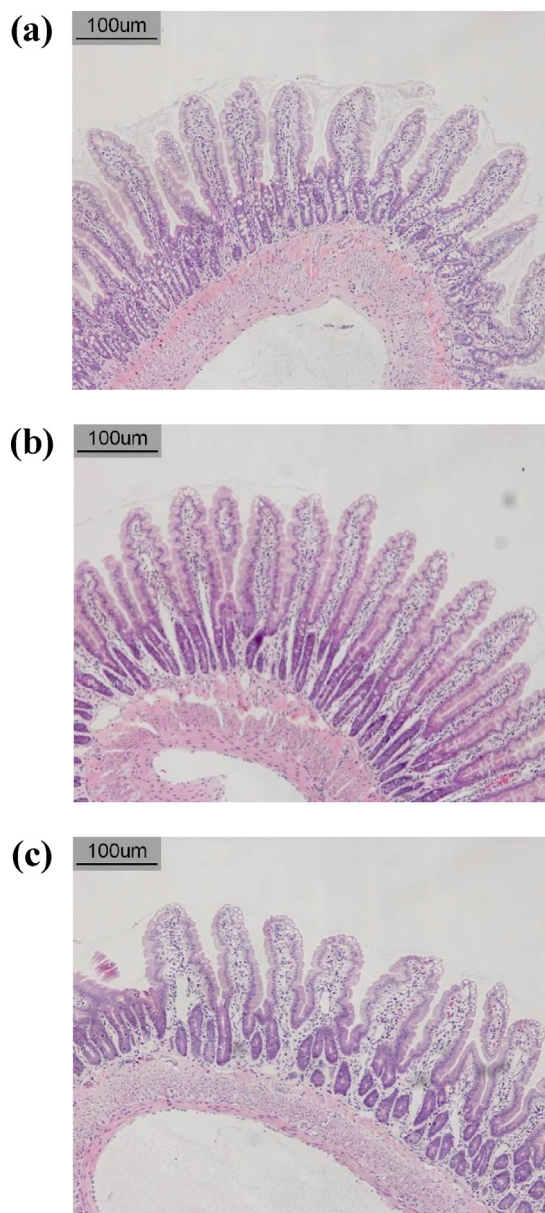


Fig. 6. Representative histological sections of jejunal segments at 24 h after oral administration of DW (a), F1 (b) and F2 (c) to rats. The scale bars represent 100 μm .

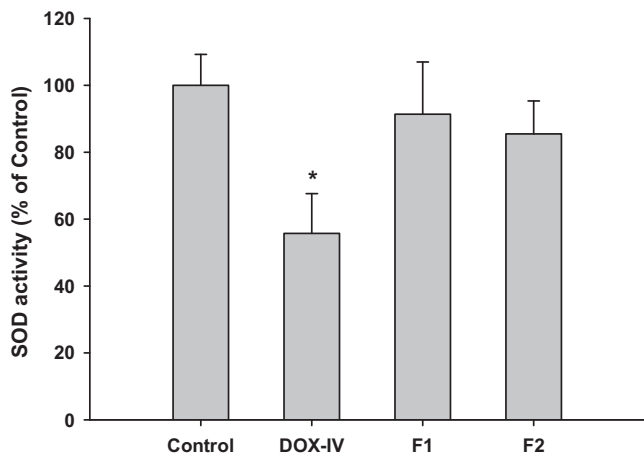


Fig. 7. SOD activity in heart tissue after intravenous injection of saline (control) and DOX solution (DOX-IV) and after oral administration of F1 and F2 to rats ($n=3$). *, Significantly different from the other groups ($p<0.05$).

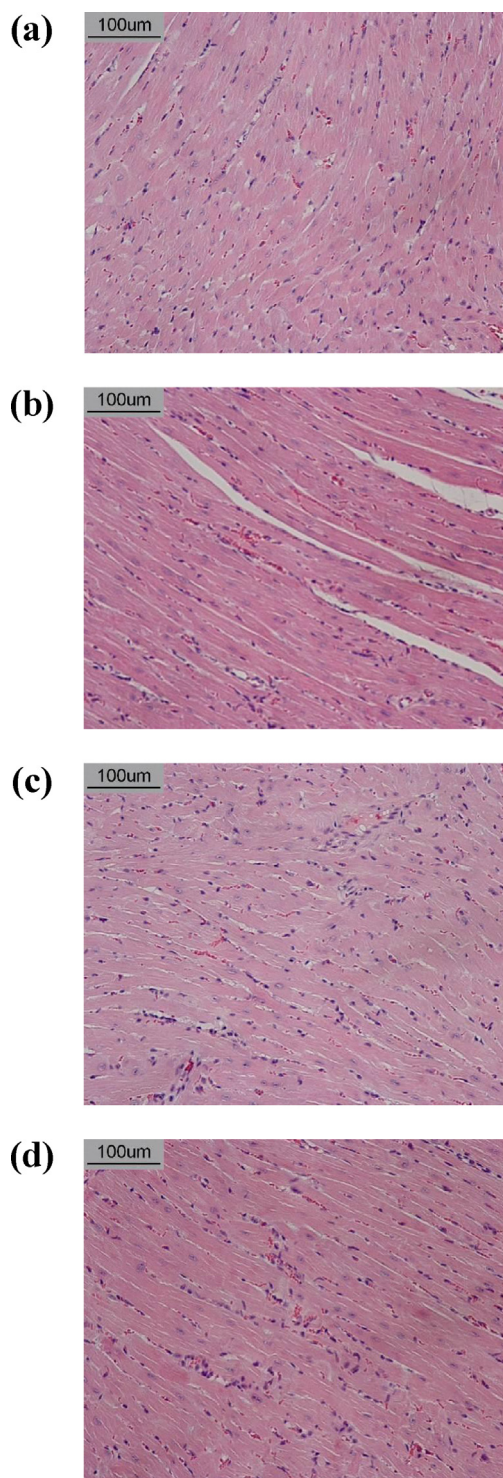


Fig. 8. Representative histological sections of heart segments after intravenous injection of saline (a) and DOX solution (b) and after oral administration of F1 (c) and F2 (d) to mice. The scale bars represent 100 μm .

were formulated by the construction of pseudo ternary phase diagram (Fig. 1). The pseudo ternary phase diagram has been widely used to determine the concentration range of components for the existence of microemulsions (Constantinides et al., 1996; Yin et al., 2009). The mixture of a low and high HLB non-ionic surfactant was used as the S_{mix} of DOX formulation, based on several previous studies reporting a successful preparation of a stable W/O microemulsion using various combinations of low and high HLB

non-ionic surfactants (Cheng et al., 2008; Constantinides et al., 1994, 1996; Gundogdu et al., 2011; Karasulu et al., 2007). The nano-sized round droplet and relatively low viscosity were observed in the prepared DOX formulations (Figure 2 and Table 1), which are consistent with previously reported oral W/O microemulsions (100–600 cp) (Cheng et al., 2008; Gundogdu et al., 2011; Qi et al., 2011).

Colloidal systems including microemulsion are diluted by the gastrointestinal fluid upon oral administration, and thus the characteristics of F1 and F2 after dilution were evaluated. Since oral dilution factor in humans has not been clarified yet, it was assumed to be 500-fold in this study, based on relevant previous studies using the oral dilution factors of approximately 100–2200-fold (Amidon et al., 1995; Cheng et al., 2008; Ke et al., 2008; Yin et al., 2009). In the *in vitro* dilution study, the leakage of only minor portions (less than 10%) of DOX into the outer bulk aqueous phase was observed after the 500-fold dilution of DOX formulation (Table 1). This result suggests that there is no burst release of DOX when the DOX formulations are diluted, and that the phase conversion may occur primarily into W/O/W rather than O/W emulsion.

Drug release characteristics of DOX formulations were evaluated using the dialysis method (Fig. 3). Compared with the DOX solution, slower and sustained release of DOX was observed in the DOX formulations. Since the different appearance profiles of DOX in the receptor side were observed, it is obvious that the penetration process of DOX through the dialysis membrane is not the rate-limiting step in the overall release process of DOX from the inner phase of W/O microemulsions to the receptor side. Moreover, since the molecular cut off of dialysis membrane used is 6–8 kDa, it is unlikely that the droplet of emulsion itself may penetrate the dialysis membrane. Thus, this result may be attributed to the slow diffusion of DOX through the oil phase of W/O microemulsions being the rate-limiting step in the overall release process of DOX from W/O microemulsions. Taken together, those pseudo ternary phase diagram and characterization data in terms of droplet size, morphology, viscosity, drug loading, and drug release suggest that DOX-loaded emulsion-based colloidal nanosystems have been successfully prepared (Figs. 1–3, Table 1).

The Caco-2 cell monolayer is widely used as an *in vitro* model of the human small intestinal mucosa to predict the intestinal absorption of a drug. The correlation between the *in vitro* apparent permeability coefficient across Caco-2 monolayers and the *in vivo* fraction of oral dose absorbed is well established (Artursson and Karlsson, 1991; van Breemen and Li, 2005). Moreover, Caco-2 cell assay is widely known as a useful *in vitro* model for determining the absorptive characteristics of a drug and elucidating its transport mechanism (Yu and Zeng, 2007). Thus, the intestinal permeation mechanism of DOX solution and formulations was investigated using Caco-2 cell model.

No significant cellular toxicity of DOX solution in Caco-2 cells was observed for 2 h (Fig. 4a), which is consistent with a previous study reporting no significant effect of 0.1-mM DOX on Caco-2 cell viability up to 6-h exposure (Silva et al., 2011). Our recent study has revealed that the absorptive transport of DOX across Caco-2 cell monolayers occurs primarily *via* the paracellular pathway (Kim et al., 2013). In this study, medium chain tri-glyceride (Captex 355) was incorporated as the oil phase of both F1 and F2. Medium chain glycerides have been reported to markedly enhance the intestinal permeability of paracellular marker compounds (Cheng et al., 2008). However, evidence on the paracellular enhancing activity of Tween 80 or Span 80 (the surfactant mixture of F1) has not yet been reported (Aungst, 2000). Thus, Captex 355 seems to be responsible for the significantly higher P_{app} of F1 and F2 compared with the DOX solution (Fig. 4b). The F2 contains Capmul MCM (medium chain mono- and di-glyceride) and labrasol as a surfactant mixture. It

has been reported that medium chain mono- and di-glycerides are more active than tri-glyceride as a membrane permeation enhancer (Aungst, 2000). Moreover, labrasol has been reported to enhance the intestinal permeation of a paracellular marker compound, mannitol, and a poorly absorbed antibiotic, gentamicin (Hu et al., 2001; Sha et al., 2005). Thus, the difference in surfactant mixture between F1 and F2 seems to be mainly responsible for the significantly higher P_{app} of F2 compared with F1 (Fig. 4b). The change in TEER values has been generally accepted as an indicator of tight junction integrity, which is the major determinant of paracellular permeation (Maher et al., 2009; Yu and Zeng, 2007). The reduction of TEER value by F1 and F2 during the 2-h transport study suggests that DOX formulations may enhance the absorptive transport of DOX at least partly *via* the paracellular pathway. Moreover, the restoration of TEER value during 22 h after wash-out of the formulations and change to fresh media suggests that the paracellular permeation enhancing effects of F1 and F2 are reversible.

The *in situ* intestinal absorption and *in vivo* oral bioavailability of DOX formulations were evaluated using the rat model, based on a good correlation between the fraction of oral dose absorbed in rats and that in humans (Fagerholm, 2007; Yoon et al., 2011). The results of the *in situ* closed loop study in rats suggest that the intestinal absorption of DOX may be in the following order: F2 > F1 > DOX solution (Table 2), which is consistent with the results of the *in vitro* transport study in Caco-2 cells (Fig. 4b). In the *in vivo* rat pharmacokinetic study, 10-mg/kg oral dose of DOX solution were selected. Oral doses of 10–20 mg/kg were used in several previous studies for the oral delivery of DOX (Benival and Devarajan, 2012; Choi et al., 2011; Jain et al., 2012; Kalaria et al., 2009; Ke et al., 2008). Moreover, our recent study has revealed that DOX solution exhibits linear pharmacokinetics at the oral dose range of 20–100 mg/kg (Kim et al., 2013). After oral administration of DOX solution and formulations, systemic DOX exposures were in the following order: F2 > F1 > DOX solution (Table 3), which is consistent with the *in vitro* Caco-2 cell and *in situ* close loop studies (Fig. 4b and Table 2). As discussed earlier, the lipidic components of DOX formulations such as Captex 355, Capmul MCM and labrasol may be responsible for the differences in oral bioavailability of DOX between the DOX solution and the oral formulations F1 and F2.

The intestinal toxicity of DOX formulations in rats was evaluated by histological H&E staining. As shown in Fig. 6, no significant intestinal toxicity of DOX solution, F1 and F2 in rats was observed, which is consistent with the results of the Caco-2 cell study where the restoration of TEER values (Fig. 4c) as well as no significant cellular toxicity (Fig. 4a) were observed. In addition, because cardiac toxicity is the major complication of the DOX therapy, the activity of SOD, a cardiac toxicity marker, and histological test using H&E staining of the DOX solution, F1 and F2 in mice and rats were evaluated (Benival and Devarajan, 2012). Significant SOD reduction (Fig. 7) and marked disruption of fine structure in heart tissues (Fig. 8b) indicate the significant cardiac toxicity of intravenous DOX therapy (Benival and Devarajan, 2012; Jain et al., 2012; Kalaria et al., 2009). However, markedly reduced cardiotoxicity in terms of SOD level (Fig. 7) and heart histopathology (Figs. 8a, c, and d) was observed in oral F1 and F2. Thus, these results in intestinal and cardiac toxicity studies suggest that oral DOX formulations prepared in this study are less toxic than conventional intravenous DOX formulations, indicating a potentially safe oral delivery system for DOX.

To the best of our knowledge, this study is the first report on the oral delivery of DOX through the enhancement of intestinal permeation *via* the paracellular pathway. Moreover, very few attempts have been made to develop colloidal nanosystems based on W/O microemulsions for the oral delivery of paracellularly transported BCS class III drugs including DOX. Therefore, this study provides

new insights for the application of microemulsion in oral DOX delivery via the paracellular pathway.

5. Conclusions

Medium chain glycerides-based colloidal nanosystems based on W/O microemulsions containing Captex 355, Capmul MCM, and/or labrasol were developed for the oral delivery of DOX. The DOX formulations were successfully prepared by the construction of the pseudo-ternary phase diagram, and their droplet size distribution, viscosity, drug loading, and drug release were characterized. Compared with the DOX solution, the DOX formulations enhanced the absorptive transport of DOX across the Caco-2 cell monolayers at least partly due to the paracellular-enhancing effects of their lipidic components. Moreover, the *in situ* intestinal absorption and *in vivo* oral bioavailability of DOX in rats were markedly enhanced in the DOX formulations. In addition, no discernible damage was observed in the rat jejunum after oral administration of the DOX formulations, and the cardiac toxicity was significantly reduced when compared with the intravenous DOX solution. Taken together, the medium chain glycerides-based colloidal nanosystems prepared in this study represent a potentially effective oral delivery system for DOX.

Conflict of interest

The authors report no conflict of interest.

Acknowledgements

This work was supported by the National Research Foundation of Korea (NRF) grant funded by the Korean Government (MSIP) (Nos. 2009-0083533 and 2011-0016040).

References

- Amidon, G.L., Lennernas, H., Shah, V.P., Crison, J.R., 1995. A theoretical basis for a biopharmaceutical drug classification: the correlation of *in vitro* drug product dissolution and *in vivo* bioavailability. *Pharm. Res.* 12, 413–420.
- Artursson, P., Karlsson, J., 1991. Correlation between oral drug absorption in humans and apparent drug permeability coefficients in human intestinal epithelial (Caco-2) cells. *Biochem. Biophys. Res. Commun.* 175, 880–885.
- Aungst, B.J., 2000. Intestinal permeation enhancers. *J. Pharm. Sci.* 89, 429–442.
- Benival, D.M., Devarajan, P.V., 2012. Lipomer of doxorubicin hydrochloride for enhanced oral bioavailability. *Int. J. Pharm.* 423, 554–561.
- Bromberg, L., 2008. Polymeric micelles in oral chemotherapy. *J. Control. Release* 128, 99–112.
- Bromberg, L., Alakhov, V., 2003. Effects of polyether-modified poly(acrylic acid) microgels on doxorubicin transport in human intestinal epithelial Caco-2 cell layers. *J. Control. Release* 88, 11–22.
- Cheng, M.B., Wang, J.C., Li, Y.H., Liu, X.Y., Zhang, X., Chen, D.W., Zhou, S.F., Zhang, Q., 2008. Characterization of water-in-oil microemulsion for oral delivery of earthworm fibrinolytic enzyme. *J. Control. Release* 129, 41–48.
- Choi, J.S., Piao, Y.J., Kang, K.W., 2011. Effects of quercetin on the bioavailability of doxorubicin in rats: role of CYP3A4 and P-gp inhibition by quercetin. *Arch. Pharm. Res.* 34, 607–613.
- Constantinides, P.P., Scalart, J.P., Lancaster, C., Marcello, J., Marks, G., Ellens, H., Smith, P.L., 1994. Formulation and intestinal absorption enhancement evaluation of water-in-oil microemulsions incorporating medium-chain glycerides. *Pharm. Res.* 11, 1385–1390.
- Constantinides, P.P., Welzel, G., Ellens, H., Smith, P.L., Sturgis, S., Yiv, S.H., Owen, A.B., 1996. Water-in-oil microemulsions containing medium-chain fatty acids/salts: formulation and intestinal absorption enhancement evaluation. *Pharm. Res.* 13, 210–215.
- DeMario, M.D., Ratain, M.J., 1998. Oral chemotherapy: rationale and future directions. *J. Clin. Oncol.* 16, 2557–2567.
- Dong, Y., Feng, S.S., 2005. Poly(D,L-lactide-co-glycolide)/montmorillonite nanoparticles for oral delivery of anticancer drugs. *Biomaterials* 26, 6068–6076.
- Fagerholm, U., 2007. Prediction of human pharmacokinetics – gastrointestinal absorption. *J. Pharm. Pharmacol.* 59, 905–916.
- Gundogdu, E., Alvarez, I.G., Karasulu, E., 2011. Improvement of effect of water-in-oil microemulsion as an oral delivery system for fexofenadine: *in vitro* and *in vivo* studies. *Int. J. Nanomed.* 6, 1631–1640.
- Hu, Z., Tawa, R., Konishi, T., Shibata, N., Takada, K., 2001. A novel emulsifier, labrasol, enhances gastrointestinal absorption of gentamicin. *Life Sci.* 69, 2899–2910.
- Jain, S., Patil, S.R., Swarnakar, N.K., Agrawal, A.K., 2012. Oral delivery of doxorubicin using novel polyelectrolyte-stabilized liposomes (layersomes). *Mol. Pharm.* 9, 2626–2635.
- Jha, S.K., Karki, R., Venkatesh, D.P., Geethalakshmi, A., 2011. Formulation development & characterization of microemulsion drug delivery systems containing antiulcer drug. *Int. J. Drug Dev. Res.* 3, 336–343.
- Kalaria, D.R., Sharma, G., Beniwal, V., Ravi Kumar, M.N., 2009. Design of biodegradable nanoparticles for oral delivery of doxorubicin: *in vivo* pharmacokinetics and toxicity studies in rats. *Pharm. Res.* 26, 492–501.
- Karasulu, H.Y., Karabulut, B., Goker, E., Guneri, T., Gabor, F., 2007. Controlled release of methotrexate from w/o microemulsion and its *in vitro* antitumor activity. *Drug Deliv.* 14, 225–233.
- Kawakami, K., Yoshikawa, T., Hayashi, T., Nishihara, Y., Masuda, K., 2002a. Microemulsion formulation for enhanced absorption of poorly soluble drugs: II. *In vivo* study. *J. Control. Release* 81, 75–82.
- Kawakami, K., Yoshikawa, T., Moroto, Y., Kanaoka, E., Takahashi, K., Nishihara, Y., Masuda, K., 2002b. Microemulsion formulation for enhanced absorption of poorly soluble drugs: I. Prescription design. *J. Control. Release* 81, 65–74.
- Ke, W., Zhao, Y., Huang, R., Jiang, C., Pei, Y., 2008. Enhanced oral bioavailability of doxorubicin in a dendrimer drug delivery system. *J. Pharm. Sci.* 97, 2208–2216.
- Kim, J.E., Cho, H.J., Kim, J.S., Shim, C.K., Chung, S.J., Oak, M.H., Yoon, I.S., Kim, D.D., 2013. The limited intestinal absorption via paracellular pathway is responsible for the low oral bioavailability of doxorubicin. *Xenobiotica* 43, 579–591.
- Koga, K., Takarada, N., Takada, K., 2010. Nano-sized water-in-oil-in-water emulsion enhances intestinal absorption of calcein, a high solubility and low permeability compound. *Eur. J. Pharm. Biopharm.* 74, 223–232.
- Le Lay, K., Myon, E., Hill, S., Riou-Franca, L., Scott, D., Sidhu, M., Dunlop, D., Launois, R., 2007. Comparative cost-minimisation of oral and intravenous chemotherapy for first-line treatment of non-small cell lung cancer in the UK NHS system. *Eur. J. Health Econ.* 8, 145–151.
- Maher, S., Leonard, T.W., Jacobsen, J., Brayden, D.J., 2009. Safety and efficacy of sodium caprate in promoting oral drug absorption: from *in vitro* to the clinic. *Adv. Drug Deliv. Rev.* 61, 1427–1449.
- Qi, J., Zhuang, J., Wu, W., Lu, Y., Song, Y., Zhang, Z., Jia, J., Ping, Q., 2011. Enhanced effect and mechanism of water-in-oil microemulsion as an oral delivery system of hydroxysafflor yellow A. *Int. J. Nanomed.* 6, 985–991.
- Saitoh, R., Sugano, K., Takata, N., Tachibana, T., Higashida, A., Nabuchi, Y., Aso, Y., 2004. Correction of permeability with pore radius of tight junctions in Caco-2 monolayers improves the prediction of the dose fraction of hydrophilic drugs absorbed by humans. *Pharm. Res.* 21, 749–755.
- Schwarzbach, M.H., Eisold, S., Burguete, T., Willeke, F., Klein-Bauernschmitt, P., Schlehofer, J.R., Herfarth, C., Ridder, R., von Knebel Doeberitz, M., 2002. Sensitization of sarcoma cells to doxorubicin treatment by concomitant wild-type adeno-associated virus type 2 (AAV-2) infection. *Int. J. Oncol.* 20, 1211–1218.
- Sha, X., Yan, G., Wu, Y., Li, J., Fang, X., 2005. Effect of self-microemulsifying drug delivery systems containing labrasol on tight junctions in Caco-2 cells. *Eur. J. Pharm. Sci.* 24, 477–486.
- Silva, R., Carmo, H., Dinis-Oliveira, R., Cordeiro-da-Silva, A., Lima, S.C., Carvalho, F., Bastos Mde, L., Remiao, F., 2011. *In vitro* study of P-glycoprotein induction as an antidotal pathway to prevent cytotoxicity in Caco-2 cells. *Arch. Toxicol.* 85, 315–326.
- van Breemen, R.B., Li, Y., 2005. Caco-2 cell permeability assays to measure drug absorption. *Expert Opin. Drug Metab. Toxicol.* 1, 175–185.
- Yin, Y.M., Cui, F.D., Mu, C.F., Choi, M.K., Kim, J.S., Chung, S.J., Shim, C.K., Kim, D.D., 2009. Docetaxel microemulsion for enhanced oral bioavailability: preparation and *in vitro* and *in vivo* evaluation. *J. Control. Release* 140, 86–94.
- Yoon, I.S., Choi, M.K., Kim, J.S., Shim, C.K., Chung, S.J., Kim, D.D., 2011. Pharmacokinetics and first-pass elimination of metoprolol in rats: contribution of intestinal first-pass extraction to low bioavailability of metoprolol. *Xenobiotica* 41, 243–251.
- Yoon, I., Han, S., Choi, Y.H., Kang, H.E., Cho, H.J., Kim, J.S., Shim, C.K., Chung, S.J., Chong, S., Kim, D.D., 2012. Saturable sinusoidal uptake is rate-determining process in hepatic elimination of docetaxel in rats. *Xenobiotica* 42, 1110–1119.
- Yu, L., Zeng, S., 2007. Transport characteristics of zolmitriptan in a human intestinal epithelial cell line Caco-2. *J. Pharm. Pharmacol.* 59, 655–660.
- Zhang, Z., Feng, S.S., 2006. Nanoparticles of poly(lactide)/vitamin E TPGS copolymer for cancer chemotherapy: synthesis, formulation, characterization and *in vitro* drug release. *Biomaterials* 27, 262–270.

Proliferation and chondrogenic differentiation of human adipose-derived mesenchymal stem cells in sodium alginate beads with or without hyaluronic acid

Dong-Hwan Kim · Dae-Duk Kim · In-Soo Yoon

Received: 29 January 2013 / Accepted: 19 February 2013 / Published online: 28 February 2013
© The Korean Society of Pharmaceutical Sciences and Technology 2013

Abstract Human adipose-derived mesenchymal stem cells (AD-MSCs) have attracted much interest as an alternative to autologous chondrocytes and bone marrow-derived mesenchymal stem cells for cell-based therapy to repair cartilage defects. Sodium alginate (SA) beads have been widely known as a conventional stem cell delivery system for cartilage repair. Hyaluronic acid (HA) has been known to induce cell proliferation and chondrogenic differentiation. Herein, we prepared AD-MSCs-encapsulating SA beads with HA (SA–HA beads) and without HA (SA beads). Then, the morphology, proliferation, and chondrogenic differentiation of AD-MSCs cultured in SA–HA beads or SA beads with a conventional chondrogenic media were evaluated. There was no discernible difference in the morphology of AD-MSCs between SA–HA and SA beads. However, the proliferation (MTT optical density and DNA contents) and chondrogenic differentiation (s-GAG contents and type II collagen staining) of AD-MSCs were significantly enhanced in SA–HA beads as compared to SA beads. The present results suggest that HA can be added to SA beads-based cell delivery systems of AD-MSCs in order to improve their chondrogenesis-inducing capacity for repair of cartilage defects.

Keywords Human adipose-derived mesenchymal stem cells · Sodium alginate beads · Hyaluronic acid · Proliferation · Chondrogenic differentiation

Abbreviations

SA	Sodium alginate
HA	Hyaluronic acid
MSCs	Mesenchymal stem cells
AD-MSCs	Adipose-derived mesenchymal stem cells
BM-MSCs	Bone marrow-derived mesenchymal stem cells
DMEM-HG	Dulbecco's modified eagle's medium–high glucose
TGF- β 1	Transforming growth factor- β 1
ITS	Insulin–transferrin–selenium
CM	Chondrogenic medium (serum-free DMEM-HG supplemented with 10 ng/mL of TGF- β 1, 50 nM ascorbate, 100 nM dexamethasone, and 5 μ g/mL of ITS)
EM	Expansion medium (DMEM-HG supplemented with 10 % fetal bovine serum)
SA–HA beads	HA-containing SA beads
SA beads	HA-free SA beads

D.-H. Kim · D.-D. Kim
College of Pharmacy and Research Institute of Pharmaceutical Sciences, Seoul National University, Seoul 151-742, Republic of Korea

I.-S. Yoon (✉)
College of Pharmacy, Mokpo National University, Jeonnam 534-729, Republic of Korea
e-mail: isyoon@mokpo.ac.kr

Introduction

During past decades, the treatment of cartilage defects has been greatly hindered by the limited self-repair capacity of the cartilage (Erickson et al. 2002; Heng et al. 2004). Recently, tissue engineering technologies using cells and suitable delivery systems have been developed to aid the

repair of cartilage defects (Ma et al. 2003; Guilak et al. 2004). Autologous chondrocytes implantation was approved for the repair of symptomatic cartilage defects of the femoral condyle (De Bie 2007). However, it has suffered from donor site morbidity and low in vitro cell proliferation capacity (Ochi et al. 2001). Therefore, bone marrow-derived mesenchymal stem cells (BM-MSCs) have been recognized as an alternative to autologous chondrocytes due to their high proliferation capacity and chondrogenic potential (Johnstone et al. 1998; Li et al. 2005). Yet, the clinical application of BM-MSCs remains to be challenging due to the donor site damage and highly invasive donating procedure with severe pain (Kern et al. 2006). Instead of BM-MSCs, adipose-derived mesenchymal stem cells (AD-MSCs) have recently attracted much interest for cartilage regeneration (Lin et al. 2005; Yoon et al. 2011). AD-MSCs can be obtained by a simple liposuction procedure from subcutaneous adipose tissue with minimal donor site morbidity and pain (Zuk et al. 2001, 2002). Moreover, it has been reported that AD-MSCs are comparable to BM-MSCs with respect to the multi-lineage potential, growth kinetics, and cells senescence (De Ugarte et al. 2003).

It has been well known that three-dimensional (3D) culture condition is required to direct the differentiation of AD-MSCs into the chondrogenic lineage (Heng et al. 2004). Therefore, various biomaterial scaffolds in the form of sponges or hydrogels have been developed to provide 3D culture condition and serve as cell delivery systems for repair of cartilage defects. Among them, synthetic polymers (e.g., polylactic acid, polyglycolic acid, polylactic acid-polyglycolic acid) or natural polymers (e.g., collagen, alginate, chitosan, gelatin, hyaluronic acid) have been proved to be suitable biomaterials for cartilage tissue engineering (Nehrer et al. 1997; Gugala and Gogolewski 2000; Lahiji et al. 2000; Lohmann et al. 2000; Ma et al. 2003; Chung et al. 2011; Yoon et al. 2011).

Alginate is a linear polysaccharide with repeating blocks consisting of (1-4)-linked β -D-mannuronate and α -L-guluronate. Alginate and its water-soluble sodium salt have been used in food and pharmaceutical industry due to their good thickening or gelling property even at moderate concentrations (Chung et al. 2011). Especially, sodium alginate (SA) beads have been widely recognized as a conventional stem cell delivery system for repair of cartilage defects and as a model 3D culture system in research areas related to chondrogenesis of stem cells (Brian et al. 2010). It has been reported that SA bead culture can induce the chondrogenic differentiation of human articular chondrocytes, BM-MSCs, and AD-MSCs (Chubinskaya et al. 2001; Ma et al. 2003; Awad et al. 2004).

Hyaluronic acid (HA) is a linear polysaccharide with repeating blocks consisting of D-glucuronic acid and D-N-acetylglucosamine, which is a major component of

extracellular matrix (ECM) of the cartilage. Several previous studies have reported that HA can enhance cell proliferation and chondrogenic differentiation via various mechanisms including CD44-mediated cytoplasmic signal transduction pathway (Miralles et al. 2001; Yoon et al. 2011). Therefore, it seems plausible that cell proliferation and chondrogenic differentiation in SA beads could be further improved by the addition of HA to SA beads. This hypothesis could be supported by a previous study that rat chondrocytes cultured in HA-containing SA beads exhibited significantly-enhanced cell proliferation and chondrogenic differentiation profiles as compared to those in HA-free SA beads (Miralles et al. 2001). However, little information is available regarding the comparison between HA-containing and HA-free SA beads with respect to the proliferation and chondrogenic differentiation of AD-MSCs, which further investigation is required.

Herein, we therefore report on the proliferation and chondrogenic differentiation of AD-MSCs in SA beads with or without HA. AD-MSCs-encapsulating SA beads with HA (represented as 'SA-HA beads') or without HA (represented as 'SA beads') were prepared and cultured in conventional chondrogenic media. Then, cell morphology, proliferation, and chondrogenic differentiation were evaluated by 3-(4,5-dimethylthiazol-2-yl)-2,5-diphenyl tetrazolium bromide (MTT) staining, MTT assay/DNA assay, and sulfated glycosaminoglycans (s-GAG) assay/type II collagen immunohistochemistry, respectively.

Materials and methods

Materials

HA was purchased from Shandong Freda Biochem Co., Ltd. (1,040 kDa; Jinan, China). SA (250 kDa; medium viscosity; guluronate residue:mannuronate residue = 30:70; issued from *Macrocystis pyrifera*), Trypsin/EDTA, type I collagenase (250 U/mg), Alcian blue 8GX, dexamethasone, ascorbate, and insulin-transferrin-selenium (ITS) were purchased from Sigma-Aldrich (St. Louis, USA). Dulbecco's modified Earle's medium-high glucose (DMEM-HG) was purchased from BioWhittaker (Wakersville, MD). Penicillin-streptomycin was purchased from Lonza (Basel, Swiss). Recombinant human transforming growth factor-beta1 (TGF- β 1) was purchased from Strathmann Biotec (Hamburg, Germany). All other chemicals were from standard laboratory suppliers and were of the highest purity available.

Isolation and expansion of AD-MSCs

Isolation and expansion of AD-MSCs were performed as previously described (Yoon et al. 2011). Briefly, human

subcutaneous adipose tissue samples were obtained from elective liposuction of healthy females with informed consents as approved by the institutional review boards of Asan Medical Center (Seoul, Korea). The liposuction waste tissue was digested with 250 U/mL of type I collagenase for 90 min at 37 °C, and centrifuged at 300×*g* for 10 min to obtain the stromal cell fraction. The cell suspension was layered onto histopaque-1077 (Sigma-Aldrich), and centrifuged at 840×*g* for 10 min. The supernatant was discarded, and the cell band buoyant over histopaque was collected. Retrieved cell fraction was cultured overnight at 37 °C/5 % CO₂ in expansion medium (EM; DMEM-HG supplemented with 10 % fetal bovine serum, 100 U/mL of penicillin, and 100 mg/mL of streptomycin). The resulting cell population (AD-MSCs) was maintained over 3–5 days until 80–90 % confluence, which were represented as passage 1. AD-MSCs were sub-cultured after 85 % confluence, and used for experiment at passage 3–4. Culture medium was changed every 48 h.

Preparation and 3D chondrogenic culture of AD-MSCs-encapsulating SA beads with HA (SA–HA beads) or without HA (SA beads)

400 mg of SA was dissolved in 10 mL of PBS, resulting in 4 % SA solution. The SA solution was heated on a hot plate with stirring thoroughly. The resulting homogeneous SA solution was sterilized using 0.22- μ m filter and stored in a refrigerator at 4 °C. 70 mg of HA was dissolved in 10 mL of PBS, resulting in 0.7 % HA solution. The HA solution was heated on a hot plate with stirring thoroughly. The resulting homogeneous HA solution was sterilized using 0.22- μ m filter and stored in a refrigerator at 4 °C. 10.2 mL of 1 M CaCl₂ stock solution was added to 89.8 mL of double-distilled water in 100 mL volumetric flask, resulting in 102 mM CaCl₂ solution. The CaCl₂ solution was sterilized using 0.22- μ m filter and stored at 4 °C.

2 % SA solution with or without 0.35 % HA was prepared by diluting 4 % SA solution with same volume of 0.7 % HA solution or PBS, respectively. AD-MSCs were resuspended in the resulting polymer solution at 5 × 10⁶ cells/mL in a 50 mL conical tube. The cell-polymer mixture was dripped into 1 mL of pre-warmed CaCl₂ solution as previously described (Guo et al. 1989; Estes et al. 2010). After incubation at 37 °C for 5 min, CaCl₂ solution was discarded, and the resulting beads were cultured in 24 well plate with a conventional chondrogenic media (CM; serum-free DMEM-HG supplemented with 10 ng/mL of TGF- β 1, 50 nM ascorbate, 100 nM dexamethasone, 5 μ g/mL of ITS, 100 U/mL of penicillin, and 100 mg/mL of streptomycin).

Morphology of AD-MSCs

The morphology of AD-MSCs cultured in SA–HA beads or SA beads for 14 days were evaluated by MTT staining (Yoon et al. 2011). After 14 days of 3D chondrogenic culture, the beads were transferred to new 24-well plates. Then, 900 μ L of culture media and 100 μ L of MTT solution were added to the beads. After 4-h incubation at 37 °C in 5 % CO₂, the culture media and MTT solution were discarded. Then, the stained beads were washed twice with PBS and observed under light microscopy (200×).

Proliferation of AD-MSCs

Proliferation of AD-MSCs cultured in SA–HA beads or SA beads was evaluated by MTT assay and the quantification of genomic DNA. For MTT assay, the beads were transferred into new 24-well plates after 1, 7, and 14 days of 3D chondrogenic culture, and 1 mL of fresh CM was added. After adding 100 μ L of MTT solution (5 mg/mL in PBS) to each well, the beads were incubated for 4 h at 37 °C in a 5 % CO₂ incubator. The resulting MTT formazan crystals were dissolved with 1.0 mL of DMSO. Plates were shaken for 20 min, and then 100 μ L supernatant in each well was transferred to a 96-well plate. The absorbance at 490 nm was measured by a microplate reader (Emax, Molecular Devices Corporation, Sunnyvale, CA). Beads containing no cells were used as control. For the quantification of genomic DNA, the genomic DNA was isolated from the beads after 1, 7, and 14 days of 3D chondrogenic culture. The isolation of genomic DNA was performed using DNeasy tissue kit (QIAGEN; Chatsworth, USA) according to the manufacturer's protocol. After tenfold dilution of the isolated genomic DNA, the absorbance at 260 nm was measured by a microplate reader.

Chondrogenic differentiation of AD-MSCs

Chondrogenic differentiation of AD-MSCs in SA–HA beads or SA beads was evaluated by s-GAG content and type II collagen immunohistochemistry. The s-GAG content was determined by the reported dimethylmethylene blue (DMMB) method (Farndale et al. 1986). After 1, 7, and 14 days of 3D chondrogenic culture, the beads were digested with papain for 48 h at 60 °C in 20 mM sodium phosphate buffer (pH 6.8) containing 1 mM ethylenediaminetetraacetic acid (EDTA) and 2 mM dithiothreitol (DTT). Then, 2.5 mL of DMMB dye solution was added to 100 μ L of digested sample, and the absorbance at 525 nm was measured by a microplate reader. Bovine chondroitin sulfate was used to prepare standard solution for calibration. The DMMB dye solution was prepared by dissolving 16 mg of DMMB in 1 L of distilled water containing

3.04 g of glycine, 2.37 g of NaCl and 95 mL of 0.1 M HCl. Type II collagen immunohistochemistry was performed as described previously (Estes et al. 2010). After 14 days of 3D chondrogenic culture, the beads were transferred into 20 mL of paraformaldehyde solution and fixed for 4 h at room temperature or overnight at 4 °C. After fixation, the beads were dehydrated in 30, 50, 70, 80, and 100 % ethanol during 30 min for each reagent at room temperature, and incubated with 50 % ethanol/50 % xylene and 100 % xylene during 30 min for each reagent at room temperature. After dehydration, the beads were embedded in paraffin and cut into slices with thickness of 6–10 µm using a microtome. The slices were placed on Superfrost/Plus microscope slides and dried overnight in a 37 °C slide warmer. Immunohistochemistry was performed using a standard indirect three step immunoperoxidase technique. The primary antibody was a murine monoclonal antibody raised against human type II collagen (MAB1330, Chemicon). The stained beads were observed under light microscopy (100×).

Statistical analysis

A *p* value <0.05 was considered to be statistically significant using Student's *t* test for unpaired data. Data were expressed as mean ± standard deviation.

Results and discussion

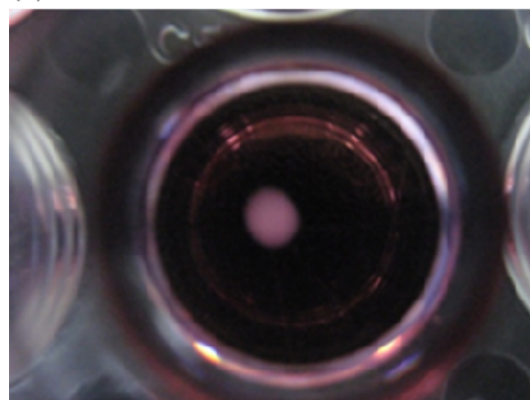
Morphology of AD-MSCs

AD-MSCs-encapsulating SA–HA beads or SA beads were successfully prepared and cultured in chondrogenic media for 14 days as shown in Fig. 1. The morphology of AD-MSCs cultured in SA–HA beads or SA beads for 14 days were evaluated by MTT staining (Fig. 2). AD-MSCs are known to show a spindle-like fibroblastic morphology in 2D culture systems such as culture dish or flask (Kim et al. 2007). However, as shown in Fig. 2, a number of stained round aggregates were dispersed within the beads, indicating that the two beads provided an appropriate 3D culture condition for cell survival. There was no discernible difference in cell morphology between the two beads.

Proliferation of AD-MSCs

The proliferation of AD-MSCs cultured in SA–HA beads or SA beads for 1, 7, and 14 days was evaluated by MTT assay and DNA assay (Fig. 3). In MTT assay, optical density values of SA–HA beads were significantly higher than those of SA beads at 7 and 14 days (Fig. 3a). In DNA assay, DNA contents of SA–HA beads were significantly

(a) SA bead



(b) SA-HA bead

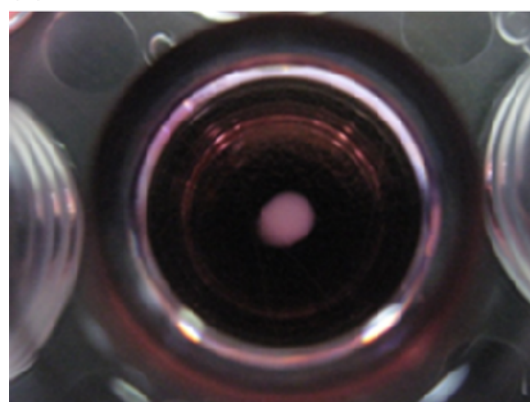


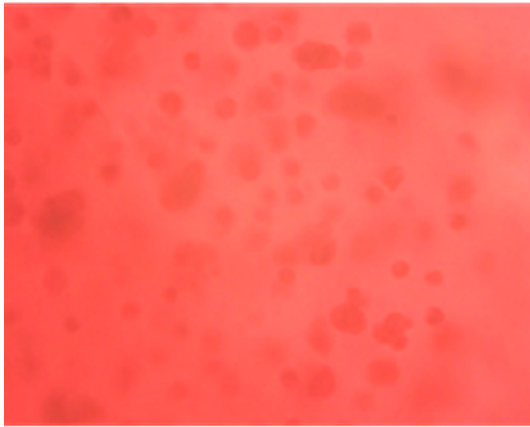
Fig. 1 AD-MSCs-encapsulating SA beads (a) or SA–HA beads (b) in chondrogenic media

higher than those of SA beads at 14 days (Fig. 3b). These results suggest that the proliferation of AD-MSCs encapsulated in SA beads could be enhanced by the addition of HA to SA beads.

Chondrogenic differentiation of AD-MSCs

Chondrogenic differentiation of cultured AD-MSCs in SA–HA beads or SA beads for 1, 7, and 14 days was evaluated by s-GAG assay (Fig. 4) and collagen type II immunohistochemistry (Fig. 5). The s-GAG, a main matrix element of the cartilage, has been considered as a marker for chondrogenic differentiation (Kang et al. 2009; Estes et al. 2010). Normalized s-GAG contents with respect to DNA contents of SA–HA beads were significantly higher than those of SA beads at 14 days (Fig. 4). Moreover, in Fig. 5, brown-colored area (indicating type II collagen) of SA–HA beads was larger than that of SA beads. In the cartilage, chondrocytes and proteoglycan are entrapped in collagen fibrillar network. Type II collagen is the predominant collagen fiber and generally considered as the primary marker for chondrogenic differentiation (Estes et al. 2010;

(a) SA bead



(b) SA-HA bead

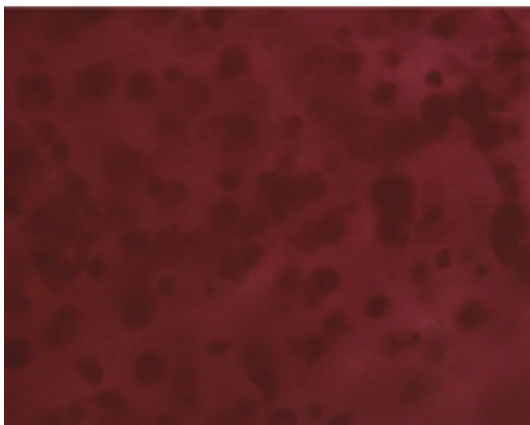


Fig. 2 MTT staining of AD-MSCs-encapsulating SA beads (a) or SA-HA beads (b) after 14 days of chondrogenic culture

Yoon et al. 2011). These results suggest that the chondrogenic differentiation of AD-MSCs encapsulated in SA beads could be enhanced by the addition of HA to SA beads.

Possible reasons for the enhanced proliferation and chondrogenic differentiation of AD-MSCs in SA-HA beads as compared to SA beads

In this study, 2 % SA beads with or without 0.35 % HA have been prepared. The composition of the beads was chosen referring to a previous study on SA-HA beads (1.2–2.4 % SA and 0.35 % HA), which reported that sufficient HA retentions (more than 55 % of initial amount of HA) could be achieved in the SA-HA beads during 28-day culture period (Lindenhayn et al. 1999). Regarding the enhanced proliferation of AD-MSCs in SA-HA beads as compared to SA beads, it has been reported that human and porcine chondrocytes exhibit an enhanced proliferation when cultured in HA-containing SA beads, as compared to

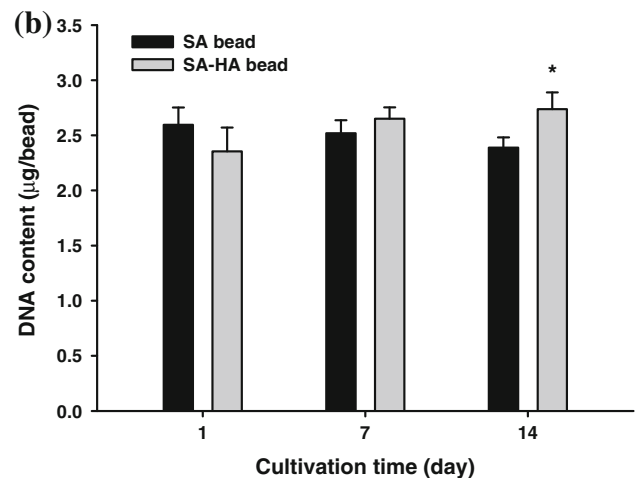
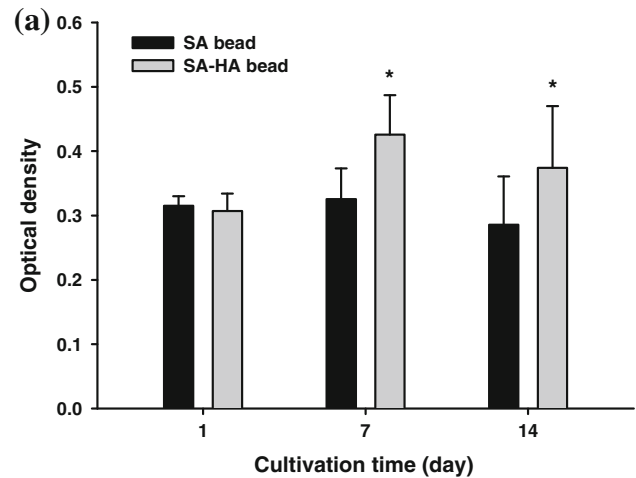


Fig. 3 MTT optical densities (a) and DNA contents (b) of AD-MSCs-encapsulating SA beads or SA-HA beads after 1, 7, and 14 days of chondrogenic culture ($n = 3$). *Significantly different from the 'SA bead' group ($p < 0.05$)

that in HA-free SA beads (Lindenhayn et al. 1999), which is consistent with the present data. HA is known to induce protein kinase activity through CD44 receptor and activates a cytoplasmic signal transduction pathway, resulting in nuclear translocation of extracellular signal-regulated kinase 1 to stimulate cell proliferation (Knudson et al. 2000; Slevin et al. 1998). Regarding the enhanced chondrogenic differentiation of AD-MSCs in SA-HA beads as compared to SA beads, it has been reported that HA enhances cell-cell contact by modulating the pericellular matrix in the cell condensation process, which is the initial stage of chondrogenesis (Knudson 2003). Moreover, interactions between HA and CD44 are known to play an important role in maintaining chondrocytic phenotypes (Ponta et al. 2003; Yoon et al. 2011). Therefore, the higher level of proliferation and chondrogenic differentiation of AD-MSCs in SA-HA beads than SA beads could be attributed to the above-mentioned biological functions of

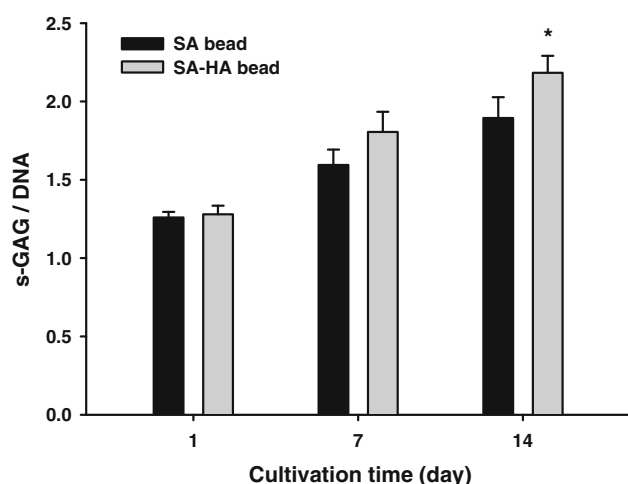
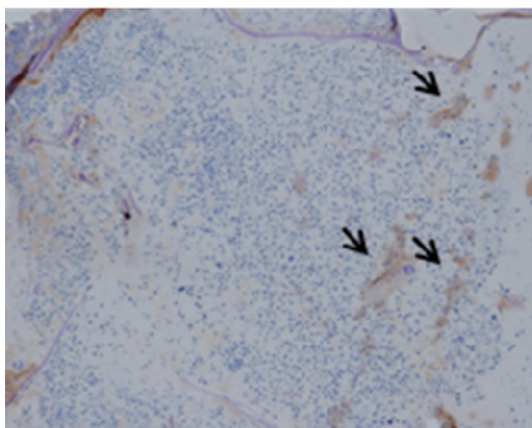


Fig. 4 Normalized s-GAG contents with respect to DNA contents of AD-MSCs-encapsulating SA beads or SA-HA beads after 1, 7, and 14 days of chondrogenic culture ($n = 3$). *Significantly different from the 'SA bead' group ($p < 0.05$)

(a) SA bead



(b) SA-HA bead

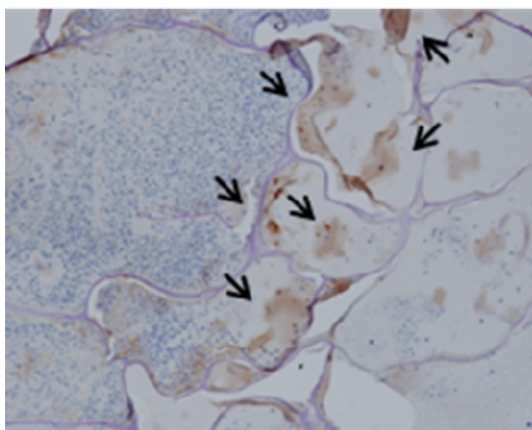


Fig. 5 Type II collagen immunohistochemistry of AD-MSCs-encapsulating SA beads (a) or SA-HA beads (b) after 14 days of chondrogenic culture. Arrows show examples of reddish-brown chromogen indicating type II collagen. (Color figure online)

HA, but precise mechanisms cannot be clarified by the present data, which further investigation is required.

Conclusions

In this study, the proliferation and chondrogenic differentiation of AD-MSCs in SA beads with or without HA have been reported. AD-MSCs-encapsulating SA-HA beads or SA beads were prepared and cultured in conventional chondrogenic media. Then, cell morphology, proliferation, and chondrogenic differentiation were evaluated by MTT staining, MTT assay/DNA assay, and s-GAG assay/type II collagen immunohistochemistry, respectively. There was no discernible difference in the morphology of AD-MSCs between SA-HA and SA beads. However, the proliferation (MTT optical density and DNA contents) and chondrogenic differentiation (s-GAG contents and type II collagen staining) of AD-MSCs were significantly enhanced in SA-HA beads as compared to SA beads. The present results suggest that HA can be added to SA beads-based cell delivery systems of AD-MSCs in order to improve their chondrogenesis-inducing capacity for repair of cartilage defects.

Acknowledgments This study was supported by the National Research Foundation of Korea (NRF) grant funded by the Korean government (MEST) (No. 2011-0030635).

References

- Awad HA, Wickham MQ, Leddy HA, Gimble JM, Guilak F (2004) Chondrogenic differentiation of adipose-derived adult stem cells in agarose, alginate, and gelatin scaffolds. *Biomaterials* 25: 3211–3222
- Chubinskaya S, Huch K, Schulze M, Otten L, Aydelotte MB, Cole AA (2001) Gene expression by human articular chondrocytes cultured in alginate beads. *J Histochem Cytochem* 49:1211–1220
- Chung CW, Kang JY, Yoon IS, Hwang HD, Balakrishnan P, Cho HJ, Chung KD, Kang DH, Kim DD (2011) Interpenetrating polymer network (IPN) scaffolds of sodium hyaluronate and sodium alginate for chondrocyte culture. *Colloids Surf B* 88:711–716
- De Bie C (2007) Genzyme: 15 years of cell and gene therapy research. *Regen Med* 2:95–97
- De Ugarte DA, Morizono K, Elbarbary A, Alfonso ZC, Zuk PA, Zhu M, Dragoo JL, Ashjian P, Thomas B, Benhaim P, Chen I, Fraser J, Hedrick MH (2003) Comparison of multi-lineage cells from human adipose tissue and bone marrow. *Cells Tissues Organs* 174:101–109
- Diekman Brian O, Rowland Christopher R, Lennon Donald P, Caplan Arnold I, Guilak Farshid (2010) Chondrogenesis of adult stem cells from adipose tissue and bone marrow: induction by growth factors and cartilage-derived matrix. *Tissue Eng Part A* 16: 523–533
- Erickson GR, Gimble JM, Franklin DM, Rice HE, Awad H, Guilak F (2002) Chondrogenic potential of adipose tissue-derived stromal cells in vitro and in vivo. *Biochem Biophys Res Commun* 290:763–769

- Estes BT, Diekman BO, Gimble JM, Guilak F (2010) Isolation of adipose-derived stem cells and their induction to a chondrogenic phenotype. *Nat Protoc* 5:1294–1311
- Farndale RW, Buttle DJ, Barrett AJ (1986) Improved quantitation and discrimination of sulphated glycosaminoglycans by use of dimethylmethylene blue. *Biochim Biophys Acta* 883:173–177
- Gugala Z, Gogolewski S (2000) In vitro growth and activity of primary chondrocytes on a resorbable polylactide three dimensional scaffold. *J Biomed Mater Res* 49:183–191
- Guilak F, Awad HA, Fermor B, Leddy HA, Gimble JM (2004) Adipose-derived adult stem cells for cartilage tissue engineering. *Biorheology* 41:389–399
- Guo J, Jourdan GW, McCallum DK (1989) Culture and growth characteristics of chondrocytes encapsulated in alginate beads. *Connect Tissue Res* 19:277–297
- Heng BC, Cao T, Lee EH (2004) Directing stem cell differentiation into the chondrogenic lineage in vitro. *Stem Cells* 22:1152–1167
- Johnstone B, Hering TM, Caplan AI, Goldberg VM, Yoo JU (1998) In vitro chondrogenesis of bone marrow-derived mesenchymal progenitor cells. *Exp Cell Res* 238:265–272
- Kang JY, Chung CW, Sung JH, Park BS, Choi JY, Lee SJ, Choi BC, Shim CK, Chung SJ, Kim DD (2009) Novel porous matrix of hyaluronic acid for the three-dimensional culture of chondrocytes. *Int J Pharm* 369:114–120
- Kern S, Eichler H, Stoeve J, Klüter H, Bieback K (2006) Comparative analysis of mesenchymal stem cells from bone marrow, umbilical cord blood, or adipose tissue. *Stem Cells* 24:1294–1301
- Kim WS, Park BS, Sung JH, Yang JM, Park SB, Kwak SJ, Park JS (2007) Wound healing effect of adipose-derived stem cells: a critical role of secretory factors on human dermal fibroblasts. *J Dermatol Sci* 48:15–24
- Knudson CB (2003) Hyaluronan and CD44: strategic players for cell-matrix interactions during chondrogenesis and matrix assembly. *Birth Defects Res C* 69:174–196
- Knudson W, Casey B, Nishida Y, Eger W, Kuettner KE, Knudson CB (2000) Hyaluronan oligosaccharides perturb cartilage matrix homeostasis and induce chondrocytic chondrolysis. *Arthritis Rheum* 43:1165–1174
- Lahiji A, Sohrabi A, Hungerford DS, Frondoza CG (2000) Chitosan supports the expression of extracellular matrix proteins in human osteoblasts and chondrocytes. *J Biomed Mater Res* 51:586–595
- Li WJ, Tuli R, Okafor C, Derfoul A, Danielson KG, Hall DJ, Tuan RS (2005) A three-dimensional nanofibrous scaffold for cartilage tissue engineering using human mesenchymal stem cells. *Biomaterials* 26:599–609
- Lin Y, Luo E, Chen X, Liu L, Qiao J, Yan Z, Li Z, Tang W, Zheng X, Tian W (2005) Molecular and cellular characterization during chondrogenic differentiation of adipose tissue-derived stromal cells in vitro and cartilage formation in vivo. *J Cell Mol Med* 9:929–939
- Lindenhayn K, Perka C, Spitzer RS, Heilmann HH, Pommerening K, Mennicke J, Sittinger M (1999) Retention of hyaluronic acid in alginate beads: aspects for in vitro cartilage engineering. *J Biomed Mater Res* 44:149–155
- Lohmann CH, Schwartz Z, Niederauer GG, Carnes DL Jr, Dean DD, Boyan BD (2000) Pretreatment with platelet derived growth factor-BB modulates the ability of costochondral resting zone chondrocytes incorporated into PLA/PGA scaffolds to form new cartilage in vivo. *Biomaterials* 21:49–61
- Ma HL, Hung SC, Lin SY, Chen YL, Lo WH (2003) Chondrogenesis of human mesenchymal stem cells encapsulated in alginate beads. *J Biomed Mater Res A* 64:273–281
- Miralles G, Baudoin R, Dumas D, Baptiste D, Hubert P, Stoltz JF, Dellacherie E, Mainard D, Netter P, Payan E (2001) Sodium alginate sponges with or without sodium hyaluronate: in vitro engineering of cartilage. *J Biomed Mater Res* 57:268–278
- Nehrer S, Breinan HA, Ramappa A, Shortkroff S, Young G, Minas T, Sledge CB, Yannas IV, Spector M (1997) Canine chondrocytes seeded in type I and II collagen implants investigated in vitro. *J Biomed Mater Res* 38:95–104
- Ochi M, Uchio Y, Tobita M, Kuriwaka M (2001) Current concepts in tissue engineering technique for repair of cartilage defect. *Artif Organs* 25:172–179
- Ponta H, Sherman L, Herrlich PA (2003) CD44: from adhesion molecules to signalling regulators. *Nat Rev Mol Cell Biol* 4:33–45
- Slevin M, Krupinski J, Kumar S, Gaffney J (1998) Angiogenic oligosaccharides of hyaluronan induce protein tyrosine kinase activity in endothelial cells and activate a cytoplasm signal transduction pathway resulting in proliferation. *Lab Invest* 78:987–1003
- Yoon IS, Chung CW, Sung JH, Cho HJ, Kim JS, Shim WS, Shim CK, Chung SJ, Kim DD (2011) Proliferation and chondrogenic differentiation of human adipose-derived mesenchymal stem cells in porous hyaluronic acid scaffold. *J Biosci Bioeng* 112:402–408
- Zuk PA, Zhu M, Mizuno H, Huang JW, Futrell J, Katz AJ, Benhaim P, Lorenz HP, Hedrick MH (2001) Multilineage cells from human adipose tissue: implications for cell-based therapies. *Tissue Eng* 7:211–228
- Zuk PA, Zhu M, Ashjian P, de Ugarte DA, Huang JI, Mizuno H, Alfonso ZC, Fraser JK, Benhaim P, Hedrick MH (2002) Human adipose tissue is a source of multipotent stem cells. *Mol Biol Cell* 13:4279–4295



Pharmaceutical nanotechnology

Chitosan oligosaccharide–arachidic acid-based nanoparticles for anti-cancer drug delivery

Ubonvan Termsarasab^{a,1}, Hyun-Jong Cho^{b,1}, Dong Hwan Kim^a, Saeho Chong^a, Suk-Jae Chung^a, Chang-Koo Shim^a, Hyun Tae Moon^{a,*}, Dae-Duk Kim^{a,*}

^a College of Pharmacy and Research Institute of Pharmaceutical Sciences, Seoul National University, Seoul 151-742, Republic of Korea

^b College of Pharmacy, Kangwon National University, Chuncheon 200-701, Republic of Korea

ARTICLE INFO

Article history:

Received 6 September 2012

Received in revised form 28 October 2012

Accepted 11 November 2012

Available online 19 November 2012

Keywords:

Arachidic acid

Chitosan oligosaccharide

Doxorubicin

Head and neck cancer

Self-assembly

ABSTRACT

Chitosan oligosaccharide–arachidic acid (CSOAA) conjugate was successfully synthesized and used for the development of self-assembled nanoparticles for doxorubicin (DOX) delivery. The molar substitution of AA on CSO and critical micelle concentration (CMC) of CSOAA were measured. Physicochemical properties of DOX-loaded CSOAA-based nanoparticles, such as particle size, zeta potential and morphology, were also characterized. The DOX-loaded CSOAA-based nanoparticles showed spherical shape with a mean diameter of 130 nm and positive charge. According to the result of *in vitro* release test, DOX-loaded CSOAA-based nanoparticles exhibited sustained and pH-dependent drug release profiles. The CSOAA showed negligible cytotoxicity in FaDu, human head and neck cancer, cells. Cellular uptake of DOX in FaDu cells was higher in the nanoparticle-treated group compared to the free DOX group. The anti-tumor efficacy of DOX-loaded nanoparticles was also verified in FaDu tumor xenografted mouse model. These results suggested that synthesized amphiphilic CSOAA might be used for the preparation of self-assembled nanoparticles for anti-cancer drug delivery.

© 2012 Elsevier B.V. All rights reserved.

1. Introduction

Polymeric nanoparticles have been widely investigated as drug carriers for anti-cancer agents (Cho et al., 2011; Choi et al., 2012; Kaida et al., 2010; Kolishetti et al., 2010; Yoon et al., 2012). Self-assembly based on amphiphilic polymer has been widely investigated because it has many interesting properties. Amphiphilic polymers can form stable nanoparticles composed of a hydrophobic core and a hydrophilic shell in an aqueous environment. Poorly water-soluble drugs can be encapsulated in the internal hydrophobic cavity, which can improve their solubility and bioavailability (Aliabadi et al., 2005; Kwon, 2003; Li and Tan, 2008). The nano-size and hydrophilic shell of these self-assembled nanoparticles can impede elimination by the reticuloendothelial system (RES) and have an enhanced permeability and retention (EPR) effect as a passive targeting strategy, leading to effective accumulation of drugs at the tumor region (Maeda et al., 2000).

Doxorubicin (DOX) is an anthracycline antibiotic that is commonly used in the treatment of various types of cancer, such as hematological malignancies, breast carcinomas, ovarian

carcinomas, bronchogenic carcinomas, and soft-tissue sarcomas. DOX has also exhibited therapeutic effects for head and neck cancer (Airoidi et al., 2008), which includes several types of tumor localized in the oral cavity, nose, throat, sinuses, and salivary glands (Cho et al., 2012a). The response rate for anti-cancer therapeutics is known to be relatively low in head and neck cancer, with a survival benefit of about 10 weeks for patients with recurrent/metastatic disease (Reuter et al., 2007). Although DOX shows high potential anti-cancer efficacy, its clinical application is limited because of its severe side effects, especially cardiotoxicity and myelosuppression (Kratz et al., 2007; Wildiers et al., 2008). Therefore, it is thought that tumor-targeting strategy can minimize these side effects (Cho et al., 2012b).

Chitosan (CS) is a linear cationic polysaccharide composed of randomly distributed β -(1–4)-linked D-glucosamine and N-acetyl-D-glucosamine units, produced by the deacetylation of chitin. CS has been regarded as an attractive material for the development of drug delivery systems due to its biocompatibility, biodegradability, and low toxicity (Kumar et al., 2004; Muzzarelli and Muzzarelli, 2005). Moreover, CS has free primary amino groups, allowing for further chemical modification. However, the major drawback of CS is its poor solubility at physiological pH. Recently, many researchers have investigated chitosan oligosaccharide (CSO), a low-molecular-weight CS, because it can be soluble in water and several organic solvents under physiologically relevant conditions (Vishu Kumar

* Corresponding authors. Tel.: +82 2 880 7870; fax: +82 2 873 9177.

E-mail addresses: htmoon@snu.ac.kr (H.T. Moon), ddkim@snu.ac.kr (D.-D. Kim).

¹ These authors have equally contributed.

et al., 2004). CSO has been modified with hydrophobic residues, such as alkyl groups, cholesterol, tocopherol, and deoxycholic acid (Chae et al., 2005). These hydrophobically modified CSOs can form self-assembled nanoparticles, which can be used as carriers for tumor-targeted drug and gene delivery.

In this study, arachidic acid (AA), as a fatty acid, was conjugated to a CSO backbone to make an amphiphilic CSO derivative. DOX was loaded into the self-assembled nanoparticles based on chitosan oligosaccharide–arachidic acid (CSOAA). The physicochemical properties of DOX-loaded CSOAA-based nanoparticles, such as particle size, zeta potential and morphology, and *in vitro* drug release behavior were investigated. *In vitro* cytotoxicity and cellular uptake efficiency were evaluated in head and neck cancer cells, and *in vivo* anti-tumor efficacy was also assessed in the head and neck cancer xenografted mouse model.

2. Materials and methods

2.1. Materials

Chitosan oligosaccharide (CSO; average molecular weight = 5 kDa, degree of acetylation >90%) was purchased from Kitto Life Co., Ltd. (Seoul, Korea). Arachidic acid (AA), 1-ethyl-3-(3-dimethylaminopropyl) carbodiimide (EDC), N-hydroxysuccinimide (NHS), and deuterium oxide were purchased from Sigma–Aldrich Co. (St. Louis, MO, USA). Dimethylsulfoxide- d_6 (DMSO- d_6) was purchased from Cambridge Isotope Laboratories Inc. (Andover, MA, USA). Doxorubicin hydrochloride (DOX HCl) was obtained from Boryung Pharmaceutical Co. (Seoul, Korea). Minimum essential medium (MEM), penicillin, streptomycin, and fetal bovine serum (FBS) were obtained from Gibco Life Technologies, Inc. (Grand Island, NY, USA). All other chemicals were of reagent grade and were used without further purification.

2.2. Synthesis and characterization of CSOAA

Amphiphilic CSOAA was synthesized from CSO and AA. Briefly, CSO (0.2 mmol) and AA (0.6 mmol) were dissolved separately in 20 ml DMSO each at 50 °C for 15 min. Carboxyl groups of AA were activated by adding EDC and NHS (1.5 mol/mol AA) and it was stirred at room temperature for 30 min. Then, activated AA solution was dripped into the CSO solution for 5 min. The coupling reaction was conducted for a further 12 h, and then 4 ml of deionized distilled water (DDW) was added. The pH of the mixture was adjusted to 3.5 with 1 N HCl and stirred for 30 min. The mixture was precipitated by adding acetone (ten times the volume of mixture) and centrifuged (8608 × g, 30 min) to remove unreacted AA. The precipitation step was repeated three times. Next, the precipitate was dispersed with DDW and dialyzed with dialysis membrane (molecular weight cut-off = 1 kDa; Spectrum Laboratories, Laguna Hills, CA, USA) against DDW for 24 h. The dialyzed products were lyophilized.

The conjugation of CSOAA was confirmed by Fourier transform infrared (FTIR) spectroscopy and ^1H -nuclear magnetic resonance (NMR) analyses. FTIR spectra were obtained with a JASCO FTIR 4200 spectrometer (JASCO Company Ltd., Hachioji, Japan) by KBr method. The ^1H NMR spectra were obtained using a Varian FT 500-MHz NMR spectrometer (Varian Inc., Palo Alto, CA, USA). Samples (15 mg/ml) were dissolved in DMSO- d_6 . The molar substitution (MS) of CSOAA, which is total number of moles of reacted AA per one mole of CSO, was determined by integration of the values of the proton peaks from the ^1H NMR spectra. MS of CSOAA was obtained using a linear regression line generated from standard samples with various molar ratios between AA and CSO (0.5:1, 1:1, 2:1, 3:1, and 4:1). The standard samples were prepared by homogeneously mixing CSO and AA in DDW/tetrahydrofuran (THF) mixture

(1:1, v/v). THF was removed by evaporation and the resultant was lyophilized. The ratio of integration area (1.23/1.81 ppm) of each standard sample was calculated.

2.3. Preparation and characterization of nanoparticles

To investigate the self-assembly behavior of CSOAA, the critical micelle concentration (CMC) of CSOAA was determined by using pyrene as a fluorescence probe. The fluorescence emission spectrum of pyrene (6×10^{-7} M) was recorded at 360–450 nm in the CSOAA concentration range from 10^{-4} to 1 mg/ml. The excitation wavelength was 334 nm and the slit openings for excitation and emission were set at 10 and 3 nm, respectively. The intensity ratio of the first peak (I_1 , 373 nm) to the third peak (I_3 , 384 nm) was calculated to determine the CMC.

Blank self-assembled nanoparticles were prepared by dissolving CSOAA in DDW, vortexing for 15 min, and filtering through a 0.2- μm syringe filter (Minisart RC 15; Sartorius Stedim Biotech GmbH, Goettingen, Germany).

DOX base was used as a hydrophobic drug and encapsulated into the CSOAA nanoparticles by a solvent evaporation method. To prepare DOX base according to a reported method (Cho et al., 2012b), DOX HCl was reacted with triethylamine in DMSO for 12 h, and then lyophilized. To make DOX-loaded nanoparticle, DOX base (1 mg) was dissolved in 1 ml DMSO and DDW mixture (1:1, v/v). CSOAA (7.5 mg) was added to that mixture and vortexed for 10 min. The solvent was evaporated under a nitrogen gas stream for 4 h at 70 °C. DOX-loaded CSOAA-based self-assembled nanoparticles were obtained by resuspending the polymer and drug composite film with 1 ml DDW. That suspension was gently stirred for 15 min and further heated at 70 °C for 15 min. Unloaded drug was eliminated with a 0.22- μm syringe filter.

The encapsulation efficiency (EE) of the DOX in nanoparticles was determined by disrupting DOX-loaded nanoparticles with 100× the volume of DMSO. DOX was analyzed quantitatively by Waters high-performance liquid chromatography (HPLC) system (Waters Co., Milford, MA, USA), equipped with a reversed-phase C-18 column (Xbridge RP18, 250 mm × 4.6 mm, 5 μm ; Waters Co.), a separation module (Waters e2695), and a fluorescence detector (Waters 2475). The mobile phase consisted of 0.1 M sodium acetate buffer (pH 4.0, adjusted with acetic acid) and acetonitrile (71:29, v/v), and the eluent was monitored at excitation and emission wavelengths of 470 nm and 565 nm, respectively, with a flow rate of 1.0 ml/min. The injection volume for drug analysis was 20 μl . The EE value was calculated using the following equation:

$$\text{EE (\%)} = \frac{\text{actual amount of DOX in nanoparticle}}{\text{theoretical amount of DOX in nanoparticle}} \times 100. \quad (1)$$

The mean diameter and zeta potential values of the blank nanoparticles and DOX-loaded nanoparticles were measured by a dynamic light scattering (DLS) method (ELS-Z, Photal; Otsuka Electronics Co. Ltd., Osaka, Japan). The morphological shapes of self-assembled nanoparticles were observed under transmission electron microscopy (TEM; LIBRA 120; Carl Zeiss, Oberkochen, Germany). The samples were placed on a copper grid coated with carbon film, dried at 20 °C, and photographed.

2.4. *In vitro* DOX release

In vitro release studies were performed in phosphate-buffered saline (PBS; pH 5.5, 6.8, and 7.4, adjusted with phosphoric acid) at 37 °C. DOX-loaded CSOAA-based nanoparticles (150 μl) were placed in a mini GeBA-flex tube (molecular weight cut-off = 12–14 kDa). That tube was then transferred to 10 ml release medium and kept in the horizontal shaker at 37 °C and 50 rpm of rotation speed. An aliquot (0.2 ml) of the release medium was

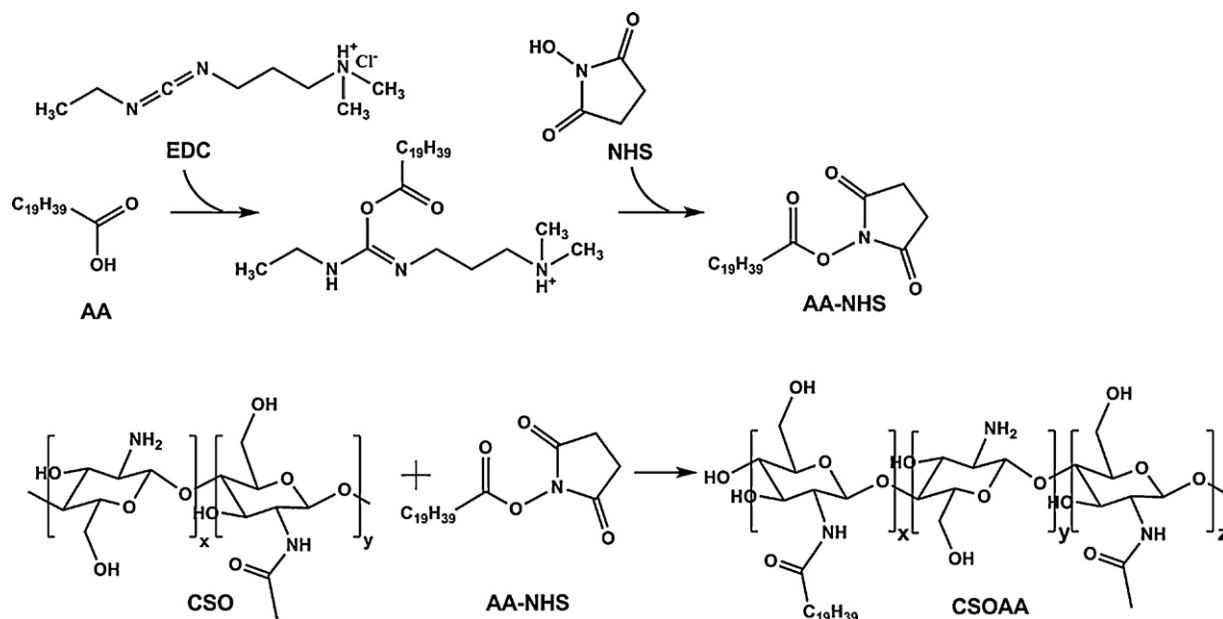


Fig. 1. Synthetic scheme of CSOAA.

periodically collected (at 1, 2, 3, 4, 6, 9, 12, 24, 48, 72, 96, 120, and 144 h) and the same volume of fresh medium was replaced. The released DOX was quantitatively analyzed by HPLC system.

2.5. *In vitro* cytotoxicity of CSOAA

FaDu cells were purchased from the Korean Cell Line Bank (Seoul, Korea). These cells were cultured in MEM containing 10% FBS, 100 U/ml penicillin, and 100 μ g/ml streptomycin at 37 °C under 5% CO₂ atmosphere and 95% relative humidity. The cytotoxicity of CSOAA was determined by a 3-(4,5-dimethylthiazol-2-yl)-5-(3-carboxymethoxyphenyl)-2-(4-sulfophenyl)-2H-tetrazolium (MTS)-based assay. Cells were seeded in 96-well plates at a density of 1.0×10^4 cells per well. After 24 h of incubation, the cell culture medium was replaced with 200 μ l medium containing various concentrations (5–500 μ g/ml) of CSOAA and incubated for 12 and 24 h. After discarding the culture medium, cells were treated with the MTS-based CellTiter 96 AQueous One Solution Cell Proliferation Assay Reagent (Promega Corp., Madison, WI, USA) at 37 °C for 4 h, according to the manufacturer's protocol. The spectrophotometric absorbance of samples was measured at a wavelength of 490 nm using an EMax Precision Microplate Reader (Molecular Devices, Sunnyvale, CA, USA).

2.6. *In vitro* cellular uptake

Cellular uptake efficiency was evaluated by flow cytometry analysis. FaDu cells were seeded in 6-well plates at a density of 6×10^5 cells per well and grown overnight at 37 °C. The culture medium was then removed, and the cells were incubated with free DOX or the DOX-loaded CSOAA-based nanoparticles at an equivalent DOX concentration (50 μ g/ml) for 1 h. After washing with PBS (pH 7.4) at least three times, the cells were detached and centrifuged. The supernatant was then removed and the cell pellets were resuspended with PBS containing 2% (v/v) FBS. DOX uptake was analyzed using a Calibur fluorescence-activated cell sorter equipped with CELLQuest software (Becton Dickinson Biosciences, San Jose, CA, USA).

2.7. *In vivo* anti-tumor efficacy

Female BALB/c nude mice (5 weeks old; Charles River) were used to prepare a tumor-bearing mouse model for evaluating anti-cancer efficacy. Mice were maintained in a light-controlled room kept at a temperature of 22 ± 2 °C and a relative humidity of $55 \pm 5\%$ (Animal Center for Pharmaceutical Research, College of Pharmacy, Seoul National University, Seoul, Korea). Experimental protocols used were approved by the Animal Care and Use Committee of the College of Pharmacy, Seoul National University. BALB/c nude mice bearing FaDu tumors were prepared by subcutaneous injection of 3×10^6 cells in the right back. Tumor size was measured with Vernier calipers and tumor volume (mm³) was calculated according to the following formula: volume = $0.5 \times$ longest diameter \times shortest diameter². Measuring tumor volume and weighing body weight started 10 days post-inoculation, when the tumor volume reached about 50–100 mm³. The mice were divided into three groups: control, DOX solution, and DOX-loaded CSOAA-based nanoparticles. Both DOX solution and DOX-loaded nanoparticles were injected intravenously at a dose of 25 mg/kg on days 6, 8, 11, and 13. The tumor volume and body weight were monitored for 18 days.

2.8. Statistical analysis

Statistical analyses were performed using analysis of variance. All experiments were performed at least three times and the data are presented as mean \pm standard deviation (SD).

3. Results

3.1. Synthesis and characterization of CSOAA

The CSOAA conjugate was synthesized by EDC- and NHS-mediated amide bond formation between the carboxylic group of AA and the amine group of CSO. The synthesis scheme is shown in Fig. 1. EDC can react with the carboxylic group of AA to form an EDC active ester, and the NHS ester intermediate forms rapidly. The intermediate can then react with the primary amine of CSO to form an amide bond.

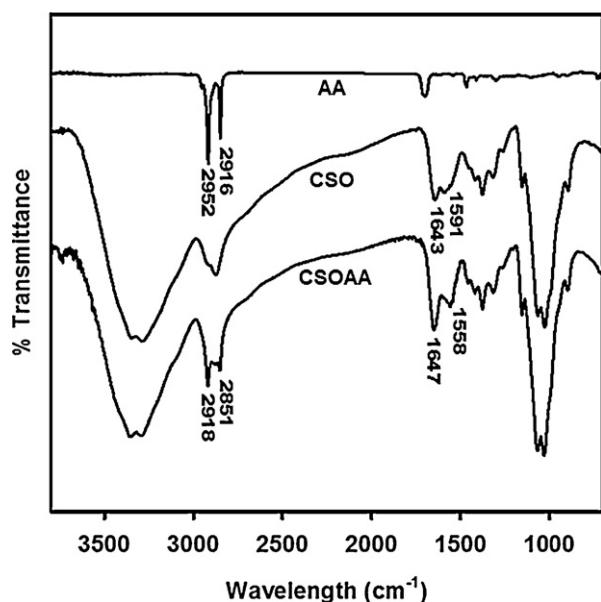


Fig. 2. FTIR spectra of AA, CSO, and CSOAA.

The structural characterization of CSOAA was performed using FTIR and ^1H NMR. The FTIR spectrum (Fig. 2) confirmed the synthesis of the CSOAA conjugate. Absorption bands of CSO at 1591 and 1643 cm^{-1} were assigned to N–H bending of the deacetylated amine ($-\text{NH}_2$) and carbonyl stretching of a non-deacetylated amide ($\text{NHC}=\text{OCH}_3$; amide I band), respectively. After the reaction, the amine peak at 1591 cm^{-1} of CSO disappeared and a new absorption band at 1558 cm^{-1} in the spectrum of CSOAA was observed, which was associated with the formation of a new amide bond (amide II band). Additionally, absorption bands at 2918 and 2851 cm^{-1} of CSOAA represented stretching vibrations of the acyl chain, $-\text{CH}_2-$ and $-\text{CH}_3$ of AA, respectively. The conjugation of AA to CSO was also confirmed by ^1H NMR analysis (Fig. 3). The ^1H NMR spectrum of CSOAA exhibited proton signals for both CSO and AA. Although the proton peaks of the glucosamine ring of CSO overlapped with the DMSO- d_6 solvent, the proton peaks at 0.86 and 1.23 ppm indicated

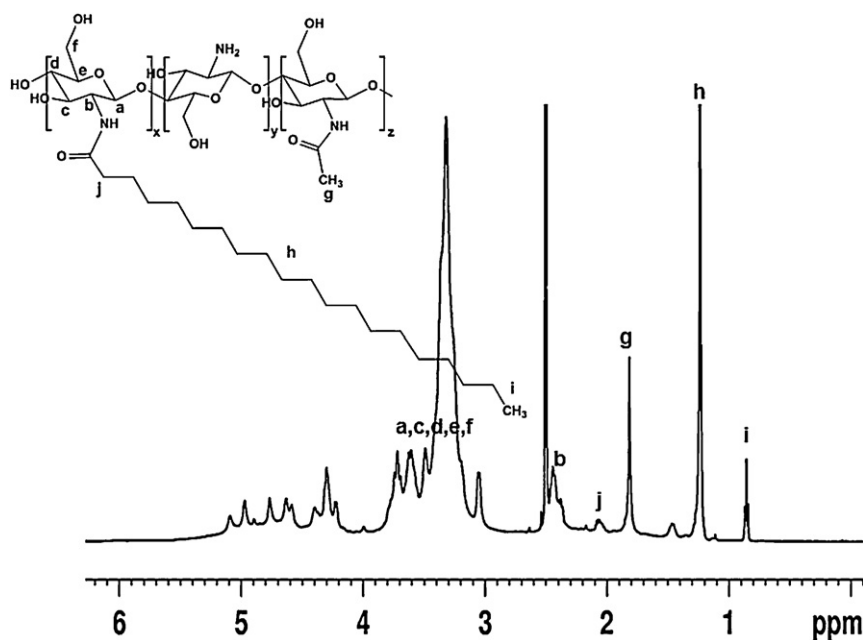


Fig. 3. ^1H NMR spectrum of CSOAA. CSOAA was dissolved in DMSO- d_6 for ^1H NMR analysis.

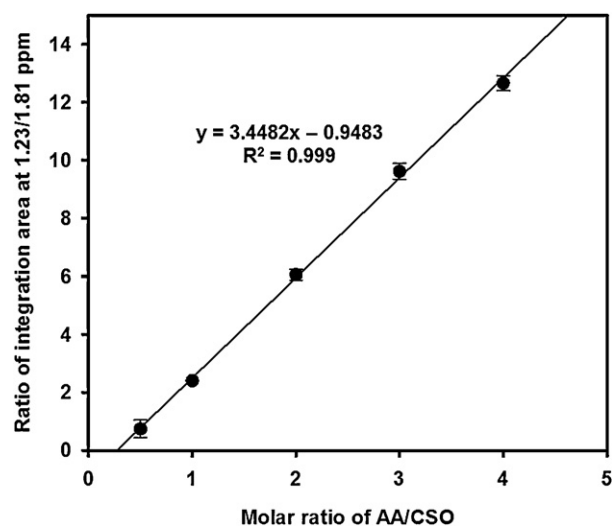


Fig. 4. The correlation between the ratio of integration area (1.23/1.81 ppm) and molar ratio of AA/CSO based on their physical mixture. Each point represents the mean \pm SD ($n = 3$).

a terminal methyl group ($-\text{CH}_3$) and an alkyl chain ($-\text{CH}_2-$) of AA, respectively. Furthermore, a new proton peak of $-\text{CH}_2-$ of AA linked with a carbonyl group was seen at 2.07 ppm in the ^1H NMR spectrum of the CSOAA conjugate, whereas that peak was absent in the spectrum of a physical mixture of CSO and AA (Supplementary Fig. 1S). This result indicated that AA was successfully conjugated to the CSO backbone via amide bond formation.

To calculate the MS of CSOAA, the homogeneous physical mixtures of CSO and AA (at different molar ratios) were prepared as standard samples and analyzed by ^1H NMR. As shown in Fig. 4, the linear regression line was generated by plotting the ratio of integration area between peak of the alkyl chain protons of AA ($\delta = 1.23\text{ ppm}$; $-\text{CH}_2-$) and the N-acetyl protons of CSO ($\delta = 1.81\text{ ppm}$; $\text{NH}-\text{CO}-\text{CH}_3$) according to the molar ratio of AA/CSO. The MS of CSOAA was 1 (mole of AA/mole of CSO), calculated from the equation of regression line with its ^1H NMR integration ratio (1.23/1.81 ppm), when the initial molar ratio

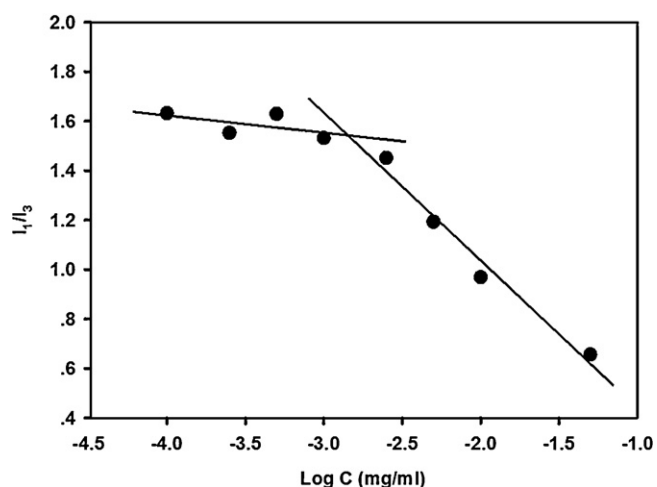


Fig. 5. Determination of the CMC of CSOAA. Fluorescence intensity ratio (I_{373}/I_{384}) was plotted against CSOAA concentration.

(AA/CSO) was 3 in the conjugation reaction. The chemical yield of CSOAA was 61.2%.

The self-assembly behavior of CSOAA in the aqueous phase was investigated by fluorescence measurements, using pyrene as a fluorescence probe (Fig. 5). CMC can be determined by measuring the intensity ratio (I_1/I_3) between the first (373 nm) and third (384 nm) emission peaks of pyrene according to the CSOAA concentration. As shown in Fig. 5, the CMC of CSOAA was 1.42 $\mu\text{g}/\text{ml}$.

3.2. Preparation and characterization of CSOAA-based self-assembled nanoparticles

Blank self-assembled nanoparticles (without drug loading) were prepared by dissolving CSOAA in the aqueous solution. The formation of nanoparticles was confirmed by measuring particle size and zeta potential values. To load DOX into the CSOAA-based nanoparticles, a solvent evaporation method was used. The mean diameter and zeta potential values were measured by DLS and are shown in Table 1. The mean diameter of blank nanoparticles was smaller than that of DOX-loaded nanoparticles (73.67 ± 3.91 nm vs. 130.00 ± 5.76 nm). The polydispersity index of the DOX-loaded nanoparticles was 0.23 ± 0.02 , indicating a narrow size distribution of nanoparticles (Fig. 6a). The zeta potential value was also increased slightly after loading DOX into the nanoparticles (from 7.58 ± 0.62 mV to 12.98 ± 0.55 mV). The spherical shape of the DOX-loaded CSOAA-based nanoparticles was observed by TEM (Fig. 6b). No aggregation of CSOAA-based nanoparticles was observed in that image. The loading amount of DOX in the nanoparticles was measured by HPLC analysis and the EE was $53.12 \pm 2.60\%$.

3.3. In vitro DOX release

DOX release patterns from nanoparticles were investigated under different pH conditions (pH 5.5, 6.8 and 7.4) at 37°C (Fig. 7). DOX release from the CSOAA-based nanoparticles was monitored for 6 days. Sustained drug release was observed and it was dependent on the pH of the release medium. About 30% of DOX was released in the first 12 h under all pH conditions. After that, the amounts of DOX released from CSOAA-based nanoparticles increased as the pH value of the releasing medium decreased. After 6 days, DOX was completely released at pH 5.5; in contrast, 78% and 64% of DOX was released at pH 6.8 and 7.4, respectively.

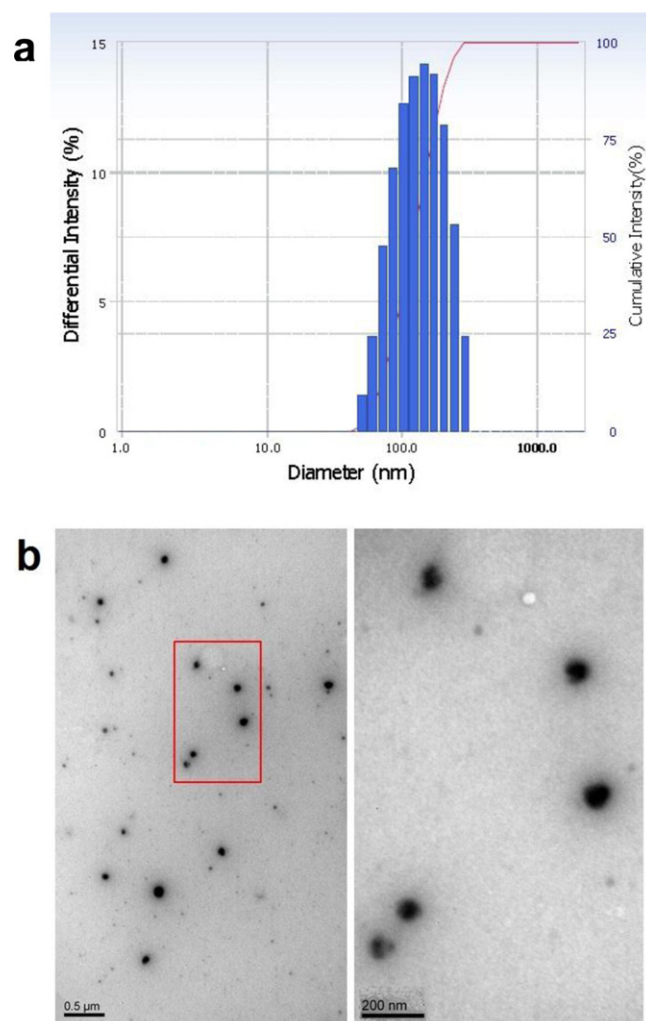


Fig. 6. Morphology and size distribution of DOX-loaded CSOAA-based nanoparticles. (a) The size distribution of DOX-loaded CSOAA-based nanoparticles was determined by dynamic light scattering. The CSOAA:DOX weight ratio was 7.5:1. (b) TEM images of DOX-loaded CSOAA-based nanoparticles were shown. Bar lengths are 500 (left) and 200 (right) nm, respectively.

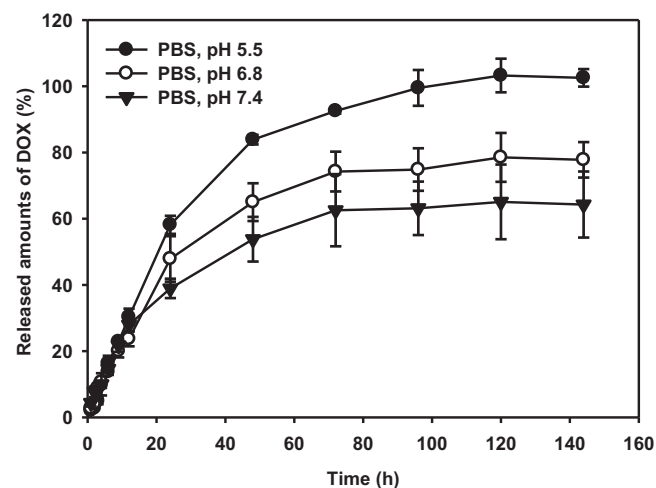


Fig. 7. In vitro DOX release profiles from CSOAA-based self-assembled nanoparticles. Drug release profiles from CSOAA:DOX = 7.5:1 formulation at different pH conditions (pH 5.5, 6.8, and 7.4) are shown. Each point represents the mean \pm SD ($n = 3$).

Table 1
Characteristics of CSOAA-based nanoparticles.

Formulation	Mean diameter (nm, mean \pm SD)	Polydispersity index	Zeta potential (mV)	Encapsulation efficiency (%)
Blank nanoparticles	73.67 \pm 3.91	0.32 \pm 0.01	7.58 \pm 0.62	–
CSOAA:DOX (7.5:1)	130.00 \pm 5.76	0.23 \pm 0.02	12.98 \pm 0.55	53.12 \pm 2.60

Values are presented as mean \pm SD ($n \geq 3$).

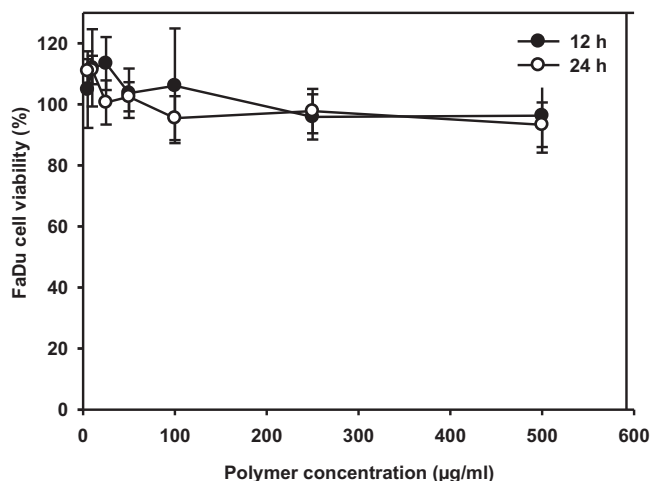


Fig. 8. *In vitro* cytotoxicity tests of CSOAA in FaDu cells. Various concentrations of CSOAA were incubated for 12 and 24 h in FaDu cells. Cell viability (%) was determined by an MTS-based assay. Each point represents the mean \pm SD ($n = 4$).

3.4. *In vitro* cytotoxicity test

To examine the cytotoxicity of CSOAA, cell viability was measured in FaDu cells, a head and neck cancer cell line. The cells were treated with various concentrations of CSOAA for 12 and 24 h. As shown in Fig. 8, FaDu cell viability (%) was over 90% for all CSOAA concentrations tested. Thus, it can be concluded that CSOAA had no severe toxicity for FaDu cells.

3.5. *In vitro* cellular uptake study

The cellular uptake efficiency of DOX in FaDu cells was investigated by flow cytometry. Fluorescence intensity was assumed to be

proportional to the amount of DOX internalized into the cells. Fig. 9 shows that higher amount of DOX from CSOAA-based nanoparticles was taken up into the cells than from the DOX solution group.

3.6. *In vivo* anti-tumor efficacy

In vivo anti-tumor efficacy of DOX-loaded nanoparticles was assessed in a FaDu tumor-bearing mouse model. DOX solution and DOX-loaded CSOAA-based nanoparticles were injected intravenously on days 6, 8, 11, and 13. Tumor volume (mm^3) and body weight (g) were monitored for 18 days. As shown in Fig. 10a, tumor growth inhibition in the DOX-loaded nanoparticle-treated group was significantly higher than in either the DOX solution-treated group or the control group ($p < 0.05$). After 18 days of treatment with DOX solution or DOX-loaded nanoparticles, tumor volumes were $44.63 \pm 9.02\%$ and $25.24 \pm 5.61\%$ of that for control group. No significant difference in body weight change was observed among the three groups; control, DOX solution-, and DOX-loaded nanoparticle-treated groups (Fig. 10b).

4. Discussion

In this study, CSOAA was successfully synthesized as a hydrophobically modified CSO for the preparation of self-assembled nanoparticles. The synthesis of CSOAA conjugate was confirmed by ^1H NMR analysis, but accurate substitution ratio (AA to CSO) might not be obtained from ^1H NMR spectrum of CSOAA. From ^1H NMR analysis of CSOAA, the proton peak of the glucosamine ring of CSO could be overlapped with the solvent peak and deacetylation degree of CSO was not obviously determined. Because of these limitations, the correlation between the integration ratio (1.23/1.81 ppm) and molar ratio of AA/CSO, based on physical mixture, was evaluated in this investigation (Fig. 4). With the input of the integration ratio (1.23/1.81 ppm) of CSOAA conjugate into this regression line, the stoichiometric ratio of CSOAA can

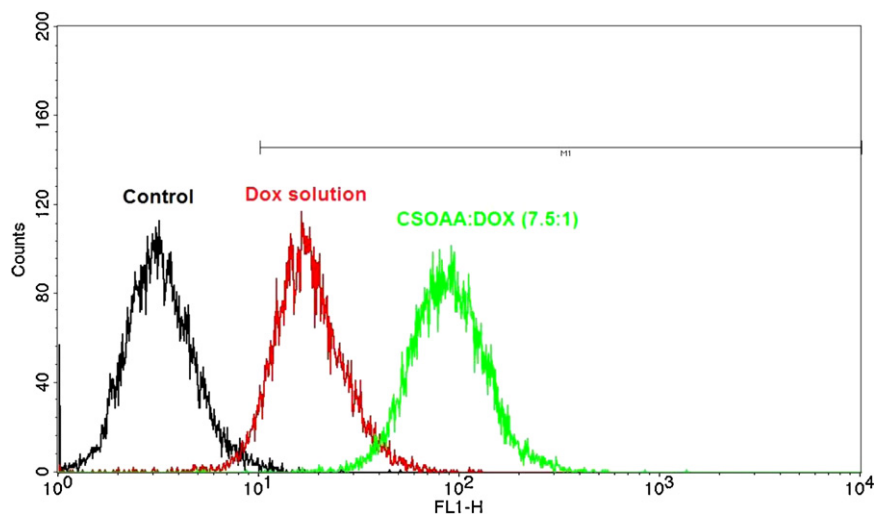


Fig. 9. Cellular uptake efficiency of DOX analyzed by flow cytometry. DOX solution and DOX-loaded nanoparticles were incubated for 1 h. The colors indicate each experimental group (black: control, red: DOX solution group, green: DOX-loaded nanoparticle group). (For interpretation of the references to color in this figure legend, the reader is referred to the web version of this article.)

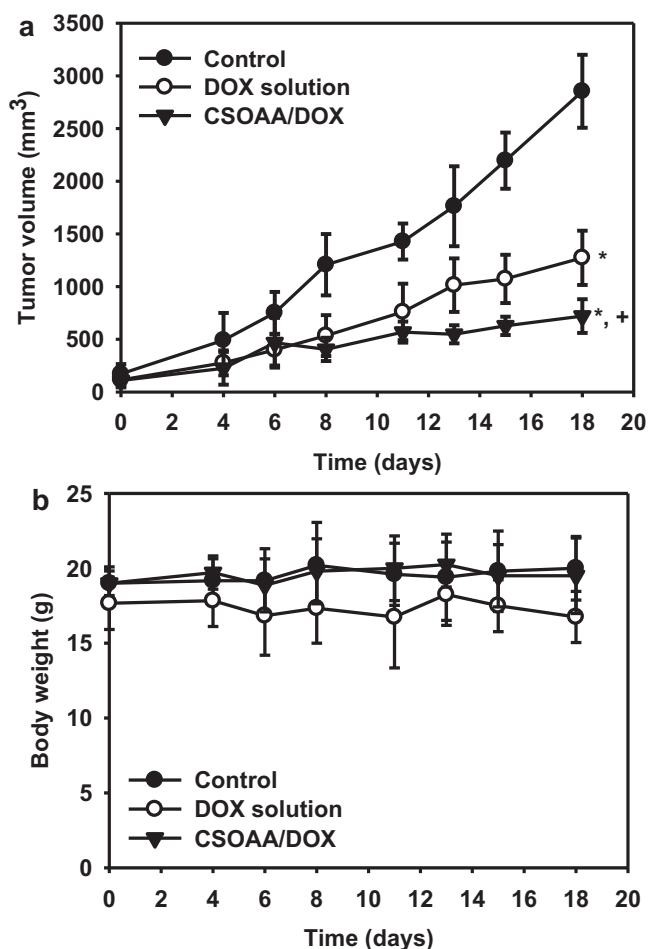


Fig. 10. Anti-tumor efficacy test of DOX-loaded CSOAA-based nanoparticles in a FaDu tumor-bearing BALB/c nude mouse model. (a) Tumor volume (mm³) profiles according to the time (days) for 18 days were shown. DOX solution and DOX-loaded nanoparticles were injected intravenously on days 6, 8, 11, and 13. Each point indicates the mean \pm SD ($n \geq 4$). (b) Body weight (g) was monitored. Each point indicates the mean \pm SD ($n \geq 4$). * $P < 0.05$ vs. control group; + $P < 0.05$ vs. DOX solution group.

be determined more accurately. It is assumed that established assay (Fig. 4) could help identify the synthesis of CSOAA and calculate substitution ratio. The CMC value is also an important characteristic of micellar structured nanoparticle. The CMC value of CSOAA was significantly lower than those of low-molecular-weight surfactants in water (Lee et al., 1998). It can be concluded that CSOAA can form stable nanoparticulate structures at its low concentration after dilution with a large volume of body fluids.

The CSOAA synthesized could readily produce self-assembled nanoparticles in aqueous solution because of its amphiphilic property. The AA part could constitute an internal hydrophobic core, while CSO could provide a hydrophilic outer shell of the nanoparticles. The DOX-loaded CSOAA-based self-assembled nanoparticles were prepared by a solvent evaporation method. This method can provide several advantages over dialysis methods, such as the short preparation period and high drug loading efficiency (Park et al., 2004). DOX-loaded CSOAA-based nanoparticles exhibited <200 nm of mean diameter and narrow size distribution, high drug encapsulation efficiency, and negligible cytotoxicity. Because of these properties, it is assumed that DOX-loaded CSOAA-based nanoparticles can effectively accumulate in the tumor region via the EPR effect and exhibit reduced uptake by RES (Maeda et al., 2000; Yuan et al., 1995).

The sustained and pH-dependent drug release patterns from the CSOAA-based nanoparticles developed were observed (Fig. 7).

Sustained drug release can lead to reduced *in vivo* drug clearance and maintenance of effective drug concentrations for tumor growth inhibition. Additionally, larger amount of DOX was released at acidic pH, simulating the endocytic compartment of cancer cells, compared with normal pH condition (pH 7.4). This difference may have been due to the slack structure of the nanoparticle, following protonation of amino groups in CSO and the higher solubility of DOX at an acidic pH. These results indicate that DOX-loaded CSOAA-based nanoparticles can be highly accumulated and release a large amount of drug in tumor tissues, with less DOX delivery to non-tumor regions. Moreover, enhanced drug release at pH 5.5 can imply endosomal escape of the drug and its improved transport to the cell nucleus.

As shown in Fig. 9, larger amount of DOX from nanoparticle-treated group was taken up to the cells compared to that from DOX solution group. This result may be explained by the interaction between the positively charged surface of the CSOAA-based nanoparticle and the negatively charged cellular membrane, and subsequent endocytosis of nanoparticles (Chavanpatil et al., 2006; Lee et al., 2011; Zauner et al., 1998). Furthermore, fatty acid-modified CS nanoparticles have been reported to form self-assembled nanoparticles with a multi-hydrophobic core (You et al., 2007). A hydrophobic minor core may help the internalization of nanoparticles into the cells by inserting fatty acids into the cell membrane.

FaDu cells were selected as a head and neck cancer cell line for this investigation. As shown in Fig. 10a, DOX-loaded CSOAA-based nanoparticles exhibited significant inhibitory effects on FaDu tumor growth, compared with both the control and DOX solution-treated groups. The physicochemical properties of drug-loaded nanoparticles, sustained drug release, and passive targeting, via mainly an EPR effect, may explain the efficient tumor growth inhibition by DOX-loaded CSOAA-based nanoparticles. In conclusion, the self-assembled CSOAA-based nanoparticle developed can be used as an anti-cancer drug delivery system, especially for head and neck cancer therapy.

5. Conclusions

CSOAA was synthesized for the preparation of self-assembled nanoparticles for DOX delivery. Its CMC value was relatively low and it could form self-assembled nanoparticles in an aqueous environment with a narrow size distribution. DOX-loaded CSOAA-based nanoparticles showed a sustained and pH-dependent drug release profile. It seemed that the nanoparticulate structure and drug release profile of the nanoparticles influenced on the cellular uptake and anti-tumor activity. DOX-loaded CSOAA-based nanoparticles significantly inhibited FaDu tumor growth *in vivo*. Considering all experimental results in this study, CSOAA-based self-assembled nanoparticles may be a promising carrier for anti-cancer drug delivery.

Acknowledgements

This work was supported by the National Research Foundation of Korea (NRF) grant funded by the Korean government (MEST) (No. 2011-0030635) and the MarineBio Research Program (NRF-C1ABA001-2011-0018561).

Appendix A. Supplementary data

Supplementary data associated with this article can be found, in the online version, at <http://dx.doi.org/10.1016/j.ijpharm.2012.11.018>.

References

- Airoldi, M., Cattel, L., Milla, P., Pedani, F., Garzaro, M., Dosio, F., 2008. Paclitaxel and pegylated liposomal doxorubicin in recurrent head and neck cancer: clinical and unexpected pharmacokinetic interactions. *Anticancer Res.* 28, 2519–2527.
- Aliabadi, H.M., Brocks, D.R., Lavasanifar, A., 2005. Polymeric micelles for the solubilization and delivery of cyclosporine A: pharmacokinetics and biodistribution. *Biomaterials* 26, 7251–7259.
- Chae, S.Y., Son, S., Lee, M., Jang, M.K., Nah, J.W., 2005. Deoxycholic acid-conjugated chitosan oligosaccharide nanoparticles for efficient gene carrier. *J. Control. Release* 109, 330–344.
- Chavanpatil, M.D., Khadair, A., Panyam, J., 2006. Nanoparticles for cellular drug delivery: mechanisms and factors influencing delivery. *J. Nanosci. Nanotechnol.* 6, 2651–2663.
- Cho, H.J., Chong, S., Chung, S.J., Shim, C.K., Kim, D.D., 2012a. Poly-L-arginine and dextran sulfate-based nanocomplex for epidermal growth factor receptor (EGFR) siRNA delivery: its application for head and neck cancer treatment. *Pharm. Res.* 29, 1007–1019.
- Cho, H.J., Yoon, H.Y., Koo, H., Ko, S.H., Shim, J.S., Lee, J.H., Kim, K., Kwon, I.C., Kim, D.D., 2011. Self-assembled nanoparticles based on hyaluronic acid-ceramide (HA-CE) and Pluronic® for tumor-targeted delivery of docetaxel. *Biomaterials* 32, 7181–7190.
- Cho, H.J., Yoon, I.S., Yoon, H.Y., Koo, H., Jin, Y.J., Ko, S.H., Shim, J.S., Kim, K., Kwon, I.C., Kim, D.D., 2012b. Polyethylene glycol-conjugated hyaluronic acid-ceramide self-assembled nanoparticles for targeted delivery of doxorubicin. *Biomaterials* 33, 1190–1200.
- Choi, J.S., Seo, K., Yoo, J.W., 2012. Recent advances in PLGA particulate systems for drug delivery. *J. Pharm. Invest.* 42, 155–163.
- Kaida, S., Cabral, H., Kumagai, M., Kishimura, A., Terada, Y., Sekino, M., Aoki, I., Nishiyama, N., Tani, T., Kataoka, K., 2010. Visible drug delivery by supramolecular nanocarriers directing to single-platformed diagnosis and therapy of pancreatic tumor model. *Cancer Res.* 70, 7031–7041.
- Kolishetti, N., Dhar, S., Valencia, P.M., Lin, L.Q., Karnik, R., Lippard, S.J., Langer, R., Farokhzad, O.C., 2010. Engineering of self-assembled nanoparticle platform for precisely controlled combination drug therapy. *Proc. Natl. Acad. Sci. U. S. A.* 107, 17939–17944.
- Kratz, F., Ehling, G., Kauffmann, H., Unger, C., 2007. Acute and repeat-dose toxicity studies of the (6-maleimidocaproyl) hydrazone derivative of doxorubicin (DOXO-EMCH), an albumin-binding prodrug of the anticancer agent doxorubicin. *Hum. Exp. Toxicol.* 26, 19–35.
- Kumar, M., Muzzarelli, R.A.A., Muzzarelli, C., Sashiwa, H., Domb, A., 2004. Chitosan chemistry and pharmaceutical perspectives. *Chem. Rev.* 104, 6017–6084.
- Kwon, G.S., 2003. Polymeric micelles for delivery of poorly water-soluble compounds. *Crit. Rev. Ther. Drug Carrier Syst.* 20, 357–403.
- Lee, J.Y., Choi, Y.S., Suh, J.S., Kwon, Y.M., Yang, V.C., Lee, S.J., Chung, C.P., Park, Y.J., 2011. Cell penetrating chitosan/doxorubicin/TAT conjugates for efficient cancer therapy. *Int. J. Cancer* 128, 2470–2480.
- Lee, K., Kwon, I., Kim, Y.H., Jo, W., Jeong, S., 1998. Preparation of chitosan self-aggregates as a gene delivery system. *J. Control. Release* 51, 213–220.
- Li, L., Tan, Y.B., 2008. Preparation and properties of mixed micelles made of Pluronic polymer and PEG-PE. *J. Colloid Interface Sci.* 317, 326–331.
- Maeda, H., Wu, J., Sawa, T., Matsumura, Y., Hori, K., 2000. Tumor vascular permeability and the EPR effect in macromolecular therapeutics: a review. *J. Control. Release* 65, 271–284.
- Muzzarelli, R., Muzzarelli, C., 2005. Chitosan chemistry: relevance to the biomedical sciences. *Adv. Polym. Sci.* 186, 151–209.
- Park, J.H., Kwon, S., Nam, J.O., Park, R.W., Chung, H., Seo, S.B., Kim, I.S., Kwon, I.C., Jeong, S.Y., 2004. Self-assembled nanoparticles based on glycol chitosan bearing 5 beta-cholanic acid for RGD peptide delivery. *J. Control. Release* 95, 579–588.
- Reuter, C.W., Morgan, M.A., Eckardt, A., 2007. Targeting EGF-receptor-signalling in squamous cell carcinomas of the head and neck. *Br. J. Cancer* 96, 408–416.
- Vishu Kumar, A.B., Varadaraj, M.C., Lalitha, R.G., Tharanathan, R.N., 2004. Low molecular weight chitosans: preparation with the aid of papain and characterization. *Biochim. Biophys. Acta* 1670, 137–146.
- Wildiers, H., Jurcut, R., Ganame, J., Herbots, L., Neven, P., De Backer, J., Denys, H., Cocquyt, V., Rademakers, F., Voigt, J.U., 2008. A pilot study to investigate the feasibility and cardiac effects of pegylated liposomal doxorubicin (PL-DOX) as adjuvant therapy in medically fit elderly breast cancer patients. *Crit. Rev. Oncol. Hematol.* 67, 133–138.
- Yoon, H.Y., Koo, H., Choi, K.Y., Lee, S.J., Kim, K., Kwon, I.C., Leary, J.F., Park, K., Yuk, S.H., Park, J.H., Choi, K., 2012. Tumor-targeting hyaluronic acid nanoparticles for photodynamic imaging and therapy. *Biomaterials* 33, 3980–3989.
- You, J., Hu, F.Q., Du, Y.Z., Yuan, H., Ye, B.F., 2007. High cytotoxicity and resistant-cell reversal of novel paclitaxel loaded micelles by enhancing the molecular-target delivery of the drug. *Nanotechnology* 18, 495101.
- Yuan, F., Dellian, M., Fukumura, D., Leunig, M., Berk, D.A., Torchilin, V.P., Jain, R.K., 1995. Vascular permeability in a human tumor xenograft: molecular size dependence and cutoff size. *Cancer Res.* 55, 3752–3756.
- Zauner, W., Ogris, M., Wagner, E., 1998. Polylysine-based transfection systems utilizing receptor-mediated delivery. *Adv. Drug Deliv. Rev.* 30, 97–113.

이중 가교제 또는 알긴산에 의해 물리적인 안정성이 향상된 히알루론산 마이크로입자의 제조

김동환 · 송충길 · Prabagar Balakrishnan · 박충근* · 최애진* · 정석재 · 심창구 · 김대덕#
서울대학교 약학대학 약제학과, *농촌진흥청 국립원예특작과학원 인삼특작부 약용작물과
(Received October 21, 2010; Revised February 4, 2011; Accepted February 11, 2011)

Preparation of Hyaluronic Acid Microspheres with Enhanced Physical Stability by Double Cross-link or Alginate

Dong-Hwan Kim, Chung Kil Song, Prabagar Balakrishnan, Chun-Geon Park*, Ae-Jin Choi*,
Suk-Jae Chung, Chang-Koo Shim and Dae-Duk Kim#

College of Pharmacy, Seoul National University, Seoul 151-742, Korea

*Department of Herbal Crop Research, National Institute of Horticultural & Herbal Science, RDA, Eumseong 369-873, Korea

Abstract — Hyaluronic acid (HA) is a natural polymer consisting of disaccharide units of D-glucuronic acid and N-acetyl-D-glucosamine. It has a great potential and success in cosmetic and biomedical applications. However, native HA is highly soluble and easily metabolized by enzymes such as hyaluronidase. Thus, various studies have been reported on modifying the physicochemical properties of HA, while maintaining its biocompatibility. For controlled drug delivery, many trials for fabricating HA microspheres were achieved under chemical reaction. The HA microspheres fabricated to improve the physical stability of HA using adipic acid dihydrazide (ADH) by cross-linking reaction has been reported earlier, however it lacks the desired physical stability and rapidly decomposes by swelling or enzymes. Therefore, we prepared double cross-linked HA microspheres (DC-HA microspheres) and alginate containing HA microspheres (AC-HA microspheres) to enhance its physicochemical properties. DC-HA microspheres were prepared using trisodium trimetaphosphate (STMP) under cross-linking reaction after ADH cross-linking reaction. AC-HA microspheres were prepared by adding alginate as a networking polymer. These microspheres were characterized by morphology, particle size, zeta potential, stability against hyaluronidase. Results showed that the DC-HA and AC-HA microspheres are more stable than that of HA microspheres.

Keywords □ hyaluronic acid, microsphere, cross-linker, adipic acid dihydrazide, trisodium trimetaphosphate, alginic acid

히알루론산(hyaluronic acid, HA)은 아미노산과 우론산으로 이루어진 다당류의 하나로 고등동물의 세포외 기질이나 연결조직, 관절과 눈의 초자체나 탯줄 등에 존재하는 생체 내 물질이며, 글루쿠론산과 N-아세틸글루코사민이 반복되는 구조로 분자량이 10만~500만 정도되는 고분자 화합물이다(Fig. 1).¹⁻³⁾ 히알루론산은 세균의 침입이나 독물의 침투를 막고, 세포 부착 및 염증 반응 조절에 관여할 뿐 아니라, 관절 내에서는 윤활액의 역할을 하는 특징을 가진다.⁴⁻⁷⁾

히알루론산은 생체 내 구성물질이기 때문에 면역성을 유발하지 않고 생체적합성과 생분해성의 특징을 가져 조직공학이나 약

물전달시스템에 적용시키기에 적합한 물질로 많은 연구가 진행되고 있으며, 필러, 상처치료 그리고 약물의 수송체 등의 여러 방면에서 이용되고 있다.^{8,9)} 그러나 히알루론산은 프리라디칼에 의해 분해되거나 히알루노니다제(hyaluronidase)와 같은 효소에 의

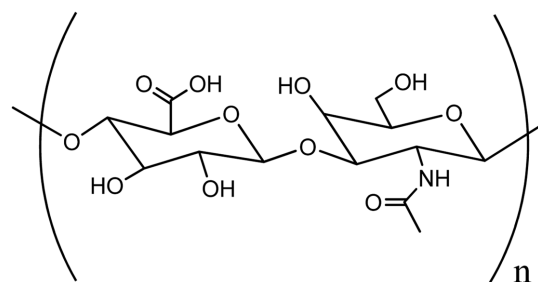


Fig. 1 – Chemical structure of hyaluronic acid.

#본 논문에 관한 문의는 저자에게로
(전화) 02-880-7870 (팩스) 02-873-9177
(E-mail) ddkim@snu.ac.kr

해 분해되어 생체내 안정성이 낮은 단점을 지니고 있다. 따라서 많은 연구자들이 히알루론산의 생체적합성을 유지하면서 안정성을 증가시키는 방법으로 물리화학적인 성질을 변화시켜 적용하고 있다. 대표적인 히알루론산의 생체 내 안정성을 증가시키는 방법으로 가교제를 이용하여 히알루론산 마이크로입자 또는 수화젤을 제조하여 약물을 전달하거나 지지체로 사용하는 연구가 많이 진행되고 있으며,^{10,11)} 기존의 1차 가교로 만들어진 히알루론산 지지체에 2차 가교를 통하여 물리적 안정성을 증진시키려는 연구가 진행되었다.^{12,13)} 그러나 약물전달체로 개발된 히알루론산 마이크로입자의 물리적 특성을 상승시킬 수 있는 방법에 대한 연구는 상대적으로 많은 연구가 진행되어있지 않은 상태이다.

본 연구에서는 2차 가교를 통해 히알루론산 겔을 형성하던 방법을 마이크로입자의 제조에 처음으로 적용해 보고자 하였다. 기존에 알려진 히알루론산 마이크로입자의 제조방법 중 하나인 가교제 아디프산디하이드라지드(adipic acid dihydrazide, ADH)를 통하여 마이크로 입자를 제조한 후 트리메타인산삼나트륨(trisodium trimetaphosphate, STMP)으로 2차 가교반응을 시키거나 알긴산을 추가하여 히알루론산 마이크로입자 내부에 네트워크 폴리머를 형성하여 생체내 안정성을 높이고자 하였다.¹⁴⁾ 제조된 히알루론산 마이크로입자들은 물리적 성질 및 히알루노니다제에 대한 저항성 등을 측정하여 약물수송체로서의 가능성을 평가하였다.

실험방법

시약 및 기기

히알루론산(hyaluronic acid, 1040 kDa)은 Shandong Freda Biochem(jinan, 중국)에서 구입하였다. 미네랄오일(mineral oil), 소르비탄 모노올레이트(Span 80)은 Samchun pure chemical(한국)에서 구입하였고, 아디프산디하이드라지드(Adipic acid dihydrazide, ADH), 트리메타인산삼나트륨(Trisodium Trimetaphosphate, STMP), 알긴산(alginic acid), 에틸-3-[3-디메틸 아미노] 프로필 카르보디이미드(ethyl-3-[3-dimethyl amino] propyl carbodiimide, EDC), 히알루노니다제(Hyaluronidase)는 Sigma-Aldrich(St Louis, MO, 미국)에서 구입하였다. 이소프로필알코올(isopropyl alcohol, IPA)은 Fisher scientific Inc(미국)에서 구입하였고 염화칼슘(CaCl₂)은 Yakuri pure chemicals(Kyoto, 일본)에서 구입하여 사용하였으며, 그 외의 시약은 특급 또는 1급을 사용하였다. 기기는 교반기(mechanical stirrer)를 Daihan scientific Co.(한국)에서 구입하여 사용하였고, 입도분석기 및 제타전위측정기(ELS-Z)는 Otsuka Electronics Co.(Hirakata, 일본)에서 구입하였으며, 전자주사현미경(scanning electronic microscopy, SEM)은 JEOL(Tokyo, 일본)사의 JSM-5310LV 모델을 사용하였다.

히알루론산 마이크로입자의 제조

히알루론산 마이크로입자(HA microspheres)의 제조는 에멀전 가교반응을 통하여 진행하였다. 가교제 ADH를 25 mg 포함한 5 ml 히알루론산 수용액(0.5%(w/v))을 400 mg의 span 80이 들어 있는 20 ml 미네랄 오일에 첨가한 후 교반기(기계)를 이용하여 1000 rpm의 속도로 교반하여 히알루론산 W/O 에멀전을 형성하였다. 교반을 시작하지 30분 후, 30 mg의 EDC(0.5 ml)을 상기 에멀전에 서서히 가하여 완전히 분산되게 한 후 HCl(0.1 N, 0.1 ml)를 서서히 가하여 상온에서 24시간 동안 가교반응을 진행하였다(Fig. 2a). 24시간 후 30 ml의 IPA를 넣고 1500 rpm에서 5분간 원심분리하여 히알루론산 마이크로입자를 수득한 후 IPA를 이용한 세척과정을 3번 반복하였다. 수득한 히알루론산 마이크로입자에 남아있는 용매는 동결건조과정을 통하여 완전히 제거하여 HA microspheres를 얻었다.

이중 가교된 히알루론산 마이크로입자의 제조

이중 가교된 히알루론산 마이크로입자(double-crosslinked HA microspheres, DC-HA microspheres)는 1차 가교제인 25 mg의 ADH와 2차 가교제인 25 mg의 STMP를 포함하는 5 ml 히알루론산 수용액(0.5%(w/v))을 상기 언급된 히알루론산 마이크로입자 제조방법과 동일하게 ml 미네랄 오일에 가하여 W/O 에멀전을 형성하여 1차 가교반응을 진행하였다. 1차 가교반응 후 NaOH(0.1 N, 0.5 ml)를 넣어 약 알칼리 환경에서 3시간 동안 STMP의 이중가교 반응을 진행하였다(Fig. 2b). 2차 반응 후 IPA를 이용하여 상기 언급된 방법과 같이 세척한 후 동결건조하여 DC-HA microspheres를 얻었다.

알긴산을 포함한 히알루론산 마이크로입자의 제조

알긴산을 포함한 히알루론산 마이크로입자(Alginate containing HA microsphere, AC-HA microsphere)는 25 mg의 가교제(ADH)가 포함된 5 ml 히알루론산 : 알긴산나트륨(8:2, 7:3, 5:5) 수용액(0.5%(w/v))을 준비한 후 상기 언급된 히알루론산 마이크로입자 제조방법과 동일하게 W/O 에멀전을 형성하여 가교반응을 진행하였다. 가교반응 후 마이크로입자내에 폴리머 네트워크 형성을 위하여 알긴산의 반응물질인 CaCl₂(0.1 N, 0.1 ml)을 넣어 3시간 동안 반응시킨 후 IPA를 이용하여 상기 언급된 방법과 같이 세척한 후 동결건조하여 알긴산이 포함된 AC-HA microspheres를 얻었다.

마이크로입자의 물리적 특성 평가

제조된 마이크로입자의 형태는 gold coating 후 주사전자현미경 이용하여 측정하였다. 또한 입자의 수화안정성을 평가하기 위하여 제조된 마이크로입자를 PBS에서 30분 동안 수화한 후, 건조하여 gold coating 하고 주사전자현미경을 이용하여 측정하였다. 제조된 마이크로입자의 크기는 주사전자현미경의 이미지를

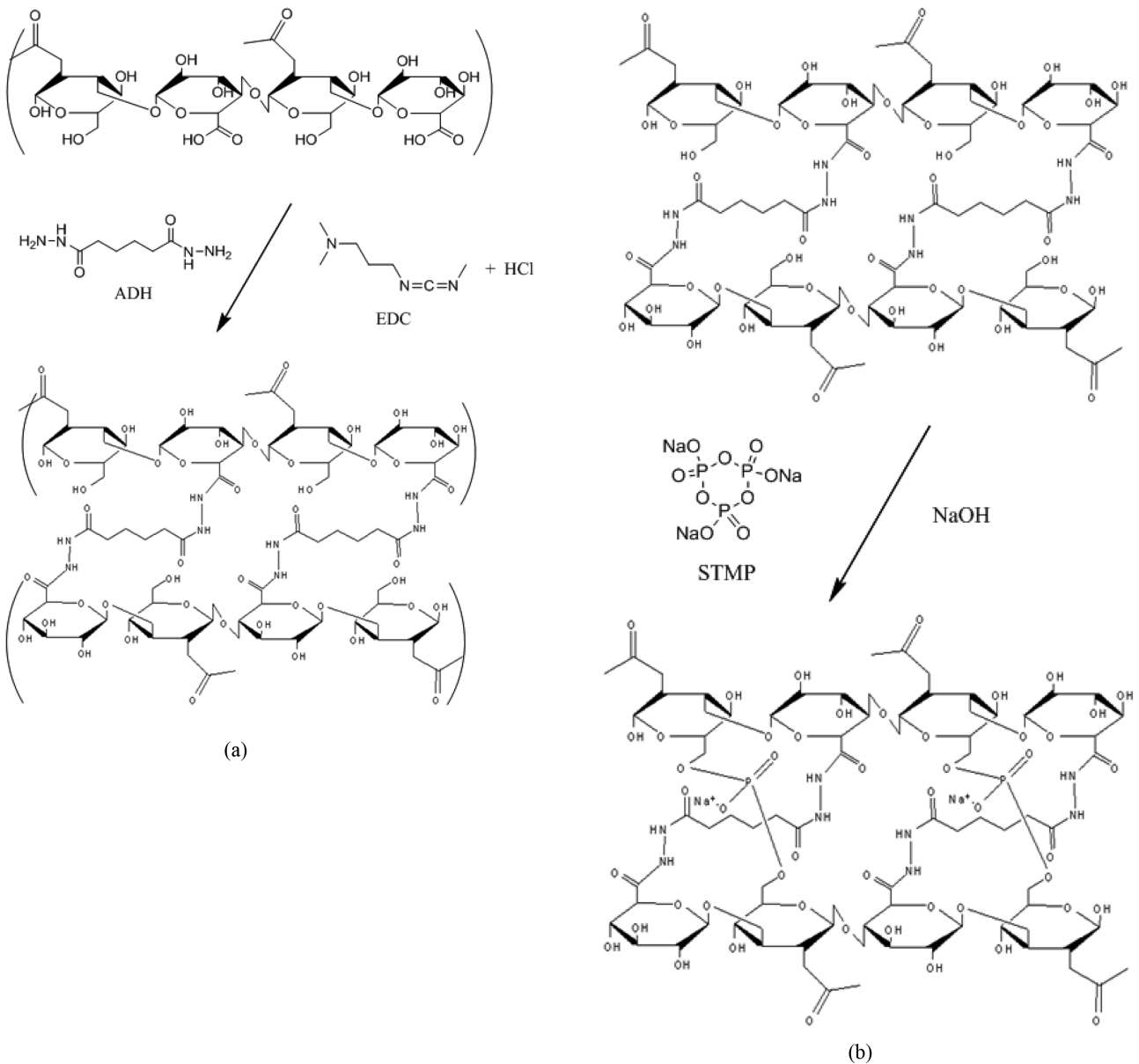


Fig. 2 – Schematic of chemical reaction for preparation of HA microspheres (a) and DC-HA microspheres (b).

바탕으로 크기를 측정하였으며,¹⁴⁾ 제타전위측정기를 이용하여 마이크로입자의 표면전하를 측정하였다.

분해효소에 대한 저항력 측정

제조된 마이크로입자의 생체내 분해효소에 대한 저항성은 히알루노니다제에 의한 분해정도를 통하여 유추하였다. 히알루론산 마이크로입자(10 mg)를 히알루노니다제 500 U/ml을 포함하는 10 ml의 PBS에 첨가 후 37°C에서 항온처리하였다. 0.5, 1, 2, 3, 6 그리고 12시간에 샘플을 취하여 1500 rpm에서 5분간 원심분리하고 상층액을 제거한 후 완전히 건조시켜 히알루론산 마이크로입자의 무게를 측정하였다. 히알루노니다제에 의한 히알루론

산 마이크로입자의 분해정도는 식(1)로부터 계산하였다.^{15,16)}

$$\% \text{ Degradation} = \frac{W_0 - W_t}{W_0} \times 100 \tag{1}$$

W_0 는 마이크로입자의 처음 무게이고 W_t 은 시간 t 에서의 마이크로입자의 무게이다. W_0 는 10 mg으로 동일하게 하였다.

결과 및 고찰

히알루론산 마이크로입자의 표면형태

히알루론산 마이크로입자의 형태는 SEM을 이용하여 관찰하

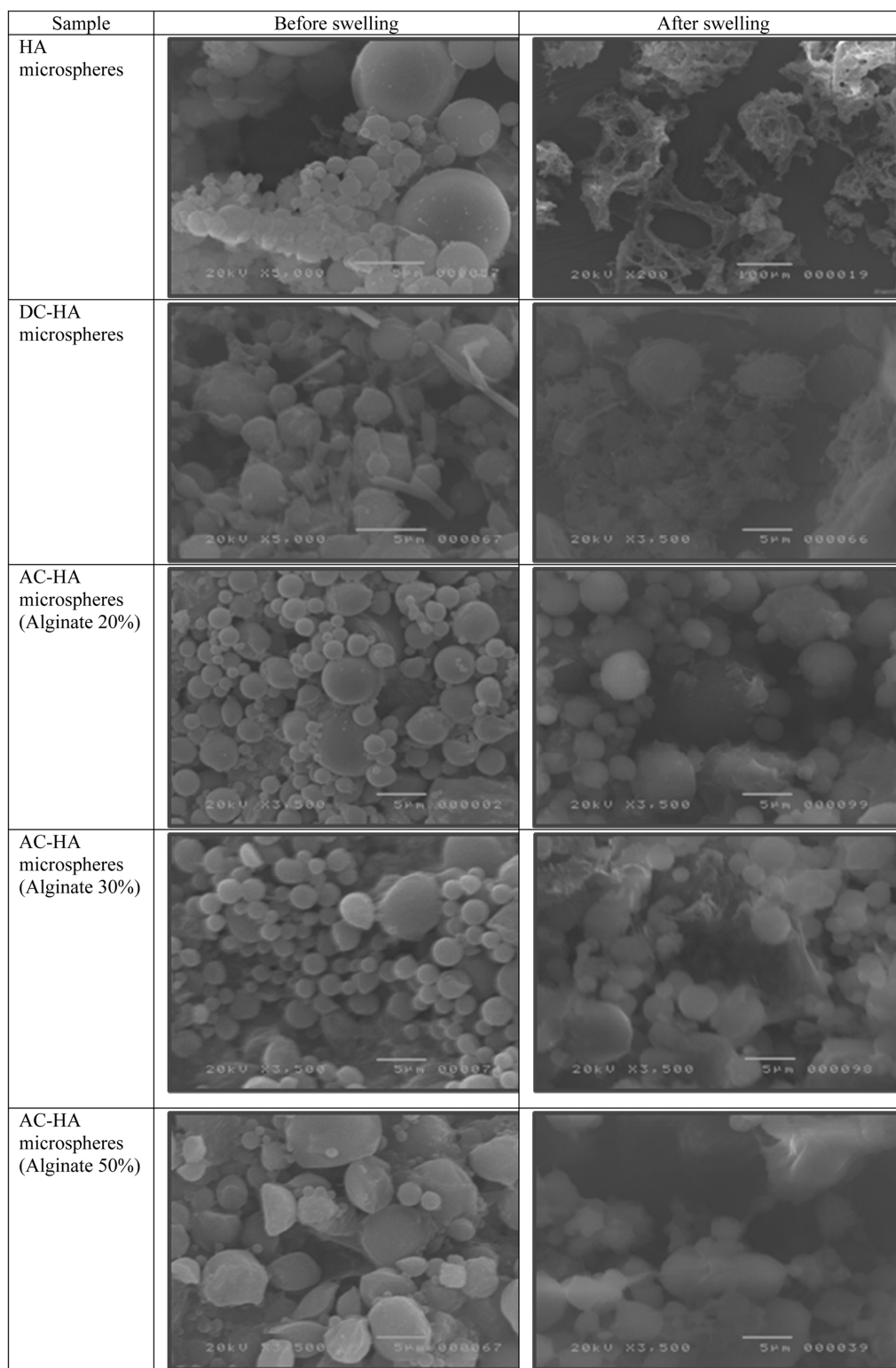


Fig. 3 – The morphology of HA microspheres.

었다(Fig. 3). 수화 전의 HA microspheres는 표면이 매끄러운 구형이었다. 두 가지 종류의 가교제로 이중 가교시킨 DC-HA microspheres의 경우, 구형입자에 막대 형상의 불순물이 관찰되

었는데 이는 1차 가교반응에서 쓰인 HCl과 2차 가교반응에서 쓰인 NaOH의 잔해인 NaCl 염으로 보인다. 그리고 AC-HA microspheres는 알긴산이 20% 포함된 입자(AC-HA microspheres,

Alginate 20%)에서 매끄러운 구형의 마이크로 입자가 형성되었으나, 알긴산의 비율이 30%였을 때는 일부 구형의 입자가 불규칙한 형태를 나타내었으며, 50%의 경우는 대부분의 입자가 불규칙한 형태를 나타내는 것을 확인할 수 있었다. 이는 알긴산의 비율이 높아지면 상대적으로 히알루론산의 비율이 낮아져서, 입자의 형성에 가장 중요한 영향을 미치는 ADH의 가교 수가 적어지기 때문에 상대적으로 입자 형성이 분완전 해졌기 때문인 것으로 생각된다. 30분간 수화 후의 HA microspheres는 구형 입자의 형태를 유지하지 못하고 대부분 녹거나 분해된 것을 확인할 수 있었다. DC-HA microspheres의 경우 HA microspheres에 비하여 구형의 입자를 유지하였고, AC-HA microspheres에서도 수화 전·후의 입자의 형태가 유지되었다.

수화 전후의 히알루론산 마이크로 입자의 모양을 확인해 본 결과, STMP로 이중 가교를 시킨 DC-HA microspheres 또는 알긴산이 함유된 AC-HA microspheres의 경우, HA microspheres에 비해서 형태의 변화가 적은 것을 확인하였다. 이는, 이중 가교나 알긴산에 의한 입자 내부의 네트워크 형성이 수상에서의 히알루론산 마이크로입자의 안정성을 증가시켰기 때문인 것으로 생각된다.

입자크기 및 표면전하

히알루론산 마이크로입자의 크기는 제조방법과는 상관없이 수백 나노미터에서 수십 마이크로미터 이내의 분포를 나타내었다 (Table I). DC-HA microspheres와 AC-HA microspheres (Alginate 20, 30%)의 입자크기는 고른 분포를 보였으나 HA microspheres와 AC-HA microspheres (Alginate 50%)의 입자크기는 분포가 일정하지 않은 것으로 관찰되었다. 또한 가교제의 양이 늘어났을 때 입자 크기가 증가한다는 선행 연구결과들이 있었으나,^{14,17)} 본 연구에서는 HA microspheres에 비해 DC-HA microspheres의 입자의 크기 변화는 관찰되지 않았다. 본 실험에서 제조한 이중 가교의 경우, Fig. 2에서와 같이 가교제인 ADH와 STMP의 결합부위가 다르기 때문에 입자의 크기에 영향을 미치지 않은 것으로 생각된다.

히알루론산 마이크로입자의 표면전하는 -30~40 mV 정도의 강한 음전하를 나타내었으며 이중 가교나 알긴산을 첨가한 경우에도 그 변화는 크지 않았다. 50%의 알긴산이 함유된 히알루론산 마이크로입자(AC-HA, Alginate 50%)의 경우, 표면전하는

Table I – Size distribution and zeta potential of HA microsphere

Samples	Particle size (μm)	Zeta potential (mV)
HA microspheres	0.5-15	-39.97±14.54
DC-HA microspheres	0.5-10	-35.02±6.41
AC-HA (Alginate 20%) microspheres	0.5-10	-33.70±6.53
AC-HA (Alginate 30%) microspheres	0.5-10	-29.19±15.64
AC-HA (Alginate 50%) microspheres	0.5-15	-48.17±18.15

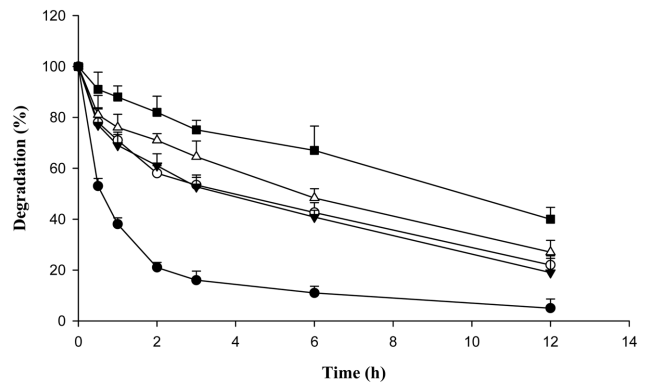


Fig. 4 – Resistance of HA microspheres against hyaluronidase. (●) HA microspheres; (○) DC-HA microspheres; (▼) AC-HA microspheres (20%); (△) AC-HA microspheres (30%); (■) AC-HA microspheres (50%).

-48.17 mV로서 다른 입자에 비해 낮았지만 통계적인 유의성 있는 차이는 보이지 않았다.

히알루론산 분해효소에 대한 저항력

히알루론산 마이크로입자의 생체내 효소에 대한 안정성 평가는 히알루노니다제에 의한 마이크로입자의 분해정도로 평가하였다 (Fig. 4). HA microsphere의 경우 히알루노니다제에 노출된 후 입자의 무게가 급격히 감소하여 30분 후 원래 무게의 53%만 남았으며 3시간 후는 대부분이 분해되었다. 그러나 DC-HA microsphere의 경우는 3시간 후 원래 무게의 53.4%가 남았고 이후 일정한 속도로 분해되었다. DC-HA microspheres는 Fig. 2에서 나타낸 것과 같이 1차 가교제인 ADH와 2차 가교제인 STMP가 히알루론산을 가교시켜 주기 때문에 가교제 ADH만을 사용한 HA microspheres에 비해 생체내 효소에 대한 안정성이 증가됨을 알 수 있었다. 또한 알긴산을 20% 포함한 AC-HA microspheres도 3시간 후 원래 무게의 52.7%가 남았고 DC-HA microspheres와 비슷한 속도로 분해되었다. 그리고 알긴산의 비율이 높아질수록 AC-HA microspheres의 분해정도가 줄어드는 것을 볼 수 있었다. 이는 알긴산과 히알루론산의 네트워크 폴리머 구조와 알긴산의 존재가 히알루론산에 대한 분해효소의 접촉에 장애물로 작용하여 저항성을 가지는 것이라 생각된다. 그리고 알긴산의 비율이 높아질수록 입자의 분해정도가 줄어드는 것은 안정성 증가의 원인 외에도 입자내의 히알루론산이 차지하는 양이 줄어든 것이 큰 원인이라고 생각된다.

이러한 분해정도 평가를 통하여 히알루론산 마이크로입자의 생체내 효소 저항성을 확인 하였고, 이는 이중가교나 입자내부의 폴리머 네트워크 형성을 통하여 제조된 히알루론산 마이크로 입자의 경우가 하나의 가교제로 사용된 마이크로 입자에 비하여 생체내 효소에 대한 저항성이 증가되었기 때문인 것으로 생각된다.

결 론

생체적합 고분자물질인 히알루론산을 마이크로입자의 형태로 제조하여 약물의 방출을 조절할 수 있는 전달체로 이용하려는 연구가 계속적으로 진행되고 있다. 본 연구에서 제조한 이중 가교된 DC-HA microspheres와 알긴산이 포함된 AC-HA microspheres는 입자크기가 수 마이크로미터이고 대략 -30 mV의 표면전하를 가진 균일한 형태를 나타내었다. 또한, DC-HA microspheres와 AC-HA microspheres는 가교제를 하나만 사용한 HA microspheres에 비해 수화 후에도 입자의 형태를 안정적으로 유지하고 생체내 분해효소에 대한 안정성 또한 증가하는 것을 확인하였다. 이러한 결과들로부터, DC-HA microspheres와 AC-HA microspheres는 가교제 하나만을 사용한 HA microspheres에 비해 약물 방출 속도를 늦출 수 있을 것으로 예상되며, 향후 서방형 약물 전달체로서의 가능성을 검토할 필요가 있을 것으로 생각된다.

감사의 말씀

이 논문은 2010년도 정부(농촌진흥청)의 재원으로 국립원예특작과학원 인삼특작부 약용작물과의 지원을 받아 수행된 연구임 (NO. PJ006921).

참고문헌

- 1) Laurent, T., Laurent, U. and Fraser, J. R. : Functions of hyaluronan. *Ann. Rheum. Dis.* **54**, 429 (1995).
- 2) Laurent, T., Laurent, U. and Fraser, J. R. : The structure and function of hyaluronan: An overview. *Immunol. Cell Biol.* **74**, A1 (1996).
- 3) Chen, W. and Abatangelo, G. : Functions of hyaluronan in wound repair. *Wound Repair Regen.* **7**, 79 (1999).
- 4) Scott, J. : Extracellular matrix, supramolecular organisation and shape. *J. Anat.* **187**, 259 (1995).
- 5) Collis, L., Hall, C., Lange, L., Ziebell, M., Prestwich, R. and Turley, E. : Rapid hyaluronan uptake is associated with enhanced motility: implications for an intracellular mode of action. *FEBS Letters* **440**, 444 (1998).
- 6) Toole, B. : Hyaluronan in morphogenesis, *Semin. Cell Dev. Biol.* **12**, 79 (2001).
- 7) Gerdinand, B. and Hallgren, R. : Dynamic role of hyaluronan (HYA) in connective tissue activation and inflammation. *J. Intern. Med.* **242**, 49 (1997).
- 8) Kim, A., Checla, D. M. and Chen, W. : Characterization of DNAhyaluronan matrix for sustained gene transfer. *J. Control. Release* **90**, 81 (2003).
- 9) Freed, L. E., Vunjak-Novakovic, G., Biron, R. J., Eagles, D. B., Lenov, D. C., Barlow, S. K. and Langer, R. : Biodegradable polymer scaffolds for tissue engineering. *Biotechnology* **12**, 689 (1994).
- 10) Kang, J. Y., Chung, C. W., Sung, J. H., Park, B. S., Choi, J. Y., Lee, S. J., Choi, B. C., Shim, C. K., Chung, S. J. and Kim, D. D. : Novel porous matrix of hyaluronic acid for the three-dimensional culture of chondrocytes. *Int. J. Pharm.* **369**, 114 (2009).
- 11) Yunand, Y. : Hyaluronan microspheres for sustained gene delivery and site-specific targeting. *Biomaterials* **25**, 147 (2004).
- 12) Zhao, X. B., Fraser, J. E., Alexander, C., Lockett, C. and White, B. J. : Synthesis and characterization of a novel double crosslinked hyaluronan hydrogel. *J. Mater. Sci.* **13**, 11 (2002).
- 13) Zawko, S., Suri, S., Truong, Q. and Schmidt, C. : Photopatterned anisotropic swelling of dual-crosslinked hyaluonic acid hydrogels. *Acta Biomater.* **5**, 14 (2009).
- 14) Dulong, V. : Hyaluronan-based hydrogels particles prepared by crosslinking with trisodium trimetaphosphate. Synthesis and characterization. *Carbohydr. Polym.* **57**, 1 (2004).
- 15) Scott, A., Zawko, Shalu S., Quan, T. and Chrestine, E. Schmidt : Photopatterned anisotropic swelling of dual cross-linked hyaluronic acid hydrogels. *Acta Biomater.* **5**, 14 (2009).
- 16) Zhao, X. B., Fraser, J. E., Alexander, C., Lockett, C. and White, B. J. : Synthesis and characterization of a novel double crosslinked hyaluronan hydrogel. *J. Mater. Sci.* **13**, 11 (2002).
- 17) Cheon, J. W., Shim, C. K., Chung, S. J. and Kim, D. D. : Effect of tripolyphosphate (TPP) on the controlled release of cyclosporin a from chitosan-coated lipid microparticles. *J. Kor. Pharm. Sci.* **39**, 59 (2009).